Imperial College London

# Tuning Morphology of Hybrid Organic/Metal Sulfide Solar Cells

Andrew John MacLachlan

Department of Physics

Imperial College London

A thesis submitted in fulfilment of the requirements for the degree of

Doctor of Philosophy

May 2015

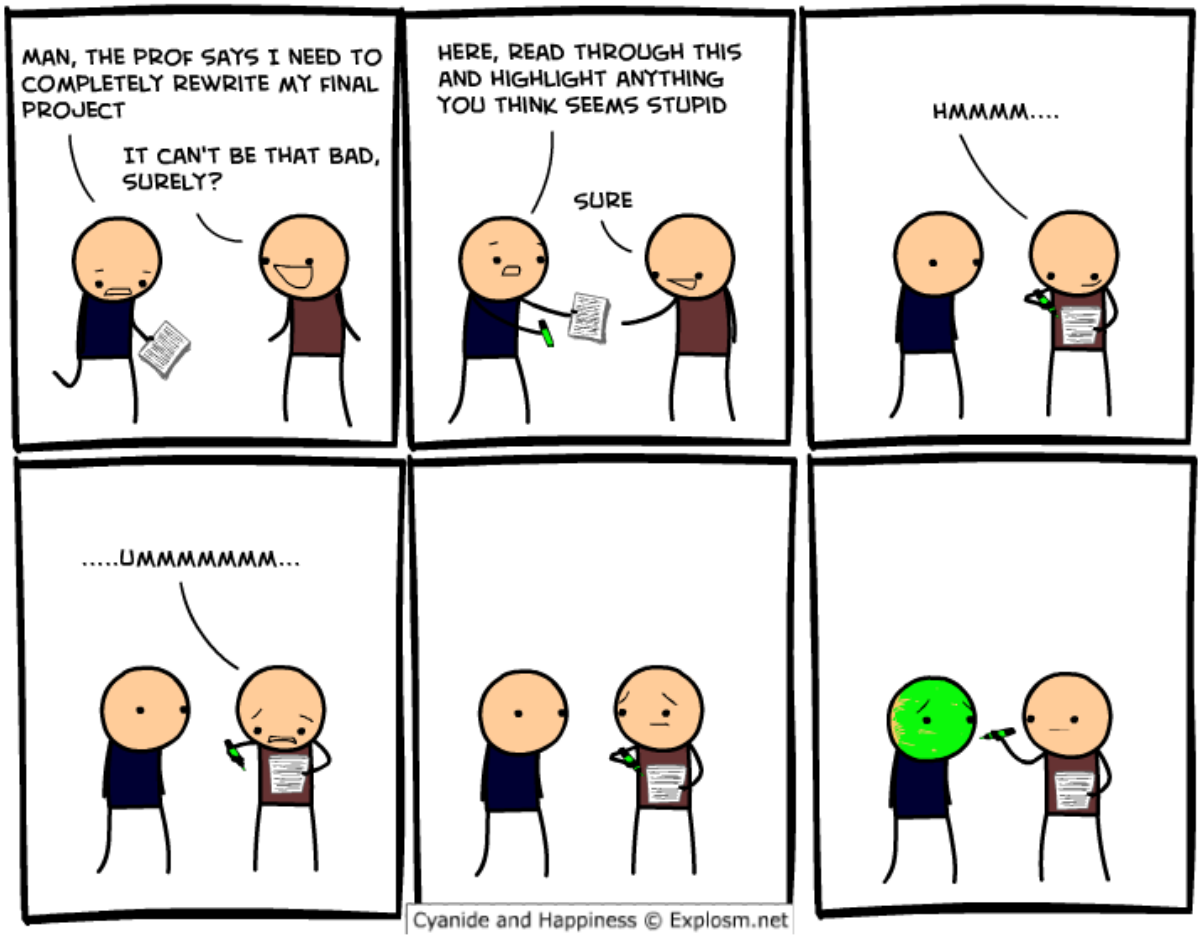
# Abstract

This thesis explores the influence that morphology plays in hybrid organic/inorganic solar cells. This is studied for a range of different materials systems.

A series of cadmium xanthate complexes were synthesised, for use as *in-situ* precursors to CdS nanoparticles in hybrid poly(3-hexylthiophene-2,5-diyl (P3HT)/CdS solar cells. The heterojunction morphology of these hybrid P3HT/CdS blends was found to be dependent on the ligand moiety of the precursor used. The formation of CdS domains was studied by time-resolved materials characterisation techniques and directly imaged using electron microscopy. A combination of transient absorption spectroscopy (TAS) and photovoltaic device performance measurements was used to show the intricate balance required between charge photogeneration and having percolated domains in order to effectively extract charges to maximize device power conversion efficiencies. An analogous method was also applied to a P3HT/$Sb_2S_3$ system.

Following on from the previous work, a non-toxic alternative to CdS and $Sb_2S_3$ was explored. Bismuth xanthates were thermally decomposed to form hybrid polymer/$Bi_2S_3$ heterojunctions with two distinctly different morphologies. The bismuth xanthates were found to form nanorods *in-situ,* within the solid-state polymer matrix, as well as mesostructured arrays of $Bi_2S_3$ rods that were later infiltrated with a polymer, using a two-step method. TAS was used to study the charge generation yield in both these systems and hybrid photovoltaic devices were also fabricated.

Finally, through a collaboration with The Institute of Photonic Sciences (ICFO), TAS was used to study two separate organic semiconductor/$Bi_2S_3$ BHJs. The first of which was a P3HT/$Bi_2S_3$ nanoparticle blend solar cell. The charge generation yield in this system was investigated and then compared to a novel thiol-functionalised P3HT based block copolymer (P3HT-SH). Secondly, TAS was used to obtain a better understanding of the charge transfer at several interfaces in a vertically structured $Bi_2S_3$ nanorod array that was filled with 2,2',7,7'-Tetrakis-(N,N-di-4-methoxyphenylamino)-9,9'-spirobifluorene (SPIRO).


MAN, THE PROF SAYS I NEED TO COMPLETELY REWRITE MY FINAL PROJECT
IT CAN'T BE THAT BAD, SURELY?
HERE, READ THROUGH THIS AND HIGHLIGHT ANYTHING YOU THINK SEEMS STUPID
SURE
HMMMM....
.....UMMMMMMM...
Cyanide and Happiness © Explosm.net

# Declaration of Originality

Except where specific reference is made to the contributions of others, this thesis represents my own work. No part of it has been submitted to satisfy the requirements of any other degree at this or any other university.

Andrew J MacLachlan

May 2015

# Copyright Declaration

The copyright of this thesis rests with the author and is made available under a Creative Commons Attribution Non-Commercial No Derivatives licence. Researchers are free to copy, distribute or transmit the thesis on the condition that they attribute it, that they do not use it for commercial purposes and that they do not alter, transform or build upon it. For any reuse or redistribution, researchers must make clear to others the licence terms of this work.

# Acknowledgements

Over the course of my PhD I have received help, guidance and so much more from a vast number of people. I literally would not have got through it without many of your contributions.

I would first of all like to thank my two supervisors, Saif and Jenny. Saif, your perpetual enthusiasm and optimism is truly remarkable. Under someone else's guidance I may have given up on certain aspects of this work, but you made me persist. Jenny, I think I'm safe in saying I don't think I'll ever meet someone with a mind like yours. Your attention to detail and critical comments on my work have been of great assistance. Thank you both for all your help and support.

A PhD is somewhat of a team effort and many people have helped me in the lab along the way. With regards to synthesis, thank you to Thierry, Irene and also to Thomas. For help with device and film fabrication, thank you to Simon D, Nurlan, Pabitra, Mike, Luis and Neha. For spectroscopy many thanks to Luke, Flannan, Ute, Stoichko, Annalisa and Simon K. Many of you contributed in more ways than one and some of your work has made it into this thesis. Thank you as well to the many collaborators outside of my research group that have provided samples for this work, particularly Luis and Yiming for their contributions used in Chapter 6.

The support I've received has extended far beyond just academic help. I have had an unbelievably great time during my PhD and I've made friends that I know I will keep in touch with for the rest of my life. The basement has provided me with the cake club, the crossword, Burn's Night Twister, squash games, the sauna and countless beers in the Holland Club and more recently h-bar. So thank you to all members, past and present (In alphabetical order, so as to not offend anyone): Adrian, Alice, Andreas, Anna, Annalisa, Baz, Chaz, Ching Hong, Clare, Dan B, Dan C, Elisa, Ernest, Fi, Flannan, Florian, Florent, Freddie, George, Harry, Henry, Irene, James, Korn, Li, Luis, Luke, Madeleine, Mike , Neha, Nurlan, Pabitra, Scot, Seb, Simon D, Simon K, Siva, Steph, Steve, Stoichko, Thierry, Thomas, Ute, Yiming and Yvonne.

From home, I would like to thank my parents, for supporting me and also trying really hard to learn what it is that I do. Also I'd like to thank Ireney, particularly for during the write-up process. Thank you for all the teas and love. I hope I can be as helpful when your time comes.

# List of Publications

Solution Processed Bismuth Sulfide Nanowire Array Core/Silver Sulfide Shell Solar Cells Cao, Y.; Bernechea, M.; Maclachlan, A. J.; Zardetto, V.; Creatore, M.; Haque, S.; Konstantatos, G. *Chemistry of Materials* 2015, *27,* 3700.

Polymer/nanocrystal hybrid solar cells: Influence of molecular precursor design on film nanomorphology, charge generation and device performance MacLachlan, A. J.; Rath, T.; Cappel, U. B.; Dowland, S. A.; Amenitsch, H.; Knall, A-C.; Buchmaier, C.; Trimmel, G.; Nelson, J.; Haque, S. A. *Advanced Functional Materials* 2015, *3*, 409.

Improved electronic coupling in hybrid organic-inorganic nanocomposities employing thiol-functionalized P3HT and bismuth sulfide nanocrystals Martinez, L.; Higuchi, S.; MacLachlan, A. J.; Stavrinadis, A.; Miller, N.C.; Diedenhofen, S. L.; Bernechea, M.; Sweetnam, M.; Nelson, J.; Haque, S. A.; Tajima, K.; Konstantatos, G. *Nanoscale* 2014, *6*, 10018.

Solution-Processed Mesoscopic $Bi_2S_3$: Polymer Photoactive Layers MacLachlan, A. J.; O'Mahony, F. T.; Sudlow, A. L.; Hill, M. S.; Molloy, K. C.; Nelson, J.; Haque, S. A. *ChemPhysChem* 2014, *15*, 1019.

Photoinduced electron and hole transfer in CdS:P3HT nanocomposite films: effect of nanomorphology on charge separation yield and solar cell performance Dowland, S. A.; Reynolds, L. X.; MacLachlan, A.; Cappel, U. B.; Haque, S. A. *J. Mater. Chem. A* 2013, *1*, 13896.

Influence of crystallinity and energetics on charge separation in polymer–inorganic nanocomposite films for solar cells Bansal, N.; Reynolds, L. X.; MacLachlan, A.; Lutz, T.; Ashraf, R. S.; Zhang, W.; Nielsen, C. B.; McCulloch, I.; Rebois, D. G.; Kirchartz, T. *Scientific reports* 2013, *3*.

Charge photogeneration in hybrid solar cells: A comparison between quantum dots and in situ grown CdS Reynolds, L. X.; Lutz, T.; Dowland, S.; MacLachlan, A.; King, S.; Haque, S. A. *Nanoscale* 2012, *4*, 1561.

Thermal decomposition of solution processable metal xanthates on mesoporous titanium dioxide films: a new route to quantum-dot sensitised heterojunctions Lutz, T.; MacLachlan, A.; Sudlow, A.; Nelson, J.; Hill, M. S.; Molloy, K. C.; Haque, S. A. *PCCP* 2012, *14*, 16192.

Effect of Multiple Adduct Fullerenes on Microstructure and Phase Behaviour of P3HT: Fullerene Blend Films for Organic Solar Cells Guilbert, A. A.; Reynolds, L. X.; Bruno, A.; MacLachlan, A.; King, S. P.; Faist, M. A.; Pires, E.; Macdonald, J. E.; Stingelin, N.; Haque, S. A. *ACS nano* 2012, *6,* 3868.

# Table of Contents

Abstract ..... 3

Declaration of Originality ..... 7

Copyright Declaration ..... 9

Acknowledgements ..... 11

List of Publications ..... 13

Table of Contents ..... 15

List of Figures ..... 19

List of Tables ..... 27

Acronyms and Abbreviations ..... 29

Chapter 1

Introduction ..... 31

Challenges of the Modern World ..... 33

Renewable Energy ..... 34

Photovoltaics ..... 35

References ..... 37

Chapter 2

Background and Theory ..... 39

Photovoltaics ..... 41

A Brief History ..... 41

Semiconductors and Photovoltaics ..... 41

Electrical Characterisation of Photovoltaics ..... 43

Organic Semiconducting Polymers ..... 45

The Bulk Heterojuntion Solar Cell ..... 48

Hybrid Organic/Inorganic Solar Cells ..... 50

*Ex-situ* Polymer/Nanoparticle Solar Cells ..... 51

*In-situ* Polymer/Nanoparticle Solar Cells ..... 55

Project Aims and Motivation ..... 57
References ..... 59

Chapter 3

Experimental Methods and Techniques ..... 63
Materials Syntheses ..... 65
Cadmium Xanthate Complexes ..... 65
Antimony Xanthate Complexes ..... 66
Bismuth Xanthate Complexes ..... 67
Thin Film and Device Fabrication ..... 68
Substrates ..... 68
Electron Selecting Oxide Layers ..... 68
Seed Layers ..... 69
Active Layers ..... 69
Top Contacts ..... 70
Experimental Characterisation Techniques ..... 71
UV-Vis Absorption Spectroscopy (UV-Vis) ..... 71
Photoluminescence Spectroscopy (PL) ..... 71
Raman Spectroscopy ..... 71
X-ray Diffraction (XRD) ..... 71
Grazing Incidence Wide Angle X-ray Scattering (GIWAXS) and Grazing Incidence Small Angle Scattering (GISAXS) ..... 71
Transmission Electron Microscopy (TEM) ..... 72
Thermogravimetric Analysis (TGA) ..... 72
Transient Absorption Spectroscopy (TAS) ..... 72
Current Voltage Measurements ..... 74
References ..... 75

## Chapter 4

Control of Hybrid Film Nanomorphology in P3HT/Metal Sulfide Solar Cells ..... 77
Abstract ..... 79
Introduction ..... 81
Experimental ..... 85
Cadmium Xanthate ..... 85
Antimony Xanthate ..... 86
Results and Discussion ..... 87
Film Morphology and Nanoparticle Growth ..... 87
Photophysical Properties ..... 95
Photovoltaic Devices ..... 101
Antimony Sulfide ..... 104
Conclusions ..... 114
References ..... 116

## Chapter 5

Synthesis of $Bi_2S_3$ Utilising the *In-situ* Decomposition of Bismuth Xanthates ..... 119
Abstract ..... 121
Introduction ..... 123
Experimental ..... 125
Bismuth Sulfide/Polymer Blend Heterojunctions ..... 125
Mesostructured Bismuth Sulfide ..... 125
Results and Discussion ..... 126
Polymer/$Bi_2S_3$ Blend Heterojunctions ..... 126
Solution-processed Mesoscopic Polymer:$Bi_2S_3$ Photoactive Layers ..... 135
Conclusions ..... 143
References ..... 144

## Chapter 6

Transient Absorption Spectroscopy of Hybrid $Bi_2S_3$ Solar Cells ..... 147

Abstract ..... 149

Introduction ..... 151

Experimental ..... 155

Polymer/$Bi_2S_3$ Nanoparticle Blends ..... 155

$Ag_2S$ Coated $Bi_2S_3$ Nanowires ..... 155

Results and Discussion ..... 157

Polymer/$Bi_2S_3$ Nanoparticle Blends ..... 157

$Ag_2S$ Coated $Bi_2S_3$ Nanowires ..... 166

Conclusions ..... 175

References ..... 176

## Chapter 7

Conclusions and Future Work ..... 179

Conclusions ..... 181

Suggestions for Further Work ..... 184

References ..... 185

# List of Figures

Figure 1.1 - World total primary energy supply from 1971 to 2012 by fuel in millions of tonnes of oil equivalent (MTOE). This figure is taken from "Key World Energy Statistics" by the International Energy Agency.[4] **Peat and oil shale are aggregated with coal. ***Includes geothermal, solar, wind, heat, etc. ..... 33

Figure 1.2 - Average annual solar irradiance over a 3 year average, accounting for day and night and also cloud cover. The black dots represent the total surface area of the planet required to be covered in solar cells, with a power conversion efficiency of 8%, in order to account for the current total worldwide energy demand.[10] ..... 35

Figure 2.1 - (Left) Energy level diagram showing the combination of 2 AOs to give the bonding and anti-bonding MOs and also the resulting MOs for a combination of 4 atoms. (Right) The crystal case where there are so many MOs with energies so close together that they appear to be a continuum and are referred to as bands. ..... 42

Figure 2.2 - Current-voltage plot of an example photovoltaic device. The solid line is from a device measured in the light and the dotted line for a device measured in the dark..... 43

Figure 2.3 - The equivalent circuit for a solar cell comprising a current source (delivering $I_{SC}$), a diode, and two resistances which represent the non-ideality within the device – a shunt resistance ($R_{sh}$) in parallel, and a series resistance ($R_s$) in series..... 45

Figure 2.4 - Examples of some structures of semiconducting polymers: polypyrrole (PPy), polyacetylene (PA), poly(p-phenylene vinylene) (PPV), polyanaline (PAn), polythiophene (PT) and polyfluorene (PF).46

Figure 2.5 - Conjugated backbone of PA showing the overlapping $p_z$ orbitals and how the band gap decreases with increasing conjugation length. ..... 46

Figure 2.6 - Schematic diagram illustrating the basic function of an organic excitonic solar cell. The yellow arrow represents the absorption of a photon, creating a bound electron-hole pair, referred to as an exciton. This exciton is split at an interface between the donor and the acceptor, and the charges are transported to the relevant electrodes. ..... 47

Figure 2.7 - Schematic diagram of an ideal bulk heterojunction (left) and a more random mixture of the donor and acceptor (right)..... 48

Figure 3.1 - Schematic diagram of a transient absorption spectroscopy (TAS) setup. On the right some example data is given, illustrating the two different operational modes: constant time and constant probe wavelength. Some common examples of the processes that can be observed are also shown as

cartoons, with the red arrows representing excitations caused by the pump pulse and then the green arrows representing excitations caused by the probe, either in a single material or in a two-component system after charge transfer, shown by the blue dashed arrow, ..... 73

Figure 4.1 - General chemical structure of the Cd-xanthate precursors used (bispyridine cadmium(II) dithiocarbonate) along with the different R Group moieties. It should also be noted that in the case of the heptyl xanthate, there are no pyridine adducts present, as due to the branched side chains, good solubility is already obtained without them. The synthesis and characterisation of these materials are present in Chapter 3. ..... 85
Figure 4.2 - Chemical structure of the antimony xanthate precursors used in this chapter. ..... 86
Figure 4.3 - Bright field TEM (transmission electron microscopy) images of thin films of hybrid P3HT/CdS heterojunctions, fabricated from a series of Cd-xanthate precursors with increasing ligand moieties from left to right. The darker regions of contrast are indicative of a higher concentration of cadmium. ..... 87
Figure 4.4 - a) Thermogravimetric analysis (TGA) of the thermal decomposition of the Cd-xanthates (Ethyl, Propyl, Butyl, Pentyl, Heptyl) investigated in this study. b) X-ray diffraction patterns of P3HT/CdS nanocomposite layers prepared from the different Cd-xanthates via thermal annealing at 160°C for 60 min. The main peaks of both the hexagonal as well as the cubic phase are labelled with their Miller indices. ..... 88
Figure 4.5 – a) GIWAXS patterns of P3HT/Cd xanthate films measured between 22.9 and 35° 2 theta during a heating run from room temperature to 200°C with a heating rate of 10°C/min showing the evolution of the most intense peak of CdS at around 27° 2 theta. b) 2D-surface plots of the GIWAXS patterns above vs temperature. ..... 90
Figure 4.6 – Normalised integrated intensity of the GIWAXS patterns of the different P3HT/metal xanthate samples calculated between 22.9 and 35° 2 theta plotted versus reaction time and temperature. ..... 91
Figure 4.7 - GISAXS images of the samples at different temperatures (50, 100, 125, 150, 175, 200 °C) during the heating run. The red boxes indicate the vertical areas used for integration. ..... 93
Figure 4.8 - Left: Temperature-dependent evolution of the vertical cuts of the GISAXS patterns of the investigated samples. The increasing temperature (T) is indicated with an arrow in the Ethyl sample. Right: Integrated Intensities of the GISAXS patterns measured during the heating run compared with those of GIWAXS. ..... 94
Figure 4.9 - a) Steady-state absorption measurements of P3HT/CdS heterojunctions normalised at 520 nm. b) Photoluminescence quenching measurements relative to a neat P3HT sample (excited at 567 nm). c) Femtosecond transient absorption (fs-TAS) decays of samples measured at 1270 nm,

corresponding to the P3HT exciton absorption. d) Normalised parameters from each of the other figures showing the trends observed from each of the different techniques. ..... 95
Figure 4.10 - Transient absorption spectroscopy (TAS) decays at 980 nm using an excitation wavelength of 400 nm exciting predominantly CdS domains a) and 567 nm exciting exclusively P3HT domains b). All traces are scaled by the amount of pump light absorbed. The amplitudes of all signals at both wavelengths are plotted in c) with the data normalised to the highest signal in d). ..... 97
Figure 4.11 - a) Current-voltage characteristics of representative devices, b) average power conversion efficiencies (PCE) and short circuit currents (Jsc) of an average of the 10 devices with the highest PCE, c) average fill factors (FF) and open circuit voltages (Voc) of the same 10 most efficient devices. ..... 101
Figure 4.12 – a) Incident photon to current conversion efficiency measurements (IPCE) of typical devices fabricated from each of the different precursor ligands. b) IPCE measurements normalised to the maximum IPCE fraction for each device. ..... 102
Figure 4.13 - a) UV-Vis absorptance measurements of P3HT/$Sb_2S_3$ blend films on a range of different seed layers, as well as the absorptance of the seed layers themselves. b) X-Ray diffraction patterns of identical films, along with a reference pattern for stibnite. ..... 105
Figure 4.14 - a) Transient absorption spectra of a P3HT/$Sb_2S_3$ blend film on a glass substrate, without any seed layers, plotted at 10 µs. This sample was excited with a wavelength of 567 nm. b) Transient absorption decays of films on different seed layers, excited at 567 nm or 700 nm and probed at 980 nm. All samples were excited with the same approximate number of photons and are scaled for the amount of pump light absorbed. c) Amplitude of all signals at 1 µs as well as their halftimes. ..... 106
Figure 4.15 - a) Transient absorption decays of P3HT/$Sb_2S_3$ blends with an equal blend ratio. Samples were excited using a pump wavelength of 567 nm. b) The same samples pumped at 700 nm. All decays are monitoring the decay at 980 nm, are excited with the same approximate number of photons and are scaled for the amount pump light absorbed. ..... 108
Figure 4.16 – TEM images of a P3HT/$Sb_2S_3$ blend film with a volume ratio of 1:1.4, fabricated using the Ethyl xanthate a) and the Pentyl xanthate b) at the same level of magnification. c) The same Pentyl film at a different region of the sample where the film has curled. d) Histogram of the approximate particle size distribution of the Ethyl film and e) the Pentyl film. ..... 109
Figure 4.17 – a) Current-voltage measurements of the optimum devices fabricated a range of blend ratios, as well as with the highest blend ratio without a P3HT capping layer (No Top). The measurements performed in the light are represented by the solid lines and the dark curves are shown by the dotted lines. b) Average characteristic device parameters of all working photovoltaic devices. c) Average PCE and $J_{SC}$ plotted for all the working device and the same for $V_{OC}$ and FF d). ..... 110
Figure 4.18 – a) Current-voltage curves of the optimum devices fabricated in this study, as well as these devices measured after masking. The solid lines are measurements made in the light and dotted lines

represent dark curves. b) Tabulated average characteristic device parameters for the devices in this series, as well as the values for the devices with the highest PCE after masking. c) Incident photon to current conversion efficiencies of these masked devices. ..... 112

Figure 5.1 - a) UV-Vis absorption spectra of a typical polystyrene (PS)/$BiEX_3$ blend film as spun (red) and after annealing (black). b) Raman spectra of the same films, as spun (red) and after annealing (black), both labelled with their approximate stretches. c) X-ray diffraction (XRD) pattern of a typical PS/$Bi_2S_3$ blend film, fabricated by annealing at 160°C (black) as well as a reference pattern for bismuthinite (01-075-1306) (red). The Miller indices have been assigned from the reference pattern. d) A more focussed area of the same measurement in c) (black) superimposed with a double Gaussian fit (red). This fit was used to calculate the FWHM and ultimately the mean particle size using the Scherrer equation. ..... 126
Figure 5.2 - Transmission electron microscopy (TEM) images of typical PS/$Bi_2S_3$ films at different levels of magnification. Images (a-c) were taken by myself using the Jeol 2000 TEM (further details in Chapter 3) and (d,e) were kindly provided by Shu Chen from the Materials Department, Imperial College London using a Titan electron microscope. ..... 128
Figure 5.3 - UV-Vis absorptance spectra of three different polymer/$Bi_2S_3$ blends. b) Structures of P3HT, F8TAA and $BiEX_3$/$BiPX_3$. (c-e) TEM images of the same three blends as in a) at the same level of magnification. ..... 129
Figure 5.4 - a) Transient absorption spectra of P3HT (black) and F8TAA (green) blended with $Bi_2S_3$ and exciting just the $Bi_2S_3$ by exciting at 700 nm. b) Transient absorption decays at 1000 nm for the same blend films. Are signals are scaled by the amount of pump light absorbed. ..... 131
Figure 5.5 - Current voltage measurements in the light of P3HT/$Bi_2S_3$ devices with (green) and without (red) a thin polymer blocking layer compared to a neat polymer active layer (black). Devices are shown fabricated with P3HT using the bismuth ethyl xanthate precursor a) and the pentyl xanthate b) and also using F8TAA with the bismuth ethyl xanthate c). ..... 132
Figure 5.6 - Schematic diagram of heterojunction formation, showing the formation of the mesoporous absorbing layer after the spin coating and annealing of a soluble bismuth xanthate precursor ($BiEX_3$), followed by a surface treatment and filling of the pores with a hole conducting polymer. ..... 135
Figure 5.7 - a) Absorptance of a thin film of spin coated bismuth xanthate precursor (black), the resulting $Bi_2S_3$ films after annealing (red) and the annealed film infiltrated with P3HT (green). b) Raman spectrum of a typical $Bi_2S_3$ film after annealing. ..... 136
Figure 5.8 - Scanning electron microscopy (SEM) images of the mesostructured $Bi_2S_3$ films on a flat ZnO layer. a) Top down image of a typical film used for further measurements. b) Cross sectional image of

the same film as in a). (c-f) Top down images of films with a lower coverage of $Bi_2S_3$ and annealed at different temperatures. ..... 137
Figure 5.9 - a) X-ray diffraction (XRD) patterns of mesoscopic $Bi_2S_3$ films annealed at a range of temperatures, with a bismuthinite references pattern (01-075-1306). The large peak labelled with an asterisk corresponds to the ZnO underlayer. b) Average crystallite size for each of the films calculated using the Scherrer equation. The crystal size has been measured for 3 different peaks and is also given as an average. ..... 138
Figure 5.10 - UV-Vis absorptance of mesoscopic films annealed at the range of temperatures in this study. ..... 139
Figure 5.11 - a) Transient absorption spectrum at 1 μs after excitation of a mesoscopic film infiltrated with P3HT after a surface treatment with pyridine. b) Transient absorption decay of the same film with and without the pyridine treatment at a probe wavelength of 980 nm. c) Transient decays for films annealed at a range of temperatures after 700 nm excitation and d) 510 nm excitation. All signals are scaled by the amount of pump light absorbed. ..... 139
Figure 5.12 - a) Current voltage plot of the most efficient device in the light. b) IPCE measurement of the device shown in a) with the absorption profile of the device overlaid (red dash). c) Current-voltage plots of a device being light soaked, with the trend in the characteristic parameters shown in d)..... 141

Figure 6.1 - Chemical structure of thiol-functionalised block copolymer P3HT-SH. ..... 152
Figure 6.2 - a) UV-Vis absorptance measurements of P3HT/$Bi_2S_3$ blend films with a range of blend ratios, labelled by the relative weight percent of $Bi_2S_3$ in the film. b) TAS spectrum of an 80% film using an excitation wavelength of 510 nm and plotting the ΔAbs at 1 μs after excitation. c) Transient absorption decays of the range of blend films excited at 700 nm and probed at 980 nm. d) The same films after excitation at 510 nm, probing at 980 nm. Both sets of decays are excited using the same approximate number of photons and are scaled for the number of photons absorbed. ..... 157
Figure 6.3 - a) TAS decays of films of P3HT/$Bi_2S_3$ blends containing an 80% weight ratio of $Bi_2S_3$ annealed at a range of temperatures under atmospheric conditions. Samples were excited with at 510 nm, probed at 980 nm and are scaled for the amount of pump light absorbed. b) The initial amplitudes (500 ns) and halftimes of these same films. ..... 159
Figure 6.4 - Transient absorption decays of P3HT/$Bi_2S_3$ films fabricated with no ligand exchange and with either an exchange with pyridine or EDT, excited at either 510 nm a) or 700 nm b) and probing at 980 nm. All traces are excited using approximately the same number of photons and are scaled for the amount of pump light absorbed. c) UV-Vis absorptance spectra of the same three films. d) Initial amplitudes (500 ns) and halftimes of the traces plotted for each of the ligands. ..... 160

Figure 6.5 - a) Normalised UV-Vis absorption spectra of a typical polymer/Bi2S3 fabricated with either P3HT (black) or the block copolymer P3HT-SH (green). b) TAS spectra of the same films, excited at 510 nm and normalised to the maximum ΔAbs value. ..... 161
Figure 6.6 - TAS decays of polymer/$Bi_2S_3$ blend films containing P3HT (black), P3HT-SH (green) or a mixture of both (magenta) excited at either 700 nm a) or 510 nm b). All decays are probed at 980 nm, excited with approximately the same number of photons and scaled for the amount of pump light absorbed. c) Initial ΔAbs of the decays (500 ns) as well as the halftimes d). ..... 162
Figure 6.7 - Diagram of the energy level alignment in the ternary P3HT:P3HT-SH/$Bi_2S_3$ blend heterojunctions. All energy levels are not to scale and are intended solely to illustrate to approximate shape of the energy landscape. ..... 163
Figure 6.8 - (left) Diagram of the device architecture used in this section along with the a cartoon of the approximate energy levels of each of the different layers (right). The energy levels are not to scale and are ended solely as guide to illustrate the energy landscape. ..... 166
Figure 6.9 - a) Cartoon energy level diagram of the heterojunction used in this measurement. The green arrows represent the absorption of the 510 nm pump light from the laser. b) TAS spectra of the system at a range of times after excitation. c) TAS decays at the wavelengths of interest from the spectra. d) The same decays normalised to the same initial amplitude. All signals are scaled for the amount of pump light absorbed. ..... 168
Figure 6.10 - a) TAS spectra, at various times, of a heterojunction with a structure identical to that in Figure 6.9, only with the FTO replaced with plain glass. b) TAS decay at 1600 nm. Both sets of data are pumped at 510 nm and is scaled for the amount of pump light absorbed. ..... 169
Figure 6.11 - a) TAS spectra at 300 µs for different structures containing $Bi_2S_3$ (Bi), $Ag_2S$ (Ag) and SPIRO on $TiO_2$ (Ti) b) TAS decays of the same structures at 1600 nm. All samples are excited with a pump wavelength of 510 nm with the same power and decays are scaled for the amount of pump light absorbed. ..... 170
Figure 6.12 - Diagram illustrating the possible ground-state transitions that could result in a negative TAS signal at sub-band gap energies (1600 nm) due to their suppression after excitation. The red arrow represents direct excitation of an electron from the HOMO of SPIRO into the conduction band of $Bi_2S_3$ and the blue arrows represent the excitation into sub-band gap trap/surface states in the metal sulfides. ..... 171
Figure 6.13 - a) Incident photon conversion efficiencies (IPCEs) of the 4 devices presented in Table 6.2 with different amounts of $Ag_2S$. b) Steady-state absorptance measurements of the analogous heterojunctions used for the spectroscopy. c) TAS decays measured after a 510 nm excitation and probed at 1600 nm for the heterojunctions along with the amplitudes at 1 µs and the halftimes d). Al

samples were excited using the same approximate number of photons and were scaled for the amount of pump light absorbed. ..... 172
Figure 6.14 - (a,b,c,d) Top-down SEM images of nanostructures fabricated with no $Ag_2S$, 4 Cycles, 16 Cycles and 32 Cycles respectively. (e,f,g,h) Side-on SEM images of the same sample as is located above. Scale bars are 500 nm. Figure kindly provided by Yiming Cao. ..... 174

# List of Tables

Table 5.1 - Characteristic parameters of the devices shown in Figure 5.5. *The numerical values recorded are stored to 6 decimal places, so the values of 0 are $<5x10^{-7}$. ..... 134

Table 6.1 - Tabulated characteristic parameters of solar cells fabricated using each of the different polymer/$Bi_2S_3$ combinations. ..... 164

Table 6.2 - Tabulated characteristic device parameters for the optimum device achieved using varied amounts of $Ag_2S$ to coat the $Bi_2S_3$ rods. ..... 166

# Acronyms and Abbreviations

| | |
|---|---|
| AO | Atomic Orbital |
| BHJ | Bulk Heterojunction |
| $BiEX_3$ | Bismuth(III) O-ethyl Dithiocarbonate |
| $BiPX_3$ | Bismuth(III) O-pentyl Dithiocarbonate |
| $Bi_2S_3$ | Bismuth Sulfide |
| CB | Conduction Band |
| CdSe | Cadmium Selenide |
| CdSe | Cadmium Sulfide |
| $CuInS_2$ | Copper Indium Sulfide |
| $CuInSe_2$ | Copper Indium Selenide |
| CuSCN | Copper Thiocyanate |
| DI | Deionised |
| DMSO | Dimethyl Sulfoxide |
| $E_g$ | Band Gap |
| EQE | External Quantum Efficiency |
| $Fe_2S$ | Iron Sulfide |
| FF | Fill Factor |
| GISAXS | Grazing Incidence Small Angle X-ray Scattering |
| GIWAXS | Grazing Incidence Wide Angle X-ray Scattering |
| HOMO | Highest Occupied Molecular Orbital |
| $I_L$ | Incident Light Power |
| ICFO | The Institute of Photonic Sciences |
| IPA | Isopropyl Alcohol |
| ITO | Indium Tin Oxide |
| $J_{SC}$ | Short-Circuit Current |
| LUMO | Lowest Unoccupied Molecular Orbital |
| MDMO-PPV | Poly[2-methoxy-5-(3′,7′-dimethyloctyloxy)-1,4-phenylenevinylene] |
| MEH-PPV | Poly[2-methoxy-5-(2’-ethylhexyloxy)-1,4-phenylene vinylene] |
| MO | Molecular Orbital |
| MTOE | Millions of Tonnes of Oil Equivalent |
| $P_{Max}$ | Maximum Power |
| P3HT | Poly(3-hexylthiophene-2,5-diyl) |
| PA | Polyacetylene |
| PAn | Polyanaline |
| PbS | Lead Sulfide |
| PbSe | Lead Selenide |

| | |
|---|---|
| PCBM | [6,6]-phenyl-C61-butyric Acid Methyl Ester |
| PC70BM | [6,6]-phenyl-C71 Butyric Acid Methyl Ester |
| PCE | Power Conversion Efficiency |
| PCPDTBT | Poly[2,6-(4,4-bis-(2-ethylhexyl)-4H-cyclopenta[2,1-b;3,4-b']dithiophene)-alt-4,7-(2,1,3-benzothiadiazole)] |
| PDTPBT | Poly(2,6-(N-(1-octylnonyl)dithieno[3,2-b:20,30-d]pyrrole)-alt-4,7-(2,1,3-benzothiadiazole)) |
| PF | Polyfluorene |
| PIA | Photoinduced Absorption Spectroscopy |
| PL | Photoluminescence Spectroscopy |
| PPV | Poly(p-phenylene vinylene) |
| PPy | Polypyrrole |
| PSiF-DBT | Poly[(2,7-silafluorene)-alt-(4,7-di-2-thienyl-2,1,3-benzothiadiazole)] |
| PT | Polythiophene |
| QD | Quantum Dot |
| $R_s$ | Series Resistance |
| $R_{sh}$ | Shunt Resistance |
| $SbEX_3$ | Antimony(III) O-ethyl Dithiocarbonate |
| $SbPX_3$ | Antimony(III) O-pentyl Dithiocarbonate |
| SPIRO | 2,2',7,7'-tetrakis(N,N-di-p-methoxyphenylamine)-9,9'-spirobi-fluorene |
| SnS | Tin Sulfide |
| TAS | Transient Absorption Spectroscopy |
| TEM | Transmission Electron Microscopy |
| TGA | Thermogravimetric Analysis |
| $(TMS)_2S$ | Bis(trimethylsilyl) sulfide |
| TOP:Se | Trioctylphosphine-selenide |
| TOPO | Trioctylphosphineoxide |
| UV-Vis | UV-Vis Absorption Spectroscopy |
| $V_{OC}$ | Open-Circuit Voltage |
| VB | Valence Band |
| XRD | X-ray Diffraction |
| ZnO | Zinc Oxide |

# Chapter 1

## Introduction

***Searle:*** *Icarus, how close is this to full brightness?*

***Icarus:*** *At this distance of 36 million miles, you are observing the sun at two percent of full brightness.*

***Searle:*** *Two percent? Can you show me four percent?*

***Icarus:*** *Four percent would result in irreversible damage to your retinas.*

*Sunshine (2007)*[1]

## Challenges of the Modern World

The world in which we live is a rapidly changing landscape. The age of the earth is estimated at approximately 4.54 billion years,[2,3] but in just the last 50 years we have witnessed the development of countless inventions, from the microwave oven and MRI scanner, to the internet and smartphones. This rapid increase in the amount of technology used by the population has caused our need for energy, to power these devices, to sky-rocket. Figure 1.1 illustrates the worldwide increase in consumption over the past 40 years, depicting over a twofold increase as a result of our desire to become a more technologically advanced civilisation.

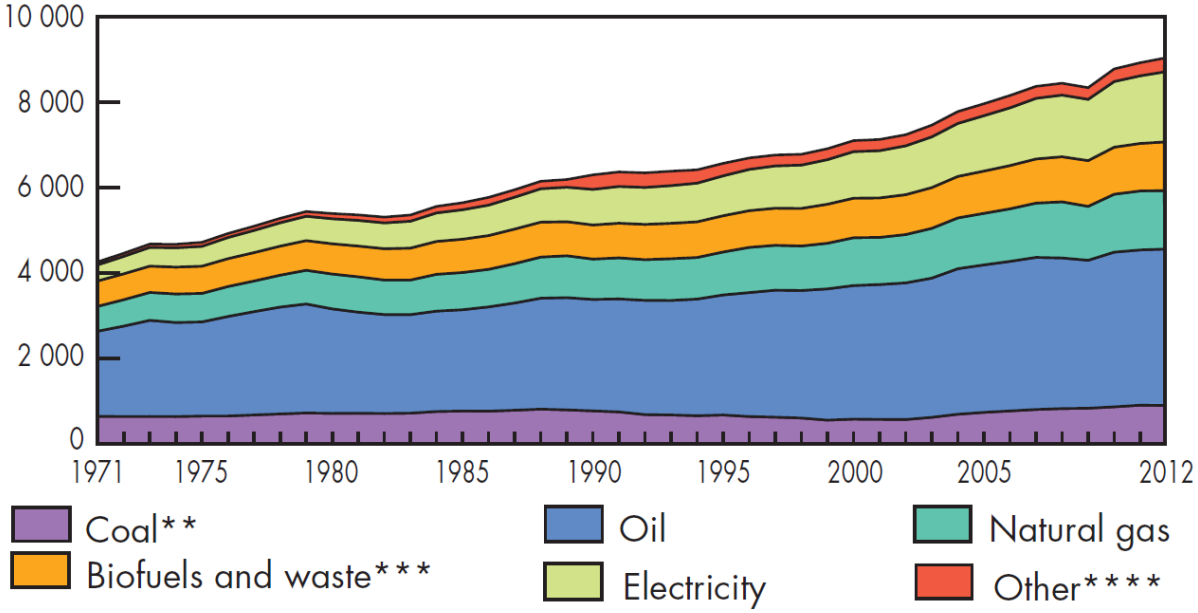



*Figure 1.1 - World total primary energy supply from 1971 to 2012 by fuel in millions of tonnes of oil equivalent (MTOE). This figure is taken from "Key World Energy Statistics" by the International Energy Agency.[4] **Peat and oil shale are aggregated with coal. ***Includes geothermal, solar, wind, heat, etc.*

There are three motivations to discuss the current energy situation of the planet. Firstly, fossil fuels, which make up 81.7% of the consumption in Figure 1.1, are a finite resource. The numbers presented for the remaining amounts of each of these resources often vary drastically, and as a result are not greatly important. However, it is undeniable that the earth has finite amount of these materials, and at some point in the future, if we continue to consume them, their reserves will become completely exhausted. Secondly, there is the issue of security of energy supply. Almost all parts of the world require energy, but the requirement distribution over the planet does not match the distribution of resources. This is true of the current situation, but as different parts of the world begin, or continue, to develop at varying rates, this mismatch of resource distribution will become even more prominent. Global politics is an extremely complex and important issue, and one far beyond the scope of this thesis. It is however pertinent to note, that the advantages for a country to be in control of its own energy supply, rather

than rely on the trade of resources with another, is obvious even to the layman. The final reason to discuss the current energy landscape, is that it is probable that using fossil fuels contributes to changes in the climate. Climate change is blamed on several human activities, but the one which appears to have the greatest effect is the release of the greenhouse gas $CO_2$ into the earth's atmosphere. If we continue to release greenhouses gases at the currently forecasted rate, we are likely to see a rise in the global average temperature of 3.6°C.[5] The implications of this rise would be catastrophic and irreversible.

The obvious solution to reduce the usage of the finite resources of the planet, that appear to contribute to climate change and are uneven distributed around the globe, is to develop an energy source that is created locally, doesn't emit $CO_2$ and is available in infinite supply. While this may, at first thought, sound like a concept from a science fiction novel, there are currently many solutions that fit these criteria and come under the umbrella term of renewable energy. In 2012 it was reported that the world relied on renewable sources for around 13.2% of its total primary energy supply, and in 2013 renewables accounted for almost 22% of global electricity generation.[6] Renewables here includes energy derived from solar, wind, geothermal, hydro and some forms of biomass.

## Renewable Energy

Renewable energy can be defined as energy derived from natural processes that are replenished at a faster rate than they are consumed.[6] There are several different forms of renewable sources that are currently being utilised, including sunlight, wind, rain, tides, waves, biomass and geothermal heat. The important point to note is that there is never going to be one source that will become a complete solution for the entire planet. Geothermal heat is a good example of a well utilised resource, but that is only available in isolated spots over the globe. Even the more widespread sources, such as sunlight and wind, are not at an equal power over the entire Earth. It is certain that an energy mix that is made up of entirely renewable sources will have to utilise a number of different technologies.

Several countries around the world are already producing a reasonable amount of their electricity from renewable sources. According to the Global Wind Energy Council the global wind power cumulative capacity is currently at 318.1 GW, an increase of over 18 times the amount in the year 2000.[7] Also, Germany, with 1.4 million photovoltaic systems installed, generated a peak of 23.1 GW hours at lunchtime on Monday 9 June 2014, equivalent to 50.6% of its total electricity need.[8]

Although there are several different renewable sources and, as mentioned before, a mix of many of these sources should be utilised, the power of sunlight certainly seems to have the highest potential. The sun strikes the Earth with a power of $1.08 \times 10^{14}$ kW and if only 0.1% of this energy was harvested at an efficiency of 10% then this would account for almost 4 times the world's generating capacity of about

3 TW. Or in other words, the total solar radiation hitting the Earth's surface annually is more than 7,500 times the world's total annual energy consumption of 4.5 x $10^{20}$ J.[9]

## Photovoltaics

There are two major ways to harvest the energy from the sun, using either the heat or the light. When harvesting the heat of the sun, it is most commonly used to heat water. This water can then either, through convection, be used to drive a turbine and generate electricity, or, as is quite commonly seen on the rooves of manly Mediterranean villas, the warmed water is used in a heat exchanger to raise the temperature of the water used in the house. The second method to harness the sun's energy is through the use of photovoltaics. The operation of a photovoltaic device, or solar cell, will be discussed further in the Background and Theory Section of this report, but in essence, the sunlight is converted directly into electricity.

From the numbers given for the total solar radiation hitting the Earth's surface it is easy to see why the development of efficient methods to harvest solar energy is a very desirable solution to meet our energy needs for the future. Figure 1.2 shows the annual sunlight energy hitting the earth's surface. The six black dots account for the total surface area of the planet required to be covered in solar cells, with a power conversion efficiency of 8%, in order to account for the current total worldwide energy demand.

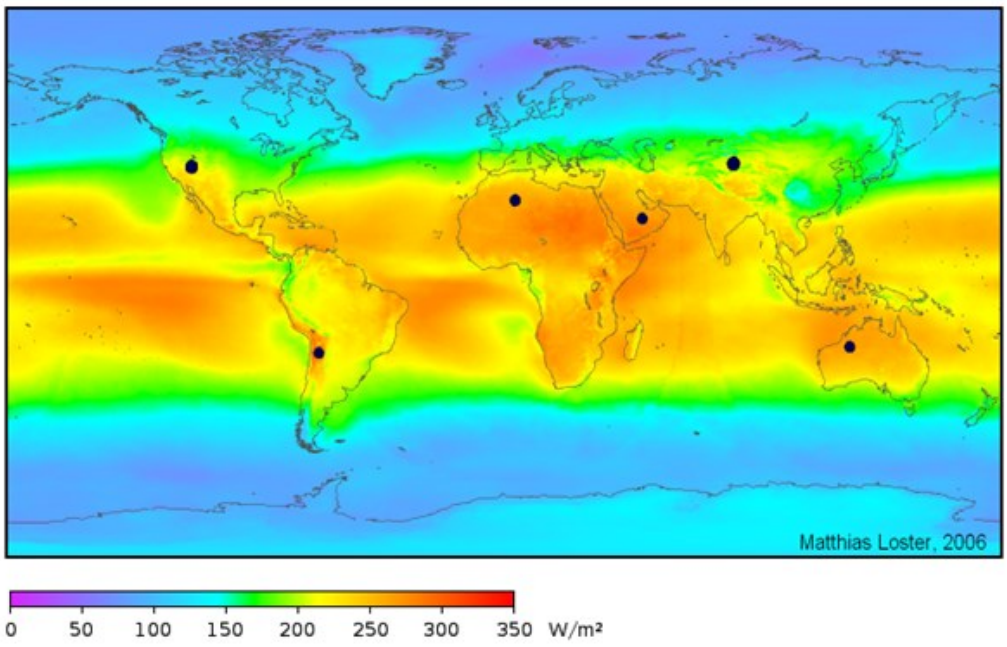



*Figure 1.2 - Average annual solar irradiance over a 3 year average, accounting for day and night and also cloud cover. The black dots represent the total surface area of the planet required to be covered in solar cells, with a power conversion efficiency of 8%, in order to account for the current total worldwide energy demand.[10]*

There are a variety of different solar cell technologies that are currently being investigated, and new solutions are being developed all the time. There are now reports of grid parity across the developed world, using crystalline silicon based technologies.[11,12] The costs of these solar cells are still relatively high, and as a result, they are only cost-effective in a few locations. The manufacturing costs of this technology are slowly reducing, however, there is a greater potential for gains through a paradigm shift. Such a shift was made through the development of cheaper alternatives to traditional solar cells, whose manufacturing costs were reduced by utilising materials that have the ability to be made using high throughput, solution processing techniques. This is the field of plastic electronics and devices of this nature will be discussed in more detail in the Background and Theory section. As well as a reduced cost, these devices also have the advantage of being able to be fabricated on flexible substrates. This allows them to be used in locations previously unavailable to the heavier silicon alternatives, and to be manufactured in such a way that they are fully integrated into building materials, instead of being bolted on top. It is the development of these such cheaper, solution processable alternatives that this work is focussed on, both in studying new materials, and understanding the internal processes that govern their performance.

# References

(1) *Sunshine.* [Film] Directed by: Danny Boyle. UK: Fox Searchlight Pictures; 2007.

(2) Dalrymple, G. B. *Geological Society, London, Special Publications* 2001, *190*, 205.

(3) Manhes, G.; Allègre, C. J.; Dupré, B.; Hamelin, B. *Earth. Planet. Sci. Lett.* 1980, *47*, 370.

(4) *Key World Energy Statistics*, International Energy Agency, 2014.

(5) *World Energy Outlook*, International Energy Agency, 2013.

(6) Agency, I. E. www.iea.org/aboutus/faqs/renewableenergy/, 2015.

(7) *Global Wind Report Annual Market Update 2013*, Global Wind Energy Council, 2013.

(8) Vidal, J.; The Guardian: 2014.

(9) *Survey of Energy Resources*, World Energy Council, 2007.

(10) Loster, M. http://www.ez2c.de/ml/solar_land_area/, 2010.

(11) Kelly-Detwiler, P.; Forbes: http://www.forbes.com/sites/peterdetwiler/2012/12/26/solar-grid-parity-comes-to-spain/, 2012.

(12) Peixe, J.; Oil Price: http://oilprice.com/Latest-Energy-News/World-News/Spain-Achieves-Grid-Parity-for-Solar-Power.html, 2012.

# Chapter 2

## Background and Theory

***Brand:*** *Maybe we've spent too long trying to figure all this out with theory.*

*Interstellar (2014)*[1]

# Photovoltaics

## A Brief History

Edmond Becqueral, a French physicist who studied the solar spectrum, was the first to report the photovoltaic effect in 1839, when he observed that an electric current was generated when light was shone onto a silver coated platinum electrode immersed in an electrolyte.[2] Forty years later, the first solid state photovoltaic devices were constructed after the discovery of the photoconductivity of selenium. In 1876, William Adams and Richard Day found that a photocurrent could be induced when a sample of selenium was contacted with two heated platinum contacts.[3] However, it was not until the 1950s that potentially useful quantities of power were produced, due to the development of high quality silicon wafers, manufactured for applications in solid state electronics.[4]

## Semiconductors and Photovoltaics

In an extremely simplistic sense, only two things are required for a material, or set of materials to make an effective photovoltaic device. It has to absorb light, in order to facilitate the generation of free charges, and it must be able to conduct those free charges to a load, where it can be made to do work. One additional requirement for making a 'good' device is that charge should only flow in one direction through the circuit created. It is therefore advantageous to create an asymmetry across the device in order to drive current in a single direction. Semiconductors have a number of properties that fulfil the simple criteria mentioned and are currently the only materials used in solar cells. It is therefore important to discuss where the properties that give rise to their aptitude for photovoltaic applications come from.

In a single atom, electrons are distributed according to Pauli's exclusion principle, across quantised energy levels that are the eigenvalues of the Schrödinger equation. The eigenfunctions corresponding to these energy levels give the probability of finding an electron at a given position in relation to the nucleus. The collective term for the combination of the energetic and spatial distribution associated with each level is an atomic orbital (AO). Bringing two atoms together leads to the formation of new orbitals that represent the complete system of both atoms. These are referred to as the molecular orbitals (MO). This happens because the total energy of the new MOs is lower than the sum of the separate AOs. The term used to describe the occupied MOs is the bonding molecular orbitals. There are also orbitals formed that have a higher energy than the separate AOs and these are called anti-bonding molecular orbitals. As more atoms are introduced into the molecule an increasing number of electrons fill an increasing number of MOs. The biggest example of molecule is an inorganic crystal, which can be

considered as an infinite lattice of atoms. In a crystal, there are so many MOs that the energy levels are close enough together that they appear continuous and are then called bands. This is shown schematically in Figure 2.1.

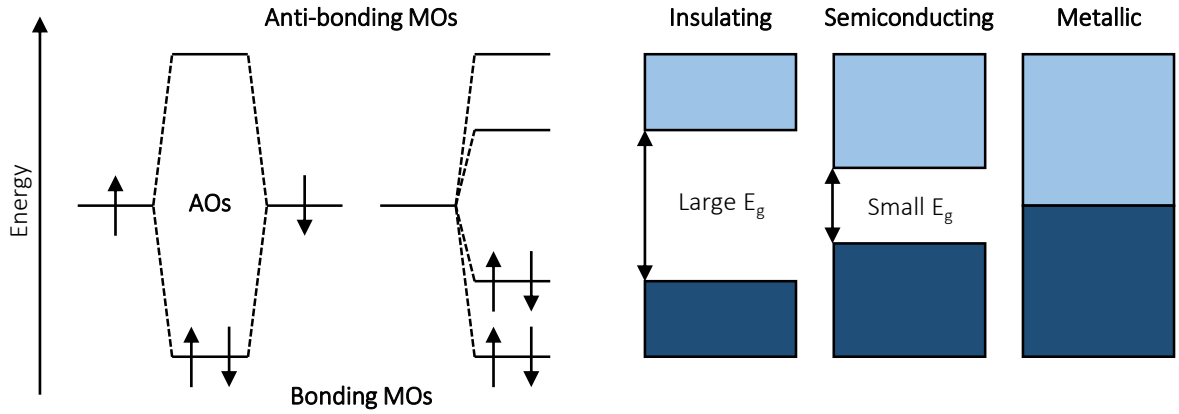



*Figure 2.1 - (Left) Energy level diagram showing the combination of 2 AOs to give the bonding and anti-bonding MOs and also the resulting MOs for a combination of 4 atoms. (Right) The crystal case where there are so many MOs with energies so close together that they appear to be a continuum and are referred to as bands.*

A material is considered a semiconductor when there is a gap in energy between the highest occupied molecular orbital (HOMO) and the lowest unoccupied molecular orbital (LUMO), referred to as the band gap ($E_g$), of between 0.5 and 4 eV (these limits are widely accepted but arbitrarily defined). In an inorganic semiconductor the filled MOs are referred to as the valence band (VB) and the unfilled MOs are the conduction band (CB). A metal can be defined as a material where there is no energy gap, or even an overlap, between the VB and the CB. In a semiconductor electrons can be promoted from the VB into the CB by: either absorption of a photon, if the band gap is equal to, or of lower energy than, the energy of the photon absorbed, or by injecting an electron using the transfer from a higher energy state. Electrons in the CB can be thought of as free to move through the crystal, as there is a continuum of empty states available to them. An electron will diffuse between these states, or drift in an electric field. Similarly, positive charges (holes) are free to move through the VB. It is this conductance after an external push that gives these materials their name of semiconductors.

The intrinsic properties of a semiconductor can be, and often are, defined by the amount of dopants added to the material. A dopant atom can be added into an inorganic crystal lattice to either add an extra electron, compared to the surrounding atoms, or remove an electron. The conduction properties of the semiconductor can be controlled by the amount of dopant atoms that are added. If a sufficient amount of doping is added then a semiconductor can be made to conduct as well as a metal. If a semiconductor is doped such that it has a higher electron conductivity, then it is termed n-type and if doped such that it has a higher hole conductivity then is termed p-type. The combination of an n-type

and a p-type semiconductor can be used to create a *pn*-junction. The addition of these two materials in contact with each other creates a type of diode that has the desired asymmetry for a practical photovoltaic device. Considering the fact that the arbitrary band gap limits for a semiconductor are 0.5 - 4 eV (2480 - 310 nm), which covers the entire solar spectrum, these materials are ideal for the task of generating electricity, following the absorption of a photon and separation of charges using the asymmetry that can be inherently built in.

## Electrical Characterisation of Photovoltaics

Before discussing the operational principles of a photovoltaic device, it is necessary to clarify a few fundamental parameters that are used to describe device performance, as well as how a device is measured.

A photovoltaic device is measured by placing a cell in the light and measuring the current output at a range of applied voltages. An example of a so called current-voltage plot is shown in Figure 2.2. The solid line is from a device measured in the light and the dotted line is from a device measured in the dark.

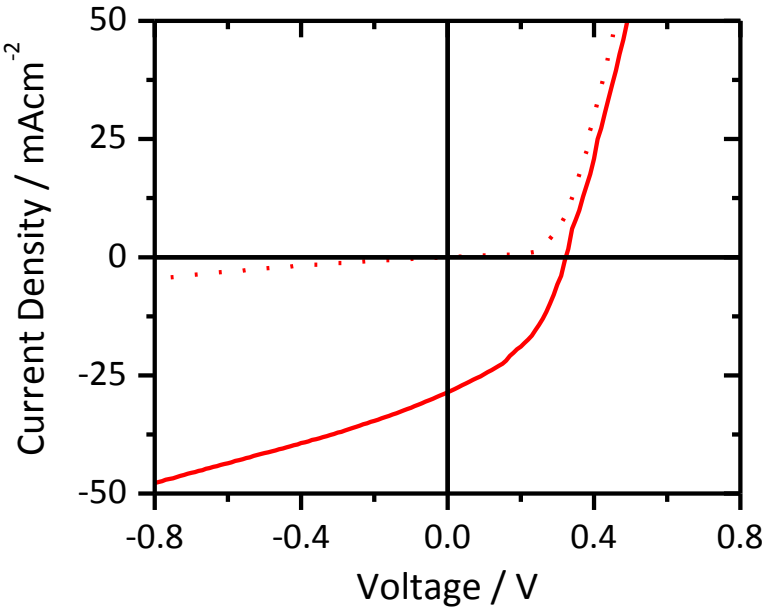



*Figure 2.2 - Current-voltage plot of an example photovoltaic device. The solid line is from a device measured in the light and the dotted line for a device measured in the dark.*

Perhaps the most important definition is the overall efficiency of the cell. This is given by the ratio of the maximum power output of the cell ($P_{max}$) and the incident light power ($I_L$)

$$PCE = \frac{P_{max}}{I_L} \times 100\%$$

**Equation 1** – Power conversion efficiency (PCE)

Other than the $P_{max}$, there are two other key parameters that are important in defining the performance of a solar cell. These points are the current when the voltage is zero, referred to as the short-circuit current ($J_{SC}$), and the voltage when the current in zero, called the open-circuit voltage ($V_{OC}$).

Another term often quoted is the fill factor (FF), which is defined as the ratio of the maximum power of the cell and the maximum theoretical power. This is sometimes referred to as the 'squareness' of the solar cell. For a perfect diode the FF would be 1 and the solar cell would have its $P_{Max}$ at $J_{SC}$ and $V_{OC}$.

$$FF = \frac{P_{max}}{J_{SC}V_{OC}}$$

**Equation 2** – Fill factor (FF)

In reality, solar cells never display ideal diode behaviour because power is dissipated through parasitic series and shunt resistances. An equivalent circuit for a solar cell is shown in Figure 2.3 that allows for a better understanding of the non-idealities shown in the curve in Figure 2.2. The series resistance ($R_s$) arises due to the resistance of the cell materials and contacts. This value should ideally be zero. The parallel shunt resistance ($R_{sh}$) should be infinite in a perfect solar cell. In a non-ideal device it is lower, due to leakage losses within the solar cell, arising from alternative electrical pathways through the device. The shape of the current-voltage curve gives an indication of how $R_s$ and $R_{sh}$ limit performance. Both cause the fill factor to decrease; a non-zero $R_S$ decreases the slope of the curve near $V_{OC}$, as it means the current is not increasing with voltage at the ideal rate, and a lower than infinite $R_{sh}$ leads to a slope in the current-voltage curve near $J_{SC}$ due to leakage losses.

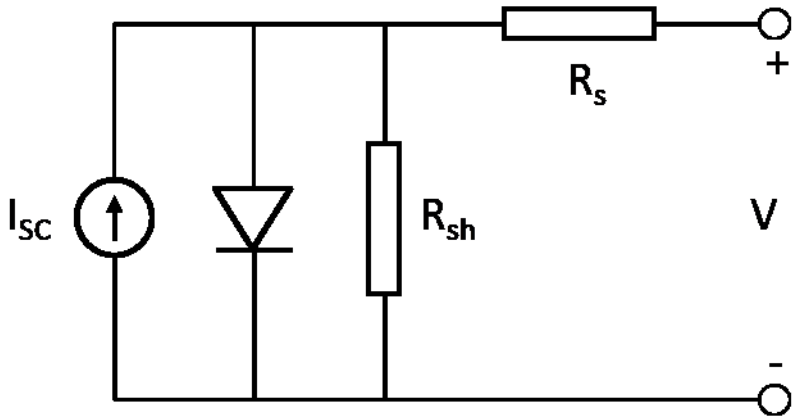



*Figure 2.3 - The equivalent circuit for a solar cell comprising a current source (delivering $I_{SC}$), a diode, and two resistances which represent the non-ideality within the device – a shunt resistance ($R_{sh}$) in parallel, and a series resistance ($R_s$) in series.*

## Organic Semiconducting Polymers

Semiconducting materials are not limited to inorganic crystals and many organic materials are also semiconducting. Perhaps the first work on semiconducting organic compounds was done by Eley *et* al. in 1953.[5] In this study the effect of temperature on the electrical conductivity of several crystalline organic powders was looked at. It was found that the materials had a band gap, which was calculated to be equal to twice the activation energy for conduction in the solids. The materials studied were phthalocyanine, coronene, anthracene and *iso*dibenzanthrone. This discovery did not spark a revolution as one might think, perhaps because the materials in question were small organic molecules and so the advantages of polymer processing were not fully realised. Work on polymers came later in the form of polypyrrole (PPy)[6] and polyaniline (PA)[7] in 1963 and 1968 respectively. Some examples of the structures of semiconducting polymers are shown in Figure 2.5. In the case of PPy the conduction was known to be due to the conjugated backbone and the effect that hetero atoms had on backbone was also studied. The polymers were made to behave as either intrinsic or extrinsic semiconductors, possessing *n*- or *p*-type characteristics. The discovery of semiconducting polymers is often attributed to Heeger, Shirakawa and MacDiarmid with their landmark *Physical Review Letters* paper in 1977.[8] The Nobel Prize in Chemistry was awarded to these three in 2000 for "*the discovery and development of conductive polymers*".[9]

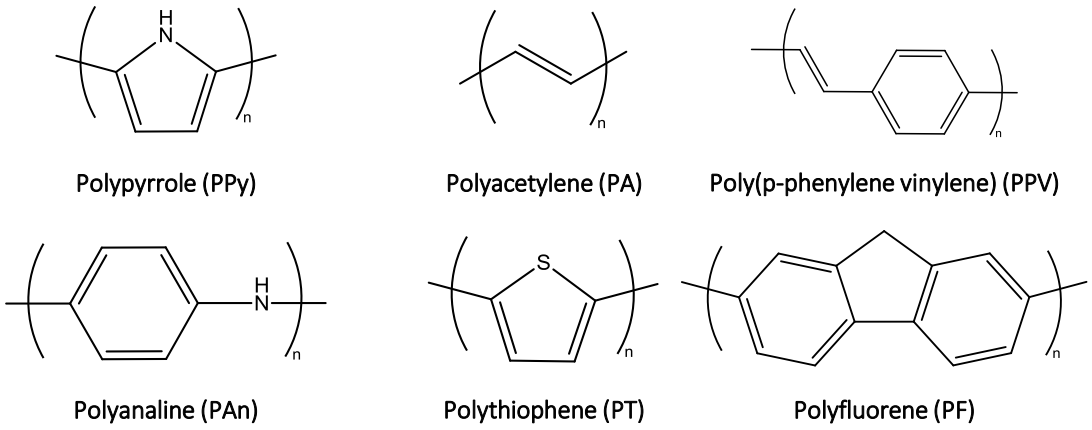



*Figure 2.4 - Examples of some structures of semiconducting polymers: polypyrrole (PPy), polyacetylene (PA), poly(p-phenylene vinylene) (PPV), polyanaline (PAn), polythiophene (PT) and polyfluorene (PF).*

The backbone of these semiconducting organic polymers is comprised of an alternating series of single and double bonds, resulting in a linear chain of overlapping $p_z$ orbitals. The higher the number of repeat units in the backbone that are conjugated the lower the band gap. This is shown for PA below in Figure 2.5.

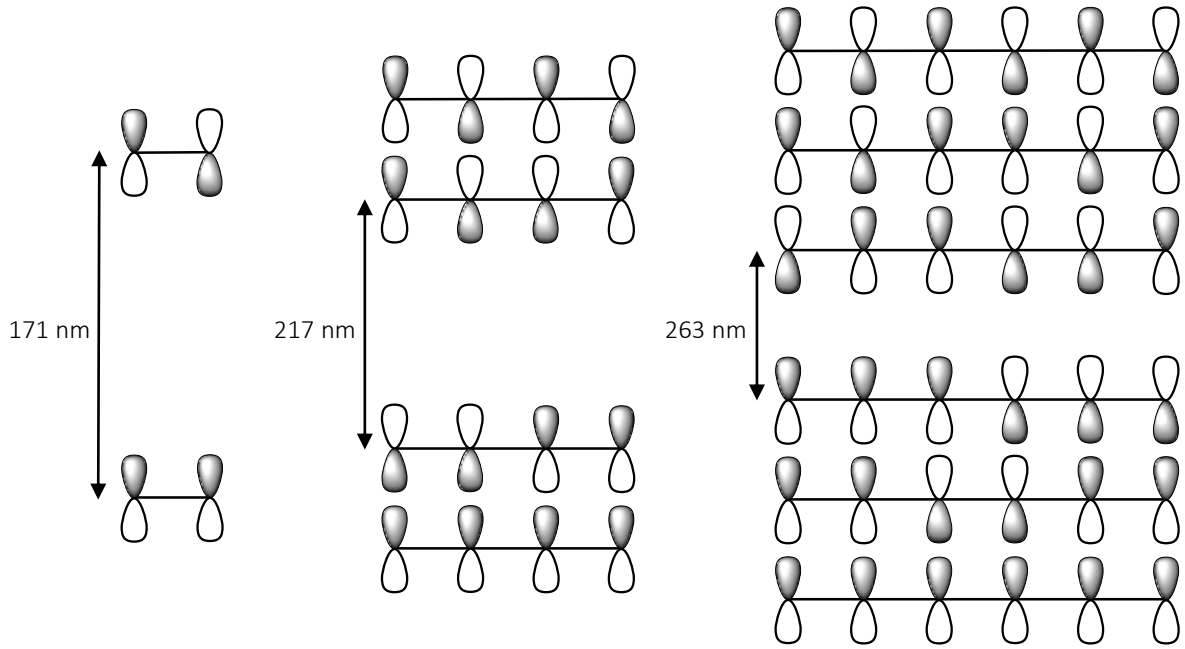



*Figure 2.5 - Conjugated backbone of PA showing the overlapping $p_z$ orbitals and how the band gap decreases with increasing conjugation length.*

This conjugated backbone of delocalised electron density is the reason for the electronic properties of these semiconducting polymers, as charges can be transported along the conjugated length of the polymer. As the conjugation length of these polymers is increased, the energy levels become more

closely spaced, but never reach the band like structure of inorganic crystals. This is because typical conjugation lengths are no more than 20 repeat units, in PTs for example.[10] The dielectric constant of these organic semiconducting polymers is much lower than an inorganic crystal. This has the effect that upon absorption of a photon a coulombically bound electron-hole pair, called an exciton, is generated, rather than free charge carriers. The reason for this is that the charges generated are not delocalised over the entire lattice, as in an inorganic material, but localised over the length of the relatively small conjugation length. This spatial confinement coupled with a lower dielectric constant for organic materials leads to the separated charges being held within a region where each charge is coulombically bound to the other.

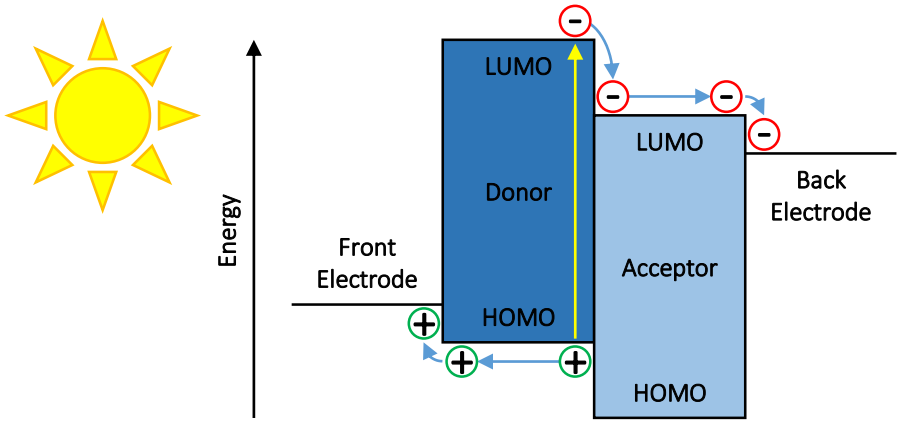



*Figure 2.6 - Schematic diagram illustrating the basic function of an organic excitonic solar cell. The yellow arrow represents the absorption of a photon, creating a bound electron-hole pair, referred to as an exciton. This exciton is split at an interface between the donor and the acceptor, and the charges are transported to the relevant electrodes.*

Figure 2.6 illustrates the basic function of an organic photovoltaic device. First, a photon is absorbed in the donor material, illustrated by the yellow arrow. As mentioned previously, this generates a coulombically bound electron-hole pair, referred to as an exciton. To split this exciton it has to diffuse to an interface between the donor and acceptor material. Due to the energy offset at this interface the electron is transferred into the LUMO of the acceptor material. The charges are now free to diffuse/drift to the corresponding electrodes.

This system has been drawn to represent a traditional donor/acceptor junction, where the donor material has HOMO and LUMO energies closer to the vacuum energy than the acceptor material, and the exciton is split by transferring an electron from the donor to acceptor. It is also possible to have an analogous system, where the light is absorbed by the material with deeper energy levels and an exciton here is split by transferring a hole to the other material. The possibility of a system whereby a combination of both of these processes happen, and photovoltaic devices based on this principle, will be discussed later in this chapter.

There are several loss mechanisms in these systems, one of which is a recombination of the coulombically bound exciton before it can be split at an interface. This loss mechanism is present because the generated excitons have to diffuse to an interface between the two materials in order to be separated. The distance an exciton can diffuse before relaxation, referred to as the exciton diffusion length, is relatively short. For PPVs the exciton diffusion length is around 5-10 nm[11] and in PTs it is about the same (~5 nm).[12] The donor material layer thickness required to absorb the maximum amount of sunlight is typically >100 nm.[13] This means that in a layered system as shown in Figure 2.6 there has to be compromise in the thickness, to allow the charges to reach the interface and, as a result, not much light will be absorbed. This mismatch of properties for optimal device performance lead to the development of the bulk heterojuntion (BHJ), in an attempt to ensure that excitons were generated no further than the typical diffusion length in the particular polymer from an interface, whilst keeping the films optically thick.

## The Bulk Heterojuntion Solar Cell

The BHJ is conceptually a very obvious enhancement of the donor/acceptor architecture, whereby the donor and acceptor material are mixed together such that both components are intertwined with each other whilst remaining interconnected to either side of the device.[14,15] This ensures that excitons are always generated close to an interface and the films can still be made optically thick.

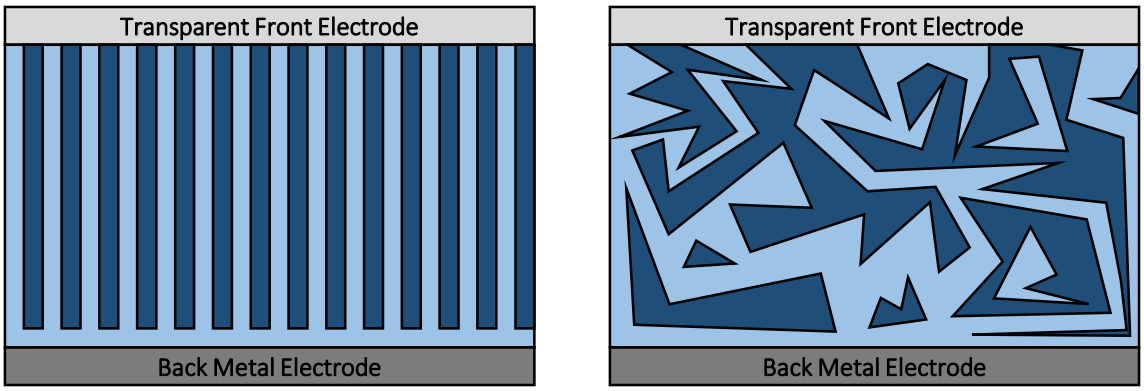



*Figure 2.7 - Schematic diagram of an ideal bulk heterojunction (left) and a more random mixture of the donor and acceptor (right).*

Figure 2.7 (left) shows the ideal case for a BHJ, where the domain sizes are no larger than the diffusion length of an exciton, but there is still perfect connectivity to the corresponding electrodes. For solar cells fabricated from semiconducting organic polymers, which are processed from solutions, it is very difficult to achieve such a morphology. Using typical processing methods the morphology of such blends are more likely to look similar to the diagram on the right. Here, there is reasonable mixing, however,

there are still large regions of either component that will not allow an exciton to diffuse to an interface. There are also islands of each material, which will mean an exciton split at these interfaces will not result in charges that can be transported to the collecting electrodes.

Despite the practical difficulties with generating BHJs similar to those above, there has been great success over recent years with the use of polymer blends mixed with fullerene derivatives, such as [6,6]-phenyl-C61-butyric acid methyl ester (PCBM).[16,17] Here the polymer is acting as the donor material, absorbing almost all of the light the system uses, and the fullerene derivative is acting as the acceptor, splitting excitons generated in the polymer and transporting electrons to the collecting electrode. State-of-the-art single junction devices using polymer/fullerene blends now regularly reach PCEs of 8-10%,[18-22] with the certified record measured at 11.0%.[23] Tandem devices, which utilise more than one heterojunction in order to harvest more of the solar spectrum, have also now achieved over 10% PCEs.[24]

The all-organic BHJs are not, however, without their flaws. In the majority of devices, 50% of the material in the active layer absorbs a relatively small amount of light. This means that it is hard to get full coverage of the solar spectrum and, as a result, efficiencies are limited. There has been some work on polymer/polymer blends, where the absorption profile of each material is designed such that they complementarily absorb different spectral regions. These devices have however only so far reached efficiencies of 4%.[25-27] Polymer/fullerene solar cells also suffer from stability issues, both chemically and morphologically.[28-31] In an attempt to develop a photovoltaic system where these issues are reduced, and to challenge for higher PCEs, the concept of the hybrid organic/inorganic solar cell was devised.

## Hybrid Organic/Inorganic Solar Cells

The definition of what constitutes a hybrid solar cell is relatively broad, however, in this thesis, the term is used to refer to a photovoltaic device where the primary interface for charge generation is at the junction between an organic and an inorganic material. The use of a hybrid system offers many advantages of an equivalent polymer/fullerene solar cell. Some of these advantages are, but not limited to:

- More complete coverage of the solar spectrum. PCBM has a low extinction coefficient in comparison to the majority of semiconducting polymers typically used in photovoltaic devices. There is therefore often incomplete absorption over the full range of the solar spectrum. The wide range of inorganic materials available have absorption profiles that cover a broad range of the spectrum and have high extinction coefficients. Inorganic materials can therefore be chosen to complement the absorption of the semiconducting polymer used. This enhances the amount of light absorbed by a device and potentially increases the produced current.
- Due to quantum confinement effects, the band gap of any inorganic material can be tuned, by changing the crystal size. This tuning, not only allows for the complementary absorption to be maximised, but also the energetics at the polymer/inorganic interface can be modified to maximise the efficiency of charge generation.
- Higher charge generation efficiency, due to the higher dielectric constant compared to semiconducting polymers. Inorganic materials demonstrate a much lower degree of excitonic character and therefore injected charges are less likely to be coulombically bound at an interface.
- Superior charge transport properties, due to an increased crystallinity.
- Increased chemical stability, in comparison to organic polymers.

Many different approaches have been investigated to create hybrid organic/inorganic heterojunctions. The first example is by the blending of inorganic nanoparticles with conjugated polymers. By mixing nanoparticles of inorganic semiconductors with conjugated polymers, *pn*-junctions can be created throughout the film that can facilitate efficient charge generation. The challenge is to generate a system that is well mixed, while still retaining sufficient electronic pathways to the electrodes to collect the generated charges. Another difficulty arises with the requirement of finding a solvent to process both the organic and inorganic component together. This often requires the nanoparticles to be capped with solubilising ligands that are detrimental to charge generation and inter-particle charge transport. Flat bilayers are a simpler route to hybrid heterojunctions. This method, however, leaves a rather low amount of interfacial area and, as such, device thickness, and therefore absorption, is sacrificed. The

need to process both components from a common solvent is, however, no longer a problem. The third example, is filling nanostructured inorganic electrodes with conjugated polymers. Here, a well-ordered inorganic semiconductor scaffold, such as, for example, vertical pillars, or straight pores is filled with a semiconducting polymer. By controlling the dimensions of the structures to be within the exciton diffusion length, the charge transfer can be optimised whilst retaining perfect connections to the electrodes. Systems of this type can be fabricated that closely resemble to ideal picture in Figure 2.7 (Left).

The most common approach is the polymer/nanoparticle blend. The other two examples are effectively a highly ordered non-mixed system and a highly ordered well mixed version of the blend. There are two main routes to these blend heterojunctions and they are categorised by the fabrication method of the inorganic component. Either, the nanoparticles can be pre-synthesised, before mixing with the semiconducting polymer, termed *ex-situ*, or the nanoparticles can be formed with the polymer matrix, termed *in-situ.*

## *Ex-situ* Polymer/Nanoparticle Solar Cells

The formation of the nanoparticles before blending with semiconducting polymers has the advantage, over *in-situ* fabricated nanoparticles, of obtaining greater control over the inorganic material produced. The size, shape, and atomic ratio are all properties that can be adjusted. As mentioned previously, one of the difficulties with these fabricated nanoparticles is the problems associated with processing two materials that are chemically very different, from a common solvent. Success with a variety of materials systems has been achieved by several groups, and a selection of the significant work is presented below.

### *Cadmium Selenide and Cadmium Sulfide*

A high level of success with inorganic nanoparticles blended with polymers has been achieved with cadmium selenide (CdSe) as studied by Greenham *et* al.[32,33] The first examples of the utilisation of polymer/nanoparticle blends are demonstrated with CdSe nanoparticles in poly[2-methoxy-5-(2'-ethylhexyloxy)-1,4-phenylene vinylene] (MEH-PPV). These devices used MEH-PPV/CdSe in a blend, with a transparent indium tin oxide (ITO) top electrode and an aluminium bottom electrode. The devices showed a maximum quantum efficiency of 12%. In order to keep the nanoparticles stable the CdSe nanoparticles were capped with trioctylphosphineoxide (TOPO). To allow electron transfer from MEH-PPV to CdSe this TOPO has to be removed, which is achieved by treatment with pyridine and redissolving in chloroform before mixing with the polymer. This requirement of surface modification is highly undesirable from a processing perspective. The process also reduces the nanocrystal solubility, as well as being detrimental to the homogeneity of the photoactive layer, subsequently reducing the device

performance.[32] The photoinduced electron transfer from different PPV derivatives to CdSe has also been studied by Greenham *et* al. using photoluminescence (PL) and photoinduced absorption spectroscopy (PIA),[34] finding that both PL quenching and PIA features are insensitive to nanocrystal size.

An increase in performance came with the modification of the CdSe from spherical particles to rods.[35-37] The reason for improved performance was threefold. Firstly, the CdSe rods allow for more efficient electron transport through the film. This is attributed to the rods' tendency to form end-to-end chains that increase penetration of the inorganic phase through the polymer.[35] The band gap was shown to be tuneable by altering the nanorod diameter, whilst increasing the nanorod length was shown to increase electron transport.[36] Secondly, the polymer poly(3-hexylthiophene-2,5-diyl) (P3HT) was used, in place of MEH-PPV, which has a higher hole mobility than PPVs. Finally, the rods were capped with pyridine instead of TOPO. This removed a ligand exchange step in processing by making the rods soluble in a pyridine/chloroform mixture. The pyridine was later removed in a thermal step. One drawback of these CdSe rods and nanocrystalline rods in general is that the improvement in charge transport, in comparison to QDs, is only observed in the direction of the alignment. For thin films formed via solution processable routes it is difficult to ensure that the alignment is along in the direction of the pathway between both electrodes. This problem can somewhat solved by the use of CdSe tetrapods, i.e. nanocrystals with four crystal arms arranged in a tetrahedral configuration. It was shown that because these crystals always have one branch aligned so as to create a channel between electrodes, they can improve electron transport in comparison to linear CdSe rods, yielding solar cells of efficiency 2.4-2.8%.[38,39] Dayal *et* al. reported a record efficiency, for CdSe tetrapods, of 3.13%.[40] This devices utilised the low band gap polymer poly[2,6-(4,4-bis-(2-ethylhexyl)-4H-cyclopenta[2,1-b;3,4-b']dithiophene)-alt-4,7-(2,1,3-benzothiadiazole)] (PCPDTBT). However, a higher efficiency was later achieved by Celik *et* al., also using PCPDTBT, but with CdSe rods instead of tetrapods.[41] These devices showed a maximum PCE of 3.42%.

Perhaps the record efficiency for cadmium based hybrid organic/inorganic solar cell has been achieved by Ren *et* al. who grafted cadmium sulfide (CdS) nanoparticles onto nanowires of P3HT.[42] These devices reached PCEs of 4.1%, by insuring a good interface between the donor and acceptor through a bridging ligand, facilitating good charge separation. The final result is indeed impressive, however the method is, in comparison to some others, extremely intricate. First, nanowires of P3HT have to produced, followed by sensitisation with the CdS nanoparticles, which also have to be synthesised separately, and finally the solution has to cast to create the thin film.

### *Lead Sulfide and Lead Selenide*

Lead sulfide (PbS) and lead selenide (PbSe) colloids can be tuned to have absorption maxima from approximately 800 nm to 2000 nm.[43] This ability to absorb lower energy light from the near to mid infrared portion of the solar spectrum is seen as a likely route to improving the efficiencies of organic based solar cells. This tunability of the absorption, i.e. the band gap, is highly dependent on particle size. This size dependent behaviour is exhibited when the exciton bohr radius (the average distance between the electron and hole in an exciton) is confined in three spatial dimensions.[44] This causes the particle to gain kinetic energy (confinement energy) and its energy spectrum becomes discrete. Semiconductors displaying this type of effect are referred to as quantum dots (QDs) and their degree of confinement can be directly observed as the exciton energy, or band gap, increases with decreasing particle size. This confinement is seen very strongly in semiconductors such as PbS and PbSe as their exciton bohr radii are particularly large (~10 nm, compared to ~1 nm for CdSe).[45] In PbS, the band gap can be tuned from 1770 to 950 nm, by changing the size from 8 to 4 nm.[46] For comparison, in CdS, by changing the size from 6 to 2 nm, the band gap is only tuned from 480 to 400 nm.[47]

The use of these lead based QDs has been explored by several groups to create BHJ type devices that absorb in the infra-red. McDonald *et* al. studied devices fabricated from blending PbS with MEH-PPV.[48] MEH-PPV was used as they required a polymer with a low ionisation potential (previously reported as between 4.9 eV and 5.1 eV)[49,50] to allow PbS with a bulk ionisation potential ~4.95 eV to inject holes into the MEH-PPV. This allows for a portion of the low energy infra-red region of the solar spectrum to be harvested by the PbS as well as the higher energy photons by the polymer. They were able to achieve the harvesting of photons far beyond 800 nm, demonstrating an infra-red photovoltaic effect, and were able to use the tunability of the QDs to change the photocurrent spectra to three regions of the infra-red spectrum. However, the external quantum efficiency (EQE) at 975 nm was extremely small (~0.0008%), calling into doubt the effectiveness of charge transfer between the PbS and MEH-PPV. The same authors were able to improve device efficiencies slightly by studying the effects of thermally annealing samples. After annealing at above 160°C the devices saw a 25-fold increase in the quantum efficiency to ~0.002%.[51]

A different approach to fabricate MEH-PPV/PbS blends was taken by Watt *et* al.,[52,53] who realised that the majority of problems that polymer/nanocrystal blends had was due to the common method of synthesising the nanoparticles separately and then combining them with the polymer. They state that the surfactant used to prepare the nanoparticles has to be removed and that any amount of this surfactant that is left after blending will result in loss of charge transfer between nanoparticle and conducting polymer, as previously seen in blends of P3HT/CdSe.[34] Secondly, the mixing approach often requires the use of co-solvents, which adversely affect nanocrystal solubility and polymer chain

orientation. Watt *et* al. developed a new route to PbS nanoparticle synthesis that worked via a one-pot method. The method they used involved mixing a sulfur precursor solution consisting of sulfur flakes dissolved in toluene with a second solution containing MEH-PPV dissolved in a toluene, dimethyl sulfoxide (DMSO), and lead acetate. Both mixtures were combined to produce PbS nanoparticles in the MEH-PPV polymer solution. The product was then centrifuged to remove the supernatant and the product was dissolved in the desired solvent for thin film fabrication. The devices were reported to have white light power conversion efficiencies under AM1.5 illumination (at 5 mW/cm$^2$) of $\eta$ = 0.7%, $J_{SC}$ = 0.13 mA/cm$^2$, $V_{OC}$ = 1 V, and FF = 28%.[52] It is pertinent to note that this light level is much lower than typical photovoltaic measurements, and these devices tend to perform better at low light levels.

PbSe has also been used in conjunction with conjugated polymers to make hybrid devices. Jiang *et* al. were the first to report a photovoltaic effect of PbSe nanocrystals and P3HT.[54] The films showed good diode characteristics with a $V_{OC}$ = 0.3 - 0.4 V, $J_{SC}$ = 0.24 mA/cm$^2$, FF = 43% and $\eta$ = 0.04%. Cui *et* al. also explored devices fabricated from blends of nanocrystalline PbSe and P3HT reporting efficiencies of $\eta$ = 0.14% under 1 sun AM1.5 illumination, with $J_{SC}$ = 1.08 mA/cm$^2$, $V_{OC}$ = 0.35 V, FF = 37% and an EQE = 1.3% at 805 nm.[55]

Seo *et* al. combined poly(2,6-(*N*-(1-octylnonyl)dithieno[3,2-*b*:20,30-*d*]pyrrole)-*alt*-4,7-(2,1,3-benzothiadiazole)) (PDTPBT) with oleic acid-capped PbS QDs.[56] A post-deposition ligand exchange using 1,2-ethanedithiol was applied to the hybrid devices. Devices exhibited a $J_{SC}$ of 13.6 mAcm$^{-2}$, $V_{OC}$ of 0.36 V, and FF of 43%, resulting in an overall PCE of 2.07%. Further optimisation, including the insertion of a $TiO_2$ layer and particle size tuning, increased the PCE to 3.78%.

The record hybrid photovoltaic efficiency was demonstrated by Liu *et* al.[57] Here, PDTPBT was combined with a $PbS_XSe_{X-1}$ alloyed nanocrystals. The nanoparticles were synthesised using bis(trimethylsilyl) sulfide ($(TMS)_2S$) and trioctylphosphine-selenide (TOP:Se) as the sulfur and selenide precursor, respectively, resulting in a large nanoparticle size of ~7 nm. The devices showed a record PCE of 5.50%, with an uncharacteristically high FF of 67%.

### *Other Metal Chalcogenides*

Other metal chalcogenides have been considered as potential candidates for hybrid polymer/nanoparticle photovoltaics. Devices based on heavy metals, particularly cadmium and lead, discussed above, have environmental safety issues associated with them. Many of the alternative metal chalcogenides that have been researched for use in hybrid photovoltaic systems have been based on non-toxic materials. Recent studies involve the inorganic materials of tin sulfide (SnS),[58] iron sulfide ($FeS_2$),[59-61] and bismuth sulfide ($Bi_2S_3$)[62-64] nanoparticles with MEH-PPV, poly[2-methoxy-5-(3′,7′-dimethyloctyloxy)-1,4-phenylenevinylene] (MDMO-PPV) or P3HT, however photovoltaic device

efficiencies are yet to beat the toxic alternatives of cadmium and lead based solar cells. Ternary metal chalcogenide QDs have also been considered for hybrid photovoltaics. Examples using hybrid solar cells based on copper indium sulfide ($CuInS_2$) [65,66] and copper indium selenide ($CuInSe_2$),[67] combined with a variety of conjugated polymers have been demonstrated.

## *In-situ* Polymer/Nanoparticle Solar Cells

*In-situ* fabricated hybrid photovoltaics are very similar to their *ex-situ* analogues, in terms of the nanostructures formed, nanoparticle sizes, the morphology of the nanocomposite, and device structure. The *in-situ* approach differs in that it attempts to overcome the problems that are generated by the use of capping ligands that are required in the *ex-situ* method.

Typically capping ligands, like long-chained amines, bulky phosphines or phosphine oxides, prevent particles agglomeration during synthesis, and control the nanoparticle shape and growth rate. This method has the advantage that a high level of control is gained over the nanoparticles, and a product with a narrow particle size distribution can be obtained. However, these ligands interfere with the fundamental processes required for solar cell function, such as, charge generation and charge transport. Removing these ligands is therefore a crucial step, in obtaining high efficiency solar cells. To this end, a lot of work has gone into the development of ligand exchange processes, to swap the long ligands used in the synthesis for smaller ones. These include an exchange to pyridine,[37,40] butylamine,[68] or thiols, such as t-butylthiol.[69,70]

*In-situ* fabrication of the inorganic component removes the capping ligands completely, both in the synthesis step and in the final device. The method requires a precursor material that can be processed with a semiconducting polymer to form a film. This precursor then has to undergo a conversion step to form the nanoparticles with the solid-state polymer matrix and have, as the only side products, molecules that are volatile at the conversion temperature. This means that a clean synthesis of the nanoparticles is performed, with no extra contaminants.

This concept was demonstrated by Beek *et* al. to form zinc oxide (ZnO) in the conjugated polymer MDMO-PPV.[71] Diethyl zinc was spin coated with the polymer in an atmosphere with 40% humidity, followed by annealing at 110°C. This formed crystalline ZnO in the polymer matrix, with only ethene and water as the bi-products, both of which are removed by the annealing step. This resulted in photovoltaic devices with a PCE of 1.1%. Oosterhout *et* al. further developed this method and achieved a PCE of 1.7%.[72]

Apart from ZnO, by far the highest volume of work, on *in-situ* polymer/nanoparticle solar cells, has been performed utilising the thermal decomposition of metal dithiocarbonate (xanthate) complexes. This

method was first utilised to fabricated solar cells by Leventis *et* al.[73] in this research group, in the year prior to my joining.

### *The Thermal Decomposition of Metal Xanthate Complexes to Form Metal Sulfides*

The method of Leventis *et* al. provides an extremely clean route to the formation of, theoretically any, metal sulfide. Unlike the ZnO formation, using diethyl zinc, which required water to convert the precursor, the decomposition of metal xanthates proceeds with only a thermal annealing step. Upon decomposition, volatile products of pyridine, alkenes and hydrogen sulfide are formed, which are all gases at the decomposition temperature. Films of P3HT/CdS were fabricated following a co-deposition of bispyridal cadmium dithiocarbonate and polymer, followed by an annealing step of 160°C in a nitrogen atmosphere. This yielded initial photovoltaic devices with a PCE of 0.7%.[73] This method was further developed by Dowland *et* al., through the optimisation of the device active layers, and the addition of a CdS seed layer, achieving a PCE of 2.17%.[74] This method was also used to demonstrate that, under equivalent conditions, the removal of the ligands, in P3HT/CdS solar cells, increased the charge generation yield and also the device efficiency, in comparison to *ex-situ* fabricated capped nanoaparticles.[75]

This method has also been show to work for other metal sulfides, including $Sb_2S_3$[76], as well as ternary systems. The record for highest efficiency for an *in-situ* hybrid polymer/inorganic solar cell is currently held by Rath *et* al. for such a ternary system.[77-80] Here, poly[(2,7-silafluorene)-alt-(4,7-di-2-thienyl-2,1,3-benzothiadiazole)] (PSiF-DBT) was blended with a copper and an indium xanthate, which decomposed to form $CuInS_2$ and gave a PCE of 2.8%.

## Project Aims and Motivation

The blue-sky aim of this project, as with many projects in the field, is to search for photovoltaic system that could potentially become a viable global renewable energy solution. Though this goal is perhaps extremely ambitious, it is not outside the realms of possibility. It is this possibility that drives us to work until the early hours of the morning, and to repeat a failed experiment, not because we believe that an error has been made, but because we hope one has been made. It is this author's hope that in pursuing this blue-sky goal that, along the way, some of the work pushes the scientific community as a whole, a small fraction closer to this goal.

More specifically, this work aims to build on the groundwork started by Leventis *et* al. on the *in-situ* decomposition of xanthate complexes. Extensive research has been undertaken on certain aspects of these systems, such as device optimisation and charge photogeneration. However, with this system, there are two main questions that are yet to be addressed: Can the morphology of hybrid photovoltaics be controlled using the *in-situ* decomposition of xanthate complexes? And, can an efficient non-toxic hybrid system be fabricated using this same methodology?

In Chapter 4, an answer to this first question was attempted to be found. The effect of tuning the solubilising ligand moiety of metal xanthate complexes was investigated. This is first applied to the system of P3HT/CdS, as this materials combination has be studied the most thus far. The effect that the alteration of the ligand had on the morphology of the system was studied in depth. This was achieved by observing the *in-situ* formation of the CdS crystals using a range of materials characterisation techniques. The effect that the different morphologies had on the photophysical properties and overall photovoltaic device performance was then studied. The information gained on this 'model' system was then briefly applied to P3HT/$Sb_2S_3$ blends, in order to investigate whether the effects of ligand size were universal. The transition from CdS to $Sb_2S_3$ was also the first step in a reduction in the toxicity of the devices.

In Chapter 5, the issue of toxicity was then further addressed, by applying the xanthate methodology to form, for the first time, $Bi_2S_3$ *in-situ*. Here, two different devices structures were investigated, borrowing inspiration from both polymer/nanoparticle blend solar cells and also solid-state dye-sensitised solar cells. Although a functional non-toxic system was fabricated, the efficiency of these devices did not challenge those of the toxic counterparts. Further investigation was required into the charge transfer between P3HT and $Bi_2S_3$.

In Chapter 6, through a collaboration with The Institute of Photonic Sciences (ICFO) in Spain, a better understanding of the charge transfer processes in polymer/$Bi_2S_3$ systems was gained. These *ex-situ*

fabricated systems had been shown to function with reasonable efficiencies, but little was known about how the systems generated charges, and also which parameters were responsible for governing their efficiency. A spectroscopic study of these systems was undertaken to gain an insight into the mechanisms of charge transfer, with the overall goal that this knowledge could be used to further increase the photovoltaic performance of these non-toxic hybrid systems.

# References


(1) *Interstellar.* [Film] Directed by: Christopher Nolan. UK: Warner Bros. Pictures; 2014.

(2) Williams, R. *The Journal of Chemical Physics* 1960, *32*, 1505.

(3) Adams, W. G.; Day, R. *Proceedings of the Royal Society of London* 1876, *25*, 113.

(4) Nelson, J. *The Physics of Solar Cells*; 2 ed.; Imperial College Press, 2003.

(5) Eley, D. *Transactions of the Faraday Society* 1953, *49*, 79.

(6) Bolto, B. *Aust. J. Chem.* 1963, *16*, 1090.

(7) De Surville, R.; Jozefowicz, M.; Yu, L. T.; Pepichon, J.; Buvet, R. *Electrochim. Acta* 1968, *13*, 1451.

(8) Chiang, C. K.; Fincher, C. R.; Park, Y. W.; Heeger, A. J.; Shirakawa, H.; Louis, E. J.; Gau, S. C.; MacDiarmid, A. G. *Phys. Rev. Lett.* 1977, *39*, 1098.

(9) Nobelprize.org 2010.

(10) Izumi, T. *J. Am. Chem. Soc.* 2003, *125*, 5286.

(11) Halls, J. J. M.; Pichler, K.; Friend, R. H.; Moratti, S. C.; Holmes, A. B. *Appl. Phys. Lett.* 1996, *68*, 3120.

(12) Kroeze, J. E.; Savenije, T. J.; Vermeulen, M. J. W.; Warman, J. M. *J. Phys. Chem. B* 2003, *107*, 7696.

(13) Clarke, T. M.; Durrant, J. R. *Chem. Rev.* 2010.

(14) Yu, G. *Science* 1995, *270*, 1789.

(15) Halls, J. J. M.; Walsh, C. A.; Greenham, N. C.; Marseglia, E. A.; Friend, R. H.; Moratti, S. C.; Holmes, A. B. *Nature* 1995, *376*, 498.

(16) Dennler, G.; Scharber, M. C.; Brabec, C. J. *Adv. Mater.* 2009, *21*, 1323.

(17) Brabec, C. J.; Gowrisanker, S.; Halls, J. J. M.; Laird, D.; Jia, S.; Williams, S. P. *Adv. Mater.* 2010, *22*, 3839.

(18) Small, C. E.; Chen, S.; Subbiah, J.; Amb, C. M.; Tsang, S.-W.; Lai, T.-H.; Reynolds, J. R.; So, F. *Nat Photon* 2012, *6*, 115.

(19) He, Z.; Zhong, C.; Su, S.; Xu, M.; Wu, H.; Cao, Y. *Nat Photon* 2012, *6*, 591.

(20) Liu, S.; Zhang, K.; Lu, J.; Zhang, J.; Yip, H.-L.; Huang, F.; Cao, Y. *J. Am. Chem. Soc.* 2013, *135*, 15326.

(21) Guo, X.; Zhou, N.; Lou, S. J.; Smith, J.; Tice, D. B.; Hennek, J. W.; Ortiz, R. P.; Navarrete, J. T. L.; Li, S.; Strzalka, J.; Chen, L. X.; Chang, R. P. H.; Facchetti, A.; Marks, T. J. *Nat Photon* 2013, *7*, 825.

(22) He, Z.; Zhong, C.; Huang, X.; Wong, W.-Y.; Wu, H.; Chen, L.; Su, S.; Cao, Y. *Adv. Mater.* 2011, *23*, 4636.

(23) Green, M. A.; Emery, K.; Hishikawa, Y.; Warta, W.; Dunlop, E. D. *Progress in Photovoltaics: Research and Applications* 2015, *23*, 1.

(24) You, J.; Dou, L.; Yoshimura, K.; Kato, T.; Ohya, K.; Moriarty, T.; Emery, K.; Chen, C.-C.; Gao, J.; Li, G.; Yang, Y. *Nat Commun* 2013, *4*, 1446.

(25) Zhou, E.; Cong, J.; Wei, Q.; Tajima, K.; Yang, C.; Hashimoto, K. *Angew. Chem. Int. Ed.* 2011, *50*, 2799.

(26) Mori, D.; Benten, H.; Kosaka, J.; Ohkita, H.; Ito, S.; Miyake, K. *ACS Appl. Mater. Interfaces* 2011, *3*, 2924.

(27) Mori, D.; Benten, H.; Okada, I.; Ohkita, H.; Ito, S. *Adv. Energy Mater.* 2014, *4*, n/a.

(28) Bertho, S.; Janssen, G.; Cleij, T. J.; Conings, B.; Moons, W.; Gadisa, A.; D'Haen, J.; Goovaerts, E.; Lutsen, L.; Manca, J.; Vanderzande, D. *Sol. Energy Mater. Sol. Cells* 2008, *92*, 753.

(29) Neugebauer, H.; Brabec, C.; Hummelen, J. C.; Sariciftci, N. S. *Sol. Energy Mater. Sol. Cells* 2000, *61*, 35.

(30) Kawano, K.; Pacios, R.; Poplavskyy, D.; Nelson, J.; Bradley, D. D. C.; Durrant, J. R. *Sol. Energy Mater. Sol. Cells* 2006, *90*, 3520.

(31) Jørgensen, M.; Norrman, K.; Krebs, F. C. *Sol. Energy Mater. Sol. Cells* 2008, *92*, 686.

(32) Greenham, N. C.; Peng, X.; Alivisatos, A. P. *Phys. Rev. B* 1996, *54*, 17628.

(33) Greenham, N. C.; Peng, X.; Alivisatos, A. P. *Synth. Met.* 1997, *84*, 545.

(34) Ginger, D. S.; Greenham, N. C. *Phys. Rev. B* 1999, *59*, 10622.

(35) Huynh, W. U.; Peng, X.; Alivisatos, A. P. *Adv. Mater.* 1999, *11*, 923.

(36) Huynh, W. U. *Science* 2002, *295*, 2425.

(37) Huynh, W. U.; Dittmer, J. J.; Libby, W. C.; Whiting, G. L.; Alivisatos, A. P. *Adv. Funct. Mater.* 2003, *13*, 73.

(38) Skaff, H. *J. Am. Chem. Soc.* 2004, *126*, 11322.

(39) Sun, B.; Marx, E.; Greenham, N. C. *Nano Lett.* 2003, *3*, 961.

(40) Dayal, S.; Kopidakis, N.; Olson, D. C.; Ginley, D. S.; Rumbles, G. *Nano Lett.* 2009, *10*, 239.

(41) Celik, D.; Krueger, M.; Veit, C.; Schleiermacher, H. F.; Zimmermann, B.; Allard, S.; Dumsch, I.; Scherf, U.; Rauscher, F.; Niyamakom, P. *Sol. Energy Mater. Sol. Cells* 2012, *98*, 433.

(42) Ren, S.; Chang, L.-Y.; Lim, S.-K.; Zhao, J.; Smith, M.; Zhao, N.; Bulović, V.; Bawendi, M.; Gradečak, S. *Nano Lett.* 2011, null.

(43) Hines, M. A.; Scholes, G. D. *Adv. Mater.* 2003, *15*, 1844.

(44) Bawendi, M. G.; Steigerwald, M. L.; Brus, L. E. *Annu. Rev. Phys. Chem.* 1990, *41*, 477.

(45) Kang, I. *Journal of the Optical Society of America. B, Optical physics* 1997, *14*, 1632.

(46) Moreels, I.; Lambert, K.; Smeets, D.; De Muynck, D.; Nollet, T.; Martins, J. C.; Vanhaecke, F.; Vantomme, A.; Delerue, C.; Allan, G.; Hens, Z. *ACS Nano* 2009, *3*, 3023.

(47) Vossmeyer, T.; Katsikas, L.; Giersig, M.; Popovic, I. G.; Diesner, K.; Chemseddine, A.; Eychmueller, A.; Weller, H. *The Journal of Physical Chemistry* 1994, *98*, 7665.

(48) McDonald, S. A. *Nature Materials* 2005, *4*, 138.

(49) Jin, S.-H.; Jang, M.-S.; Suh, H.-S.; Cho, H.-N.; Lee, J.-H.; Gal, Y.-S. *Chem. Mater.* 2002, *14*, 643.

(50) Greenwald, Y.; Xu, X.; Fourmigué, M.; Srdanov, G.; Koss, C.; Wudl, F.; Heeger, A. J. *J. Polym. Sci., Part A: Polym. Chem.* 1998, *36*, 3115.

(51) Zhang, S.; Cyr, P. W.; McDonald, S. A.; Konstantatos, G.; Sargent, E. H. *Appl. Phys. Lett.* 2005, *87*, 233101.

(52) Watt, A. *Chemical communications (1965)* 2004, *2004*, 2334.

(53) Watt, A. A. R.; Blake, D.; Warner, J. H.; Thomsen, E. A.; Tavenner, E. L.; Rubinsztein-Dunlop, H.; Meredith, P. *J. Phys. D: Appl. Phys.* 2005, *38*, 2006.

(54) Jiang, X.; Lee, S. B.; Altfeder, I. B.; Zakhidov, A. A.; Schaller, R. D.; Pietryga, J. M.; Klimov, V. I.; Zakya, H. K., Paul, A. L., Eds.; SPIE: 2005; Vol. 5938, p 59381F.

(55) Cui, D.; Xu, J.; Zhu, T.; Paradee, G.; Ashok, S. *Appl. Phys. Lett.* 2009, *88*, 183111.

(56) Seo, J.; Cho, M. J.; Lee, D.; Cartwright, A. N.; Prasad, P. N. *Adv. Mater.* 2011, *23*, 3984.

(57) Liu, Z.; Sun, Y.; Yuan, J.; Wei, H.; Huang, X.; Han, L.; Wang, W.; Wang, H.; Ma, W. *Adv. Mater.* 2013, *25*, 5772.

(58) Wang, Z.; Qu, S.; Zeng, X.; Liu, J.; Zhang, C.; Tan, F.; Jin, L.; Wang, Z. *J. Alloys Compd.* 2009, *482*, 203.

(59) Lin, Y.-Y.; Wang, D.-Y.; Yen, H.-C.; Chen, H.-L.; Chen, C.-C.; Chen, C.-M.; Tang, C.-Y.; Chen, C.-W. *Nanotechnology* 2009, *20*, 405207.

(60) Steinhagen, C.; Harvey, T. B.; Stolle, C. J.; Harris, J.; Korgel, B. A. *J. Phys. Chem Lett.* 2012, *3*, 2352.

(61) Layek, A.; Middya, S.; Ray, P. *J Mater Sci: Mater Electron* 2013, *24*, 3749.

(62) Martinez, L.; Bernechea, M.; de Arquer, F. P. G.; Konstantatos, G. *Adv. Energy Mater.* 2011, *1*, 1029.

(63) Martinez, L.; Stavrinadis, A.; Higuchi, S.; Diedenhofen, S. L.; Bernechea, M.; Tajima, K.; Konstantatos, G. *PCCP* 2013, *15*, 5482.

(64) Martinez, L.; Higuchi, S.; MacLachlan, A. J.; Stavrinadis, A.; Miller, N. C.; Diedenhofen, S. L.; Bernechea, M.; Sweetnam, S.; Nelson, J.; Haque, S. A.; Tajima, K.; Konstantatos, G. *Nanoscale* 2014, *6*, 10018.

(65) Arici, E.; Sariciftci, N. S.; Meissner, D. *Adv. Funct. Mater.* 2003, *13*, 165.

(66) Yue, W.; Han, S.; Peng, R.; Shen, W.; Geng, H.; Wu, F.; Tao, S.; Wang, M. *J. Mater. Chem.* 2010, *20*, 7570.

(67) Aldakov, D.; Lefrancois, A.; Reiss, P. *J. Mater. Chem. C* 2013, *1*, 3756.

(68) Radychev, N.; Lokteva, I.; Witt, F.; Kolny-Olesiak, J.; Borchert, H.; Parisi, J. r. *J. Phys. Chem. C* 2011, *115*, 14111.

(69) Greaney, M. J.; Das, S.; Webber, D. H.; Bradforth, S. E.; Brutchey, R. L. *ACS Nano* 2012, *6*, 4222.

(70) Webber, D. H.; Brutchey, R. L. *J. Am. Chem. Soc.* 2011, *134*, 1085.

(71) Beek, W. J. E.; Slooff, L. H.; Wienk, M. M.; Kroon, J. M.; Janssen, R. A. J. *Adv. Funct. Mater.* 2005, *15*, 1703.

(72) Oosterhout, S. D.; Koster, L. J. A.; van Bavel, S. S.; Loos, J.; Stenzel, O.; Thiedmann, R.; Schmidt, V.; Campo, B.; Cleij, T. J.; Lutzen, L.; Vanderzande, D.; Wienk, M. M.; Janssen, R. A. J. *Adv. Energy Mater.* 2011, *1*, 90.

(73) Leventis, H. C.; King, S. P.; Sudlow, A.; Hill, M. S.; Molloy, K. C.; Haque, S. A. *Nano Lett.* 2010, *10*, 1253.

(74) Dowland, S.; Lutz, T.; Ward, A.; King, S. P.; Sudlow, A.; Hill, M. S.; Molloy, K. C.; Haque, S. A. *Adv. Mater.* 2011, *23*, 2739.

(75) Reynolds, L. X.; Lutz, T.; Dowland, S.; MacLachlan, A.; King, S.; Haque, S. A. *Nanoscale* 2012, *4*, 1561.

(76) Bansal, N.; O'Mahony, F. T. F.; Lutz, T.; Haque, S. A. *Adv. Energy Mater.* 2013, *3*, 986.

(77) Rath, T.; Edler, M.; Haas, W.; Fischereder, A.; Moscher, S.; Schenk, A.; Trattnig, R.; Sezen, M.; Mauthner, G.; Pein, A.; Meischler, D.; Bartl, K.; Saf, R.; Bansal, N.; Haque, S. A.; Hofer, F.; List, E. J. W.; Trimmel, G. *Adv. Energy Mater.* 2011, *1*, 1046.

(78) Maier, E.; Rath, T.; Haas, W.; Werzer, O.; Saf, R.; Hofer, F.; Meissner, D.; Volobujeva, O.; Bereznev, S.; Mellikov, E.; Amenitsch, H.; Resel, R.; Trimmel, G. *Sol. Energy Mater. Sol. Cells* 2011, *95*, 1354.

(79) Arar, M.; Gruber, M.; Edler, M.; Haas, W.; Hofer, F.; Bansal, N.; Reynolds, L. X.; Haque, S. A.; Zojer, K.; Trimmel, G.; Rath, T. *Nanotechnology* 2013, *24*, 484005.

(80) Fradler, C.; Rath, T.; Dunst, S.; Letofsky-Papst, I.; Saf, R.; Kunert, B.; Hofer, F.; Resel, R.; Trimmel, G. *Sol. Energy Mater. Sol. Cells* 2014, *124*, 117.

# Chapter 3

## Experimental Methods and Techniques

***Dr Ian Malcolm:*** *God help us, we're in the hands of engineers.*

Jurassic *Park (1993)*[1]

# Materials Syntheses

## Cadmium Xanthate Complexes

These complexes will be referred to as cadmium xanthate complexes throughout this thesis and will be distinguished by indicating the respective R-group present in the ligand moiety.

### *Bis-pyridal cadmium(II) O-ethyl/propyl/butyl/pentyl dithiocarbonate*

Cadmium ethyl/propyl/butyl/pentyl xanthate was synthesised using the following methods that have been previously documented in the literature.[2,3] Potassium hydroxide was stirred in a 1:1 molar ratio with a primary alcohol (e.g. 1-propanol to form propyl xanthate) and a small amount of water. The solution was cooled in an ice bath followed by a dropwise addition of carbon disulfide to a slight excess (1.1 equiv.). The resulting slurry was stirred for 30 min before vacuum filtering and washing with diethyl ether. The potassium xanthate products were then recrystallised from methanol. Potassium ethyl xanthate is commercially available and was purchased from Sigma Aldrich (Potassium *O*-ethyl dithiocarbonate 140-89-6). To form the cadmium salts, an aqueous solution of the respective potassium xanthate compounds was added to a rapidly stirring aqueous solution of cadmium nitrate in a molar ratio of 2:1. The products were filtered and washed with water followed by methanol. Pyridine adducts were obtained by adding 2 equiv. of pyridine to a suspension of the cadmium xanthate in dichloromethane, solubilising the compound, followed by evaporation of the solvent. All xanthates were then recrystallised from acetone.

### *Cadmium(II) O-ethyl dithiocarbonate*

$^1$H NMR ($CDCl_3$, 400 MHz, δ): 1.50-1.47 (3H, t, $CH_3$), 4.54-4.49 (2H, q, $CH_2$), 7.48-7.45 (2H, m, *meta*CH), 7.88-7.83 (1H, m, *para*CH), 8.81-8.79 (2H, m, *ortho*CH) ppm.

Anal. calcd for $CdC_{16}N_2S_4O_2H_{20}$: C 37.50, H 3.91, N 5.47; found: C 37.52, H 3.92, N 5.59

### *Cadmium(II) O-propyl dithiocarbonate*

$^1$H NMR ($CDCl_3$, 400 MHz, δ): 1.07-1.03 (3H, t, $CH_3$), 1.93-1.84 (2H, m, $CH_2$), 4.43-4.40 (2H, t, $CH_2$), 7.48-7.45 (2H, m, *meta*CH), 7.88-7.83 (1H, m, *para*CH), 8.81-8.79 (2H, m, *ortho*CH) ppm.

Anal. calcd for $CdC_{18}N_2S_4O_2H_{24}$: C 40.00, H 4.44, N 5.19; found: C 39.79, H 4.64, N 5.19

### *Cadmium(II) O-butyl dithiocarbonate*

$^1$H NMR ($CDCl_3$, 400 MHz, δ): 1.01-0.98 (3H, t, $CH_3$), 1.55-1.45 (2H, m, $CH_2$), 1.88-1.81 (2H, m, $CH_2$), 4.48-4.45 (2H, t, $CH_2$), 7.50-7.47 (2H, m, *meta*CH), 7.90-7.85 (1H, m, *para*CH), 8.83-8.82 (2H, m, *ortho*CH) ppm.

Anal. calcd for $CdC_{20}N_2S_4O_2H_{28}$: C 42.25, H 4.93, N 4.93; found: C 41.99, H 5.04, N 4.77

### *Cadmium(II) O-pentyl dithiocarbonate*

$^1$H NMR ($CDCl_3$, 400 MHz, δ): 0.97-0.94 (3H, t, $CH_3$), 1.43-1.36 (4H, m, $CH_2CH_2$), 1.90-1.83 (2H, m, $CH_2$), 4.47-4.44 (2H, t, $CH_2$), 7.50-7.47 (2H, m, *meta*CH), 7.90-7.85 (1H, m, *para*CH), 8.83-8.81 (2H, m, *ortho*CH) ppm.

Anal. calcd for $CdC_{22}N_2S_4O_2H_{32}$: C 44.30, H 5.37, N 4.70; found: C 44.02, H 5.58, N 4.64

### *Cadmium(II) O-2,2-dimethyl-3-pentyl dithiocarbonate*

This xanthate complex was obtained through a collaboration with Graz University and will be referred to as cadmium heptyl xanthate in this thesis.

Cadmium (II) chloride (1.81 g, 9.86 mmol) was dissolved in 75 mL deionised water. Potassium O-2,2-dimethylpentan-3-yl dithiocarbonate (5.00 g, 21.7 mmol, 2.2 equiv.) which was synthesized according to literature[4] was dissolved in 75 ml of deionised water. The potassium xanthate solution was added dropwise to the cadmium chloride solution under stirring. The reaction was allowed to stir for about 2.5 hours and afterwards the white precipitate was filtered off and dried in vacuum. The precipitate was dissolved in chloroform and added to methanol to obtain a white powder, which was dried in vacuum.

$^1$H NMR ($CDCl_3$, 300 MHz, δ): 5.00 – 4.95 (1H, m, CH), 1.80 – 1.66 (2H, m, $CH_2$), 0.99 – 0.95 (12H, m, 4x$CH_3$) ppm. $^{13}$C NMR (75 MHz, $CDCl_3$, δ): 230.8 (C=S), 101.2 (CH), 36.1 (($C(CH_3)_3$)), 26.3 (3C, $C(CH_3)_3$), 23.6 ($CH_2$), 11.35 ($CH_3$-$CH_2$) ppm.

Anal. calcd for $C_{16}H_30S_4O_2Cd$: C 38.82, H 6.11, S 25.90; found: C 38.84, H 6.11, S 25.91

## Antimony Xanthate Complexes

### *Antimony(III) O-ethyl/pentyl dithiocarbonate*

These compounds are referred to as antimony ethyl/pentyl xanthate.

Antimony (III) chloride (10 g, 43.8 mmol) and potassium ethyl xanthate (16 g, 99.8 mmol, 33% excess) were placed into a round bottomed flask connected to a schlenk line and the system was put under nitrogen. Toluene (150 ml) was then added and the slurry was heated for 1 hour at 70°C. Both materials are not soluble in toluene, however, the product is. The yellow solution was then filtered to remove any unreacted starting material and rotovapped to leave a viscous oil. A small amount of hot chlorobenzene (10 ml) was added to this and the solution was filtered using a PTFE syringe filter. Best results were obtained when this was done in batches, keeping the solution warm, as the product can precipitate in the syringe. In the case of ethyl, the filtered solution was placed in the freezer to crash out of solution, vacuum filtered, washed with diethyl ether and dried in a desiccator. The pentyl xanthate did not precipitate and so the after addition of the chlorobenzene this was evaporated to leave a viscous oil.

### *Antimony(III) O-ethyl dithiocarbonate*

$^1$H NMR ($CDCl_3$, 400 MHz, δ): 1.50 (3H, t, $CH_3$), 4.67 (2H, q, $CH_2$) ppm

### *Antimony(III) O-pentyl dithiocarbonate*

$^1$H NMR ($CDCl_3$, 400 MHz, δ): 0.95 (3H, t, $CH_3$), 1.41 (4H, m, $CH_2CH_2$), 1.85 (2H, m, $CH_2$), 4.59 (2H, t, $CH_2$) ppm

## Bismuth Xanthate Complexes

### *Bismuth(III) O-ethyl/pentyl dithiocarboante*

These compounds are referred to as bismuth ethyl/pentyl xanthate.

Bismuth nitrate pentahydrate (30.92 g, 63.74 mmol) was suspended in water (500 ml). This was stirred rapidly and enough conc. HCl was added until the solution became clear (~40 ml). Potassium ethyl/pentyl xanthate, the syntheses of which are described in the Cadmium Xanthate Complexes section, was dissolved in water and added in a slight excess. In the case of the pentyl xanthate, this was (33.36 g, 198.38 mmol). The reaction was stirred for 60 mins then vacuum filtered and washed with water. The yellow product was dried overnight in a desiccator and recrystallised from acetone. The final product consisted of bright yellow 0.5 cm long needles.

### *Bismuth(III) O-ethyl dithiocarboante*

$^1$H NMR ($CDCl_3$, 400 MHz, δ): 1.55 (3H, t, $CH_3$), 4.75 (2H, q, $CH_2$) ppm

### *Bismuth(III) O-pentyl dithiocarbonate*

$^1$H NMR ($CDCl_3$, 400 MHz, δ): 0.98 (3H, t, $CH_3$), 1.45 (4H, m, $CH_2CH_2$), 1.89 (2H, m, $CH_2$), 4.67 (2H, t, $CH_2$) ppm

# Thin Film and Device Fabrication

## Substrates

When making almost any sample other than a complete device, samples were processed onto a plain glass substrate that was cut into approximately 1.25 x 1.25 cm squares by cutting a typical microscope slide into 12 smaller pieces. When full devices were made, 1.2 x 1.2 cm indium doped tin oxide (ITO) substrates (Psiotec Ltd) were used.

Before coating either of these substrates with any further layer a common cleaning procedure was used to insure a clean surface in all cases, but also to remove the protective plastic layer from the ITO substrates. Substrates were sonicated in acetone 3 times for 10 mins, deionised (DI) water and detergent (Teepol L or Decon 90) for 10 mins, followed by DI water 3 times for 10 mins, to ensure the soap was completely removed. The substrates were then sonicated in acetone twice for 10 mins followed by isopropyl alcohol (IPA) twice for 10 mins. Substrates were stored in IPA until used and blown dry with nitrogen immediately before a layer was deposited on top.

## Electron Selecting Oxide Layers

All of the devices made in the project were of an inverted architecture and as a result require an electron selective layer immediately on top of the ITO. These layers took the form of metal oxides that were spin coated and were also sometimes required in order to get the active layer to wet to the glass when plain glass was being used for spectroscopy. Two metal oxides were used, namely, $TiO_2$ and ZnO. The solutions used for each of these were as follows:

$TiO_2$ – Ethanolamine (55 µl, colourless) was added to titanium isopropoxide (70 µl, colourless). 2-methoxyethanol (1 ml, colourless) was then added and the solution was stirred for 30 mins before filtering using a 0.45 µm PTFE syringe filter. If the resulting solution was not colourless then the process was repeated with fresh ethanolamine.

ZnO – Zinc acetate dehydrate (130.7 mg) was dissolved in 2-methoxyethanl (1 ml, colourless), to which ethanolamine (36 µl, colourless) was added quickly. The solution was stirred for 30 mins before filtering using a 0.45 µm PTFE syringe filter.

Films were produced by spin coating one of these solutions at 6000 rpm with an acceleration of 2000 rpm/s for 30 seconds (6000 rpm, 2000 rpm/s, 30 s). Films were then annealed in the furnace at 450°C.

## Seed Layers

Many of the devices required a thin metal sulfide layer in between the oxide layer and the active layer. This was shown previously to markedly improve the overall efficiency of devices, possibly to encourage growth of the sulfides within the polymers at the correct side of the heterojunction.[5] CdS was often used as a seed layer even for devices not containing CdS in the heterojunction. The typical CdS seed layer method is given below and any variations of this are present in the experimental sections of the specific results chapters. Unless stated, seed layers were only used in complete devices, and not when an active layer was spun onto plain glass for characterisation e.g. photoluminescence or steady-state absorption measurements.

Cd-ethyl xanthate (100 mg) was dissolved in chlorobenzene (1 ml) and stirred for 30 mins, or until all the solid appeared dissolved. This solution was filtered using a 0.45 µm PTFE syringe filter before spin coating (6000 rpm, 2000 rpm/s, 45 s) and annealing in a nitrogen glovebox for 30 mins, typically at 160°C.

## Active Layers

The makeup of the active layers used in this project are varied and their methods would not be particularly relevant here. The specific method used is given in each of the experimental sections for each individual results chapter. Here is presented a typical method for a P3HT/CdS blend that could either be deposited on glass for any spectroscopic or materials characterisation, or as part of a device.

Cd-ethyl xanthate (150 mg) was dissolved in chlorobenzene (0.5 ml) and stirred for 30 mins, or until all the solid appeared dissolved. Separately P3HT (Sigma-Aldrich) (9.375 mg) was dissolved in chlorobenzene (0.5 ml) often using a small amount of heat (40°C). The P3HT solution would change from dark purple to an orange-red when fully dissolved. The Cd-ethyl xanthate solution was filtered using a 0.45 µm PTFE syringe filter and then added to dissolved P3HT solution. This solution was then stirred for 30 min to ensure good mixing. Careful attention was paid to the solution to make sure the P3HT had not precipitated out of solution. Best film quality was obtained with as cool a solution as possible, without the solution being so cold as to precipitate the P3HT. Typically the solution was maintained at 30-35°C before spin coating (1000 rpm, 1000 rpm/s, 60 s) and then annealing in a nitrogen glovebox for 1 hour at 160°C.

## Top Contacts

Devices were completed by evaporating $MoO_3$ (10 nm) followed by Ag (100 nm) in a vacuum of < 0.5 μbar, through a shadow mask to give a pixel area of 4.5 $mm^2$.

# Experimental Characterisation Techniques

## UV-Vis Absorption Spectroscopy (UV-Vis)

Steady-state absorption measurements were carried out using either a Shimadzu UV-1601 or a Shimadzu 2600 spectrophotometer with an ISR-2600Plus Integrating Sphere Attachment. All measurements were made under ambient conditions unless stated otherwise.

## Photoluminescence Spectroscopy (PL)

Photoluminescence measurements were made with a Horiba Jobin Yvon Fluorolog-2. All measurements were taken under ambient conditions and excitation wavelengths are presented with the relevant data.

## Raman Spectroscopy

Raman spectra were measured using a LabRAM Infinity supplied by HORIBA Jorbin Yvon Ltd. with an external 532 nm Nd-YAG 25mW laser from Laser Quantum.

## X-ray Diffraction (XRD)

X-ray diffraction was conducted with a PANalytical X'Pert Pro MRD diffractometer using Ni filtered Cu K-alpha radiation at 40 kV and 40 mA.

## Grazing Incidence Wide Angle X-ray Scattering (GIWAXS) and Grazing Incidence Small Angle Scattering (GISAXS)

These measurements were taken by Thomas Rath as part of a collaboration with Graz University. This experimental section was also provide by Thomas. Simultaneous grazing incidence wide angle X-ray scattering (GIWAXS) and grazing incidence small angle scattering (GISAXS) measurements were performed at the Austrian SAXS Beamline 5.2L of the electron storage ring ELETTRA (Italy)[6] using a similar setup as has been described elsewhere.[7] For the GISAXS measurements, the beamline has been adjusted to a q-resolution ($q=4\pi/\lambda*\sin(2\theta/2)$, $2\theta$ represents the scattering angle) between 0.1 and 3.1 $nm^{-1}$ and the X-ray energy was 8 keV. The P3HT/cadmium xanthate samples were placed in a modified domed heating cell (DHS 1100 from Anton Paar GmbH, Graz, Austria) with a grazing angle of about 0.18° and were heated from 35°C up to 200°C at a heating rate of approx. 10°C$min^{-1}$ under a nitrogen atmosphere. During the temperature scan, data were recorded with 11 s time resolution using an image intensified CCD detector (GemStar/XIDIS model, Photonic Science Ltd., Millham, UK). For

detection of the GIWAXS signal, a Pilatus 100K two-dimensional hybrid pixel array detector system (Dectris, Baden, Switzerland) was used. The angular calibration of the detectors was carried out using silver behenate powder with a d-spacing of 58.38 Å placed in a measuring capillary.

## Transmission Electron Microscopy (TEM)

Transmission electron microscopy (TEM) was conducted using a JEOL 2000 MkII electron microscope operated at 200 kV. Films for TEM were prepared by spin coating onto a sacrificial water soluble PEDOT:PSS layer coated on glass. This allowed the films to be floated off the substrates by submersion in water. Floating films were then transferred to the conductive copper grids in order to be imaged in a top-down fashion.

## Thermogravimetric Analysis (TGA)

Thermogravimetric analysis (TGA) measurements were performed in helium atmosphere using a Netzsch Jupiter STA 449C (heating rate: 10°C/min).

## Transient Absorption Spectroscopy (TAS)

Transient absorption spectroscopy (TAS) is an extremely useful technique that can be used to probe a variety of different species in a thin film or device after photoexcitation. This technique is particularly useful for comparing the relative amounts of photogenerated charges and their lifetimes across a series of thin films/devices. There were two systems that were used during this project that are referred to as micro-second transient absorption spectroscopy (µs-TAS) and femto-second transient absorption spectroscopy (fs-TAS). Almost all of the measurements taken herein were performed using µs-TAS by myself, however the fs-TAS measurements were made by Ute Cappel under my observation.

### *Micro-second Transient Absorption Spectroscopy (µs-TAS)*

A schematic diagram of µs-TAS is presented in Figure 3.1, depicting a cartoon of how the technique works, some example data of the two different modes of operation, and two examples of the mechanisms that can be probed. A sample is excited by a laser pulse (pump light) from a dye laser (Photon Technology International GL-301, sub-nanosecond pulse width) pumped by a pulsed nitrogen laser (Photon Technology International GL-3300). A monochromator is used to select a wavelength from a continuous quartz halogen lamp (Bentham IL1) (probe light) which passes through the sample and is detected using a home-built silicon ($\lambda \leq 1000$ nm) or $In_xGa_{1-x}As$ ($\lambda > 1000$ nm) photodiode. The signal from the photodiode is amplified then monitored using an oscilloscope, measuring the change in absorption of the probe light before and after the pump pulse ($\Delta$Abs).

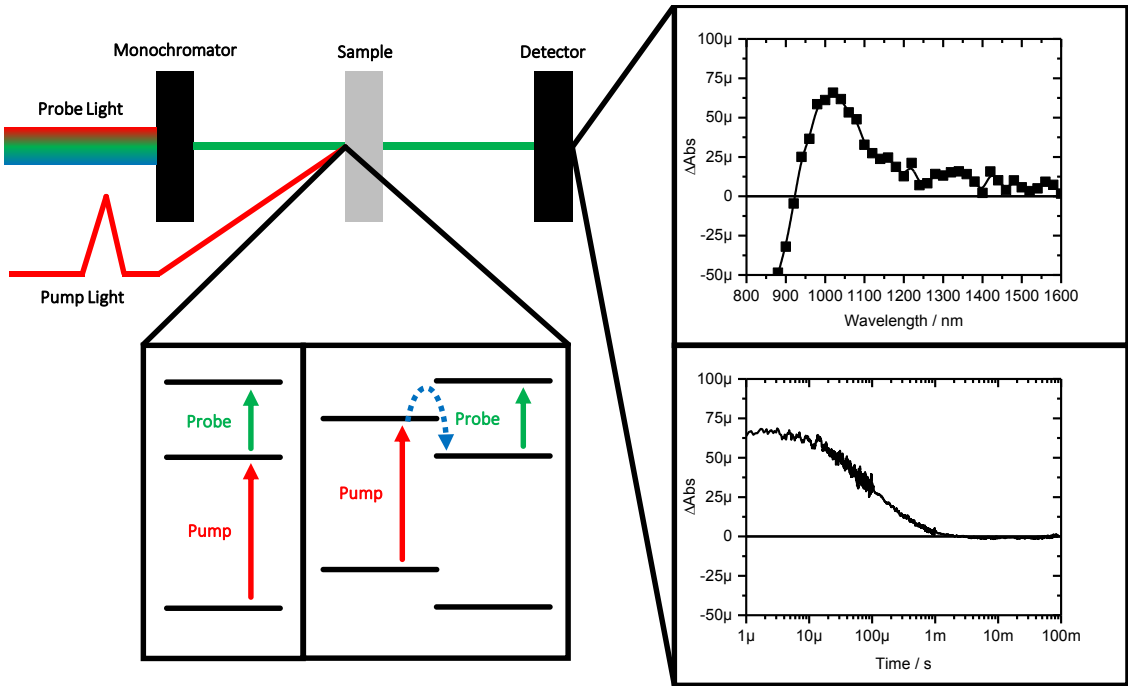



*Figure 3.1 - Schematic diagram of a transient absorption spectroscopy (TAS) setup. On the right some example data is given, illustrating the two different operational modes: constant time and constant probe wavelength. Some common examples of the processes that can be observed are also shown as cartoons, with the red arrows representing excitations caused by the pump pulse and then the green arrows representing excitations caused by the probe, either in a single material or in a two-component system after charge transfer, shown by the blue dashed arrow,*

Figure 3.1 depicts two possible systems in which a TAS signal could be observed, with the pump pulse induced transitions indicated by a red arrow and the second transitions indicated by the green arrows. The first example is a single material where the pump pulse is exciting a band-gap transition, creating a higher energy state such as an exciton. The probe light then excites a further transition, due to absorption from the exciton, a transition that wasn't possible before the pump pulse. Excitons are usually relatively short lived and as a result are not typically observed using the µs-TAS setup. The second example is of a donor/acceptor system, something that is studied much more extensively in this thesis. Here, after initial excitation of the donor material by the pump pulse, electron transfer is occurring to a donor material with a lower energy LUMO. The probe light then excites a transition in the donor material due to absorption of a polaron. This type of experiment can be very useful for studying the efficiency of a heterojunction at generating charges. However, attention has to be paid and experiments need to be carefully designed as many factors can affect the result, such as, the pump pulse being absorbed by both components.

On the right hand side of Figure 3.1 two sets of data are presented, one from each of the two modes of operation of the setup. The first is the ΔAbs at a given time (typically 1 or 10 µs) after the pump pulse for a range of wavelengths. This is used to scan the range of the detector to see what new signals are present after the pump pulse and is referred to as a transient spectrum. A positive signal indicates a new absorbing species after the pump pulse and a negative signal is due to a reduction in the amount

of a particular absorbing species. A negative signal is referred to as a bleach and is almost always due to the depopulation of the ground state. The data in Figure 3.1 shows a signal due to a polaron peaking at ~1000 nm and a negative signal due to the aforementioned ground state depopulation. The second mode of operation is constant probe wavelength. This is used after a spectrum has been taken and a feature of interest is studied in terms of its decay kinetics. This is used to investigate the lifetimes of a polaron, for example.

Unless stated otherwise, all TAS measurements are scaled by the amount of pump light absorbed.

### *Femto-second Transient Absorption Spectroscopy (fs-TAS)*

The principles behind femto-second transient absorption spectroscopy (fs-TAS) are exactly the same as µs-TAS, the major differences are the timescale that is measured and the instrumentation used to make the measurements. As mentioned previously the measurements made using this technique were performed by Ute Cappel. Here, fs-TAS was measured using pump and probe pulses generated from the output of a Solstice Ti:Sapphire regenerative amplifier (Spectra-Physics) with 800 nm 92 fs pulses with a 1 kHz frequency. The probe pulse was generated by a sapphire crystal and was split into a signal and a reference beam before the sample. The pump pulse was created using an optical parametric amplifier and a series of filters (TOPAS-NIRUVIS). It was then chopped mechanically to obtain a 500 Hz train of pulses. Both pump and probe pulses were focussed onto the same sample spot. Transient absorption spectra were calculated from the difference in detected probe light in presence and absence of the pump pulse and adjusted for fluctuations in probe intensity using the reference part of the probe beam. Transient absorption spectra at different delay times were obtained by varying the length travelled by the probe pulses prior to white light generation.

## Current Voltage Measurements

Current voltage measurements of the cells were obtained by applying an external electric field over the device and sweeping from reverse bias to forward bias while monitoring current flow using a Keithley 2400 source meter. Simulation of the AM1.5 solar spectrum was conducted using a 150W Xenon lamp (ScienceTech SS150W Solar Simulator) equipped with an IR filter (Water Filter) and AM1.5 filter (ScienceTech).

# References

(1) *Jurassic Park.* [Film] Directed by: Steven Spielberg. USA: Universal Pictures; 1993.

(2) Pradhan, N.; Katz, B.; Efrima, S. *J. Phys. Chem. B* 2003, *107*, 13843.

(3) Olson, D. C.; Piris, J.; Collins, R. T.; Shaheen, S. E.; Ginley, D. S. *Thin Solid Films* 2006, *496*, 26.

(4) Rath, T.; Edler, M.; Haas, W.; Fischereder, A.; Moscher, S.; Schenk, A.; Trattnig, R.; Sezen, M.; Mauthner, G.; Pein, A.; Meischler, D.; Bartl, K.; Saf, R.; Bansal, N.; Haque, S. A.; Hofer, F.; List, E. J. W.; Trimmel, G. *Adv. Energy Mater.* 2011, *1*, 1046.

(5) Dowland, S.; Lutz, T.; Ward, A.; King, S. P.; Sudlow, A.; Hill, M. S.; Molloy, K. C.; Haque, S. A. *Adv. Mater.* 2011, *23*, 2739.

(6) Amenitsch, H.; Rappolt, M.; Kriechbaum, M.; Mio, H.; Laggner, P.; Bernstorff, S. *J. Synchrotron Radiat.* 1998, *5*, 506.

(7) Fischereder, A.; Rath, T.; Haas, W.; Amenitsch, H.; Schenk, D.; Zankel, A.; Saf, R.; Hofer, F.; Trimmel, G. *ACS applied materials & interfaces* 2011, *4*, 382.

# Chapter 4

## Control of Hybrid Film Nanomorphology in P3HT/Metal Sulfide Solar Cells

*Morpheus*: *…sooner or later you're going to realise, just as I did, that there's a difference between knowing the path and walking the path.*

*The Matrix (1999)*[1]

## Abstract

In this chapter, molecular tuning of metal xanthate precursors is shown to have a marked effect on the heterojunction morphology of hybrid poly(3-hexylthiophene-2,5-diyl (P3HT)/CdS blends and, as a result, the photochemical processes and overall performance of *in-situ* fabricated hybrid solar cells. A series of cadmium xanthate complexes was synthesised for use as *in-situ* precursors to cadmium sulfide nanoparticles in hybrid P3HT/CdS solar cells. The formation of CdS domains was studied by simultaneous grazing incidence wide-angle X-ray scattering (GIWAXS) and grazing incidence small-angle X-ray scattering (GISAXS), revealing knowledge about crystal growth and the formation of different morphologies observed using transmission electron microscopy (TEM). These measurements show that there is a strong relationship between precursor structure and heterojunction nanomorphology. A combination of transient absorption spectroscopy (TAS) and photovoltaic device performance measurements is used to show the intricate balance required between charge photogeneration and percolated domains in order to effectively extract charges to maximize device power conversion efficiencies. An analogous method was applied to a P3HT/$Sb_2S_3$, finding that the ability to tune the morphology by precursor design was not unique to cadmium xanthates. This study presents a strong case for xanthate complexes as a useful route to designing optimal heterojunction morphologies for use in the emerging field of hybrid organic/inorganic solar cells, due to the fact that the nanomorphology can be tuned via careful design of these precursor materials.

This work formed the basis of the following publication:

Polymer/nanocrystal hybrid solar cells: Influence of molecular precursor design on film nanomorphology, charge generation and device performance MacLachlan, A. J.; Rath, T.; Cappel, U. B.; Dowland, S. A.; Amenitsch, H.; Knall, A-C.; Buchmaier, C.; Trimmel, G.; Nelson, J.; Haque, S. A. *Advanced Functional Materials* 2015, *3,* 409.

## Introduction

The morphology of both all organic heterojunctions and hybrid heterojunctions is an extremely important factor in determining the charge generation[2-5] and overall device performance.[2,5,6] In organic systems the tuning of morphology, through the use of additives, has demonstrated an enhancement in charge generation yield and device performance in small molecule systems[7] and modulate the power conversion efficiency from 2.6 to 4.5% in poly[2,6-(4,4-bis-(2-ethylhexyl)-4H-cyclopenta [2,1-b;3,4-b']dithiophene)-alt-4,7(2,1,3-benzothiadiazole)] (PCPDTBT)/[6,6]-phenyl-C71 butyric acid methyl ester (PC70BM) systems.[8]

In hybrid systems the morphology is often more difficult to change. Using the example of polymer/nanoparticle blends, the nanoparticles are a fixed shape, such as spheres, and although those spheres can have different degrees of aggregation, the domain size is fixed by the nanoparticle size. There is therefore not the same scope to introduce many different morphological phases, something that has been suggested in organic systems as the reason for success for the fullerene derivatives as acceptor materials.[9,10] These clean interfaces make hybrid polymer/nanoparticle blends a relatively simple system to study spectroscopically, but may be one of the reasons for the reduced performance compared to all current state of the art organic systems.

Experimentally there are only a few ways in which the morphology of polymer/nanoparticle blends can be altered. One possibility is changing the size of the nanoparticles and, as a result, the heterojunction interfacial area can be modified. An increase in nanoparticle size will result in a reduction of the heterojunction surface area and a decrease in nanoparticle size will have the opposite effect. The tuning of nanoparticle size is possible through traditional *ex-situ* nanoparticle synthetic routes. However, as well as changing the morphology, the chemical and physical properties of the nanoparticles will also change drastically as the ratio of surface atoms to bulk atoms changes. Alternatively, if the nanoparticle size is kept constant then the degree of aggregation between individual nanocrystals can be changed to modulate between a system that has discrete isolated particles and one where all the particles are agglomerated in large domains within of the films. This is often done by a careful mix of ligand engineering[11,12] and post deposition annealing of films.[11] Finally, the shape of the nanoparticles can be tuned in order to try to optimise the morphology, by increasing the percolation through a film by effectively elongating the nanocrystals along one of their axes. This idea has been used to induce a threefold increase in the EQE of P3HT/CdSe devices by using rod shaped particles instead of dots.[13] A combination of all three of these concepts could obviously be employed to optimise devices fabricated from an *ex-situ* approach.

In the case of *in-situ* fabricated heterojunctions it is conceptually more difficult to engineer the morphology, as one component cannot be fixed in its size and shape before film formation. This means that the approach is more haphazard and optimisation has to follow an iterative trial and error process. Previous work by the group has shown some degree of morphological tunability in P3HT/CdS films formed from the *in-situ* xanthate method by controlling the annealing temperature of the as spun films.[14] The CdS domain size was tuned from ~100 nm to ~20 nm by increasing the temperature at which the decomposition process occurred from 105°C to 160°C. This was shown to have a marked effect on the charge generation yield and the overall device performance, with a six-fold differential observed between the maximum and minimum temperatures studied. This highlights the importance that control of the morphology has on device performance. In this case, the method used was not ideal, as there were other properties that were also changed by adjusting the annealing temperature. The stability of the P3HT will be affected at high temperatures, so only a limited low temperature range can be explored using this method. The trend followed that, as a higher temperature was used, the morphology became finer and the device performance improved. It is possible the optimum morphology for this system would require an annealing temperature that would be so high as to damage the P3HT. Another possible route to tuning the morphology of *in-situ* hybrid films is through the modification of the precursor material. This avenue is relatively unexplored, but recent studies have shown that for different organic/inorganic material combinations quite different absorber layer morphologies are obtained. For example, using metal xanthates as precursors, comparatively big domain sizes have been observed for P3HT/CdS absorber layers,[14,15] while well mixed phases were observed in poly[2,7-(9,9-dioctyl-dibenzosilole)-alt-4,7-bis(thiophen-2-yl)benzo-2,1,3-thiadiazole] (PSiF-DBT)/$CuInS_2$ layers.[16] The fact that the metal xanthates used for the preparation of the P3HT/CdS layers had a small ethyl ligand moiety, while for the *in-situ* preparation of the $CuInS_2$ nanoparticles xanthates with longer and branched alkyl side chains were used, suggests that the precursor design has an influence on the nanomorphology formation.

In the first part of this chapter, an attempt was made to gain an understanding on how the metal chalcogenide nanocrystals grow within the polymer matrix using the xanthate methodology and how the nanomorphologies are formed. The idea that small changes in the solubilising alkyl groups could affect the nanocrystal growth and the nanomorphology formed was also investigated, as well as the photophysics of hybrid photoactive layers. To this end, five cadmium xanthates were investigated with different alkyl moieties, namely, ethyl, propyl, butyl, pentyl and 2,2-dimethylpent-3-yl, which is referred to as heptyl in the further course of the study. The structures of these compounds can be seen in Figure 4.1.

In the second part of this chapter, the information gained about the way in which the morphology could be tuned, by changing the solubilising ligand, was applied to a P3HT/$Sb_2S_3$ system. Bansal *et* al. showed that in blends of P3HT/$Sb_2S_3$, even with relatively large domain sizes, PCEs of over 1% could be achieved.[17] These domain sizes were in the range of 100s of nanometres, in comparison to ~20 nm with the P3HT/CdS system, and it was assumed that if these devices would show higher performance, should the domain size be reduced.

$Sb_2S_3$ is a promising candidate for use in hybrid photovoltaic and has several advantages over CdS. The toxicity of $Sb_2S_3$ is considerably less compared to CdS, and its band gap is much lower. Previous work from the group, has shown that the hole transfer in these systems is more efficient than the electron transfer.[18,19] It is therefore desirable to find a material with a lower band gap that can perform the majority of the absorption, with the polymer acting as primarily a hole transport material. The band gap of crystalline $Sb_2S_3$ is 717 nm[20] and so seems ideal for this purpose.

$Sb_2S_3$ has been used by many groups to fabricate solar cells with a range of architectures. Moon *et* al. used chemical bath deposition to form sensitised nanoporous $TiO_2$ solar cells, with 2,2',7,7'-tetrakis(*N,N*-di-*p*-methoxyphenylamine)-9,9'-spirobi-fluorene (SPIRO) as the hole conductor, and a PCE of 5.2%.[21] Chang *et* al. utilised poly(2,6-(4,4-(2-ethylhexyl)-4H-cyclopental[2,1-*b*;3,4-*b*']dithiophene)-alt-4,7(2,1,3-benzothiadiazole)) (PCPDTBT) as a hole conductor and achieved a PCE of 6.3%, also in a sensitised solar cell architecture.[22,23] Impressive results have also been achieved with alternative solid state hole conductors, including copper thiocyanate (CuSCN),[24-26] and P3HT,[23,27] as well as with a cobalt complex-based liquid electrolyte.[28] O'Mahony *et* al. demonstrated the fabrication of mesoscopic $Sb_2S_3$ layers, infiltrated with P3HT to form novel photovoltaic devices, where $Sb_2S_3$ acted as both the absorbing material and the electron transport material.[29] These light-harvesting photoanodes were fabricated using the antimony ethyl xanthate and showed preliminary efficiencies of 0.94%. After changing the method and replacing the mesoporous $Sb_2S_3$ structure with a bi-layer of P3HT/$Sb_2S_3$, a PCE of 3.28% was reported.[30]

To capitalise on the previous success of $Sb_2S_3$ in hybrid photovoltaics and utilise the observation in the beginning of this chapter, on the ability to tune morphology through ligand design, antimony(III) O-pentyl dithiocarbonate ($SbPX_3$) was synthesised and used in hybrid films. P3HT was used as the polymer material and blend films were fabricated. The effect of the seed layer on the crystallinity of the $Sb_2S_3$ was studied using UV-Vis absorption spectroscopy and X-ray diffraction (XRD). The charge generation efficiency in these blends was then studied using transient absorption spectroscopy (TAS) and the results were compared to equivalent films fabricated from antimony(III) O-ethyl dithiocarbonate

($SbEX_3$). TEM was used to image these films and rationalise the TAS results. Devices were then fabricated and optimised for the $SbPX_3$ and an equivalent device of $SbEX_3$ was made for comparison.

# Experimental

## Cadmium Xanthate

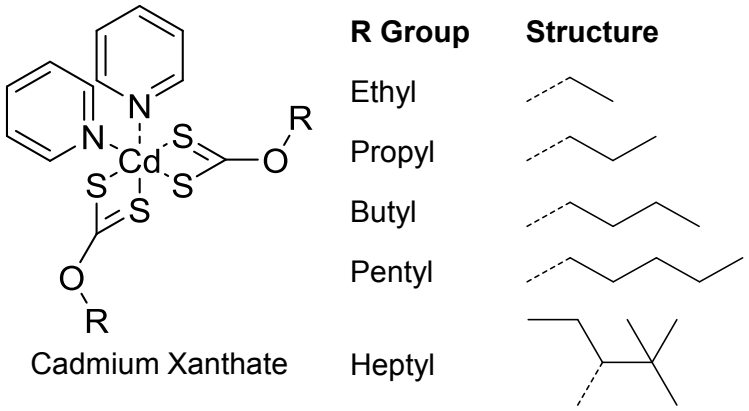



*Figure 4.1 - General chemical structure of the Cd-xanthate precursors used (bispyridine cadmium(II) dithiocarbonate) along with the different R Group moieties. It should also be noted that in the case of the heptyl xanthate, there are no pyridine adducts present, as due to the branched side chains, good solubility is already obtained without them. The synthesis and characterisation of these materials are present in Chapter 3.*

Solutions of the five xanthate precursor materials (Figure 4.1) and P3HT were made, such that after decomposition there would be approximately a 1:1 volume ratio of P3HT/CdS. This ratio was found to be the optimum for device performance in the case of the ethyl xanthate previously.[18] This required a solution containing P3HT (9.375 mg/ml) and Cd-xanthate (150 mg/ml (in the case of ethyl)) in chlorobenzene. The amount of Cd-xanathate used in each case was such that the same amount of CdS would remain in the films, as estimated by the relative molecular weights of the materials. Films were spin coated (1000 rpm (dynamic), 60 s) and annealed at 160°C in a nitrogen glovebox atmosphere for 30 min to form the hybrid polymer/inorganic networks. The architecture of the photovoltaic devices was Glass/ITO/$TiO_2$(flat)/CdS/P3HT:CdS/$MoO_3$/Ag. The methods used for the fabrication of the other layers can be found in Chapter 3.

These films were first investigated using transmission electron microscopy (TEM). The growth process of each system was then studied in detail using simultaneous grazing incidence wide-angle X-ray scattering (GIWAXS) and grazing incidence small-angle X-ray scattering (GISAXS) during the annealing process, to monitor the crystal growth and gain a better understanding of the formation of the morphology formation. Furthermore, the thin films were subjected to photophysical characterisation, including UV-VIS absorption, photoluminescence spectroscopy (PL), femto-second transient absorption spectroscopy (fs-TAS) and micro-second transient absorption spectroscopy (µs-TAS) to observe which effects the morphology has on the photophysical processes, including polymer exciton lifetimes and the relative yields and lifetimes of free charge carriers, within the device active layers. Finally, series of

photovoltaic devices were fabricated, using an inverted device architecture of ITO/$TiO_2$(flat)/CdS/P3HT:CdS/MoO3/Ag, to measure the overall effect of ligand moiety on photovoltaic performance. Comprehensive descriptions of all techniques and instruments used can be found in Chapter 3 as well as synthetic methods for any compounds synthesised.

## Antimony Xanthate

The synthesis of both the $SbEX_3$ and $SbPX_3$ are available in the Experimental Methods section. The structure of both these materials is shown in Figure 4.2.

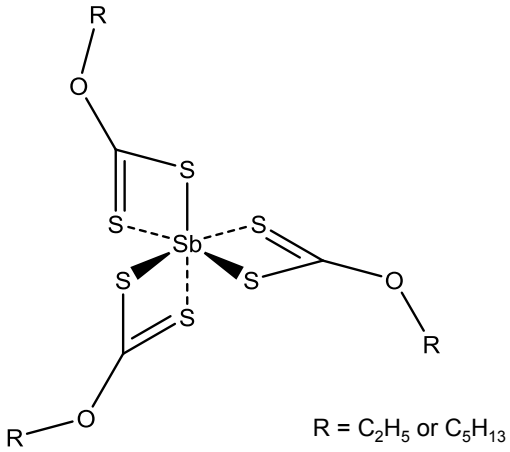



*Figure 4.2 - Chemical structure of the antimony xanthate precursors used in this chapter.*

The films used in this chapter were of a variety of different blend ratios and film thicknesses. Presented below is the method for making the found optimum active layer. Antimony pentyl xanthate ($SbPX_3$) was dissolved in chlorobenzene (360 mg/ml) and stirred for 30 min before being filtered using a 0.45 µm PTFE syringe filter. P3HT (Plextronics, Sigma-Aldrich) were dissolved in chlorobenzene (12.5 mg/ml) and stirred for 30 min. The $SbPX_3$ solution was mixed with the P3HT solution in a 4:1 volume ratio and stirred for 30 min before spin coating (1000 rpm (dynamic), 60 s) and annealing in a nitrogen glovebox for 30 min. Films fabricated using $SbEX_3$ were made using an identical method although the solution concentrations were decreased to account for the lower molecular weight of the precursor.

Films were fabricated using a variety of seed layer combinations. These were fabricated by dissolving the xanthate in chlorobenzene ($CdEX_2$ (50 mg/ml) or $SbPX_3$ (59.7 mg/ml)) and spin coating (6000 rpm, 2000 rpm/s, 45 s). These films were annealed for 30 mins at either 160°C (CdS) or 300°C ($Sb_2S_3$).

Devices were made of the architecture ITO/$TiO_2$/CdS(seed)/$Sb_2S_3$(seed)/P3HT:$Sb_2S_3$/P3HT/$MoO_3$/Ag. Details of each of these other layers can be found in Chapter 3 as well as the synthesis of $SbEX_3$ and $SbPX_3$.

# Results and Discussion

## Film Morphology and Nanoparticle Growth

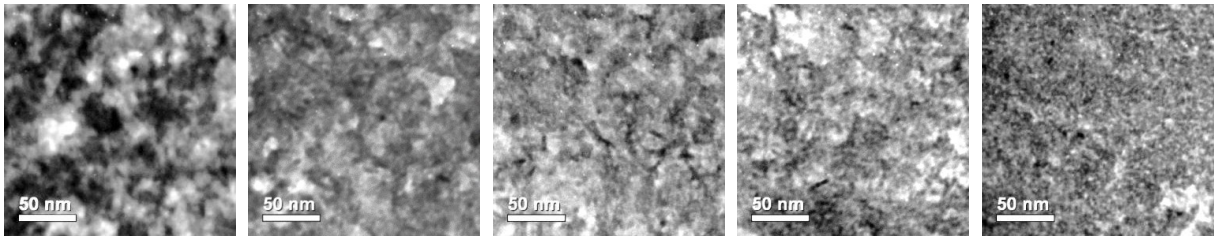



*Figure 4.3 - Bright field TEM (transmission electron microscopy) images of thin films of hybrid P3HT/CdS heterojunctions, fabricated from a series of Cd-xanthate precursors with increasing ligand moieties from left to right. The darker regions of contrast are indicative of a higher concentration of cadmium.*

The morphology of *in-situ* formed P3HT/CdS hybrid blend thin films was first studied using bright field TEM, typical images of which can be seen in Figure 4.3. From left to right the images show films fabricated using a xanthate precursor of increasing ligand moiety size, from ethyl through to heptyl. The contrast in the films is mainly due to electron density and so the darker regions can be considered to contain a higher cadmium content. It is apparent that as the ligand moiety is changed the morphology of the blends changes, with the domain sizes within the films becoming smaller as a larger ligand is used. Upon close inspection of the TEM image of the heptyl sample (Figure 4.3 Heptyl), discrete particles can be seen. These particles, although still observable, become less easy to isolate visually when moving towards a smaller ligand moiety on the left hand side of the figure. It appears that an increase of the alkyl chain size of the precursors results in a reduction in the aggregation of the cadmium sulfide nanoparticles upon decomposition of the xanthate precursors. It is worth noting however that the TEM images only provide a top-down look at the morphology and although there is an observable trend in this direction, it can only be assumed that the landscape looks similar in the z-direction as well. The significantly different morphologies of the P3HT/CdS hybrid films as shown in the TEM images in Figure 4.3 support the hypothesis that molecular precursor design is a valuable tool for tuning the nanomorphology of *in-situ* prepared polymer/nanocrystal absorber layers towards efficient charge generation and transport. However, target-oriented molecular design of the precursors requires knowledge of the processes going on during the *in-situ* formation of these films.

The potential reasons for the development of different nanomorphologies are numerous and could be, for example, influenced by differences in solubility or rather different miscibility of the precursor within the polymer P3HT in solution, by different phase separation or crystallisation behaviour of the metal xanthates in the precursor film, by decomposition of the xanthates and subsequent nanocrystal growth

at different temperatures, or by different growth kinetics of the nanocrystals. To understand the processes during the formation of the nanocomposite layers and to gain knowledge on which parameters are influencing the formation of the different nanomorphologies the most, the thermal annealing step was thoroughly investigated on the nanometer scale.

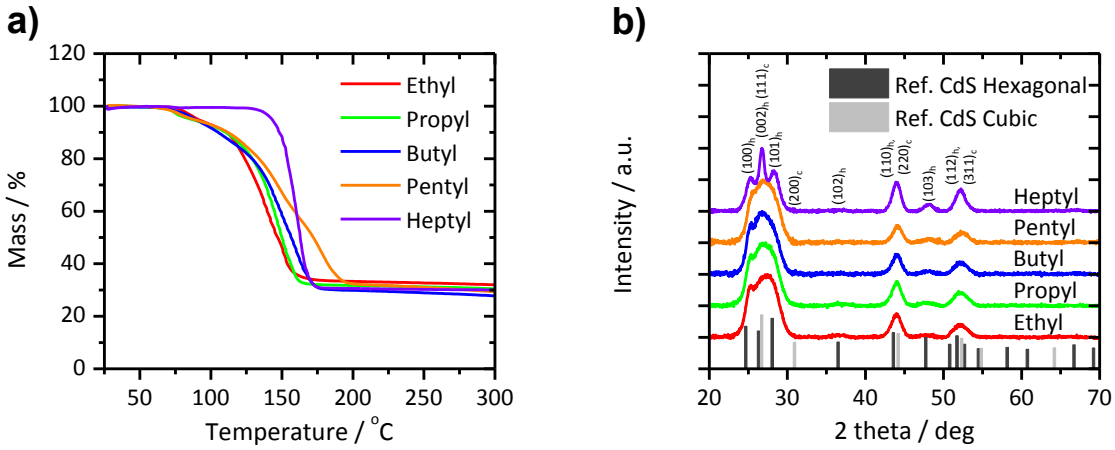



*Figure 4.4 - a) Thermogravimetric analysis (TGA) of the thermal decomposition of the Cd-xanthates (Ethyl, Propyl, Butyl, Pentyl, Heptyl) investigated in this study. b) X-ray diffraction patterns of P3HT/CdS nanocomposite layers prepared from the different Cd-xanthates via thermal annealing at 160°C for 60 min. The main peaks of both the hexagonal as well as the cubic phase are labelled with their Miller indices.*

To get a first indication about possible differences in the thermal decomposition of the different xanthates, thermogravimetric analysis (TGA) was carried out. The results presented in Figure 4.4a show that the decomposition of ethyl, propyl, butyl and pentyl xanthates proceeds via a two-step scheme. The first decomposition step starts at approximately 70°C and the second at about 120 - 130°C. While the decomposition characteristics in the first step are similar in these samples, the second step is quite different. After a mass loss of about 18%, the ethyl xanthate has an onset of a steep mass loss at 122°C while the phase of steep mass loss is shifted to slightly higher temperatures for propyl (125°C), butyl (126°C) and pentyl (130°C) xanthates. Moreover, the slope of the mass loss in the second decomposition step decreases going to higher chain length of the xanthates' ligand moiety. The heptyl xanthate shows a markedly different behaviour. It is thermally stable up to a temperature of 135°C and decomposes comparably fast in one step. This is possibly caused by the fact that in the heptyl xanthate no pyridine ligands are present, which lower the decomposition temperature of metal xanthates,[31] or could be due to the decreased number of beta hydrogens available, which facilitate the Chugaev elimination. The mass loss during the conversion of the respective Cd-xanthates to CdS is between 68 and 72%, which matches reasonably well with the theoretical value. However, it is worth noting that the Cd-xanthate-bispyridyl compounds lose about 5% less weight than theoretically expected. This could be due to incomplete complexing of all Cd-xanthate molecules with two pyridines. $^{1}$H-NMR suggests that the amount of pyridine is correct to <1%, so it is assumed that the loss of pyridines happened during transit

to measure the TGA, whereas the compounds used to make further measurements contained the correct amount of pyridine.

These distinct differences in the thermal decomposition behaviour of the investigated metal xanthates suggest possible differences in the formation/crystallisation of the CdS nanocrystals in the P3HT matrix. X-ray diffraction measurements of the P3HT/CdS nanocomposite layers prepared from the different Cd-xanthates after the thermal annealing step were performed to detect a possible variation of the crystal structure or the primary crystallite size of the CdS nanocrystals in the final stage after the heating process. Figure 4.4b shows the respective X-ray diffraction patterns and reference patterns for hexagonal CdS (PDF 41-1049) as well as cubic CdS (PDF 01-080-0019). The main peaks of both crystal structures are labelled with their Miller indices followed by the suffix h or c to indicate the hexagonal (wurtzite) or cubic (sphalerite) phase, respectively. Comparing the measured patterns with the reference patterns, it is apparent that the nanocrystals exhibit a blend of hexagonal and cubic crystal structure, which stems from mixed cubic and hexagonal stacking. This mixed layer stacking is not unusual for CdS nanocrystals and was already observed in other studies on CdS[32] as well as isostructural ZnS nanocrystals.[33] The relative amounts of cubic and hexagonal crystal phase in the samples are hard to determine due to the broadening of the peaks, however, the distribution ratio seems to be comparable in the ethyl, propyl, butyl, and pentyl samples. In the heptyl sample, the $(100)_h$ $(002)_h$ and $(101)_h$ peaks are more distinct, indicating that the overlapping $(111)_c$ peak is less intense than in the other samples, which lets us conclude that the amount of hexagonal phase might be higher in the heptyl sample. The fact that the middle peak $(002)_h$ is much more intense than the neighbouring two indicates that there is also some cubic crystal structure present, as this peak is superimposed by the $(111)_c$ peak of the cubic crystal structure. Moreover, in all samples the $(200)_c$ peak is hardly visible in the diffraction patterns and also the $(102)_h$ peak is not as pronounced as the $(103)_h$ peak, which matches findings of a previous study investigating mixed hexagonal and cubic stacking.[33] The better separation of the three peaks of the hexagonal phase in the heptyl sample could also originate from a bigger primary crystallite size in this sample, however, according to an estimation of the primary crystallite size using the Scherrer formula, the primary crystallite size in the heptyl sample is not significantly bigger than in the other samples. The broadening of the peaks for the estimation of the primary crystallite size via the Scherrer formula was determined by fitting the $(110)_h$ $(220)_c$ peak at approx. 44° 2 theta with the two individual peaks stemming from the hexagonal and cubic phase. For all samples, the primary crystallite size is approximately 7 ± 1 nm, which is in line with the size of the nanocrystals found in the TEM images. Thus, different crystallite sizes can be excluded as a possible factor leading to the different nanomorphologies of the hybrid absorber layers and it appears that the different morphologies originate from a different degree of agglomeration of the single nanocrystals.

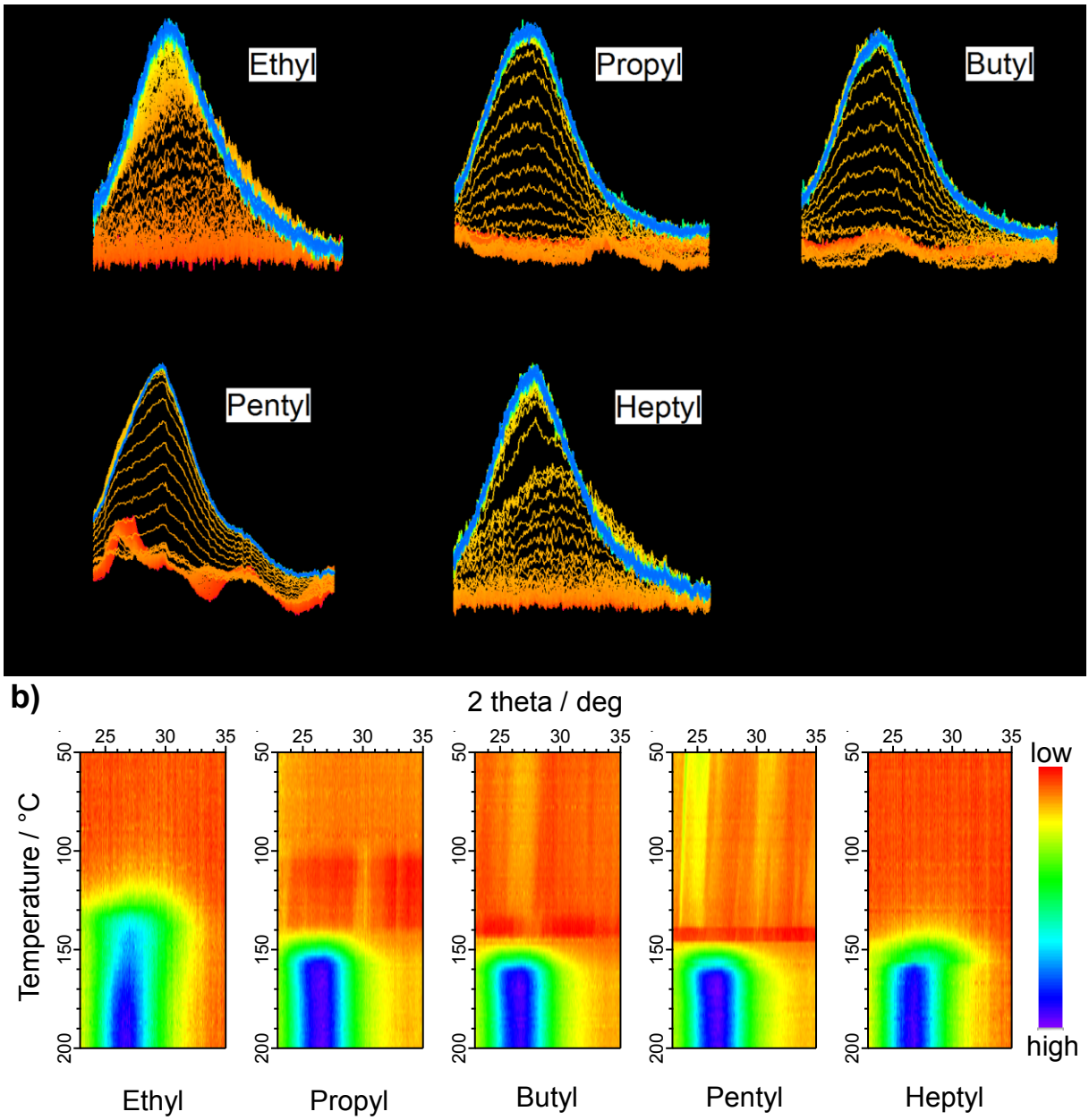



*Figure 4.5 – a) GIWAXS patterns of P3HT/Cd xanthate films measured between 22.9 and 35° 2 theta during a heating run from room temperature to 200°C with a heating rate of 10°C/min showing the evolution of the most intense peak of CdS at around 27° 2 theta. b) 2D-surface plots of the GIWAXS patterns above vs temperature.*

Next, time resolved GIWAXS measurements were performed to obtain insight into the formation of the CdS nanocrystals in the P3HT matrix. The use of synchrotron radiation and the grazing incidence setup enabled approximately 150 nm thick films, comparable to those used in devices, to be probed directly at a time resolution of 11 s. These short intervals were necessary, as it is known from former experiments that the formation of the metal sulphides from metal xanthates occurs in a quite fast reaction step.[34] Due to a limited 2 theta range of the detector used, the formation of the broad and most intense peak of CdS in the samples (superimposition of the $(110)_h$, $(002)_h$, $(101)_h$ and $(111)_c$ reflections), which is situated around 27° 2 theta, was focussed on and the 2 theta range between 22.9 and 35° 2 theta was monitored. The temperature-dependent changes in the GIWAXS patterns during a

heating run from room temperature to 200°C with a heating rate of 10°C/min are shown for all samples in Figure 4.5a. These GIWAXS patterns are also displayed as 2D-plots verses temperature in Figure 4.5b.

The evolution of the most intense peak of CdS at ~27° 2 theta can be clearly seen. The shape of the peak is slightly different to that observed in the XRD measurements shown in Figure 4.4b. This is due to peak broadening caused by the grazing incidence setup and also because of the fact that, for the other XRD measurements, much thicker films were used. However, in the GIWAXS pattern, a shoulder at about 25.5° 2 theta similar to, but not as pronounced as in, the XRD pattern is observed. Moreover, in some experiments, it can be seen that already at room temperature some weak peaks (around 23, 37, 33 and 34.5° 2 theta) are visible, which may stem from partial crystallising of the Cd-xanthate in the precursor layer. These peaks from the precursor material are present in the sample until a certain temperature where they vanish shortly before the CdS nanocrystals are formed. This behaviour is more clearly visible in Figure 4.6. Here, the normalised integrated intensity of the GIWAXS patterns of the different P3HT/metal xanthate samples calculated between 22.9 and 35° 2 theta are plotted versus reaction time along with the temperature ramp in grey.

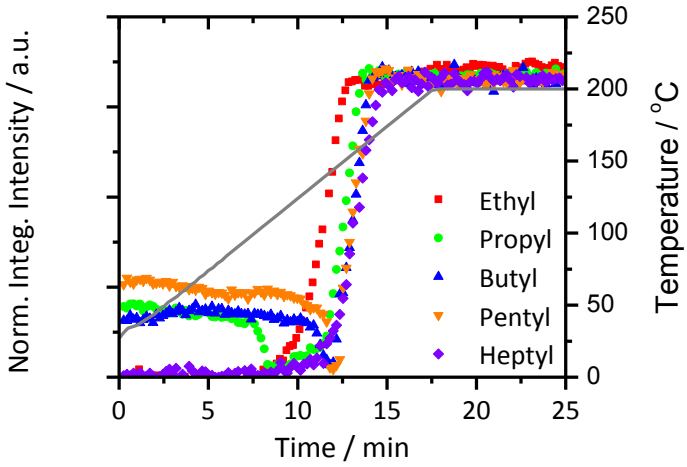



*Figure 4.6 – Normalised integrated intensity of the GIWAXS patterns of the different P3HT/metal xanthate samples calculated between 22.9 and 35° 2 theta plotted versus reaction time and temperature.*

Both the surface plots (Figure 4.5b) and the integrated intensities (Figure 4.6) illustrate that the ethyl and heptyl xanthates do not have peaks at room temperature, while in the propyl, butyl, and pentyl samples some of these previously discussed weak peaks are visible. In the pentyl xanthate sample these peaks are most significant. It is also apparent that these “precursor-peaks” disappear at different temperatures. The integrated intensity of the diffraction patterns starts to decrease in the propyl sample already slightly above 100°C while it stays stable until about 130°C in the butyl sample and until 135°C in the pentyl sample. In the ethyl and heptyl sample no “precursor-peaks” are observed and in

the integrated intensity only the formation of the CdS nanocrystals can be detected. The nanocrystal formation starts already at 125°C in the ethyl sample, which is approximately 5-10°C higher than the onset temperature of the fast second decomposition phase, as determined by TGA measurements (Figure 4.4a). In the other samples, the onset of the nanocrystal growth is shifted to slightly higher temperatures (140°C for the propyl and heptyl samples and 145°C for the butyl and pentyl samples). The fact that peaks of the precursor material are observed in the X-ray diffraction patterns of the propyl, butyl and pentyl samples suggests that the agglomeration of the nanocrystals after the heating step is influenced by a phase separation of polymer and metal xanthate phase already in the precursor layer. However, for the ethyl sample no peaks of the precursors were found, which is surprising because the ethyl sample exhibits the largest domain sizes. It is possible that also in this sample the polymer and the metal xanthates phase separate, though the precursor molecules do not form crystalline domains and thus, no peaks are visible in the X-ray diffraction pattern. The observation from the TEM images that in the heptyl sample the polymer and nanoparticle phases are well mixed (Figure 4.3), lets us conclude that the solubility and the mixing with the polymer of the heptyl xanthate, due to the branched alkyl chains, is very high and as a result no pronounced phase separation occurs in the heptyl sample.

It is interesting that the nanocrystal growth is much slower in the ethyl sample compared to the others. This can be seen in the surface plots in the 2D surface plots (Figure 4.5b) and also in the onset of the slope in the integrated intensities of these plots (Figure 4.6). The formation of the main peak of CdS in the sample at around 27° 2 theta is quite smeared over a larger temperature range, which is a significant difference compared to the other samples, where fast and abrupt nanocrystal growth is observed. After this short nanocrystal growth phase, the intensity of the peak, as well as the shape and width of the peak stay constant, indicating no further nanocrystal growth in this last phase of the heating run.

Time-resolved GISAXS measurements were performed simultaneously with the GIWAXS measurements. The GISAXS patterns of the series of xanthates at different temperatures during the heating run are shown in Figure 4.7. The areas for vertical integration are indicated with a red box in the GISAXS images and the resulting vertical cuts at $q_y = 0.058$ nm$^{-1}$ are presented in Figure 4.8.

The integrated intensities extracted from the GISAXS data reveal structural changes in the layers directly before the growth of the nanocrystals starts. These structural changes have their origin in the decomposition of the cadmium xanthates and evaporation of volatile decomposition products out of the layer, which leads to a compaction of the layer and an overall increase in electron density. This increase of electron density is also reflected in the shift of the Yoneda peak ($q_z \sim 0.45$ nm$^{-1}$) towards higher q-values during the heating run. The idea that the structural changes are stemming from the decomposition of the precursors is also supported by the fact that the observed increase of the

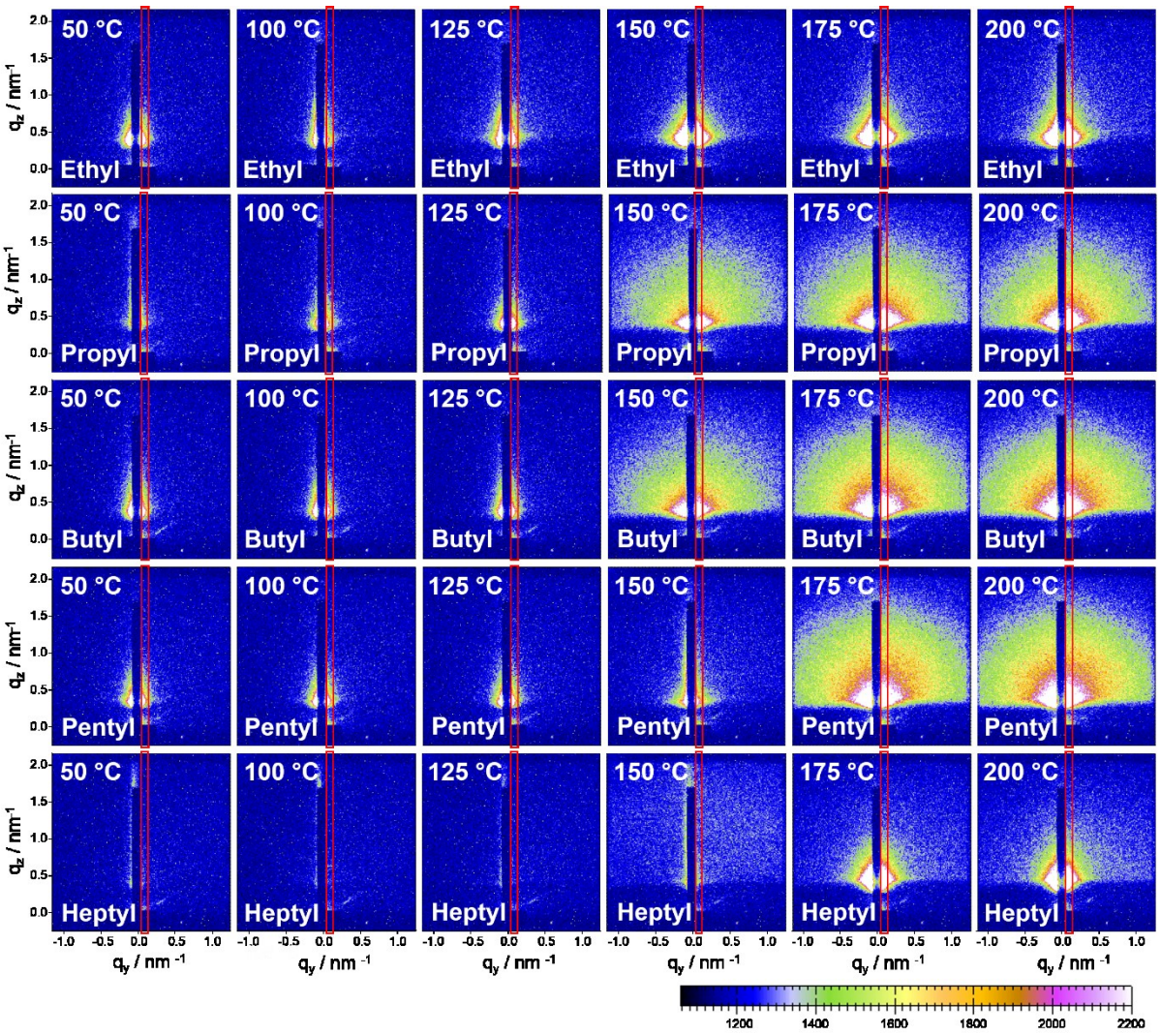



*Figure 4.7 - GISAXS images of the samples at different temperatures (50, 100, 125, 150, 175, 200 °C) during the heating run. The red boxes indicate the vertical areas used for integration.*

integrated intensity of the GISAXS signal occurs in the same phase of the heating run, where the peaks of the precursors vanish in the GIWAXS pattern.

Moreover, the GISAXS measurements suggest that there is an agglomeration of the nanocrystals after the growth phase in the ethyl sample. This is indicated by a further increase of the integrated intensity of the GISAXS signal after the nanoparticle growth has finished. This is shown in Figure 4.8 where the integrated GISAXS signal continues to increase after the GIWAXS integration has already plateaued. This might be a reason for the formation of markedly bigger domain sizes in the ethyl sample. In all the other samples, no particle aggregation after the nanoparticle growth is observed, which suggests that the nanoparticle agglomerates found in the propyl, butyl and pentyl samples are mainly already determined by the phase separation of polymer and cadmium xanthates in the precursor layer as discussed before in the GIWAXS section.

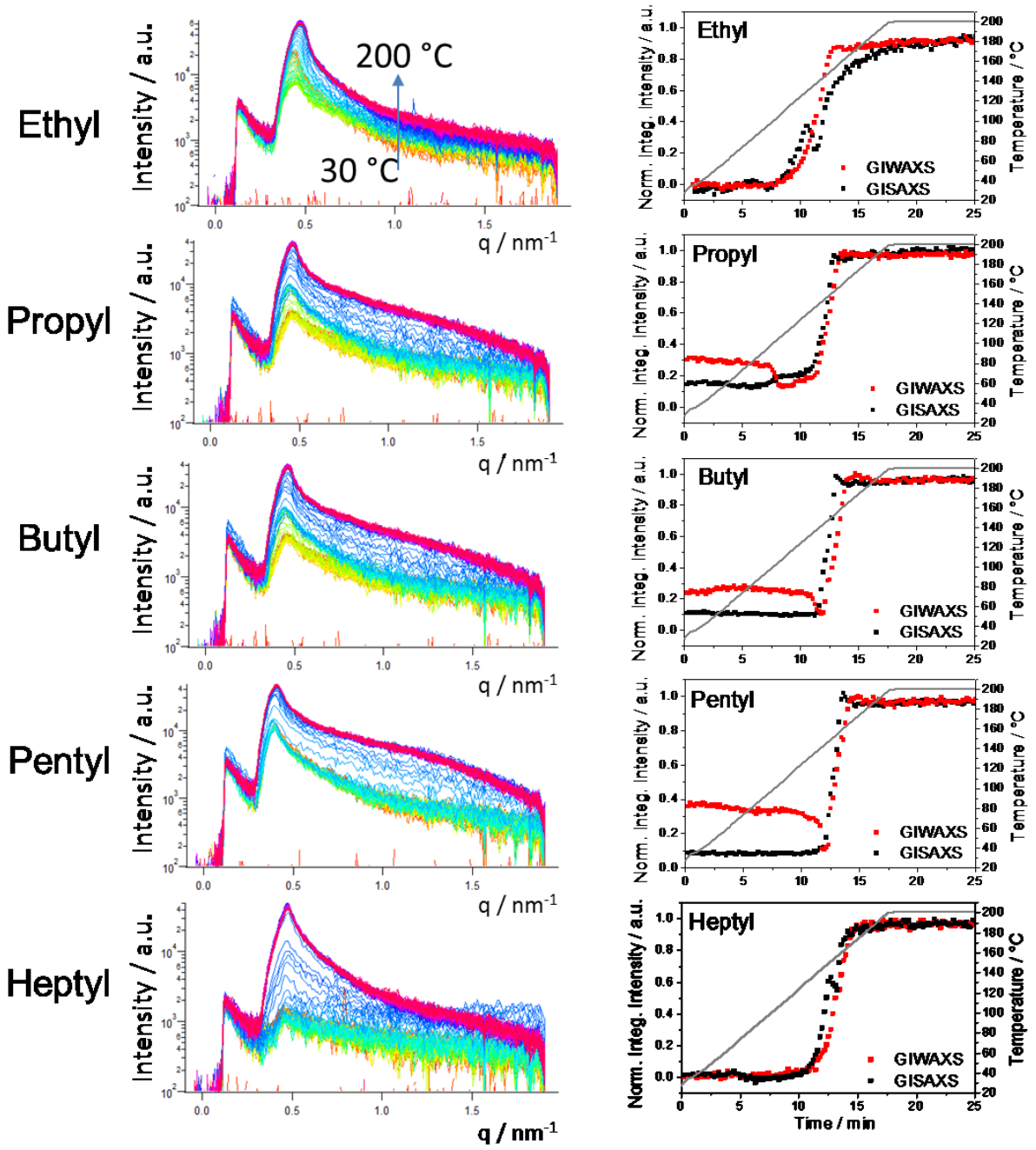



*Figure 4.8 - Left: Temperature-dependent evolution of the vertical cuts of the GISAXS patterns of the investigated samples. The increasing temperature (T) is indicated with an arrow in the Ethyl sample. Right: Integrated Intensities of the GISAXS patterns measured during the heating run compared with those of GIWAXS.*

The decomposition of metal xanthate complexes appears to be very complex in nature and changing the ligand moiety certainly seems to alter the way in which these nanocomposites are formed. It is surprising that so many different effects are observed, such as only the ethyl displaying any aggregation after decomposition and the propyl sample's precursor peaks disappearing many degrees before the decomposition stage, in contrast to the butyl and pentyl. Despite all this, the TEM images show a relative regular trend and in the following section the photophysics also appear to follow suit.

## Photophysical Properties

After gaining insight into the growth of CdS via the decomposition of the different xanthate precursors, the focus of the work was turned to study the effect that the different precursor materials and their respectively different morphologies had on the photophysical properties of these hybrid heterojunctions. Spectroscopic studies were performed on thin films prepared in an identical manner to those previously studied in the GIWAXS and GISAXS measurements and investigated using TEM.

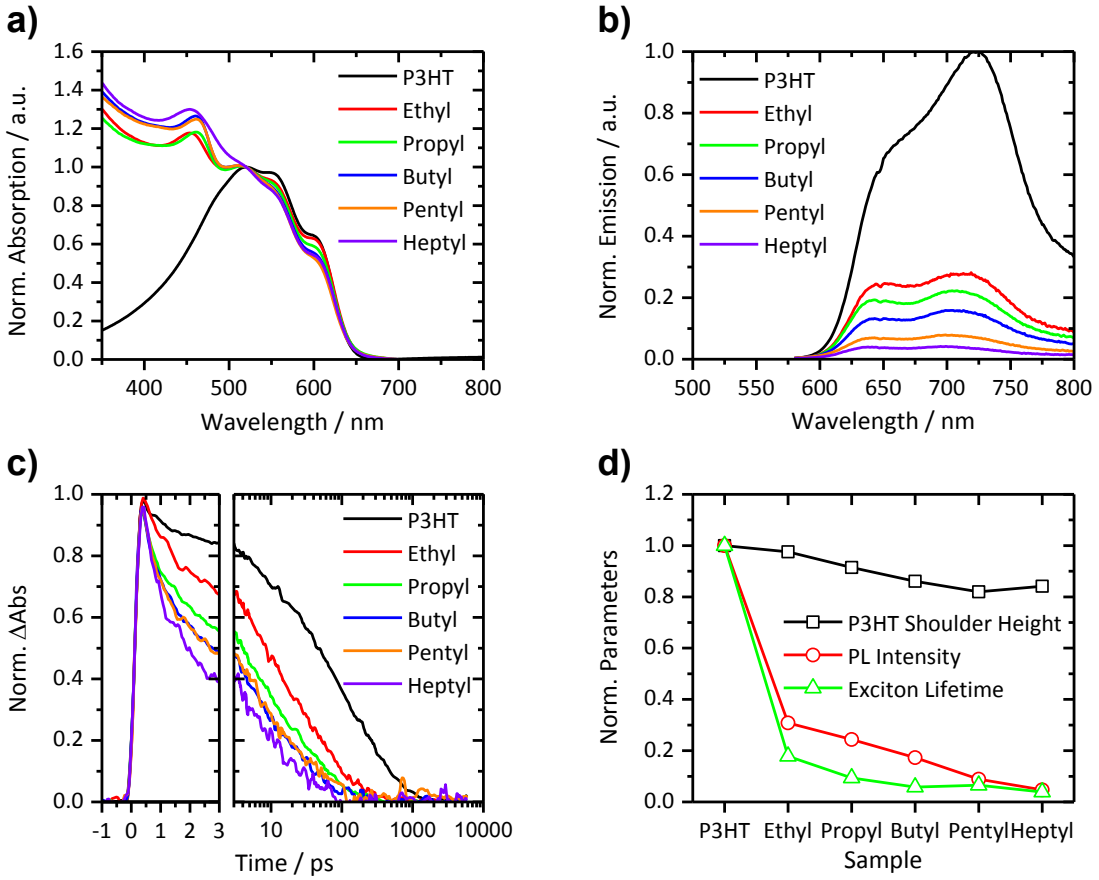



*Figure 4.9 - a) Steady-state absorption measurements of P3HT/CdS heterojunctions normalised at 520 nm. b) Photoluminescence quenching measurements relative to a neat P3HT sample (excited at 567 nm). c) Femtosecond transient absorption (fs-TAS) decays of samples measured at 1270 nm, corresponding to the P3HT exciton absorption. d) Normalised parameters from each of the other figures showing the trends observed from each of the different techniques.*

Considering first the steady-state absorption of these films, in Figure 4.9a it can be seen that the CdS nanoparticles absorb light in the high energy region of the spectrum where the P3HT does not, highlighting one of the potential advantages that a hybrid system of this type offers. The spectra have been normalised at 520 nm and plotted against a measurement of neat P3HT. A distinct trend to accompany the observation of the different morphologies is apparent. In the absorption spectrum of P3HT (shown in black) a distinct shoulder is seen at ~600 nm, a feature of the P3HT spectrum that is attributed to the degree of aggregation between adjacent polymer chains.[35] The relative size of this shoulder compared to the P3HT maximum absorption is a good indication of the level of aggregation of

P3HT, or, in other words, is an indication of crystalline P3HT domain size. In Figure 4.9a, it can be seen that as the Cd-xanthate ligand moiety length is increased, the relative height of this shoulder decreases. This can be seen more clearly in Figure 4.9d, where the black squares represent the relative absorption at 600 nm compared to the normalised absorption at 520 nm. The decrease in shoulder height indicates that as a larger ligand moiety is used, the degree of aggregation of the P3HT decreases. This observation further supports the observation from the TEM images where the P3HT domain size is visibly seen to decrease as a larger ligand moiety is used (Figure 4.3).

The nanomorphology of these photoactive layers was then probed by using the photophysical processes within these heterojunctions as an indicator. The approximate domain size of P3HT was investigated by studying the steady-state photoluminescence (PL) of these films. Since the same polymer $M_n$ and regioregularity was used for all samples, exciton quenching by CdS is believed to be the only cause of a reduced PL intensity. The P3HT was solely excited at a wavelength of 567 nm, the results of which can be seen in Figure 4.9b. There are two key observations to be made from these measurements as a longer ligand moiety is used: 1) the amount of emission from the P3HT decreases and 2) the emission is blue shifted. The emission data is summarised in Figure 4.9d, with the integrated emission relative to neat P3HT shown in red circles. An increase in exciton quenching is a typical finding which indicates a reduction in the relative domain size of a polymer blended with an acceptor material and in this system it appears that as a longer ligand moiety is used an increase in quenching is observed. We can attribute this to the P3HT excitons having, on average, a shorter distance to travel to a CdS interface, resulting in more excitons being quenched before they radiatively decay. The blue shifting in the spectral maximum is another indication of a reduction in aggregation of the P3HT, something that is observed when comparing the polymer emission in a dilute solution, where aggregation is at a minimum, and in thin film.[36,37] This has also been observed when the packing density of P3HT has been tuned through controlling the regioregularity.[38]

The decay kinetics of the P3HT excitons were studied using femtosecond transient absorption spectroscopy (fs-TAS). With this method both the photoinduced absorption of P3HT excitons and polarons can be observed.[4,39] Here the focus was on the kinetics of the P3HT excitons, which are the only absorbing species at 1270 nm.[19] Figure 4.9c shows the kinetics at a probe wavelength of 1270 nm following excitation with a 570 nm laser pulse with an intensity of 3.9 $\mu Jcm^{-2}$. Relative lifetimes of these signals were calculated from determining the times at which the signals dropped to 1/e of the original amplitude and are shown as green triangles in Figure 4.9d. It can be observed that as a larger ligand moiety is used the lifetime of the exciton is reduced. As with the other two steady-state techniques, this indicates that the domain size of the P3HT is decreasing and is in correlation with the TEM results (Figure 4.3).

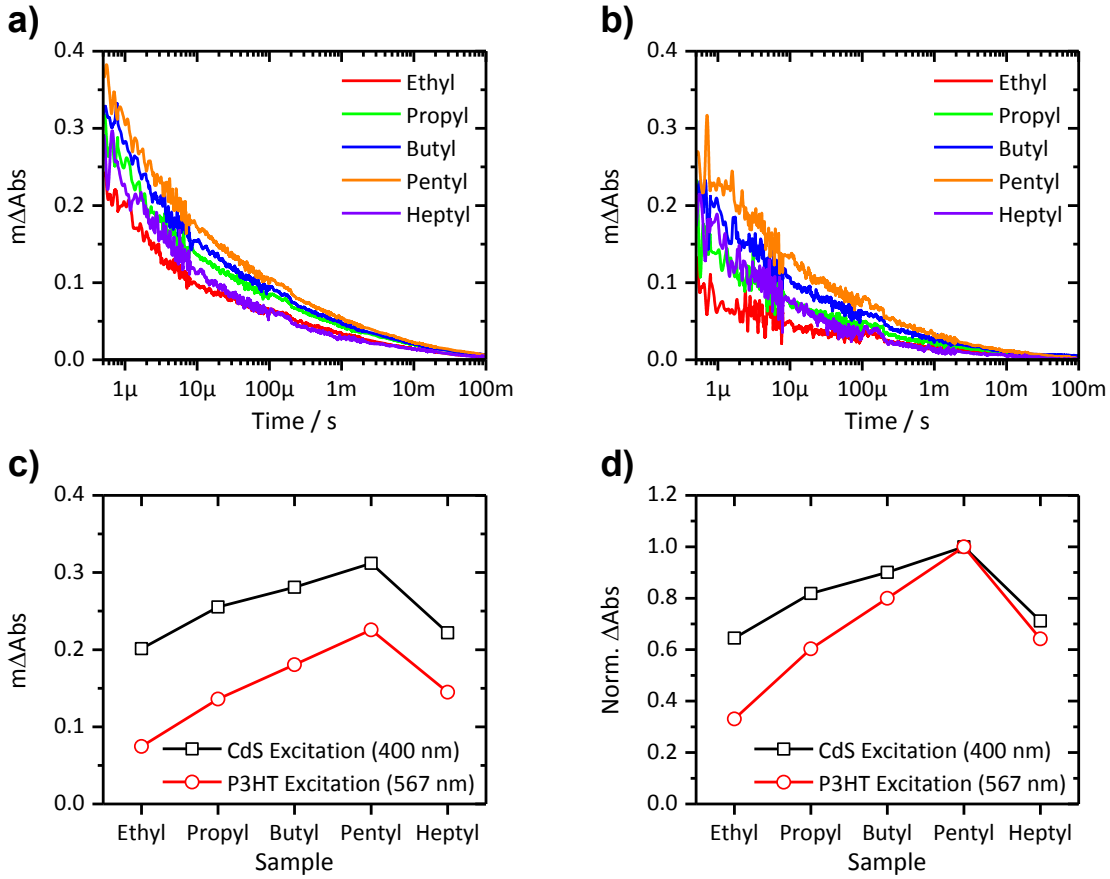



*Figure 4.10 - Transient absorption spectroscopy (TAS) decays at 980 nm using an excitation wavelength of 400 nm exciting predominantly CdS domains a) and 567 nm exciting exclusively P3HT domains b). All traces are scaled by the amount of pump light absorbed. The amplitudes of all signals at both wavelengths are plotted in c) with the data normalised to the highest signal in d).*

Although these three techniques, together with the previous results, present a strong case for the larger ligand moiety having the effect of decreasing the domain size of P3HT, these measurements alone do not directly probe the charge generation within these hybrid heterojunctions. It is still possible that the larger leaving groups could increasingly disrupt the P3HT packing when leaving the film and lead to the previous observations. To rule out this possibility and to get further information on the effectiveness of these heterojunctions at generating charges, micro-second transient absorption spectroscopy (µs-TAS) was employed to measure both the relative number of free charges generated in these 5 different systems and also the lifetime of the transient species. It is noteworthy that fs-TAS can also be used to probe the yields and dynamics of polarons as well as excitons, however on the timescales measured there is still some overlap in signal between P3HT excitons and polarons at the characteristic polaron wavelength.[19] For this reason and the fact that µs-TAS has been extensively used previously to study this system[18,40] and others similar[39,41] it was chosen instead.

The relatively low spectral overlap in the absorption of P3HT and CdS allows for each component to be excited reasonably selectively. Consequently, both the electron transfer reaction from P3HT to CdS and the converse hole transfer reaction from CdS to P3HT were separately studied. The P3HT was excited

using a pump wavelength of 567 nm, where there is no absorption by the CdS, and the CdS was excited at 400 nm where there is only a small absorption contribution from the P3HT. In both cases the signals are scaled for the number of pump photons absorbed to account for small variations in film thickness between samples and also the difference in absorbance between samples at 400 and 567 nm. Both regions were pumped with the same approximate number of photons and were probed at a wavelength of 980 nm, which has previously been shown to correlate to the P3HT hole polaron.[15,40] The transient traces are presented in Figure 4.10a and b, following the decay of the P3HT hole polaron but for clarity the amplitudes at 1 μs are plotted in Figure 4.10c and the amplitudes normalised to the maximum amplitude are shown in Figure 4.10d.

In Figure 4.10a and b the decays of all samples show the transient species to be relatively long lived, with all traces having a $t_{50\%}$ (mΔA at 300 ns) of over 10 μs. There is also an observable difference in the amplitudes of all samples in both the CdS excitation and P3HT excitation case. It can be seen that in all cases there is a higher efficiency of charge generation when exciting the CdS in comparison to when exciting the P3HT, or, in other words, the hole transfer reaction is working more effectively than the electron transfer. This is something that has previously been observed in the P3HT/CdS system prepared using ethyl-xanthates, where the charge generation yields were studied thoroughly for a range of compositions of this heterojunction.[18] The second observation is that, in both excitation cases, as a longer ligand moiety is used, the amount of charges generated steadily increases until the case of heptyl, where the yield is slightly reduced. This increase in charge generation yield can be explained by an increased mixing, as a more intimately mixed system results in excitons being generated closer to an interface and thus being more likely to separate into free charges before the exciton relaxes. This finding supports the observations in both the steady-state photoluminescence and fs-TAS exciton lifetime measurements of Figure 4.9.

It is worth noting that the percentage increase in TAS signal observed when a xanthate with a larger ligand moiety is used is much greater than the difference observed in the PL quenching. This could be explained by considering the idea that there are a two different CdS domains in the film, a large CdS interconnected network that is observed in the TEM images, as well as small isolated domains of CdS that are not connected to the large CdS network. The isolated domains would likely efficiently quench P3HT excitons, but not lead to free charges. As a larger ligand moiety is used the morphology of the interconnected CdS network may become more finely fixed and as a result the free charge yield increases. The PL quenching also increases, however to a lesser extent. This indicates that a considerable amount of the exciton quenching is performed by the isolated CdS domains that do not lead to free charges.

We can tentatively explain the reduction in yield for the heptyl case as being due to the absence of agglomeration of the nanocrystals, which leads to domain sizes becoming so small that either, there is a fast recombination pathway that is quicker than the measurement timescale, resulting in the observed signal being lower than expected by 1 μs, or, the reduced ability of the polaron to delocalise results in a lower driving energy for separation. This is consistent with the findings of Dayal et al.[42] who, using microwave conductivity measurements, observed that increasing the aspect ratio of QDs to rods and tetrapods resulted in an increase in charge generation. An alternative explanation could be that the increased amount of wurtzite relative to cubic CdS in these samples, as observed in the XRD (Figure 3b), could potentially change the polymer/nanoparticle interface and affect the amount of geminate recombination losses between bound polaron pairs.

When comparing the relative effect of changing ligand length on charge generation initiated by hole transfer, compared to electron transfer, it can be seen that the effect is relatively small. This can be most clearly seen in Figure 4.10d, where the data has been normalised. In this figure, it can be seen that when exciting the CdS phase, the difference between the ethyl and pentyl sample is an increase of approximately 50% whereas when exciting the P3HT there is an increase of 200% between the same two systems. This can be explained due to the difference in the nature of the species formed after excitation in CdS compared with in P3HT.

Upon photon absorption in P3HT it is well documented that bound excitons are formed and they have a low diffusion length of <10 nm.[43,44] The lifetime of these excitons is indeed short-lived and is what was measured previously, using fs-TAS shown in Figure 4.9c. The charge generation yield from excitons generated in the P3HT is therefore highly dependent on the degree of mixing, as a finely mixed system reduces the distance an exciton has to travel to reach an interface. In the CdS, due to the high dielectric constant, a bound exciton is not expected to be formed. Instead, free charges are likely to be present, without needing to diffuse to an interface first. These charges in CdS have been shown to have a much longer lifetime than the excitons in P3HT,[19] allowing for longer diffusion distances to an interface. The hole transfer from $Sb_2S_3$ to P3HT has also been found to occur over extremely long timescales.[29]

This observation, that hole transfer shows very little dependence on morphology, in comparison to electron transfer, has already been reported in this system. Dowland *et* al. demonstrated that the hole transfer was not highly dependent on the blend ratio of P3HT:CdS, whereas after P3HT excitation the amount of charges yielded was highly dependent on having a high amount of acceptor material.[18] It is also expected that this observation is actually even more heavily pronounced than what is observed, as there is still a small amount of light absorption by the P3HT at 400 nm. It is possible that charges

generated from absorption by P3HT at 400 nm accounts for the small dependence on ligand moiety size.

## Photovoltaic Devices

Finally, a series of complete devices was fabricated to test the overall effect of tuning the morphology through ligand moiety design. Devices were fabricated of the structure ITO/$TiO_2$(flat)/CdS/P3HT:CdS/$MoO_3$/Ag, with the P3HT:CdS layer being identically fabricated to the films used throughout the study.

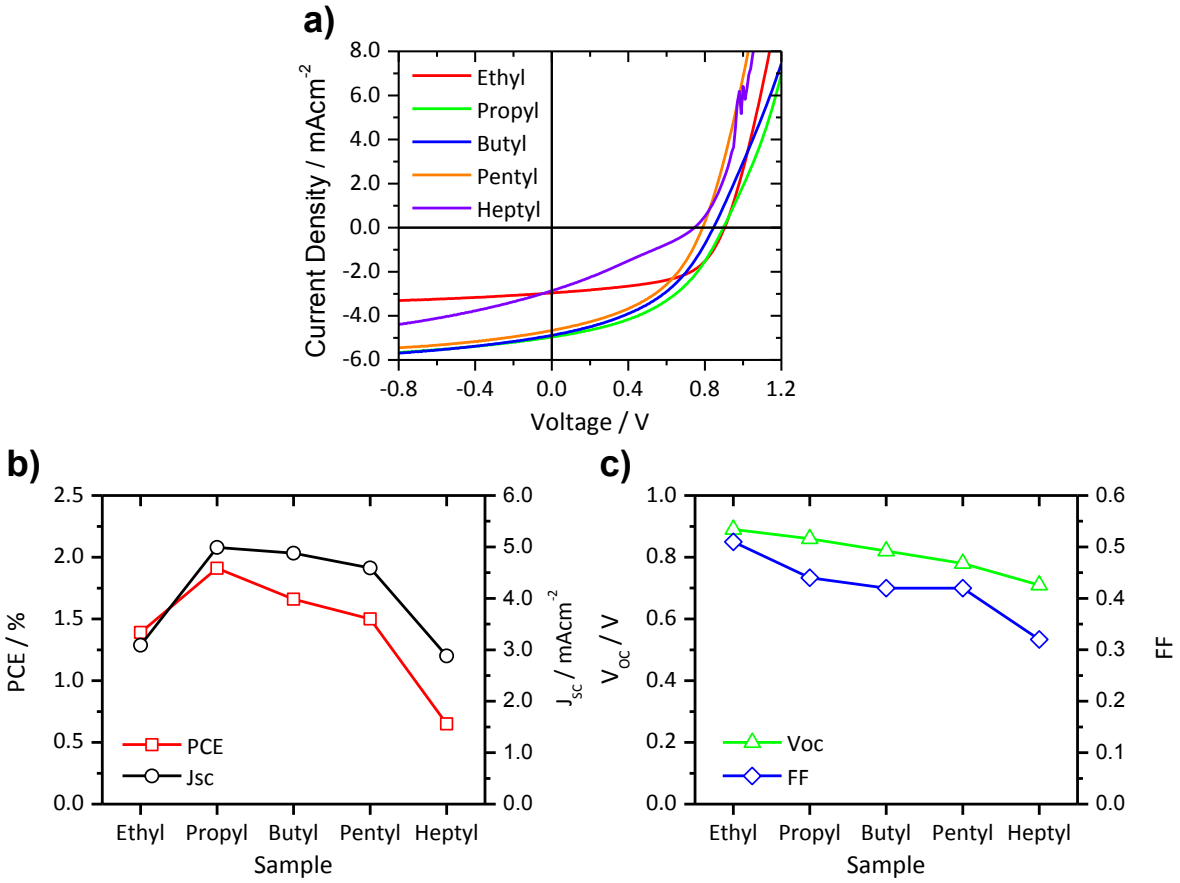



*Figure 4.11 - a) Current-voltage characteristics of representative devices, b) average power conversion efficiencies (PCE) and short circuit currents (Jsc) of an average of the 10 devices with the highest PCE, c) average fill factors (FF) and open circuit voltages (Voc) of the same 10 most efficient devices.*

*Table 4.1 – Tabulated parameters of the devices shown in Figure 4.11.*

| Sample | $J_{SC}$ / mAcm$^{-2}$ | $V_{SC}$ / V | FF | PCE / % |
|---|---|---|---|---|
| Ethyl | 3.09 ± 0.26 | 0.89 ± 0.01 | 0.51 ± 0.04 | 1.39 ± 0.05 |
| Propyl | 4.99 ± 0.20 | 0.86 ± 0.02 | 0.44 ± 0.02 | 1.91 ± 0.06 |
| Butyl | 4.88 ± 0.16 | 0.82 ± 0.02 | 0.42 ± 0.01 | 1.66 ± 0.06 |
| Pentyl | 4.59 ± 0.09 | 0.78 ± 0.02 | 0.42 ± 0.01 | 1.50 ± 0.06 |
| Heptyl | 2.88 ± 0.09 | 0.71 ± 0.04 | 0.32 ± 0.03 | 0.65 ± 0.09 |

In Figure 4.11a the current voltage characteristics are presented for representative devices for each ligand used and in Figure 4.11b and c the average characteristic device parameters are shown for the top 10 devices in terms of PCE. This data is also tabulated in Table 4.1. In Figure 4.11b it can see that

the variation in device performance is mainly governed by the short circuit current, with the devices made with the propyl ligand showing both the highest $J_{SC}$ and PCE . All other devices can be ordered by their $J_{SC}$ and PCE and be seen to have the same trend. It is pertinent to note, however, that the trend in the short circuit currents does not match the trend previously observed in the charge generation yield, as measured by µs-TAS, whereby the films made with the pentyl ligand were found to generate the highest number of charges. A correlation between charge generation yield and short circuit current is one that has been seen in several all-organic systems,[45] but is not what has been observed previously in this system. The mismatch between the optimum blend ratio for charge generation and the optimum for efficiency in complete devices in this system was recently reported.[18] This was attributed to the fact that although a higher heterojunction surface area could be created by increasing the loading of the inorganic component within the polymer and as a result increase the charge photogeneration efficiency, at a certain loading this became so high that the domain size of P3HT was reduced to a point where the charges were not effectively extracted. A similar behaviour was found for polythiophene/ZnO nanoparticle hybrid solar cells, where a finer mixed morphology led to higher charge separation yields, however, not to increased short circuit currents due to a limited hole mobility in the polymer phase because of the smaller domain sizes.[5] It is likely that an analogous problem is being observed here whereby at a given blend ratio the morphology has an optimum point where the balance between interface area and domain connectivity is found. In this system, it appears that this optimum is found with the propyl ligand. In Figure 4.11 it can be seen that both the fill factor and open circuit voltage are reduced when a metal xanthate with a longer ligand is used. This is likely due to the finer mixing resulting in an increase in the non-geminate recombination.

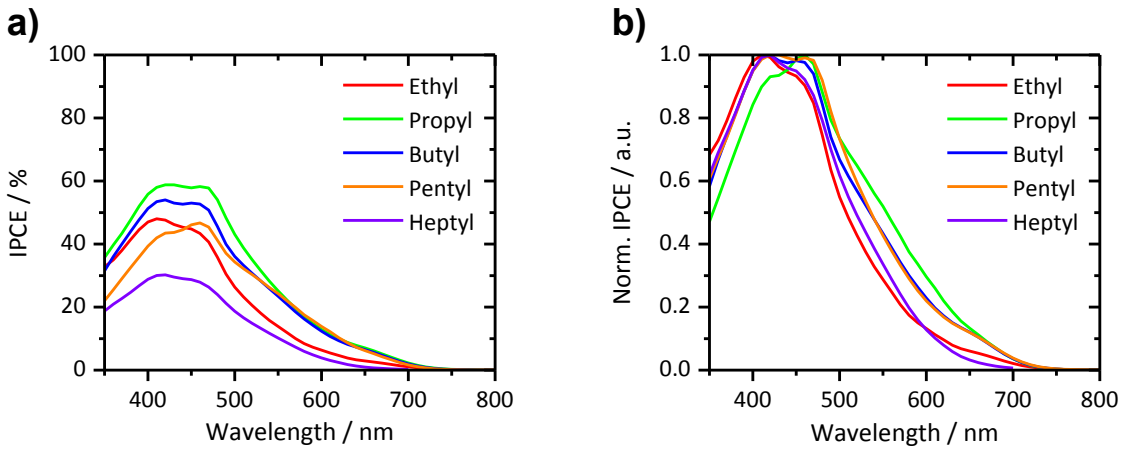



*Figure 4.12 – a) Incident photon to current conversion efficiency measurements (IPCE) of typical devices fabricated from each of the different precursor ligands. b) IPCE measurements normalised to the maximum IPCE fraction for each device.*

Incident photon current efficiency (IPCE) measurements were also made on the same devices and the results of this can be seen in Figure 4.12, with the as-measured data in a) and the data normalised to the maximum IPCE for each device in b). The device showing the highest IPCE is the propyl device. This

is in agreement with the data in Figure 4.11b, which shows the highest $J_{SC}$ from the propyl devices also. In Figure 4.12b, where the data has been normalised to the highest IPCE fraction, the results show a trend with increasing ligand length from ethyl to pentyl, but then there is a seemingly anomalous result in the case of heptyl. As the system moves to a more mixed regime, the amount of charge that is collected from absorption due to the P3HT is increased. This is highlighted by both a shift in the maximum IPCE from 400 nm in the ethyl case, to 460 nm in the pentyl case, and an increase in IPCE around 575 nm where the P3HT absorbs. In the case of heptyl however, there appears to be a reduction in the effectiveness of P3HT, and the CdS does the bulk of the work again. This is likely due to the same reasons that have been alluded to before with the morphology becoming too fine to effectively extract charges. The reason that the CdS starts to perform relatively better is perhaps due to the fact that the CdS seed layer is now contributing a considerable amount to the current produced by the device, which is unaffected by the active layer.

## Antimony Sulfide

The knowledge gained from the work on the P3HT/CdS blends was then applied to the system of P3HT/$Sb_2S_3$ in a completely analogous manner. Upon annealing a spin coated blend of P3HT/$SbPX_3$, on a glass substrate, it was clear that this did not result in crystalline $Sb_2S_3$ (See Figure 4.13a (Red)). This is visible by eye, as the band gap of amorphous $Sb_2S_3$ is approximately 554 nm and the crystalline band gap is 717 nm.[20] A crystalline product therefore appears black to the naked eye, as the entire visible spectrum is covered reasonably uniformly. Previous work on P3HT/$Sb_2S_3$ blends showed that devices generated current out as far as 750 nm, as measured by incident photon to current efficiency (IPCE) measurements.[17] Here photovoltaic devices used a seed layer below the active layer. It is expected that having crystalline $Sb_2S_3$ is paramount to high photovoltaic performance. Therefore, the conditions required to obtain such a crystalline product were investigated, before the effect of ligand moiety on morphology.

To test whether the seed layer had an effect on the crystallinity of the $Sb_2S_3$ a series of films were fabricated with a range of different seed layers. Figure 4.13a shows the UV-Vis absorptance measurements for the same blend annealed on glass (Red), CdS (Green) and CdS followed by $Sb_2S_3$ (Blue). The spectrum of just the seed layer combination of CdS and $Sb_2S_3$ are also shown (Black). When the blend is decomposed on either glass or CdS the band gap appears to be approximately 675 nm and when both seed layers are used this is shifted to approximately 750 nm. It seems that the seed layers do have an effect on the band gap. It is pertinent to note that the seed layer of $Sb_2S_3$ is annealed at a higher temperature (300°C) and is expected to be crystalline. It was not possible to fabricate suitable films of solely $Sb_2S_3$ seed layers, as the precursor would not wet on the glass without the CdS seed layer. These patchy films, without the CdS seed layer, did however cause the annealed films to have black sections where the seed layer had stuck. It is therefore reasonable to assume that the crystalline $Sb_2S_3$ seed layer is responsible for the generation of a crystalline product, within the blend, at a lower temperature.

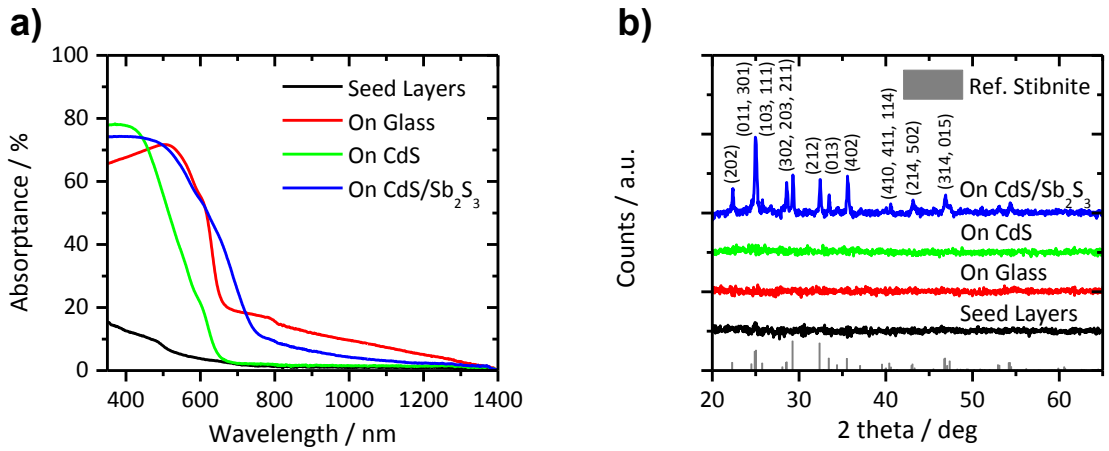



*Figure 4.13 - a) UV-Vis absorptance measurements of P3HT/$Sb_2S_3$ blend films on a range of different seed layers, as well as the absorptance of the seed layers themselves. b) X-Ray diffraction patterns of identical films, along with a reference pattern for stibnite.*

In Figure 4.13b, XRD patterns of the same 4 films are shown, along with a reference for crystalline $Sb_2S_3$ (Stibnite 01-073-033). For the films annealed on glass (Red) and CdS (Green) no peaks are visible. This supports the hypothesis that for these films an amorphous $Sb_2S_3$ is generated. However, when the CdS/$Sb_2S_3$ seed layer is used, several crystallographic planes are observed, which are in good agreement with the reference pattern for stibnite. In the measurement of just the seed layers, there is a small peak at 25° 2 theta visible. This is likely a combination of the 011, 301, 103 and 111 peaks. This amalgamation corresponds to the most intense peaks in the sample with both seed layers and the blend. This supports the assumption that the precursor forms a crystalline product when annealed at high temperatures (300°C). The low intensity, and lack of other peaks, is due to the fact that a very thin layer of $Sb_2S_3$ has been deposited. Both the UV-Vis absorptance and the XRD confirm that the seed layer has an effect on the crystallinity of the $Sb_2S_3$ in the blend, and that, of the layers tested, $Sb_2S_3$ on top of CdS, was the only combination to give a crystalline product at lower temperatures, with consistent coverage.

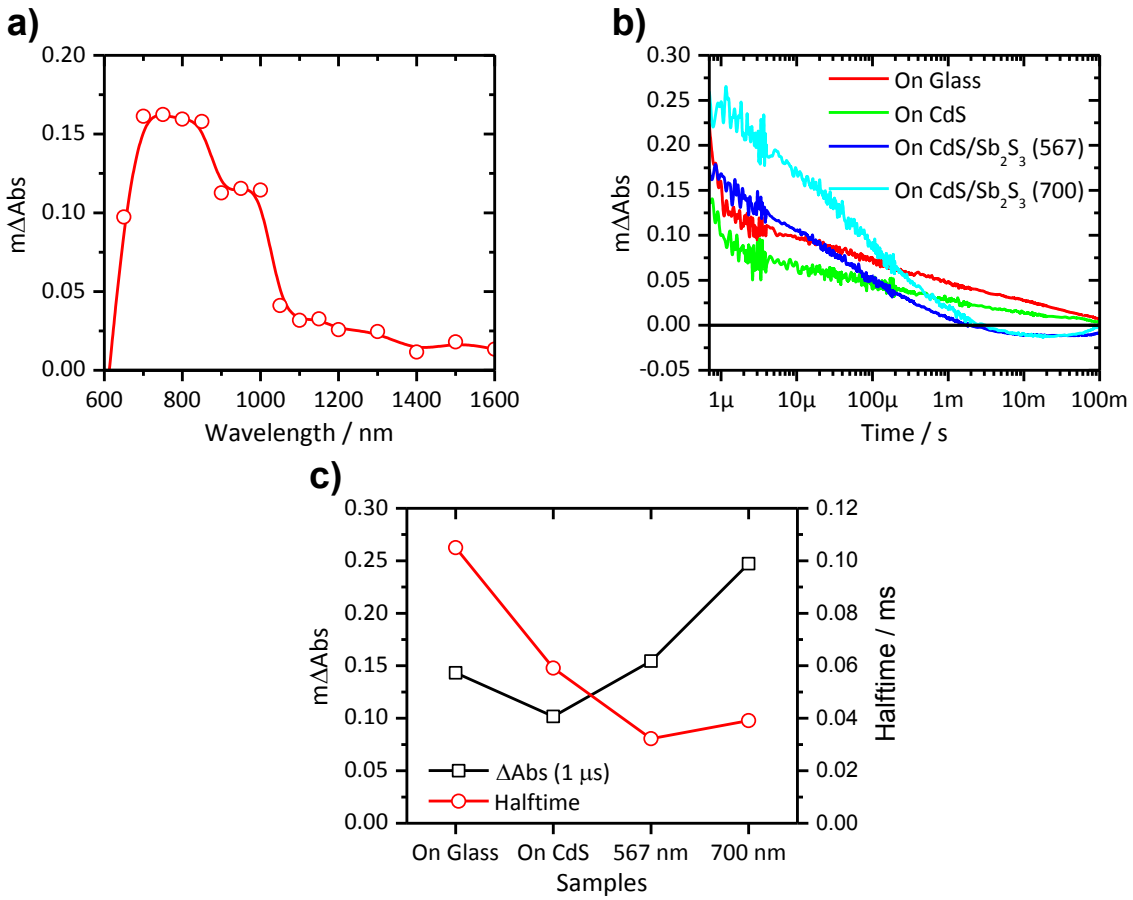



*Figure 4.14 - a) Transient absorption spectra of a P3HT/$Sb_2S_3$ blend film on a glass substrate, without any seed layers, plotted at 10 μs. This sample was excited with a wavelength of 567 nm. b) Transient absorption decays of films on different seed layers, excited at 567 nm or 700 nm and probed at 980 nm. All samples were excited with the same approximate number of photons and are scaled for the amount of pump light absorbed. c) Amplitude of all signals at 1 μs as well as their halftimes.*

TAS was then used to study the charge generation dynamics in these blends. A TAS spectrum was measured of a sample annealed on glass (Figure 4.14a), with the ΔAbs plotted at 1 μs after excitation, using a pump pulse of 567 nm. Although it was already apparent that this film was not crystalline, the more simple system was chosen as the control. The spectrum generated looks similar to that of P3HT/metal sulfide blends previously measured,[17-19] with a broad peak between 600 and 1100 nm. In this instance the peak at 1000 nm is lower in magnitude than the other at 750 nm. The reasons for the difference in the relative heights of these peaks are not fully understood. It is possible that the spectrum is not solely due to the P3HT polaron. Spectra measured previously, of the antimony ethyl xanthate decomposed on nanoporous $TiO_2$ showed a peak at approximately 700 nm that was attributed to the $Sb_2S_3$ hole. It is possible that, in this instance, the spectrum is a combination of holes in the $Sb_2S_3$ and the P3HT hole polaron. This is possible as $Sb_2S_3$ is expected to generate free charges in the bulk of the material, without separating at an interface. In addition, P3HT hole polarons are generated from electron transfer, from P3HT to $Sb_2S_3$, and potentially hole transfer from $Sb_2S_3$ to P3HT. To reduce the

amount of contribution from this possible other peak, the following kinetic decays were measured at 980 nm, as has been used for all other TAS measurements on P3HT.

Figure 4.14b shows the TAS decays for samples measured on each of the different seed layers. For the three seed layers used the decays after excitation with a pump wavelength of 567 nm, exciting both P3HT and $Sb_2S_3$, are shown. The amplitude at 1 µs as well as the halftimes are shown in Figure 4.14c. In the case of the CdS/$Sb_2S_3$ seed layer, there is also a decay after a 700 nm excitation, with the same approximate excitation photons as the 567 nm case. This sample was the only one to show any absorption at 700 nm, and therefore this was the only case where the hole transfer was able to be independently measured.

The decays for samples measured on glass and CdS look very similar. There appears to be a fast decay that has finished by 2 µs, followed by a long-lived signal, that in the case of 'On Glass', has a halftime of 0.1 ms. In the case of the blend on the CdS/$Sb_2S_3$ seed layer, there is no fast phase present. The amplitude, after this fast phase has decayed in the other samples (t > 2 µs), is higher in these traces. The halftime is however, lower in these crystalline $Sb_2S_3$ cases. The observation of a more crystalline material having a higher charge generation yield than a less crystalline system, but a faster decaying signal, is something that will also be seen with P3HT/$Bi_2S_3$ blends in Chapter 5. The reasons for this are thought to be due to the higher crystallinity resulting in a higher charge mobility in the metal sulfide. This increased mobility is believed to increase the rate of recombination, as charges move more rapidly to find either a counter charge or a trap. This phenomenon has been observed before in all-organic systems.[46] The origin of the fast phase, visible only in the amorphous $Sb_2S_3$ cases, is thought to be due to electrons injected from the P3HT, which do not travel far from the interface and, as a result, recombine relatively fast. In the crystalline $Sb_2S_3$ case, and the sample is excited at 567 nm, this fast phase is no longer present. The crystalline samples also show a negative bleach signal that is still visible 10s of milliseconds after excitation. This bleach is likely due to the depopulation of the $Sb_2S_3$ ground-state, the onset of which, has been pushed out to longer wavelengths as the crystallinity has increased. When exciting solely the $Sb_2S_3$ (700 nm), so that only the hole transfer to P3HT is being monitored, the signal is observed to be slightly higher, than when both components are excited (567 nm). The number of photons from the excitation pulse are approximately the same and the signals are scaled for the amount of pump light absorbed. The increase in signal therefore signifies an increase in the charge generation efficiency when exciting only the $Sb_2S_3$. The hole transfer in this system is therefore a more efficient process than the competing electron transfer.

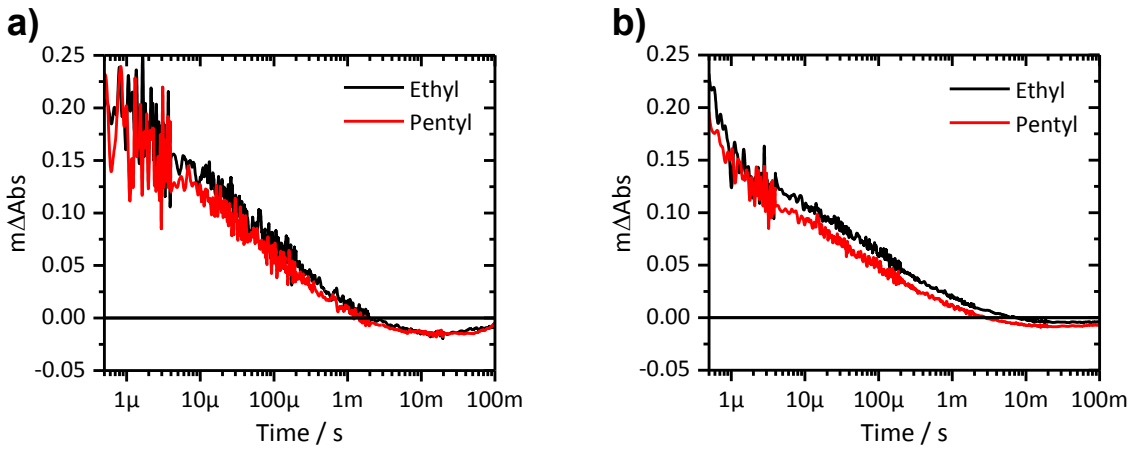



*Figure 4.15 - a) Transient absorption decays of P3HT/$Sb_2S_3$ blends with an equal blend ratio. Samples were excited using a pump wavelength of 567 nm. b) The same samples pumped at 700 nm. All decays are monitoring the decay at 980 nm, are excited with the same approximate number of photons and are scaled for the amount pump light absorbed.*

The difference in charge generation yield between equivalent films, fabricated from the Ethyl and Pentyl xanthate, was also measured. This experiment served to give an indication of the morphology in these blend films. The TAS decays after solely exciting $Sb_2S_3$ (700 nm) are shown in Figure 4.15a and after excitation of both P3HT and $Sb_2S_3$ (567 nm) in Figure 4.15b. In this instance, the blends were fabricated on the CdS/$Sb_2S_3$ seed layers, so that information about both hole and electron transfer could be eluded to. Considering first the 700 nm excitation case, the decays look very similar. The Ethyl sample has a slightly higher initial amplitude (mΔAbs (1 µs) = 0.196 vs 0.177), and the lifetimes are very similar ($t_{1/2}$ = 0.41 vs 0.34 ms). A similar decay when exciting solely the inorganic component is consistent with previous work on P3HT/CdS[18] and the previous findings in earlier on in this chapter. Any potential morphological differences between both films are expected to have little effect on the charge generation yield, as the inorganic component is expected to generate free charges without first diffusing to an interface. These charges have been shown to be much longer-lived in comparison to P3HT excitons.[19] Having a diffusion length longer than 10 nm, as in P3HT for example, reduces the dependence of charge generation on having a highly mixed system. In the 567 nm excitation case, where the P3HT is being excited as well as the $Sb_2S_3$, the situation appears similar. Both the initial amplitude and lifetime of either film are approximately the same, (mΔAbs (1 µs) = 0.157 vs 0.149) and ($t_{1/2}$ = 0.47 vs 0.27 ms). Any contribution to the charge generation by the P3HT is expected to be dependent on the morphology. So, either the P3HT doesn't generate a large amount of charges in these films, or the morphology is very similar. There also appears to be a fast decay phase in the 567 nm excitation case, that wasn't seen before in the crystalline films. The occurrence of this phase only in the 567 nm excitation case further supports the hypothesis that it is due to electron injection from P3HT.

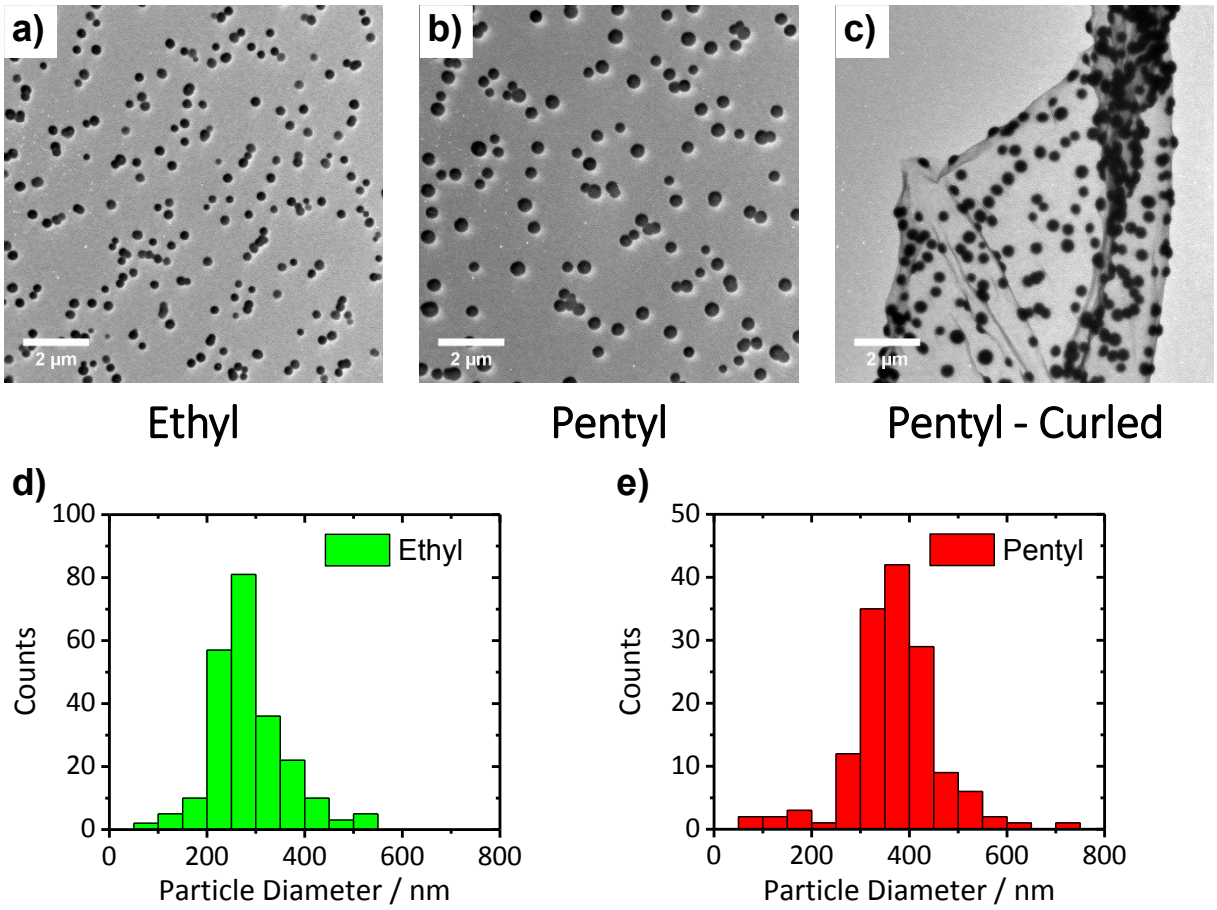
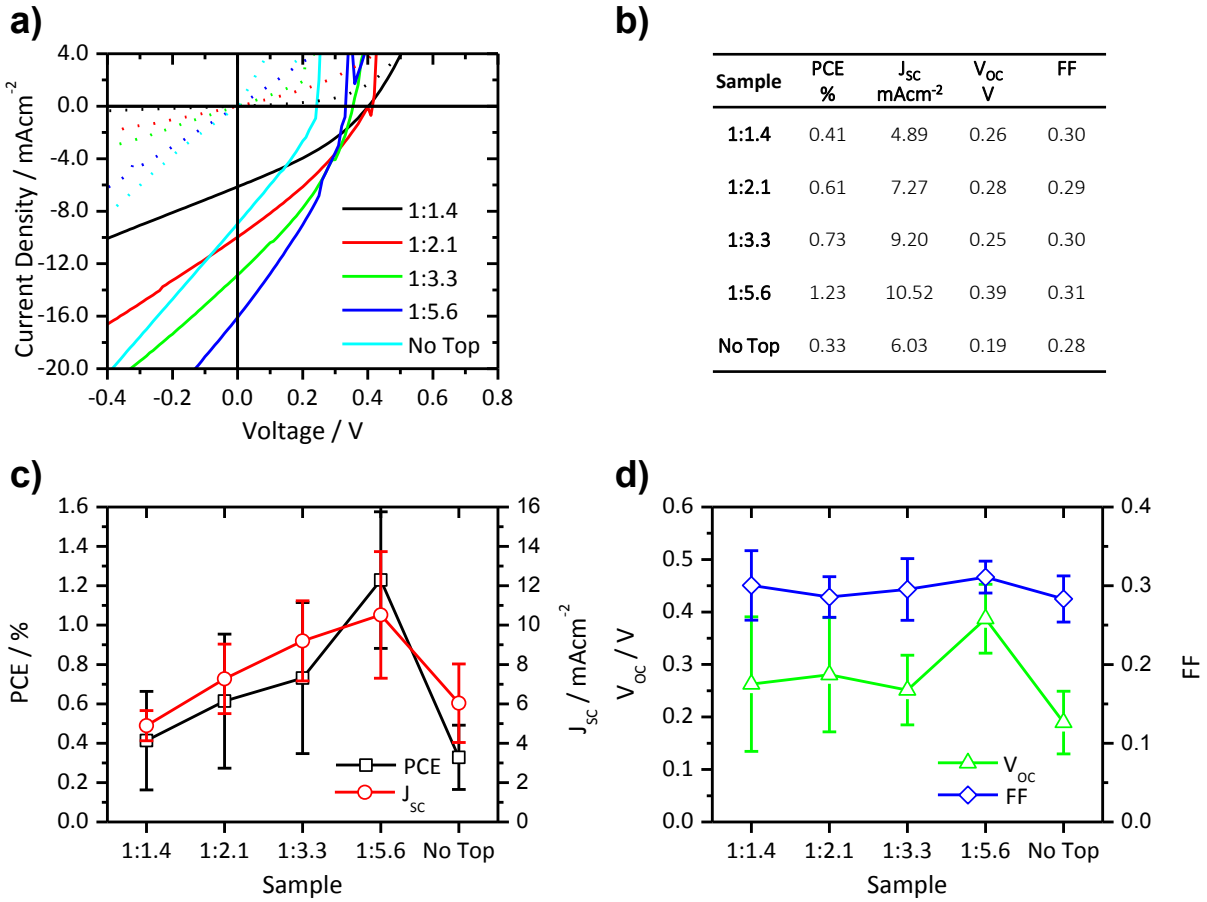



*Figure 4.16 – TEM images of a P3HT/$Sb_2S_3$ blend film with a volume ratio of 1:1.4, fabricated using the Ethyl xanthate a) and the Pentyl xanthate b) at the same level of magnification. c) The same Pentyl film at a different region of the sample where the film has curled. d) Histogram of the approximate particle size distribution of the Ethyl film and e) the Pentyl film.*

TEM was used to image the films and compare the morphology of blends fabricated using the Ethyl and Pentyl xanthate. Previously, high quality images of these blends have been difficult to image at high $Sb_2S_3$ loading amounts.[17] In this study, a volume ratio of 1:1.4 was chosen, so that the difference in morphology could be more easily resolved. Such films are shown in Figure 4.16a (Ethyl) and Figure 4.16b (Pentyl). The observed morphologies are consistent with those measured previously,[17] with an array of spherical $Sb_2S_3$ particles, evenly distributed throughout the polymer film. It is pertinent to note that the requirement of using PEDOT:PSS as a sacrificial substrate prohibits the use of the CdS/$Sb_2S_3$ seed layers. The films observed are therefore of amorphous $Sb_2S_3$. It is assumed that upon crystallising, the morphology does not change dramatically. Here, the Pentyl sample is seen to have a smaller number of larger particles, in comparison to the Ethyl. This is shown statistically, by the histograms in Figure 4.16d and e. This analysis, calculates the average particle size to be 370.6 ± 89.6 nm for Pentyl and 283.6 ± 76.6 nm for Ethyl. This observation is in contrast to the previous work on cadmium xanthate in early in the chapter, where it was found that a large ligand moiety resulted in a more finely mixed morphology. The reason for the opposite trend that is observed here can only be speculated upon, as a less detailed analysis of the decomposition process was undertaken here. A possible reason for the difference could

be due to the fact that the antimony xanthates appear to melt before decomposition. This is apparent by eye when observing the decomposition process, as the films change colour to yellow, then orange, followed by black if the product crystallises. In this yellow phase, if appropriate seed layers are not used, a neat precursor film will being to form droplets that do not wet the substrate. The TEMs do in fact reveal a morphology that appears like droplets of the $Sb_2S_3$. It is perhaps the polymer that slows down the Oswald ripening effect of these droplets, compared to when the neat precursor is annealed on glass. The longer ligand in this case could result in a longer time spent in the melt phase and give the precursor a longer time for the droplets to grow. Figure 4.16c shows a Pentyl film that has curled due to the heat generated by the electron beam. This allows the film to be viewed almost at a cross-section. Here, the $Sb_2S_3$ can be seen protruding from the polymer film, with a reasonably high contact angle. This supports the hypothesis that upon annealing droplets are formed that do not wet the substrate.

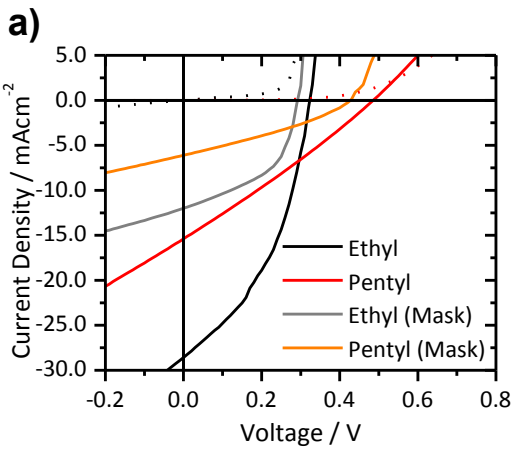



| Sample | PCE % | $J_{sc}$ mAcm$^{-2}$ | $V_{oc}$ V | FF |
|---|---|---|---|---|
| **1:1.4** | 0.41 | 4.89 | 0.26 | 0.30 |
| **1:2.1** | 0.61 | 7.27 | 0.28 | 0.29 |
| **1:3.3** | 0.73 | 9.20 | 0.25 | 0.30 |
| **1:5.6** | 1.23 | 10.52 | 0.39 | 0.31 |
| **No Top** | 0.33 | 6.03 | 0.19 | 0.28 |

*Figure 4.17 – a) Current-voltage measurements of the optimum devices fabricated a range of blend ratios, as well as with the highest blend ratio without a P3HT capping layer (No Top). The measurements performed in the light are represented by the solid lines and the dark curves are shown by the dotted lines. b) Average characteristic device parameters of all working photovoltaic devices. c) Average PCE and $J_{SC}$ plotted for all the working device and the same for $V_{OC}$ and FF d).*

An initial set of devices, shown in Figure 4.17, investigated the effect of the addition of a thin P3HT top layer, as well as the effect of altering the blend ratio. Previous work on P3HT/CdS highlighted that the blend ratio that gave the highest TAS signal did not necessarily correlate to the highest performance, or

even highest currents.[19] The current-voltage curves for the devices displaying the highest PCE are plotted in Figure 4.17a, and the average characteristic device parameters of all of the working devices are tabulated in Figure 4.17b. These tabulated values are plotted in Figure 4.17c and d, in order to more clearly highlight the trends. The highest photovoltaic performance is seen for the highest blend ratio (1:5.6), with an average PCE of 1.23%. The trend in the devices is almost entirely dependent on the increase in $J_{SC}$ observed when a higher amount of $Sb_2S_3$ is added to the active layer. This is made clear in Figure 4.17c, where the first four points lie roughly on top of one another. The hypothesis that the device efficiency could be improved upon the addition of a thin P3HT top layer is also validated here. The PCE of this device (No Top), which has the same blend ratio as the highest performing device (1:1.56), is much lower. This is partially due to a reduced $J_{SC}$, which could be due to a reduction in heterojunction surface area, if the protruding parts of $Sb_2S_3$ observed in the TEM image (Figure 4.16c) were left uncovered by P3HT. The $V_{OC}$ of this device is also lower than the rest. This is likely due to a increase in the leakage current. The difference in leakage currents can be seen in the dark curves (dotted), where the device with no P3HT top layer (No Top (cyan)) shows a higher negative current at reverse bias than the equivalent device with the top layer (1:1.56 (blue)). The amount of leakage current of all the other devices is seen to increase with the amount of $Sb_2S_3$. This suggests that the P3HT top layer is not fully optimised, as a higher amount of short-circuiting behaviour is observed as more $Sb_2S_3$ is added. The trend in $V_{OC}$ of the other devices is unclear, but there is a slight increase observed as a higher blend ratio is used. The FF of all devices seems to be fairly constant.




b)

| Sample | PCE % | $J_{sc}$ mAcm$^{-2}$ | $V_{oc}$ V | FF |
|---|---|---|---|---|
| Ethyl | 2.92 | 20.44 | 0.39 | 0.38 |
| Ethyl (Mask) | 1.68 | 12.00 | 0.29 | 0.48 |
| Pentyl | 1.52 | 11.75 | 0.47 | 0.27 |
| Pentyl (Mask) | 0.83 | 6.10 | 0.43 | 0.32 |

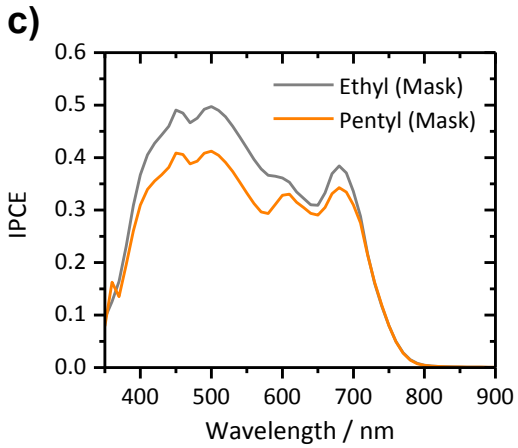



*Figure 4.18 – a) Current-voltage curves of the optimum devices fabricated in this study, as well as these devices measured after masking. The solid lines are measurements made in the light and dotted lines represent dark curves. b) Tabulated average characteristic device parameters for the devices in this series, as well as the values for the devices with the highest PCE after masking. c) Incident photon to current conversion efficiencies of these masked devices.*

In a second set of devices, a much thicker P3HT top layer was used and the optimised device fabricated from the Pentyl xanthate was compared to an equivalent ethyl device. The current-voltage curves for the devices displaying the highest PCE are plotted in Figure 4.18a, and the average characteristic device parameters of all of the working devices are tabulated in Figure 4.18b. These devices showed a very low amount of leakage current in the dark, suggesting that the amount of P3HT used in this instance was sufficient. Here, the devices utilising the Ethyl xanthate precursor, outperformed the Pentyl devices. This was mainly due to a remarkably high $J_{SC}$, which will be discussed in the next paragraph. The devices appear to quite be different in all respects. Ethyl devices demonstrate higher currents ($J_{SC}$ = 20.44 vs 11.75 mAcm$^{-2}$) and increased FF (0.38 vs 0.27). The Pentyl devices, however, show superior $V_{OC}$ (0.47 vs 0.39 V). The reason for the observed increase in efficiency by the Ethyl device is unknown. The more finely mixed morphology observed in the TEM images could explain the increase in $J_{SC}$, however only a small increase in the charge generation was measured using TAS. To understand the reasons for this difference, a more in depth study is required into the materials properties of the different $Sb_2S_3$ formed.

The remarkably high $J_{SC}$s measured for all devices, an average 20.44 $mAcm^{-2}$ for the Ethyl devices, and 28.58 $mAcm^{-2}$ for the device with the highest PCE, brought into question the measurement technique. The highest theoretical $J_{SC}$ possible, based on a material with a band gap of 750 nm, that collects all of the AM 1.5 spectrum at 100 $mWcm^{-2}$ above this energy, is just below 25 $mAcm^{-2}$. A few of the devices in this study exceeded this theoretical maximum, so the optimum devices were illuminated through a shadow mask. The performance of the masked devices dropped to approximately 50% the unmasked values. Masking of devices using P3HT and a $MoO_3$/Ag top contact is not normally necessary, and in the past for these devices has shown not to make any significant difference to the performance. The P3HT used in this section was different to that used in all other parts of the thesis and it is possible that higher laterally connectivity is being observed here. The effect is so much so that the $J_{SC}$ is twice as high without masking and the pixel area is effectively twice as large as the area marked out by the $MoO_3$/Ag contact. As a result, the efficiencies quoted on these P3HT/$Sb_2S_3$ devices should be considered as overestimated, but the trends observed are still valid.

In Figure 4.18c the incident photon to current efficiency (IPCE) measurements for the optimum (masked) Ethyl and Pentyl devices are shown. The onset of current is seen to extend out to just beyond 750 nm and have an IPCE maximum at around 500 nm. This is consistent with what has been observed previously.[17] There is also, an apparent dip in the IPCE between 500 and 650 nm. This is believed to be due to the P3HT absorption that is not contributing to the photocurrent as efficiently as the $Sb_2S_3$. This observation was also made by O'Mahony[29] *et* al. in P3HT/mesoporous $Sb_2S_3$ devices.

## Conclusions

In summary, this study shows how the nanomorphology of *in-situ* prepared hybrid solar cells can be tuned efficiently by the design of the molecular nanocrystal precursors. Small changes in the structure of the used metal xanthates induced significant changes in the obtained absorber layer nanomorphologies. In the case of the cadmium xanthates studied, the longer alkyl chains of the xanthate moieties lead to a better mixing of the polymer and nanoparticle phase, to smaller domain sizes and a lower crystallinity of the polymer phase in the P3HT/CdS absorber layers. The formation of these different morphologies is determined by agglomeration of the nanocrystals, which have a similar size in all the investigated samples. As suggested by time resolved X-ray scattering measurements, the agglomeration of the nanocrystals is influenced by growth temperature and kinetics of the nanocrystals as well as phase separation of polymer and metal xanthate phase already in the precursor layer.

The different nanomorphologies strongly influence the optoelectronic properties of the absorber layers and in turn also the performance of the hybrid solar cells and a complex interplay between these parameters is disclosed by the performed characterisations. The highest level of quenching of the photoluminescence of the polymer phase by the CdS nanocrystals was found for the heptyl sample, indicating that the heptyl sample was the most intimately mixed. This was also supported by fs-TAS showing the shortest P3HT exciton lifetime in this system. However, optimum charge generation, probed by µs-TAS, was observed in the pentyl sample, showing that in the heptyl sample due to non-agglomerated nanocrystals the domain sizes are presumably too small for the efficient generation of long-lived charges, which is facilitated by bigger domain sizes. Overall, the best power conversion efficiencies were obtained with hybrid solar cells prepared using propyl xanthates. This originates from the fact that besides efficient charge generation also charge transport and recombination play a crucial role in the devices, which were found out to become more and more an issue when going to finer mixed morphologies.

In the case of the antimony xanthates studied, the ligand moiety of metal xanthate precursors has been shown, again, to have an influence on the morphology of *in-situ* fabricated polymer/nanoparticle blends. In contrast to the cadmium xanthates, when the pentyl ligand was used, larger domain sizes were observed, in comparison to equivalent films fabricated from the ethyl precursor. These domains were observed by TEM and seen to be relatively large, 370 and 280 nm, for the Pentyl and Ethyl films respectively. Domain sizes of this magnitude are much larger than seen with the previous xanthate fabricated hybrid systems and are expected to be far from optimal for solar cells, in particular, with regards to charge generation.

The crystallinity of the generated films was found to be highly dependent on the substrate material, with crystalline blend films only possible, at low temperatures, when a combination of $Sb_2S_3$, annealed at 300°C, was coated on top of a CdS seed layer. The role of the CdS layer was primarily to allow the $Sb_2S_3$ to form a consistent smooth film. Without the CdS the antimony xanthate was observed to de-wet, upon annealing, and coat only small sections of the glass or $TiO_2$ substrate.

The charge generation in the hybrid heterojunctions were found to be consistent with previous measurements, showing that the majority of charges were generated from hole transfer. The hole transfer was also seen to be fairly unaffected by the change in domain size. Electron transfer was seen to be relatively less efficient and slightly more affected by the morphology. A more pronounced change was observed when comparing films containing crystalline or amorphous $Sb_2S_3$. Upon exiting P3HT, in the amorphous case there was an observed extra fast decay phase, which was not present in the crystalline case. This is believed to be caused by a low mobility in the amorphous case, causing injected electrons to remain at the interface and recombine relatively more quickly.

Preliminary sets of photovoltaic devices were fabricated using the pentyl xanthate and an average PCE of 1.52% was achieved. Equivalent devices using the ethyl xanthate yielded an average PCE of 2.92%. This difference highlighted the dependence that the PCE has on the morphology of hybrid photovoltaics. The $J_{SC}$s of a handful of devices were measured to be higher than the theoretical limit for this material system and so steps were taken in order to mask the devices. This resulted in a reduction in the $J_{SC}$ by almost 50%, as well as the PCEs. After masking, the optimised devices still showed higher PCEs than the previously published devices, with both the Ethyl and Pentyl precursors.

Although this work did not result in the discovery of a design rule that can be applied to all xanthate precursor materials, it does demonstrate that the ligand moiety has an effect on the morphology obtained in *in-situ* hybrid photovoltaics. The findings of this study will provide a valuable tool for further research in the emerging field of hybrid solar cells, in particular, for optimising polymer/nanocrystal hybrid solar cells using non-toxic material combinations including $Bi_2S_3$ or $CuInS_2$ nanocrystals. These materials also have the advantage of having better suited absorption properties for solar cell applications compared to CdS and $Sb_2S_3$.

## References


(1) *The Matrix.* [Film] Directed by: The Wachowski Brothers. USA: Warner Bros.; 1999.

(2) Hundt, N.; Palaniappan, K.; Sista, P.; Murphy, J. W.; Hao, J.; Nguyen, H.; Stein, E.; Biewer, M. C.; Gnade, B. E.; Stefan, M. C. *Polymer Chemistry* 2010, *1*, 1624.

(3) Clarke, T. M.; Durrant, J. R. *Chem. Rev.* 2010.

(4) Guo, J.; Ohkita, H.; Benten, H.; Ito, S. *J. Am. Chem. Soc.* 2010, *132*, 6154.

(5) Oosterhout, S. D.; Koster, L. J. A.; van Bavel, S. S.; Loos, J.; Stenzel, O.; Thiedmann, R.; Schmidt, V.; Campo, B.; Cleij, T. J.; Lutzen, L.; Vanderzande, D.; Wienk, M. M.; Janssen, R. A. J. *Adv. Energy Mater.* 2011, *1*, 90.

(6) Oosterhout, S. D.; Wienk, M. M.; van Bavel, S. S.; Thiedmann, R.; Jan Anton Koster, L.; Gilot, J.; Loos, J.; Schmidt, V.; Janssen, R. A. J. *Nat Mater* 2009, *8*, 818.

(7) Wang, H.; Oey, C. C.; Djurišić, A. B.; Xie, M. H.; Leung, Y. H.; Man, K. K. Y.; Chan, W. K.; Pandey, A.; Nunzi, J.-M.; Chui, P. C. *Appl. Phys. Lett.* 2005, *87*.

(8) Zhao, L.-D.; Zhang, B.-P.; Liu, W.-S.; Zhang, H.-L.; Li, J.-F. *J. Solid State Chem.* 2008, *181*, 3278.

(9) Jamieson, F. C.; Domingo, E. B.; McCarthy-Ward, T.; Heeney, M.; Stingelin, N.; Durrant, J. R. *Chemical Science* 2012, *3*, 485.

(10) Williams, S. S.; Hampton, M. J.; Gowrishankar, V.; Ding, I. K.; Templeton, J. L.; Samulski, E. T.; DeSimone, J. M.; McGehee, M. D. *Chem. Mater.* 2008, *20*, 5229.

(11) Kang, Y. M.; Park, N. G.; Kim, D. *Appl. Phys. Lett.* 2005, *86*.

(12) Lokteva, I.; Radychev, N.; Witt, F.; Borchert, H.; Parisi, J. r.; Kolny-Olesiak, J. *J. Phys. Chem. C* 2010, *114*, 12784.

(13) Huynh, W. U.; Dittmer, J. J.; Alivisatos, A. P. *Science* 2002, *295*, 2425.

(14) Dowland, S.; Lutz, T.; Ward, A.; King, S. P.; Sudlow, A.; Hill, M. S.; Molloy, K. C.; Haque, S. A. *Adv. Mater.* 2011, *23*, 2739.

(15) Leventis, H. C.; King, S. P.; Sudlow, A.; Hill, M. S.; Molloy, K. C.; Haque, S. A. *Nano Lett.* 2010, *10*, 1253.

(16) Rath, T.; Edler, M.; Haas, W.; Fischereder, A.; Moscher, S.; Schenk, A.; Trattnig, R.; Sezen, M.; Mauthner, G.; Pein, A.; Meischler, D.; Bartl, K.; Saf, R.; Bansal, N.; Haque, S. A.; Hofer, F.; List, E. J. W.; Trimmel, G. *Adv. Energy Mater.* 2011, *1*, 1046.

(17) Bansal, N.; O'Mahony, F. T. F.; Lutz, T.; Haque, S. A. *Adv. Energy Mater.* 2013, *3*, 986.

(18) Dowland, S. A.; Reynolds, L. X.; MacLachlan, A.; Cappel, U. B.; Haque, S. A. *J. Mater. Chem. A* 2013, *1*, 13896.

(19) Cappel, U. B.; Dowland, S. A.; Reynolds, L. X.; Dimitrov, S.; Haque, S. A. *J. Phys. Chem Lett.* 2013, *4*, 4253.

(20) Versavel, M. Y.; Haber, J. A. *Thin Solid Films* 2007, *515*, 7171.

(21) Moon, S.-J.; Itzhaik, Y.; Yum, J.-H.; Zakeeruddin, S. M.; Hodes, G.; Grätzel, M. *J. Phys. Chem Lett.* 2010, *1*, 1524.

(22) Chang, J. A.; Im, S. H.; Lee, Y. H.; Kim, H.-j.; Lim, C.-S.; Heo, J. H.; Seok, S. I. *Nano Lett.* 2012, *12*, 1863.

(23) Im, S. H.; Lim, C.-S.; Chang, J. A.; Lee, Y. H.; Maiti, N.; Kim, H.-J.; Nazeeruddin, M. K.; Grätzel, M.; Seok, S. I. *Nano Lett.* 2011, *11*, 4789.

(24) Itzhaik, Y.; Niitsoo, O.; Page, M.; Hodes, G. *J. Phys. Chem. C* 2009, *113*, 4254.

(25) Tsujimoto, K.; Nguyen, D.-C.; Ito, S.; Nishino, H.; Matsuyoshi, H.; Konno, A.; Kumara, G. R. A.; Tennakone, K. *J. Phys. Chem. C* 2012, *116*, 13465.

(26) Boix, P. P.; Larramona, G.; Jacob, A.; Delatouche, B.; Mora-Seró, I.; Bisquert, J. *J. Phys. Chem. C* 2011, *116*, 1579.

(27) Lim, C.-S.; Im, S. H.; Kim, H.-j.; Chang, J. A.; Lee, Y. H.; Seok, S. I. *PCCP* 2012, *14*, 3622.

(28) Im, S. H.; Kim, H.-j.; Rhee, J. H.; Lim, C.-S.; Seok, S. I. *Energy Environ. Sci.* 2011, *4*, 2799.

(29) O'Mahony, F. T.; Cappel, U. B.; Tokmoldin, N.; Lutz, T.; Lindblad, R.; Rensmo, H.; Haque, S. A. *Angew. Chem. Int. Ed. Engl.* 2013, *52*, 12047.

(30) O'Mahony, F. T. (2014) *Solution-Processed Inorganic Semiconductors in Hybrid Photovoltaics: Mechanisms of Charge Separation and Effects of Interface Structure.* PhD Thesis. Imperial College London.

(31) Pradhan, N.; Katz, B.; Efrima, S. *J. Phys. Chem. B* 2003, *107*, 13843.

(32) Di Luccio, T.; Laera, A. M.; Tapfer, L.; Kempter, S.; Kraus, R.; Nickel, B. *J. Phys. Chem. B* 2006, *110*, 12603.

(33) Zhang, H.; Banfield, J. F. *J. Phys. Chem. C* 2009, *113*, 9681.

(34) Dunst, S.; Rath, T.; Radivo, A.; Sovernigo, E.; Tormen, M.; Amenitsch, H.; Marmiroli, B.; Sartori, B.; Reichmann, A.; Knall, A.-C.; Trimmel, G. *ACS Appl. Mater. Interfaces* 2014, *6*, 7633.

(35) Korovyanko, O. J.; Österbacka, R.; Jiang, X. M.; Vardeny, Z. V.; Janssen, R. A. J. *Phys. Rev. B* 2001, *64*, 235122.

(36) Magnani, L.; Rumbles, G.; Samuel, I. D. W.; Murray, K.; Moratti, S. C.; Holmes, A. B.; Friend, R. H. *Synth. Met.* 1997, *84*, 899.

(37) Clark, J.; Silva, C.; Friend, R. H.; Spano, F. C. *Phys. Rev. Lett.* 2007, *98*, 206406.

(38) Xu, B.; Holdcroft, S. *Macromolecules* 1993, *26*, 4457.

(39) Howard, I. A.; Mauer, R.; Meister, M.; Laquai, F. *J. Am. Chem. Soc.* 2010, *132*, 14866.

(40) Dowland, S.; Lutz, T.; Ward, A.; King, S. P.; Sudlow, A.; Hill, M. S.; Molloy, K. C.; Haque, S. A. *Adv. Mater.* 2011, *23*, 2739.

(41) Ohkita, H.; Cook, S.; Astuti, Y.; Duffy, W.; Tierney, S.; Zhang, W.; Heeney, M.; McCulloch, I.; Nelson, J.; Bradley, D. D. C.; Durrant, J. R. *J. Am. Chem. Soc.* 2008, *130*, 3030.

(42) Dayal, S.; Reese, M. O.; Ferguson, A. J.; Ginley, D. S.; Rumbles, G.; Kopidakis, N. *Adv. Funct. Mater.* 2010, *20*, 2629.

(43) Kroeze, J. E.; Savenije, T. J.; Vermeulen, M. J. W.; Warman, J. M. *J. Phys. Chem. B* 2003, *107*, 7696.

(44) Shaw, P. E.; Ruseckas, A.; Samuel, I. D. W. *Adv. Mater.* 2008, *20*, 3516.

(45) Clarke, T. M.; Ballantyne, A.; Shoaee, S.; Soon, Y. W.; Duffy, W.; Heeney, M.; McCulloch, I.; Nelson, J.; Durrant, J. R. *Adv. Mater.* 2010, *22*, 5287.

(46) Pivrikas, A.; Österbacka, R.; Juška, G.; Arlauskas, K.; Stubb, H. *Synth. Met.* 2005, *155*, 242.

# Chapter 5

## Synthesis of $Bi_2S_3$ Utilising the *In-situ* Decomposition of Bismuth Xanthates

***Cobb:*** *Now, before you bother telling me it's impossible...*

***Eames:*** *No, it's perfectly possible. It's just bloody difficult*

*Inception (2010)*[1]

## Abstract

Bismuth ethyl xanthate ($BiEX_3$) was thermally decomposed in a number of organic semiconducting polymers, including poly(3-hexylthiophene-2,5-diyl) (P3HT), to form hybrid polymer/$Bi_2S_3$ bulk heterojunctions (BHJs), analogous to those of P3HT/CdS and P3HT/$Sb_2S_3$ blends seen in Chapter 4. The $BiEX_3$ was found to decompose into nanorods within the solid-state polymer matrix. Transient absorption spectroscopy (TAS) was used to study the charge generation yield in these blends, finding that for the polymer poly(dioctylfluorene-co-bis-N,N'(2,4-dimethylphenyl)diphenylamine) (F8TAA) a moderate amount of charge generation occurred at the polymer/nanoparticle interface. The effect of altering the precursor ligand moiety length was also briefly investigated. Attempts to fabricate photovoltaic devices were unsuccessful, possibly due to the large size of the needles that formed, resulting in a short-circuiting of the devices.

In view of the limitations observed in the BHJs, the $BiEX_3$ was then used in a different manner, by spin coating the precursor and annealing without the polymer. This formed a mesostructured array of $Bi_2S_3$ needles that could be surface treated and then infiltrated with a polymer. The crystallinity of the mesostructures was found to be dependent on the annealing temperature. TAS was used to show that long-lived charge generation could be achieved at the P3HT/$Bi_2S_3$ interface. Photovoltaic devices were also successfully fabricated, overcoming the short-circuit problems observed in the BHJs. Devices, however, showed modest power conversion efficiencies, but did demonstrate current generation out to over 800 nm as measured by incident photon conversion efficiency (IPCE).

This work formed the basis of the following publication:

**Solution-Processed Mesoscopic $Bi_2S_3$: Polymer Photoactive Layers** MacLachlan, A. J.; O'Mahony, F. T.; Sudlow, A. L.; Hill, M. S.; Molloy, K. C.; Nelson, J.; Haque, S. A. *ChemPhysChem* **2014**, *15*, 1019.

## Introduction

In order to find a suitable, scalable system that has the potential to act as a global solution for the production of renewable energy, it is likely that such a solution will have to be non-toxic. Recent successes in the field of hybrid photovoltaics have been with highly toxic materials of either CdS,[2] CdSe,[3] PbS[4] and PbSe,[5] to list a few examples. The reasons why the best results have been seen with toxic materials is unknown, but the work of others has shown promising results with some less toxic alternatives, such as $CuInS_2$[6] and ZnO.[7] The amount of work on non-toxic systems is certainly less than the more successful toxic systems and some have chosen to ignore the problem of toxicity, with the hope that such progress will be made that the disadvantages of toxicity will eventually be overlooked. The best example of this is the emergence of the lead based perovskite solar cells that very quickly attracted a lot of attention after two groups published in quick succession devices of high efficiencies using this previously overlooked material.[8,9] This material is considered by some too toxic to become commercially viable, however a considerable amount of money is being invested into this technology, with the hope that the toxicity will be forgotten about when the efficiencies are too good to be ignored. It is this author's opinion however that focus should be placed on finding a non-toxic solution for the generation renewable energy.

One of the materials that stands out in the literature as under-researched appears to be $Bi_2S_3$. Bismuth is a slightly surprising metal because even though it has some very toxic neighbours in the periodic table, namely lead, polonium and, to a lesser extent, antimony, it itself is considered almost completely non-toxic. Bismuth is in fact found in quite a few medicines including Pepto-Bismol, used to treat minor digestive problems, and also some cosmetic products. $Bi_2S_3$, as well as being non-toxic, has an ideally low band-gap of around 950 nm. The previous work in this thesis and other work on hybrid photovoltaics in the group has shifted how the inorganic component is envisaged in these BHJs. They were once seen as a PCBM replacement that would act as an electron acceptor material, but would also absorb some additional light previously not harvested by the polymer. Now their role in the BHJ is that of a material that does the majority of the light absorption, with charges generated primarily through hole transfer to the polymer. This is highlighted in Chapter 4 by the TAS results, that showed the hole transfer being more efficient than the electron transfer. $Bi_2S_3$ therefore seems an ideal candidate as a material for hybrid photovoltaics, as it has a low band gap and can be a used in a device that functions almost exclusively through hole transfer.

Although there isn't much literature on the use of $Bi_2S_3$, in comparison to other materials, there has been some success by a couple of groups. Rath *et* al. reported a 4.87% efficient device based on a blend of $Bi_2S_3$ and PbS quatum dots with remarkable currents of 24.2 $mA/cm^2$.[10] P3HT/$Bi_2S_3$ blend devices have

also been shown by Martínez *et* al., albeit with slightly more modest efficiencies of 1%.[11] The decomposition of bismuth xanthates have also been used by many groups to form a variety of different $Bi_2S_3$ structures in solution, including nanorods,[12] nanowires[13] and nanoflowers.[14] This groundwork seems to suggest that using bismuth xanthate complexes in the same way as had been used to make polymer/CdS and $Sb_2S_3$ heterojunctions could yield effective novel non-toxic solar cells.

To this end bismuth xanthate complexes were used as a precursor to $Bi_2S_3$ in polymer/$Bi_2S_3$ blend solar cells. The BHJs were characterised using transient absorption spectroscopy (TAS) and photovoltaic devices were also fabricated, finding that although the BHJs were able to generate charges there were serious structural problems with devices, due to short-circuiting. To overcome this problem, the bismuth ethyl xanthate was used in a unique way, to generate a mesostructured $Bi_2S_3$ scaffold into which a hole conductor could be infiltrated. This methodology stopped the problem with device short-circuiting and yielded for the first time a working solar cell from bismuth xanthate as a precursor.

# Experimental

## Bismuth Sulfide/Polymer Blend Heterojunctions

Films used for characterisation were prepared such that there would be an approximate 1:1 volume ratio in the final annealed film. To this end bismuth ethyl xanthate ($BiEX_3$) (163 mg) was dissolved in chlorobenzene (0.5 ml) and stirred for 30 min before being filtered using a 0.45 µm PTFE syringe filter. Polymers P3HT (Sigma-Aldrich) and F8TAA (Martin Heeney, Imperial College) were dissolved in chlorobenzene (25 mg/ml) and stirred for 30 min. The $BiEX_3$ solutions were mixed with the polymer solution and stirred for 30 min before spin coating (2000 rpm, 2000 rpm/s, 60 s) and annealing in a nitrogen glovebox for 1 hour. Films fabricated using bismuth pentyl xanthate ($BiPX_3$) were made using an identical method although the solution concentrations were increased to account for the higher molecular weight of the precursor.

Devices were made of the architecture ITO/ZnO/CdS/polymer:$Bi_2S_3$/(polymer/)$MoO_3$/Ag. Details of each of these other layers can be found in Chapter 3 as well as the syntheses of $BiEX_3$ and $BiPX_3$.

## Mesostructured Bismuth Sulfide

Mesostructured $Bi_2S_3$ films were fabricated by spin coating and annealing the $BiEX_3$ solutions without mixing with a polymer solution. These solutions would not wet on the cleaned glass and so an oxide layer was used, as would be present in a device, to allow the solutions to wet. A thin seed layer of the $BiEX_3$ was also necessary to stop the thicker deposited films dewetting upon annealing. Oxide layers were prepared as described in Chapter 3.

$Bi_2S_3$ seed layers were prepared by spin coating a dilute $BiEX_3$ chlorobenzene solution (50 mg/ml) at (6000 rpm, 2000 rpm/s, 45 s) and annealing for 30 min in a nitrogen glovebox at 160°C. A thicker mesostructured layer was then fabricated, using a more concentrated solution (327 mg/ml) in chlorobenzene, spin coated at (2000 rpm, 1000 rpm/s, 60 s) and annealed at a range of temperatures (160-300°C) for 1 hour. These mesostructures were first treated by immersion in pyridine overnight before spin coating either P3HT or F8TAA on top (2000 rpm, 2000 rpm/s, 60 s), to fill in the pores.

Devices were made of the architecture ITO/ZnO/$Bi_2S_3$/polymer/$MoO_3$/Ag. Details of each of these other layers can be found in Chapter 3.

# Results and Discussion

## Polymer/$Bi_2S_3$ Blend Heterojunctions

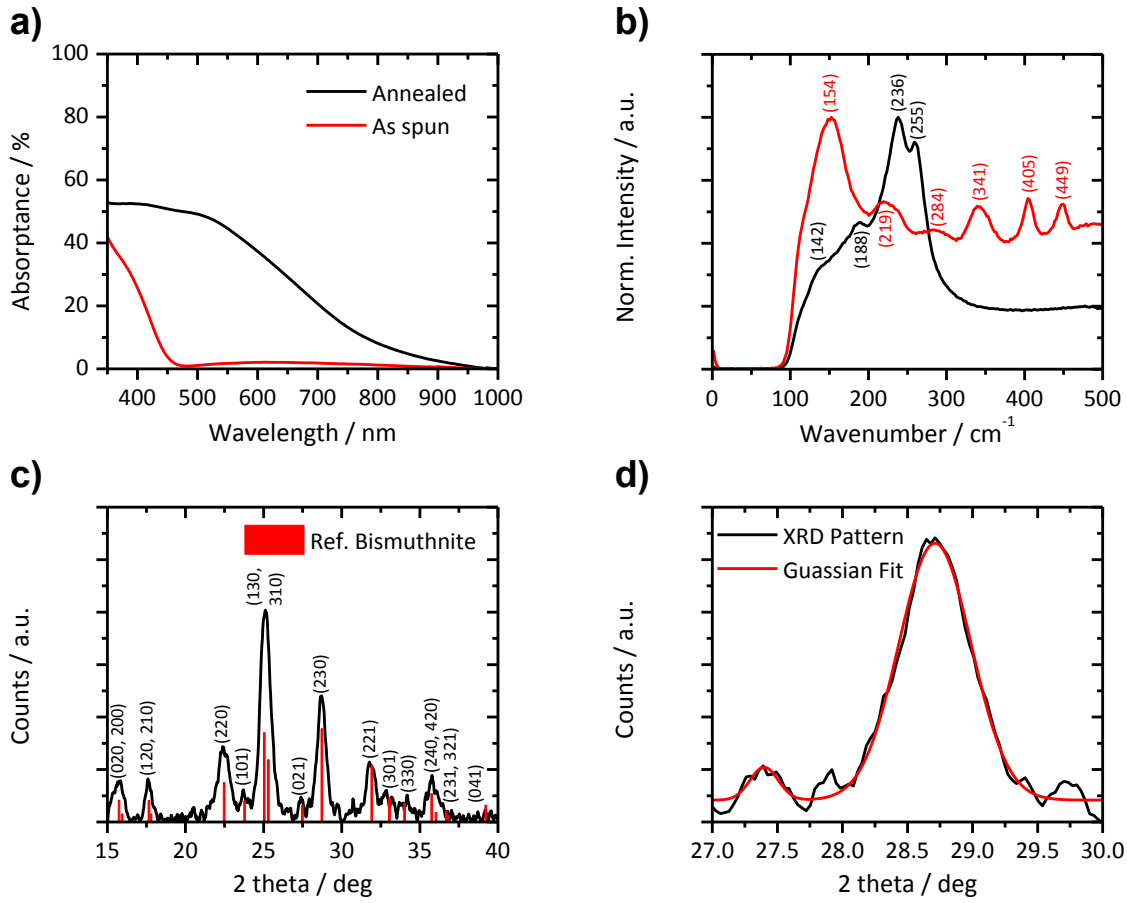



*Figure 5.1 - a) UV-Vis absorption spectra of a typical polystyrene (PS)/$BiEX_3$ blend film as spun (red) and after annealing (black). b) Raman spectra of the same films, as spun (red) and after annealing (black), both labelled with their approximate stretches. c) X-ray diffraction (XRD) pattern of a typical PS/$Bi_2S_3$ blend film, fabricated by annealing at 160°C (black) as well as a reference pattern for bismuthinite (01-075-1306) (red). The Miller indices have been assigned from the reference pattern. d) A more focussed area of the same measurement in c) (black) superimposed with a double Gaussian fit (red). This fit was used to calculate the FWHM and ultimately the mean particle size using the Scherrer equation.*

Upon decomposition of a spin coated blend of the transparent insulating polymer polystyrene (PS) and $BiEX_3$ there is a very quick transformation, from a film with a colour of pale yellow to a film that is extremely black and shiny, with a finish similar to onyx. This complete coverage of the visible region of the solar spectrum can be seen in the UV-Vis absorption spectrum in Figure 5.1a where the annealed film shows an absorption onset at approximately 950 nm. This complete coverage of the solar spectrum is one of the favourable properties of $Bi_2S_3$ that highlights it as a desirable material for hybrid solar cells. The films were further characterised using Raman spectroscopy to confirm the presence of $Bi_2S_3$ after annealing. The results of this are shown in Figure 5.1b, with the as spun film in red and the annealed film in black. The peaks observed in the as spun spectrum can be solely attributed to the $BiEX_3$ precursor, as the Raman peaks observed previously for atactic PS have been reported to be of generally weak

strength.[15] From comparison of the as spun and the annealed spectra, it is clear that there are no common peaks, which validates the assumption that the peaks observed in the as spun film are solely due to the xanthate precursor. Assignments for the peaks of $BiEX_3$ precursors are not readily available, however measurements made on copper and silver xanthates have two common peaks that are also present in Figure 5.1b. These common peaks are seen here at 405 and 449 $cm^{-1}$ and have been attributed to the COC *trans* deformation and OCC deformation respectively.[16] After the short anneal the emergence of peaks at 255, 236 and 188 $cm^{-1}$ and a shoulder at ~142 $cm^{-1}$ can be observed, along with the disappearance of all the peaks observed in the as spun film. The three vibrations observed here are consistent with previous literature findings of $Bi_2S_3$ powders.[17]

Further confirmation for the presence of $Bi_2S_3$, as well as information relating to the crystallinity of the material produced was achieved using X-ray diffraction (XRD). Figure 5.1c shows the diffraction pattern of a typical film along with a reference pattern for bismuthinite (01-075-1306). The material is observed to be quite crystalline, despite the low annealing temperature used, and in good agreement with the reference pattern. In Figure 5.1d a smaller region of the XRD pattern has been focussed on and the peaks have been fitted with a double Gaussian function. The (021) and (230) peaks at ~27.5 and 28.7° 2 theta respectively were chosen because together they met the criteria for being easily resolvable, whilst also being suitably intense. After using the Scherrer formula the mean crystallite size extracted was 15.12 nm. This is quite similar to what has been observed before in the CdS and $Sb_2S_3$ systems. It is pertinent to note that this is the average crystallite size in the (230) plane and is not necessarily the most relevant direction. This peak was however the easiest to resolve and looks representative of the other peaks in the diffraction pattern. It therefore is considered a reasonable method to get a rough idea of the crystallite size in this system.

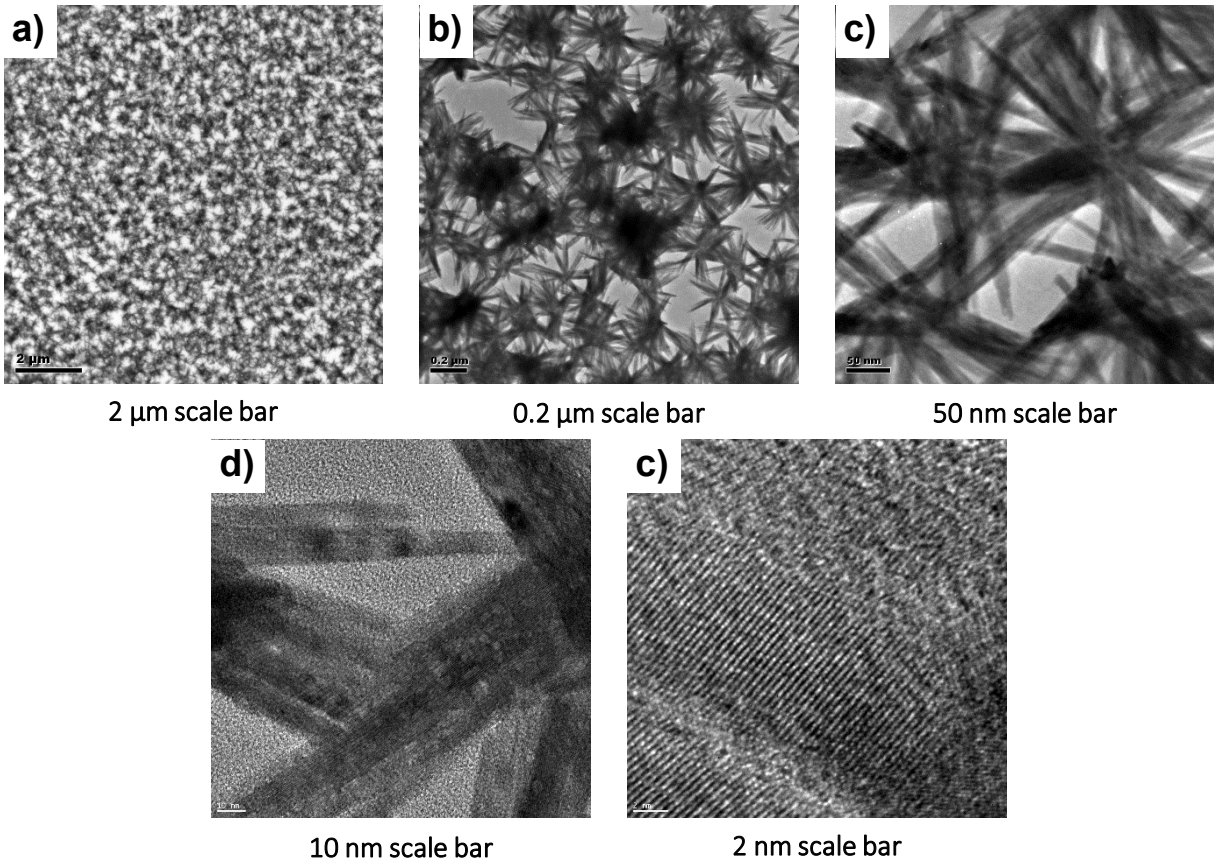



*Figure 5.2 - Transmission electron microscopy (TEM) images of typical PS/$Bi_2S_3$ films at different levels of magnification. Images (a-c) were taken by myself using the Jeol 2000 TEM (further details in Chapter 3) and (d,e) were kindly provided by Shu Chen from the Materials Department, Imperial College London using a Titan electron microscope.*

After characterising the presence of $Bi_2S_3$ with reasonably sized crystals, transmission electron microscopy (TEM) was used to image the films and see how they compared to previously observed morphologies. Figure 5.2 shows these TEM images, with (a-c) taken of the same PS/$Bi_2S_3$ blend film at a 1:1 volume ratio at different levels of magnification. Figure 5.2d and e are taken of a different, but identically produced, film using a higher powered instrument. In contrast to the previous morphologies observed for CdS and $Sb_2S_3$, the images revealed a relatively regular array of needles, seemingly emanating outwards from a central point. The individual needles are approximately 10 - 35 nm in diameter with a length of ~150 nm. The diameter of the needles corresponds roughly to the mean particle size estimated from the Scherrer equation, which suggests that the needles themselves are not comprised of a single crystal and therefore there must be a significant number of grain boundaries down the length of the needles. Figure 5.2e highlights the occurrence of crystalline domains, as the lattice fringes can be made out, perpendicular to the length of the needle. The presence of grain boundaries is not ideal for charge transport but transport still occurs between discrete quantum dots, so reasonable electron mobilities are still possible in this system. A more pressing concern is the size of the structures, with the needles being ~150 nm in length and each structure comprising of several of these needles sprouting from a central point, each cluster is approximately 300 nm in diameter. With typical hybrid

solar cells having an active layer thickness of ~100 nm, a parameter mainly limited by the mobility of hole carriers in the organic polymer, the active layer thickness in photovoltaic devices will have to be thicker than average in order to prevent the devices from short-circuiting through a single $Bi_2S_3$ structure.

Despite the large crystal sizes observed in the TEM images of Figure 5.2 the same fabrication method was applied to more relevant organic polymers that could potentially act as a hole transporting material in this system. P3HT was chosen, as it is the most common polymer from all previous work, along with F8TAA (See Figure 5.3b). F8TAA was chosen as, with a lot of the previous work, it was observed that the hole transfer from the inorganic component to the organic polymer was a more efficient process than the converse electron transfer reaction. This system, due to the broad absorption range $Bi_2S_3$, allowed for the use of a relatively high band gap material that's primary purpose would be to transport holes, but wouldn't screen the absorption of the inorganic phase, a problem that was seen for P3HT with $Sb_2S_3$.[18] The precursor with a longer ligand moiety was also used, to investigate if this had a similar effect on the domain size, as was previously observed for CdS or $Sb_2S_3$ (Chapter 4).

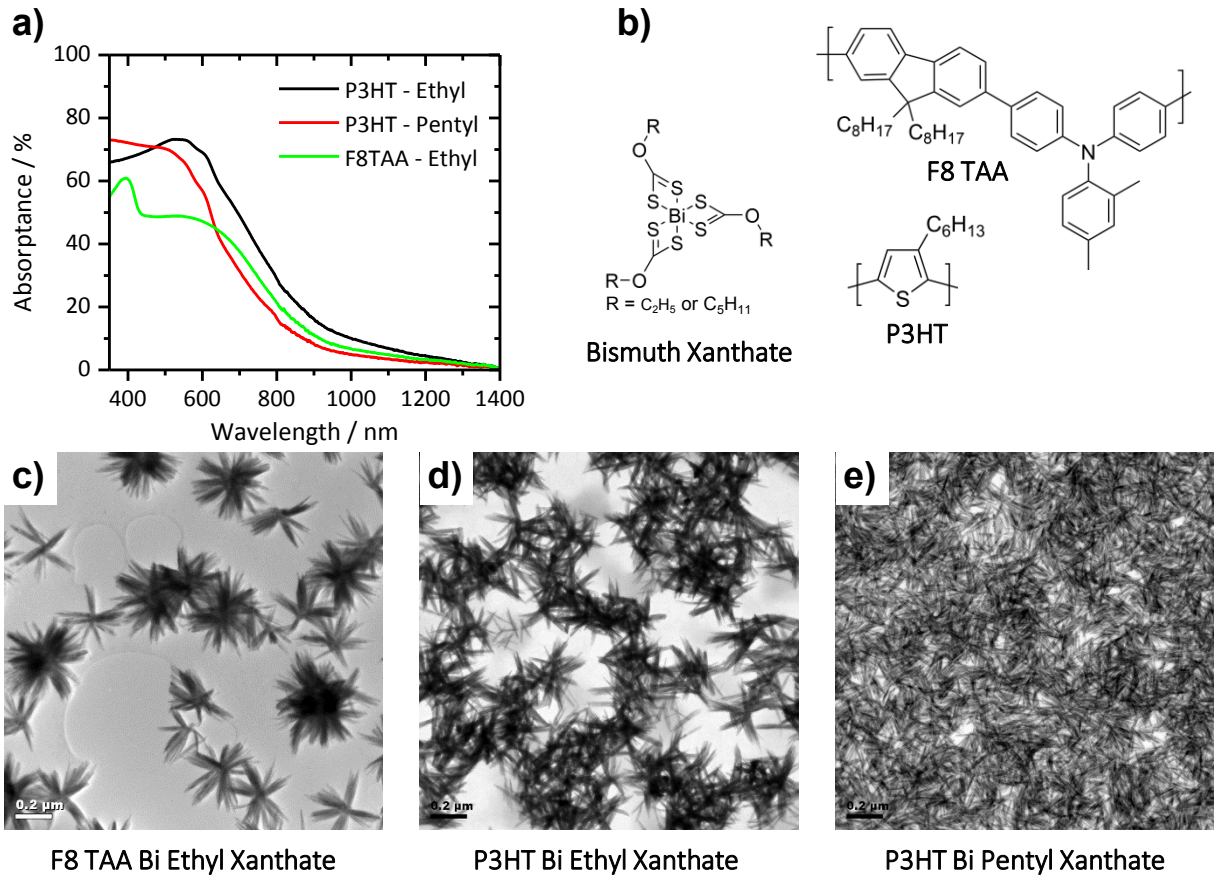



*Figure 5.3 - UV-Vis absorptance spectra of three different polymer/$Bi_2S_3$ blends. b) Structures of P3HT, F8TAA and $BiEX_3$/$BiPX_3$. (c-e) TEM images of the same three blends as in a) at the same level of magnification.*

The absorptance spectra of the three systems can be seen in Figure 5.3a. All three systems have an absorption profile that is dominated by the absorption of $Bi_2S_3$, with some small peaks at 520, 550 and 600 nm, due to P3HT and a small peak at 400 nm due to the F8TAA. The TEM images in Figure 5.3c and d reveal that the polymer does not influence the size or shape of the $Bi_2S_3$ much. The same florets of needles are observed and their dimensions are approximately the same, still appearing to be rather large for a system of this type. Figure 5.3e however the morphology is markedly different. The film still consists of needles, which are again of the same approximate size and shape, however these needles no longer emanate from a central point. Instead, these needles lie flat relative to the substrate and are well dispersed. The reasons for this observed different morphology are unknown, but it could be speculated that the florets observed using the ethyl xanthate are generated by the rods growing from a seed point. These seed points could be due to small amounts xanthate precursor that is already decomposed in solution before spin coating. The $BiEX_3$ precursor is unstable in solution and will discolour, presumably due to partial decomposition. Discolouration occurs if the solution is left at room temperature stirring for over an hour or so, or even quicker if a small amount of heat is used (50°C). The same was not observed for the $BiPX_3$, with the solution colour remaining constant for several days. It is therefore reasonable to assume that the $BiPX_3$ is more stable under the conditions used. As a result, the films made from the $BiPX_3$ may not contain as many, if any, seed points in the as spun film and as a result the decomposition occurs evenly throughout the film and not from these seed points, when the film is annealed. With the P3HT/$Sb_2S_3$ system the presence of the inorganic component prior to the blend decomposition had a large effect on the final film. It is reasonable to assume that this is also possible here.

After characterisation of the $Bi_2S_3$ with appropriate organic polymers the focus shifted to study the ability of these BHJs to photogenerate charges. Charge transfer is typically tested using photoluminescence spectroscopy (PL) and indeed this method was used in Chapter 4. However, this experiment usually follows that an emissive polymer is optically excited and the degree of emission observed from a blend film in comparison to neat polymer film is used as an indication of the level of quenching at an interface and from this the charge transfer efficiency is inferred. In this system the P3HT cannot be solely excited, as its absorption is completely overlapped with that of $Bi_2S_3$. Upon addition of the electron acceptor the emission will reduce due to the competing absorption of the $Bi_2S_3$. It is therefore difficult to resolve the emission from P3HT absorption alone. More importantly, there is the conceptual problem that $Bi_2S_3$ is no longer being considered as purely an electron acceptor. The $Bi_2S_3$ is now acting as the main absorbing component of the system and hole transfer is competing with the electron transfer. It would be possible to solely excite $Bi_2S_3$ however experiments performed showed

that no photoluminescence was observed from the $Bi_2S_3$, so the degree of quenching of at the polymer/$Bi_2S_3$ interface cannot be measured.

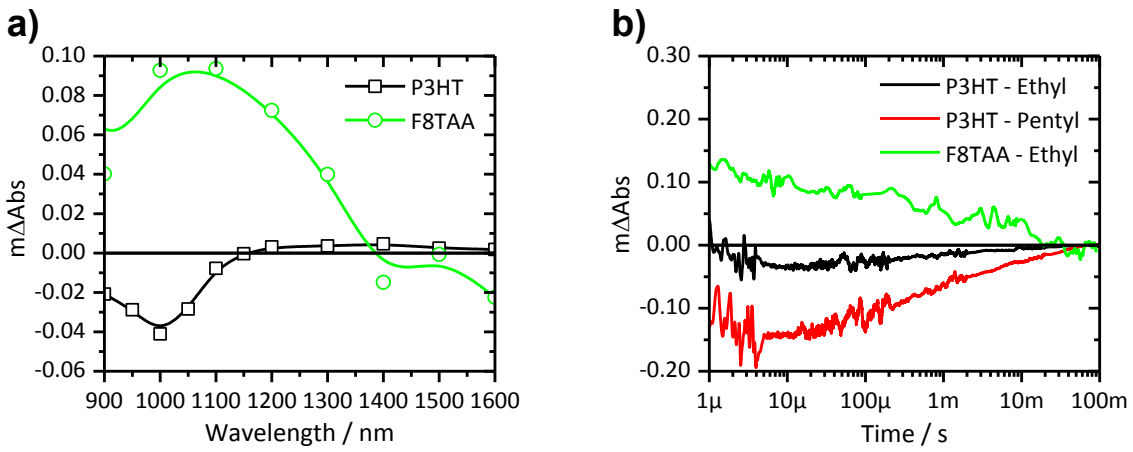



*Figure 5.4 - a) Transient absorption spectra of P3HT (black) and F8TAA (green) blended with $Bi_2S_3$ and exciting just the $Bi_2S_3$ by exciting at 700 nm. b) Transient absorption decays at 1000 nm for the same blend films. Are signals are scaled by the amount of pump light absorbed.*

Transient absorption spectroscopy (TAS) was used to test these BHJs efficiency at photogenerating charges. The results of this TAS can be seen in Figure 5.4. Considering first the spectrum of the P3HT/$Bi_2S_3$ blend (Figure 5.4a (black)) it can be see that, in contrast to previous experiments, a negative signal is observed, with a peak around 1000 nm. This bleach is likely to be due to the depopulation of the ground-state of $Bi_2S_3$, which was seen in Figure 5.3a to have an onset of around 950 – 1000 nm. This negative signal is therefore masking any possible positive signal that is being caused by P3HT polarons. The blend with F8TAA appears to have a broad weak positive signal with a peak at 1000 nm also, the difference in this case being that the superposition of the positive polaron peak and the bleach results in an overall positive signal. The decay kinetics of the three systems are shown in Figure 5.4b.

First considering the black and red traces, representing the P3HT/$Bi_2S_3$ blends fabricated with ethyl and pentyl xanthates respectively, a negative decay for both is observed. These decays are both quite long lived compared to P3HT/CdS system measured in Chapter 4. Although the observed signal is not the polaron, a reduction in ground state can be used to infer that some charge separation has occurred. The sample made from the pentyl xanthate has a considerably larger signal than the equivalent ethyl one, meaning that less of $Bi_2S_3$ is in the ground state. As both systems contain the same amount of $Bi_2S_3$ it can be inferred that more charge separation has occurred in the pentyl case. It also appears that in both samples there is an observable increase in the amplitude of the bleach that plateaus at approximately 10 µs. The most likely reason for this shape is that the lifetimes of the positive signal and the bleach signal, that are superimposed to give the overall trace, are different. The decay of the positive

polaron signal is possibly a fast process that has completely decayed by 10 µs and the bleach signal is long lived, giving an overall $t_{1/2}$ of ~0.75 ms in the case of the pentyl sample.

The F8TAA sample appears to have a reasonable positive signal that is very long lived, with a $t_{1/2}$ of ~0.45 ms. In this case there is a net positive signal, either because the extinction coefficient of the F8TAA polaron is higher than that of the P3HT polaron, or perhaps because the lifetime of the hole polaron is much longer lived. The desire to have a highly absorbing heterojunction makes this system very difficult to study spectroscopically. Although there appears to be some long lived species that are photo-induced, their nature is hard to characterise due to the overlap between two signals. As a result, attempting to optimise full photovoltaic devices seems to be the easiest way to ascertain the effectiveness of these non-toxic heterojunctions.

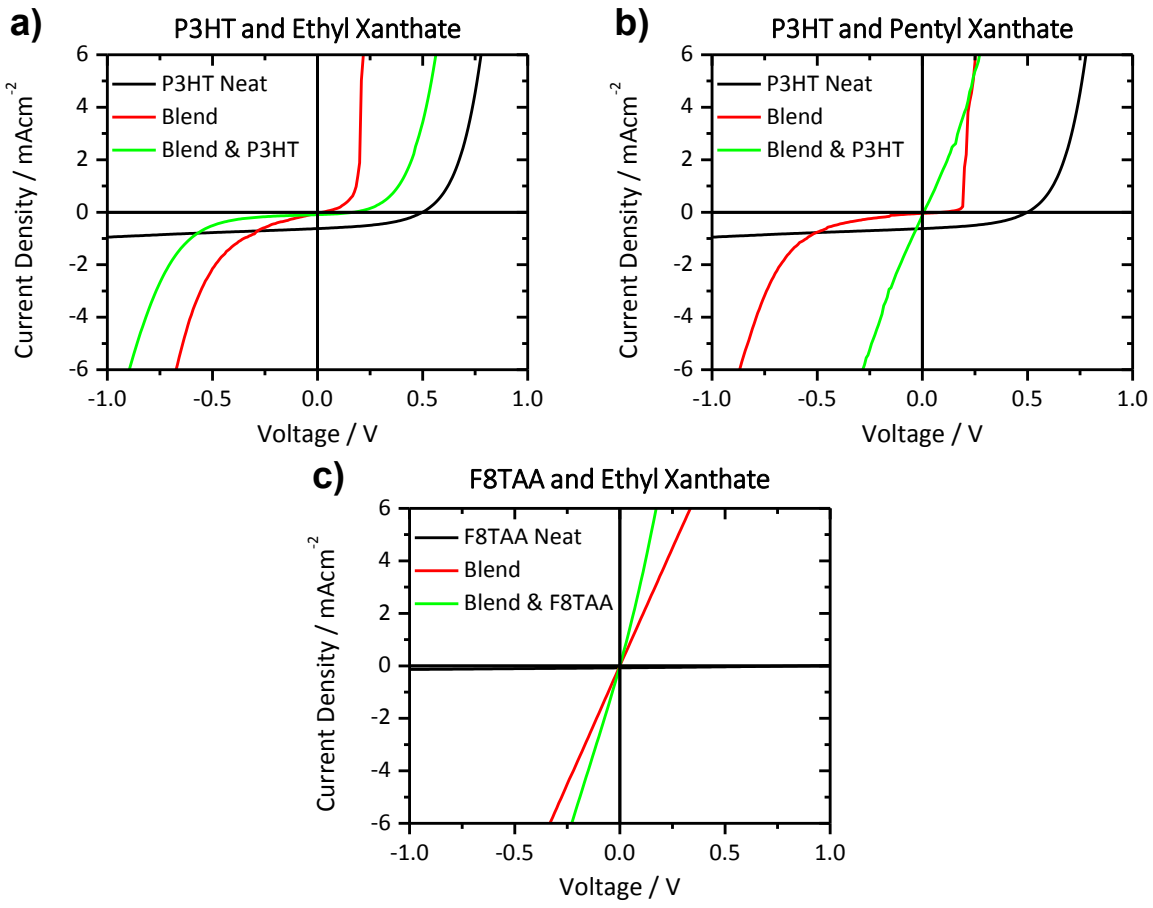



*Figure 5.5 - Current voltage measurements in the light of P3HT/$Bi_2S_3$ devices with (green) and without (red) a thin polymer blocking layer compared to a neat polymer active layer (black). Devices are shown fabricated with P3HT using the bismuth ethyl xanthate precursor a) and the pentyl xanthate b) and also using F8TAA with the bismuth ethyl xanthate c).*

Figure 5.5 shows the optimised devices based on the BHJs that have been presented previously in this chapter. Many parameters were altered during the optimisation process, including, but not limited to: active layer thickness, ratio of organic and inorganic components within the active layer, annealing temperature of the active layer, sulfide seed layer material, electron selective metal oxide layer

material, hole selective layer material, polymer blocking layer, top contact metal and device architecture. The devices shown are of an inverted structure with the configuration ITO/ZnO/CdS/Polymer:$Bi_2S_3$/(polymer/)$MoO_3$/Ag. Apart from the obvious lack of performance, one of the main disappointments with these devices was the requirement of a CdS layer to maintain even the small level of performance observed. The CdS layer was required in order to achieve a consistent completely coated film, but in doing so negates the aim of this body of work. Had these devices been more successful, the first goal would have been to investigate ways in which the devices could be processed without this layer.

Considering first Figure 5.5a, the black line represents the control device, where there is no blend and the charge generating junction is the flat interface between the CdS seed layer and a thin P3HT layer. When this P3HT layer is replaced by the blend containing approximately a 1:1 volume ratio of $Bi_2S_3$ and P3HT (red) the device is seen to lose almost all function. The $J_{SC}$ and $V_{OC}$ are massively reduced and a large leakage current is introduced. This leakage is possibly due to the spikey structures of $Bi_2S_3$ growing out of the polymer and bridging between both electrodes. In an attempt to stop this, a layer of neat P3HT was introduced (green), however the leakage is only seen to reduce slightly and still the performance is well below that of the neat polymer. In Figure 5.5b the blend device fabricated using the pentyl xanthate looks very much the same as the equivalent device in Figure 5.5a. This is slightly surprising as the morphology observed in the TEM images appeared to be much more 2D in comparison to the ethyl films and so short-circuiting didn't look as likely. In contrast however, the effect of the addition of the polymer top layer is markedly different. This layer seems to remove all diode behaviour and the device appears to behave like a resistor. In this case this is perhaps due to even more shorting of the needles between the electrodes, due to the arrangement of the needles with the blend. The polymer top layers are spin coated dynamically on top of the blends using the same solvent and so some re-dissolving of the organic part of the active layer is likely. In the pentyl case where the $Bi_2S_3$ needles appear to be lying flat on the substrate the P3HT is perhaps more easily washed off by the top polymer layer than in the ethyl case, where a more complex 3D network is formed that can perhaps hold on to the polymer more effectively. In Figure 5.5c, where the wide band gap F8TAA polymer has been used, the neat polymer control shows barely any diode behaviour and when a blend is used, with or without a top polymer blocking layer, the devices are completely short-circuited. The poor performance in the control is perhaps due to a very low mobility of this batch of F8TAA and the high level of shorting is again, possibly due to a connection of the $Bi_2S_3$ needles between the electrodes, but also due to holes that form in the polymer that can be seen in the TEM images. The characteristic parameters of these cells are tabulated in Table 5.1 for posterity.

*Table 5.1 - Characteristic parameters of the devices shown in Figure 5.5. *The numerical values recorded are stored to 6 decimal places, so the values of 0 are <5x10$^{-7}$.*

| Materials | Architecture | PCE / % | $J_{sc}$ / mAcm$^{-2}$ | $V_{oc}$ / V | FF |
|---|---|---|---|---|---|
| P3HT & Ethyl Xanthate | Neat Polymer | 0.14 | 0.62 | 0.50 | 0.44 |
| | Blend | 0.00021 | 0.039 | 0.023 | 0.23 |
| | Blend & Polymer Top Layer | 0.0056 | 0.093 | 0.17 | 0.35 |
| P3HT & Pentyl Xanthate | Blend | 0.0014 | 0.043 | 0.10 | 0.32 |
| | Blend & Polymer Top Layer | 0.00023 | 0.12 | 0.0068 | 0.27 |
| F8TAA & Ethyl Xanthate | Neat Polymer | 0.019 | 0.076 | 0.91 | 0.27 |
| | Blend | 0.00* | 0.0032 | 0.00011 | 0.00* |
| | Blend & Polymer Top Layer | 0.00* | 0.0020 | 0.00011 | 0.00* |

The performance of these blend devices is obviously rather disappointing and the use of $Bi_2S_3$ in solar cells requires a different approach. To this end an approach similar to that of O'Mahony *et* al., with their processing technique of $Sb_2S_3$,[18] was used and $Bi_2S_3$ mesostructures were generated using the $BiEX_3$ precursor. The results of these experiments are presented in the following section.

## Solution-processed Mesoscopic Polymer:$Bi_2S_3$ Photoactive Layers

There are several reasons why an alternative two-stepped approach has the potential to improve these polymer/$Bi_2S_3$ solar cells. Firstly, the low temperature constraints imposed by the low stability of the organic component are circumvented, allowing for the $Bi_2S_3$ phase to be processed at a higher temperature, something that for $Sb_2S_3$ has led to a more crystalline product and could potentially improve properties such as the charge transport in this system.[18] Secondly, by depositing the polymer in a second step, after the $Bi_2S_3$ has been formed, there should be less problems with short-circuiting in the device and polymer top layer will not partially dissolve the layer underneath. Thirdly, the two-step process will allow access to the $Bi_2S_3$ surface and there will be scope to modify the polymer/inorganic interface, something that has been shown in the literature to be highly important for the optimisation of performance in hybrid solar cells.[19-21]

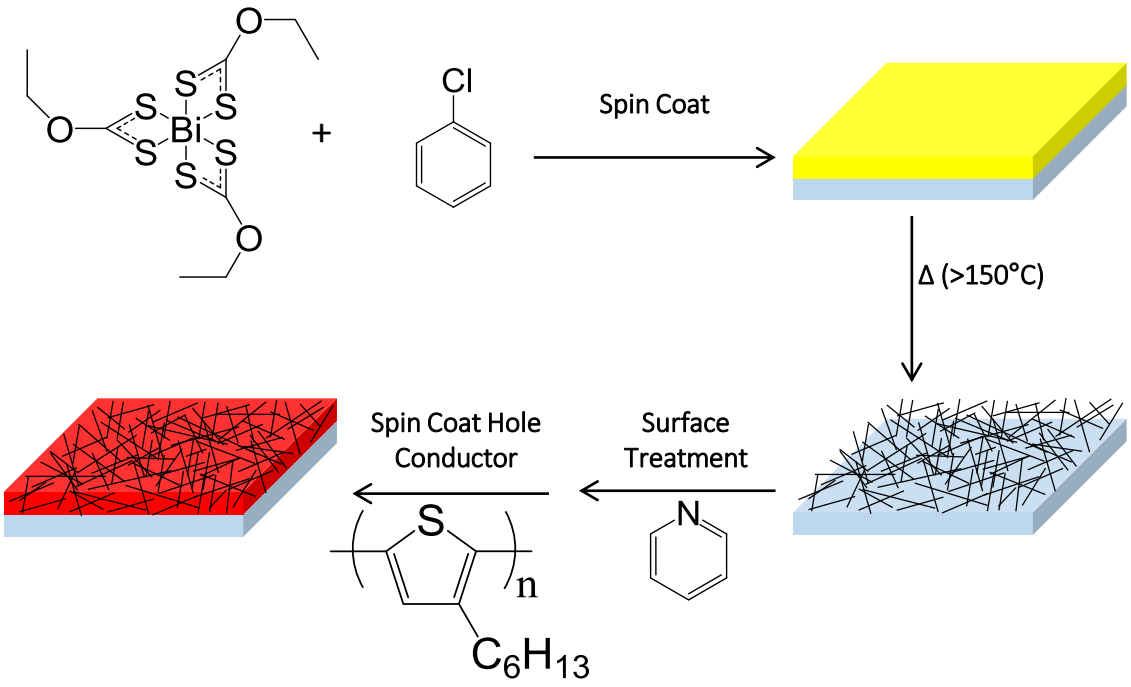



*Figure 5.6 - Schematic diagram of heterojunction formation, showing the formation of the mesoporous absorbing layer after the spin coating and annealing of a soluble bismuth xanthate precursor ($BiEX_3$), followed by a surface treatment and filling of the pores with a hole conducting polymer.*

The fabrication steps for the preparation of the mesoporous $Bi_2S_3$ films are depicted in Figure 5.6. The $BiEX_3$ precursor is first spin-coated onto a ZnO coated glass substrate from a chlorobenzene solution and then annealed in a nitrogen environment at moderate temperatures (>150°C). Films are then treated with pyridine, a ligand typically used with nanoparticles to passivate surface traps,[22] followed by the spin coating of the semiconducting polymer P3HT and finally a thermal anneal (160°C). The amount of P3HT used was such that as small a standing layer of P3HT was deposited on top of the

mesoporous structures as possible whilst still having full coverage; to best mimic a potential device structure.

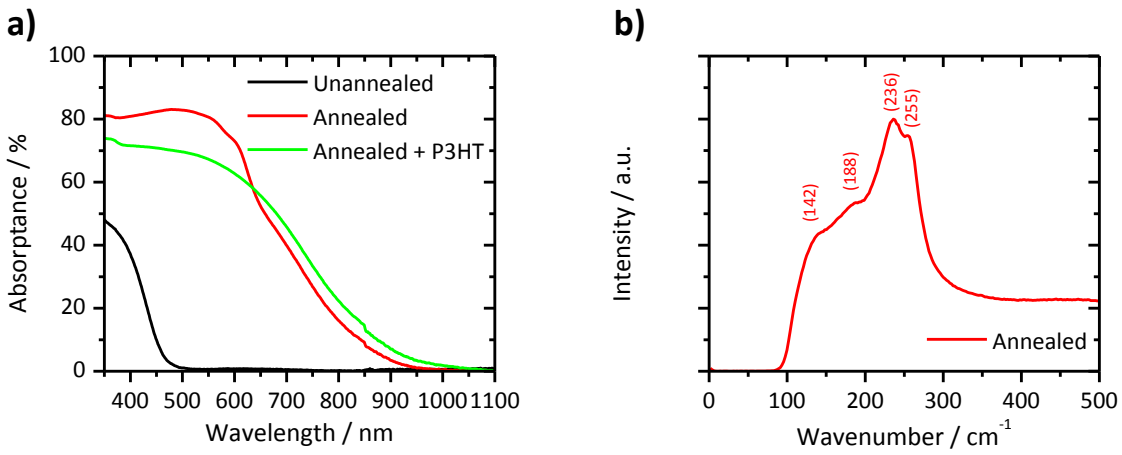



*Figure 5.7 - a) Absorptance of a thin film of spin coated bismuth xanthate precursor (black), the resulting $Bi_2S_3$ films after annealing (red) and the annealed film infiltrated with P3HT (green). b) Raman spectrum of a typical $Bi_2S_3$ film after annealing.*

The absorptance of a typical film after annealing can be seen in Figure 5.7a. The $Bi_2S_3$ films are highly absorbing across the visible range of the spectrum and extending out to almost 1000 nm, as was observed with the previous blend films. The Raman spectrum of a typical film is shown in Figure 5.7b and the results look remarkably similar to those obtained with the blends. This spectrum again confirms the presence of $Bi_2S_3$ as the vibrational modes at 188, 236 and 255 $cm^{-1}$ are again in agreement with literature values.[17]

Figure 5.8 shows scanning electron microscopy (SEM) images of these mesoscopic $Bi_2S_3$ films. Firstly, Figure 5.8a shows a top down image of a typical mesoscopic film. The films consist of an array of disorganised needles with dimensions of approximately 50 x 500 nm. This open structure appears ideal to be filled with a hole conducting polymer, having a high surface area whilst still retaining straight pathways to the flat oxide layer. A cross-sectional image of this same film is shown in Figure 5.8b and allows the thickness of the mesoscopic layers to be approximated at around 200 nm. This thickness is around the length scale of the other hybrid devices in this thesis, so the dimensions appear closer, than the *in-situ* approach, to an optimum architecture. Upon inspection of this cross section it is also apparent that the straight pathways are not perhaps well connected to the oxide under layer. The needles appear to lie horizontally on the surface rather than protrude outwards to give the often drawn idealised BHJ comb-like morphology. The horizontal alignment does, however, appear like it will not cause the short-circuiting problems that were observed using the *in-situ* method. Figure 5.8c-f show SEMs of films annealed at a range of temperatures at a lower loading level than a typical film, chosen to better view the effect that changing temperature has on the morphology. The change with temperature is a very subtle one, but can be clearly seen when comparing the two extremes. Comparing

Figure 5.8c (160°C) and f (300°C) the needles appear to increase in thickness slightly, when a higher annealing temperature is used. Due to the fact that the same amount of precursor was used in each case, this has the effect of a reduction in coverage. Indirectly this means that the surface area of the mesostructures annealed at higher temperatures is less than the lower temperature films. As the annealing temperature is increased the needles also appear to change in their overall look, with a change occurring from needles with sharp edges in the 160°C film to more smooth looking needles with rounded edges.

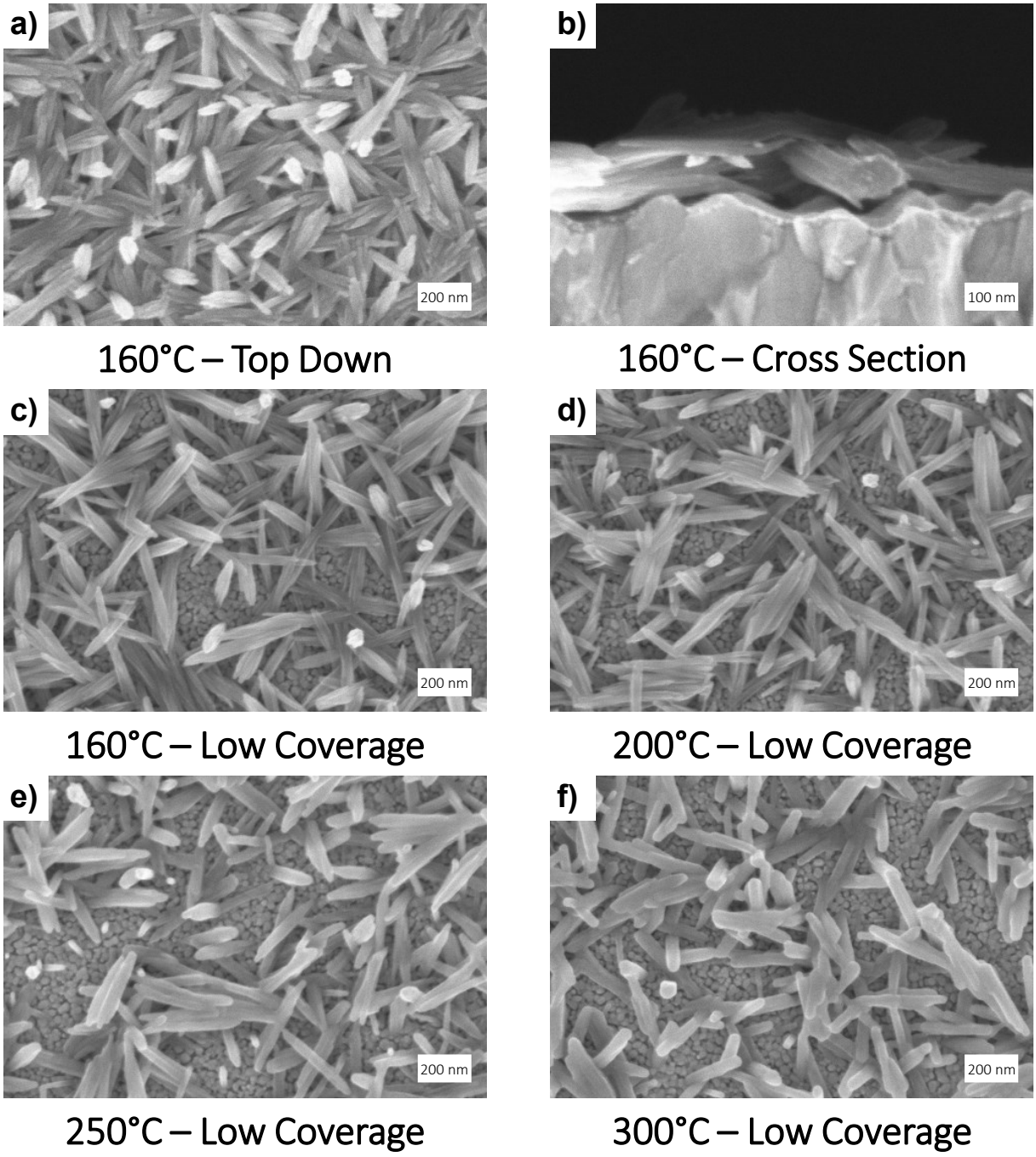



*Figure 5.8 - Scanning electron microscopy (SEM) images of the mesostructured $Bi_2S_3$ films on a flat ZnO layer. a) Top down image of a typical film used for further measurements. b) Cross sectional image of the same film as in a). (c-f) Top down images of films with a lower coverage of $Bi_2S_3$ and annealed at different temperatures.*

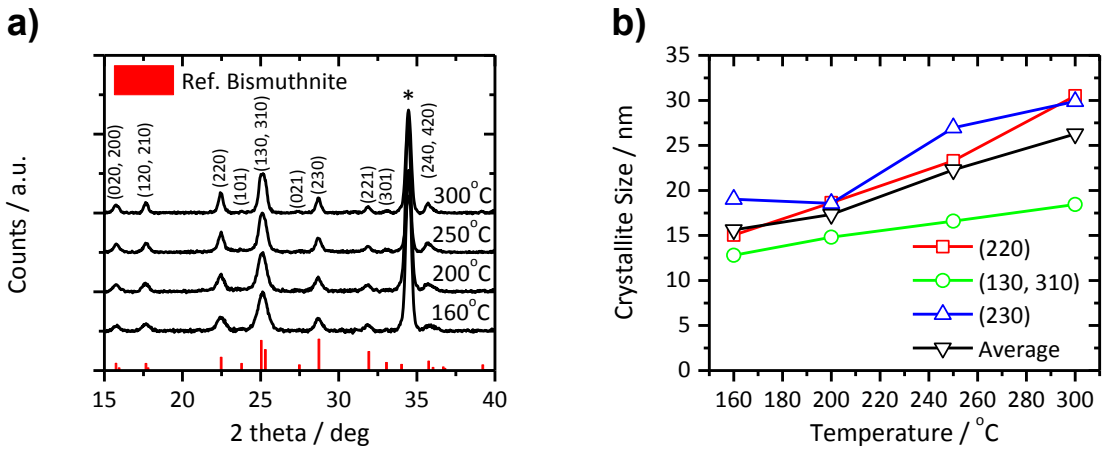



*Figure 5.9 - a) X-ray diffraction (XRD) patterns of mesoscopic $Bi_2S_3$ films annealed at a range of temperatures, with a bismuthinite references pattern (01-075-1306). The large peak labelled with an asterisk corresponds to the ZnO underlayer. b) Average crystallite size for each of the films calculated using the Scherrer equation. The crystal size has been measured for 3 different peaks and is also given as an average.*

XRD was performed on the samples to further confirm the presence of $Bi_2S_3$ and to analyse the crystallinity of the films produced. Figure 5.9a shows the XRD diffraction pattern for typical films annealed at 160, 200, 250 and 300°C, along with the reference pattern for bismuthinite (01-075-1306). Three of the peaks were analysed using the Scherrer equation in order to get an idea of the average crystallite size, namely the (220), (130, 310) and (230) peaks. The (220) and (230) were fitted with a single Gaussian peak and the (130, 310) with the combination of two. The results of this analysis are shown in Figure 5.9b for the range of decomposition temperatures. The $Bi_2S_3$ formed is highly crystalline, with an average particle size of 15.6 nm, after annealing at a relatively low temperature of 160°C. As the temperature is increased the crystallite size generally increases in all the planes measured, with a doubling of annealing temperature causing the average crystallite size to double as well. Comparing these approximations to the SEM image in Figure 5.8., it is clear that these needles are not a single crystal and are comprised of several smaller crystallites as was observed for the *in-situ* case. It is pertinent to note that the average crystallite size observed herein is large and therefore not in the regime where quantum confinement effects are expected to be observed. This is supported by the lack of shift in the absorption onset with changing crystallite size Figure 5.10. Moreover, it has been previously reported that quantum confinement effects are only observed for particles of $Bi_2S_3$ smaller than 5 nm.[23,24]

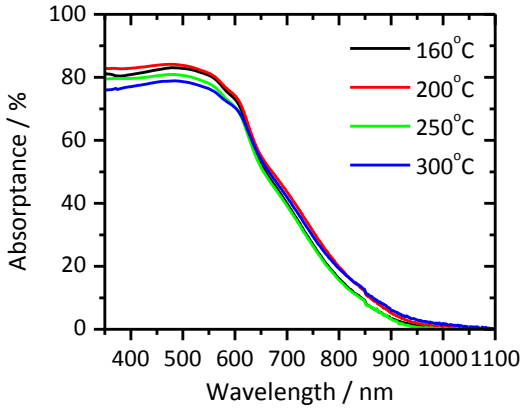



*Figure 5.10 - UV-Vis absorptance of mesoscopic films annealed at the range of temperatures in this study.*

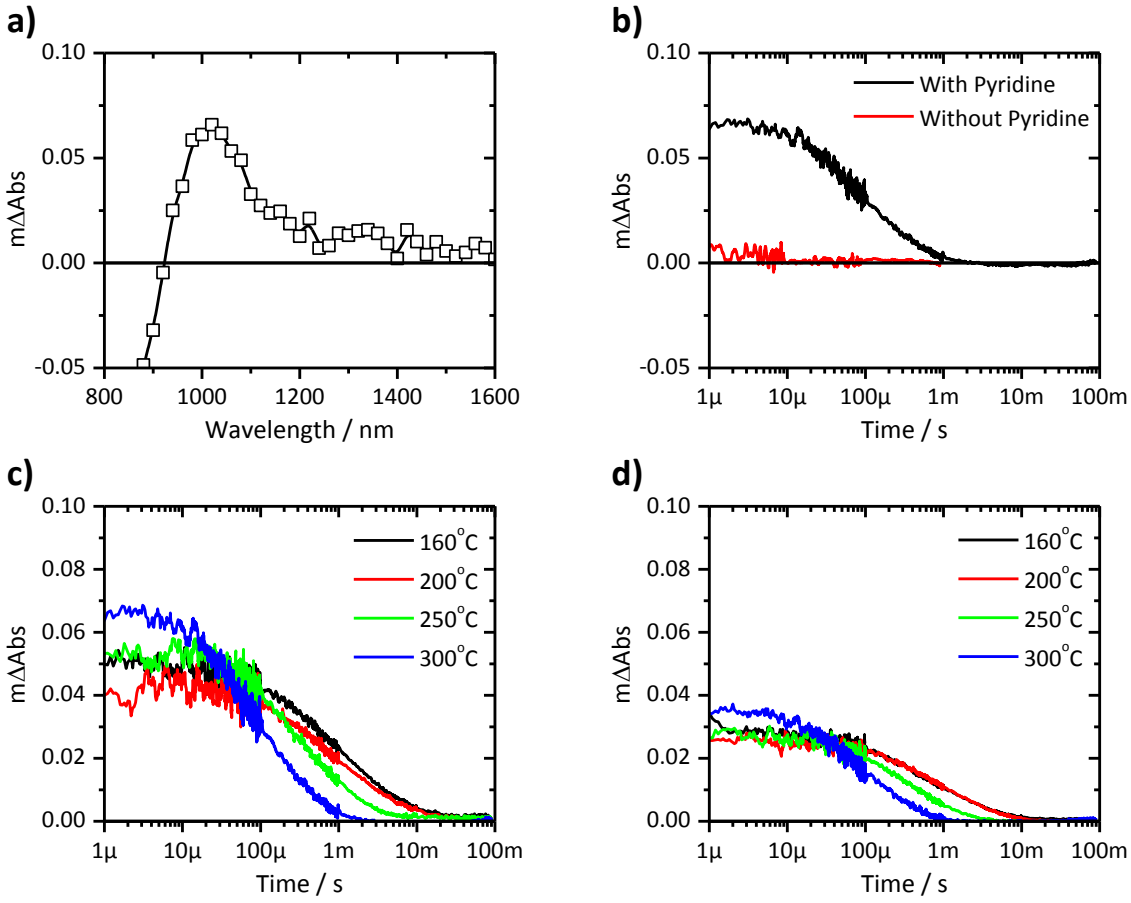



*Figure 5.11 - a) Transient absorption spectrum at 1 µs after excitation of a mesoscopic film infiltrated with P3HT after a surface treatment with pyridine. b) Transient absorption decay of the same film with and without the pyridine treatment at a probe wavelength of 980 nm. c) Transient decays for films annealed at a range of temperatures after 700 nm excitation and d) 510 nm excitation. All signals are scaled by the amount of pump light absorbed.*

The effectiveness of these novel non-toxic mesostructures at photogenerating charges was then investigated by infiltrating the porous needle network with the semiconducting polymer P3HT and the usual method of TAS was employed. A TAS spectrum was first obtained by exciting the sample using a wavelength of 700 nm, which is only absorbed by the $Bi_2S_3$ phase within the hybrid film, and probing

the photoinduced change in absorbance over a range of wavelengths (Figure 5.11a). A peak is observed at ~1000 nm, where P3HT hole polarons typically absorb.[25] At wavelengths below 1000 nm, a bleach is observed, which is likely to be due to depopulation of the ground-state of $Bi_2S_3$. This bleach probably masks the expected second peak of P3HT previously observed at ~800 nm and may also overlap slightly with the P3HT polaron peak at 1000 nm, reducing the magnitude of the signal observed. The relative magnitudes of signals in this case are therefore more important than the actual size, as the apparent yield of P3HT polarons will be consistently reduced by the $Bi_2S_3$ ground state bleach.

As mentioned in the experimental section, before infiltration with the polymer, the films were treated with pyridine, via submersion in pyridine overnight. The chemistry of this process has not been studied, but the effect on the charge generation with and without the treatment can be seen in Figure 5.11b. Here the TAS decay following the peak transient signal at 980 nm is measured and it can be seen that without the pyridine treatment no signal is observed at all. With the pyridine treatment a long lived decay is observed, with a lifetime longer than is typically observed in the hybrid systems measured in this project with CdS and $Sb_2S_3$, but also longer compared to the blend $Bi_2S_3$ films studied earlier in this chapter. The signal is however, much smaller than what was observed in the CdS and $Sb_2S_3$ systems. This could be due to a lower charge generation efficiency or could be due to the superposition of the bleach signal, reducing the overall amplitude. Figure 5.11c shows the TAS decays for a range of temperatures where only the $Bi_2S_3$ is being excited. Although the amplitudes of the lowest three temperatures are approximately similar, the 300°C sample is slightly higher in amplitude, which indicates a higher number of charges in the film 1 µs after photoexcitation. Secondly, as the annealing temperature is increased the rate of decay and therefore the rate of recombination is also increased. This change in lifetime is approximately an order of magnitude different for the 160°C and 300°C samples, with these samples having a $t_{1/2}$ (1 µs) of 760 µs and 72 µs respectively. The reasons for these observations are not completely understood but speculatively they are likely to be associated with the changing crystallinity of the samples. It has previously shown in the group that the degree of crystallinity in one component of the heterojunction directly affects the yield of long-lived charges generated at the interface, with an increase in crystallinity resulting in a higher yield of charges and a switching on of charge generation in systems with no driving force for separation.[26] In this instance it is also possible that the increase in the average crystallite size and quality is causing the increase in yield of charges due to the effect of an increased delocalisation of charges generated in the $Bi_2S_3$. The change in the lifetime of charges can be explained by considering the difference in mobility of electrons in the $Bi_2S_3$ after hole transfer to the P3HT, caused by a difference in crystallinity. $Bi_2S_3$ has previously been shown to have a high electron mobility[27] and an increase in crystallinity is likely to result in a higher mobility. An increased mobility of electrons in $Bi_2S_3$ could result in an increase in the rate of non-geminate recombination after

charge separation, due to the electrons having a greater ability to diffuse through the film. Such behaviour is often observed in all–organic photovoltaic systems.[28]

In Figure 5.11d, where both the P3HT and $Bi_2S_3$ are being excited, the signal intensities are seen to be lower than in the previous case, mΔAbs = 0.037 vs 0.067 (for the 300°C sample), but with similar lifetime, $t_{1/2}$(1 µs) = 73 vs 72 µs. This is an indication that there is very little charge generation from electron injection into the $Bi_2S_3$ from the P3HT in comparison to charge generation from the converse hole injection. The samples were excited in both cases through the P3HT layer, so the lack of generation from the polymer could be due to the pores filled with P3HT being too large to allow for exciton diffusion to the interface. Alternatively, the electron transfer from P3HT to the $Bi_2S_3$ could be inefficient in this system. It is unclear which of these explanations is more valid, however, this observation reiterates the need to find a wider band gap polymer that doesn't filter light absorption by the inorganic component and hinder the maximum currents possible from these types of devices, as previously reported.[18] Attempts in this system to use such a polymer proved unsuccessful, with F8TAA not showing any TAS signal as it did in the blend systems.

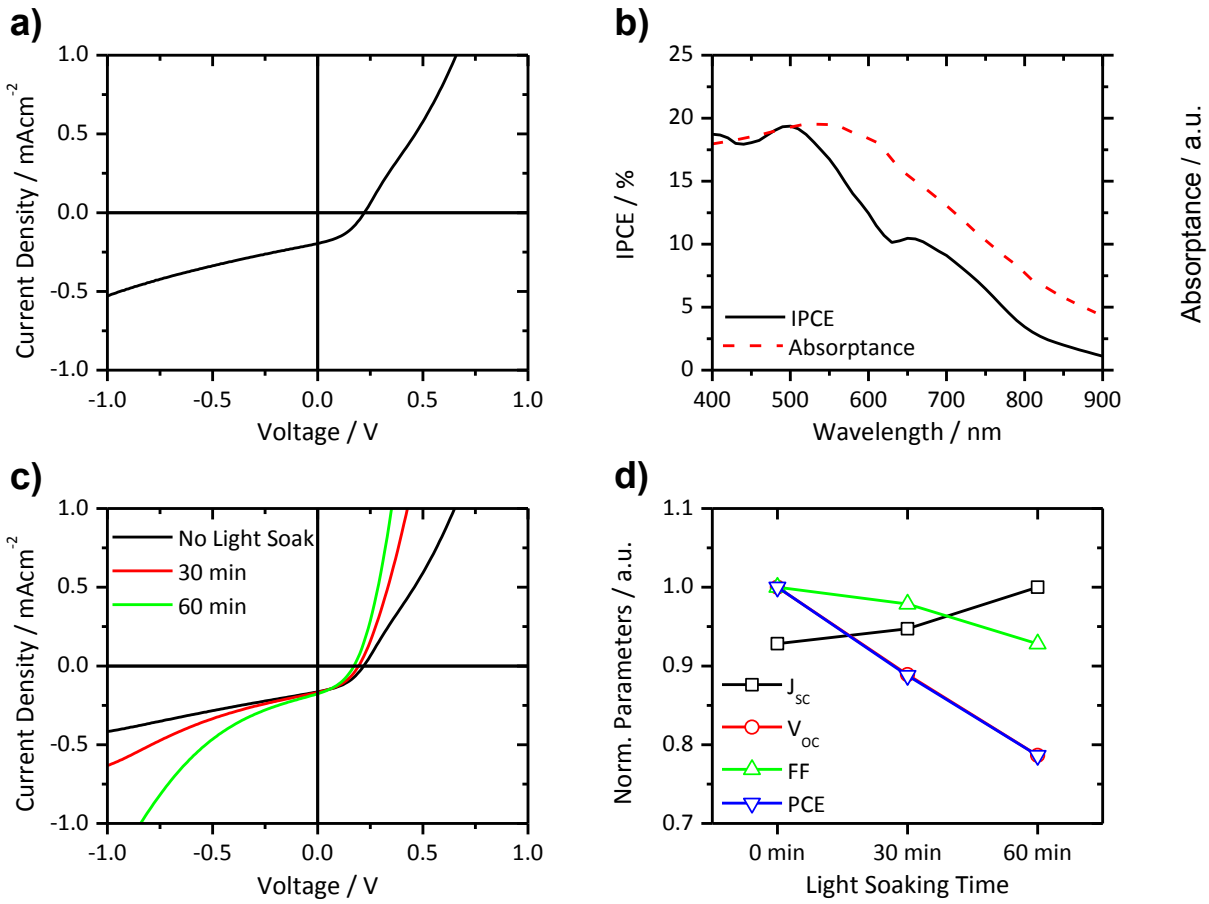



*Figure 5.12 - a) Current voltage plot of the most efficient device in the light. b) IPCE measurement of the device shown in a) with the absorption profile of the device overlaid (red dash). c) Current-voltage plots of a device being light soaked, with the trend in the characteristic parameters shown in d).*

Finally, a series of devices were produced with the same architecture as the heterojunctions studied but with $MoO_3$ and silver evaporated on top, giving a complete device structure of ITO/ZnO/$Bi_2S_3$(pyr)/P3HT/$MoO_3$/Ag. The device with the highest PCE is given in Figure 5.12a. This device has a low short circuit current of 0.018 $mAcm^{-2}$ and the $V_{OC}$ is also quite low at 0.22 V. However, typical open circuit voltages in the literature for P3HT/$Bi_2S_3$ heterjunctions are around 0.3 V.[11,29] With a performance lower than that of a neat P3HT device from the previous section it is easy to assume that perhaps the $Bi_2S_3$ is playing no part in the current generation. To check if any contribution to the photocurrent was being made by the $Bi_2S_3$, an incident photon to current efficiency (IPCE) measurement was made, the results of which can be seen in Figure 5.12b. As well as the IPCE, a scaled down absorption profile is overlaid as the red dashed line. From this data it can be seen that there is contribution from the both the $Bi_2S_3$ and the P3HT. The IPCE maximum is at 500 nm and here there is a peak due to the P3HT contribution to the photocurrent. At 400 nm and also at wavelengths higher than 650 nm the IPCE can be considered to be solely due to the $Bi_2S_3$, although the peak at 650 nm is only at an IPCE of 1%. Nevertheless, this is the first demonstration $Bi_2S_3$ fabricated from a bismuth xanthate precursor and acting as an absorber material in hybrid solar cells.

Another thing of note is the apparent “S” shape in the upper right quadrant of the current voltage plot. This is most likely due to the ZnO layer, that has been seen to require a small degree of light soaking in order to get it to function optimally. This effect has previously been linked to oxygen traps that are present in the ZnO.[30] This effect is easily removed by a small amount of light soaking, however the light soaking also in this case has the effect of degrading the device. Figure 5.12c shows a device light soaked in AM 1.5 light for an hour and the change in the characteristic device parameters is shown in Figure 5.12d. The disappearance of the double diode “S” shape happens after the first measurement and the device also immediately begins to reduce in efficiency due to mainly a drop in open circuit voltage. The fill factor also decreases slightly while the short circuit current is increased. These observations could possibly be due to an oxidation of the P3HT, which increase the mobility and allows more charges to be collected across the relatively thick device, but comes at the expense of an increase in general device degradation, increasing the recombination.

## Conclusions

In summary, this study presents the proof of concept that bismuth xanthate complexes can be used as precursors to $Bi_2S_3$ for use in hybrid solar cells. Their use has been shown to grow needle-like structures in a solid state polymer matrix and also porous mesostructures have been created that can be infiltrated with a hole conductor. The nature of the material created in both cases has been shown to be highly crystalline, even when processed at low temperatures. Both the blends and mesostructures exhibit remarkably high absorption across the entire visible region of the spectrum.

The efficiency of these materials has been difficult to measure spectroscopically due to the large ground-state absorption, but in the mesostructured case long-lived charge separation is observed, initiated primarily by hole transfer from the mesostructure to the organic polymer. The charge transfer in the mesostructured system was seen to be highly dependent on a surface treatment of the structure with pyridine, perhaps passivating surface states on the $Bi_2S_3$ and effectively turning on the charge generation.

Devices fabricated from these two systems were inefficient to say the least, with the control neat polymer devices showing the highest power conversion efficiency in all cases. Despite this, the mesostructured devices did show a contribution to the photocurrent from the $Bi_2S_3$ as measured by the IPCE. This measurement shows that it is possible to fabricate devices using this method, and with more time and investigation into the processing, use of additives and trialling of a range of different polymers, perhaps a device with a PCE of a higher significance could be obtained.

# References


(1) *Inception.* [Film] Directed by: Christopher Nolan. USS: Warner Bros. Pictures; 2010.

(2) Ren, S.; Chang, L.-Y.; Lim, S.-K.; Zhao, J.; Smith, M.; Zhao, N.; Bulović, V.; Bawendi, M.; Gradečak, S. *Nano Lett.* 2011, *11*, 3998.

(3) Dayal, S.; Kopidakis, N.; Olson, D. C.; Ginley, D. S.; Rumbles, G. *Nano Lett.* 2009, *10*, 239.

(4) Ip, A. H.; Thon, S. M.; Hoogland, S.; Voznyy, O.; Zhitomirsky, D.; Debnath, R.; Levina, L.; Rollny, L. R.; Carey, G. H.; Fischer, A.; Kemp, K. W.; Kramer, I. J.; Ning, Z.; Labelle, A. J.; Chou, K. W.; Amassian, A.; Sargent, E. H. *Nat Nano* 2012, *7*, 577.

(5) Liu, Z.; Sun, Y.; Yuan, J.; Wei, H.; Huang, X.; Han, L.; Wang, W.; Wang, H.; Ma, W. *Adv. Mater.* 2013, *25*, 5772.

(6) Rath, T.; Edler, M.; Haas, W.; Fischereder, A.; Moscher, S.; Schenk, A.; Trattnig, R.; Sezen, M.; Mauthner, G.; Pein, A.; Meischler, D.; Bartl, K.; Saf, R.; Bansal, N.; Haque, S. A.; Hofer, F.; List, E. J. W.; Trimmel, G. *Adv. Energy Mater.* 2011, *1*, 1046.

(7) Oosterhout, S. D.; Koster, L. J. A.; van Bavel, S. S.; Loos, J.; Stenzel, O.; Thiedmann, R.; Schmidt, V.; Campo, B.; Cleij, T. J.; Lutzen, L.; Vanderzande, D.; Wienk, M. M.; Janssen, R. A. J. *Adv. Energy Mater.* 2011, *1*, 90.

(8) Lee, M. M.; Teuscher, J.; Miyasaka, T.; Murakami, T. N.; Snaith, H. J. *Science* 2012, *338*, 643.

(9) Kim, H.-S.; Lee, C.-R.; Im, J.-H.; Lee, K.-B.; Moehl, T.; Marchioro, A.; Moon, S.-J.; Humphry-Baker, R.; Yum, J.-H.; Moser, J. E.; Gratzel, M.; Park, N.-G. *Sci. Rep.* 2012, *2*.

(10) Rath, A. K.; Bernechea, M.; Martinez, L.; de Arquer, F. P. G.; Osmond, J.; Konstantatos, G. *Nat Photon* 2012, *6*, 529.

(11) Martinez, L.; Stavrinadis, A.; Higuchi, S.; Diedenhofen, S. L.; Bernechea, M.; Tajima, K.; Konstantatos, G. *PCCP* 2013, *15*, 5482.

(12) Han, Q.; Chen, J.; Yang, X.; Lu, L.; Wang, X. *J. Phys. Chem. C* 2007, *111*, 14072.

(13) Koh, Y. W.; Lai, C. S.; Du, A. Y.; Tiekink, E. R. T.; Loh, K. P. *Chem. Mater.* 2003, *15*, 4544.

(14) Sun, S.-s.; Han, Q.-f.; Wu, X.-d.; Zhu, J.-w.; Wang, X. *Mater. Lett.* 2011, *65*, 3344.

(15) Ren, Y.; Murakami, T.; Nishioka, T.; Nakashima, K.; Noda, I.; Ozaki, Y. *Macromolecules* 1999, *32*, 6307.

(16) Woods, R.; Hope, G. A. *Colloids and Surfaces A: Physicochemical and Engineering Aspects* 1998, *137*, 319.

(17) Trentelman, K. *Journal of Raman Spectroscopy* 2009, *40*, 585.

(18) O'Mahony, F. T.; Cappel, U. B.; Tokmoldin, N.; Lutz, T.; Lindblad, R.; Rensmo, H.; Haque, S. A. *Angew. Chem. Int. Ed. Engl.* 2013, *52*, 12047.

(19) Radychev, N.; Lokteva, I.; Witt, F.; Kolny-Olesiak, J.; Borchert, H.; Parisi, J. r. *J. Phys. Chem. C* 2011, *115*, 14111.

(20) Akamatsu, K.; Tsuruoka, T.; Nawafune, H. *J. Am. Chem. Soc.* 2005, *127*, 1634.

(21) Wu, Y. L.; Tok, A. I. Y.; Boey, F. Y. C.; Zeng, X. T.; Zhang, X. H. *Appl. Surf. Sci.* 2007, *253*, 5473.

(22) Lokteva, I.; Radychev, N.; Witt, F.; Borchert, H.; Parisi, J. r.; Kolny-Olesiak, J. *J. Phys. Chem. C* 2010, *114*, 12784.

(23) Riley, D. J.; Waggett, J. P.; Wijayantha, K. U. *J. Mater. Chem.* 2004, *14*, 704.

(24) Peter, L. M.; Wijayantha, K. G. U.; Riley, D. J.; Waggett, J. P. *J. Phys. Chem. B* 2003, *107*, 8378.

(25) Clarke, T. M.; Ballantyne, A. M.; Nelson, J.; Bradley, D. D. C.; Durrant, J. R. *Adv. Funct. Mater.* 2008, *18*, 4029.

(26) Bansal, N.; Reynolds, L. X.; MacLachlan, A.; Lutz, T.; Ashraf, R. S.; Zhang, W.; Nielsen, C. B.; McCulloch, I.; Rebois, D. G.; Kirchartz, T.; Hill, M. S.; Molloy, K. C.; Nelson, J.; Haque, S. A. *Sci Rep* 2013, *3*, 1531.

(27) Cantarero, A.; Martinez-Pastor, J.; Segura, A.; Chevy, A. *Phys. Rev. B* 1987, *35*, 9586.

(28) Pivrikas, A.; Österbacka, R.; Juška, G.; Arlauskas, K.; Stubb, H. *Synth. Met.* 2005, *155*, 242.

(29) Martinez, L.; Higuchi, S.; MacLachlan, A. J.; Stavrinadis, A.; Miller, N. C.; Diedenhofen, S. L.; Bernechea, M.; Sweetnam, S.; Nelson, J.; Haque, S. A.; Tajima, K.; Konstantatos, G. *Nanoscale* 2014, *6*, 10018.

(30) Manor, A.; Katz, E. A.; Tromholt, T.; Krebs, F. C. *Sol. Energy Mater. Sol. Cells* 2012, *98*, 491.

# Chapter 6

# Transient Absorption Spectroscopy of Hybrid $Bi_2S_3$ Solar Cells

*Interviewer:* *HAL, despite your enormous intellect, are you ever frustrated by your dependence on people to carry out your actions?*

*HAL:* *Not in the slightest bit. I enjoy working with people…I am putting myself to the fullest possible use. Which is all, I think, that any conscious entity can ever hope to do.*

*2001: A Space Odyssey (1968)*[1]

## Abstract

In this chapter, through a collaboration with The Institute of Photonic Sciences (ICFO), transient absorption spectroscopy (TAS) was used to study two separate organic semiconductor/$Bi_2S_3$ bulk heterojunctions (BHJs). The first of which was a poly(3-hexylthiophene-2,5-diyl (P3HT)/$Bi_2S_3$ nanoparticle blend solar cell. The charge generation yield in this system was investigated and then compared to a novel thiol-functionalised P3HT based block copolymer (P3HT-SH) that, when blended with P3HT and $Bi_2S_3$ nanoparticles, to form a ternary system, demonstrated superior photovoltaic performance in comparison to a blend of P3HT/$Bi_2S_3$. TAS showed that the electron transfer yield from the P3HT/P3HT-SH to the $Bi_2S_3$ was increased in comparison to P3HT/$Bi_2S_3$ blend, thought to be due to a combination of a finer morphology and enhanced electronic coupling between the polymer and nanoparticles. An increased electronic coupling was also demonstrated by an observed increase in quenching using solution-based photoluminescence spectroscopy. The lifetime of photogenerated charges was also observed to increase in the case of the ternary system, thought to be due to an energy cascade that could exist within the films, due to a HOMO energy offset that was measured between the P3HT-SH and P3HT. Secondly, TAS was used to obtain a better understanding of the charge transfer at several interfaces in a vertically structured $Bi_2S_3$ nanorod array that was filled with 2,2',7,7'-Tetrakis-(N,N-di-4-methoxyphenylamino)-9,9'-spirobifluorene (SPIRO). These devices showed almost no photovoltaic performance without coating the $Bi_2S_3$ rods with a small amount of $Ag_2S$. The addition of the $Ag_2S$ appeared to "switch on" the functionality of the device as well as extending the light absorption into the infra-red. TAS however, showed that the charge generation yield and lifetime without the $Ag_2S$ were approximately the same and that the lack of performance was therefore due to another factor, such as electron transport in the $Bi_2S_3$ rods.

This worked formed part of the following publications:

**Improved electronic coupling in hybrid organic-inorganic nanocomposities employing thiol-functionalized P3HT and bismuth sulfide nanocrystals** Martinez, L.; Higuchi, S.; MacLachlan, A. J.; Stavrinadis, A.; Miller, N.C.; Diedenhofen, S. L.; Bernechea, M.; Sweetnam, M.; Nelson, J.; Haque, S. A.; Tajima, K.; Konstantatos, G. *Nanoscale* **2014**, *6*, 10018.

**Solution Processed Bismuth Sulfide Nanowire Array Core/Silver Sulfide Shell Solar Cells** Cao, Y.; Bernechea, M.; Maclachlan, A. J.; Zardetto, V.; Creatore, M.; Haque, S.; Konstantatos, G. *Chemistry of Materials* **2015,** *27,* 3700.

# Introduction

As was discussed in Chapter 5, there are many reasons why $Bi_2S_3$ appears to be a promising candidate for use in hybrid photovoltaic devices. However, the previous work demonstrated that the use of xanthates did not result in devices with a high photovoltaic performance. Some of the possible reasons for this system's shortcomings came from the idea that $Bi_2S_3$ has a high degree of surface trap states.[2] The density of these trap states, and their effect on the mobility, is heavily influenced by the stoichiometry between the bismuth and the sulfur.[3] The decomposition of bismuth xanthate perhaps did not result in the required stoichiometry and the method itself currently does not facilitate the option to alter the bismuth:sulfur ratio. This chapter features two systems, both of which produced $Bi_2S_3$ using methods where the stoichiometry can be, and has been, tuned to give an optimum photovoltaic performance. The first of these systems utilised a colloidal synthesis of the nanoparticles. Here, $Bi(OAc)_3$ and hexamethyldisialthiane (HMS) were used, as the bismuth and sulfur sources, respectively.[4] The second system, is synthesised via an epitaxial chemical bath growth of $Bi_2S_3$.[5] This method also offers control over the stoichiometry of the $Bi_2S_3$ produced.

Firstly, P3HT/$Bi_2S_3$ blend solar cells, which were unsuccessfully fabricated using the xanthate method in Chapter 5, were considered. These were successfully fabricated by Martínez *et* al., with power conversion efficiencies (PCEs) of 1%.[6,7] It was thought that the PCE of these devices had not been fully maximised. One of the problems these devices present is that a large amount of the light they absorb is not utilised. A possible route to increase the photovoltaic efficiency of these systems is through the improvement of the electronic coupling, between the organic and the inorganic phases. There are a few ways in which this concept has been tackled previously in the literature. It is possible to perform a ligand exchange on the insulating ligand-capped prefabricated nanoparticles with functionalised polymers. In this method a strong coordinating group (e.g. carbodithioic acid)[8] is functionalised onto a conjugated polymer and then directly anchored onto the nanocrystals by substituting the original ligands used to synthesise the particles. This concept was employed by Liu *et* al. whereby P3HT with amino acid end-functionality was synthesised to improve the dispersion of CdSe nanorods in the P3HT matrix within P3HT/CdSe hybrid solar cells.[9] It is also possible to use bifunctional ligands that act as both the coordinating ligand to the nanoparticle, which controls the nanoparticle growth with one functional group, and with the other group, is able to graft onto a functionalised conjugated polymer. This method was used to synthesise P3HT/CdSe blends by directly grafting vinyl-terminated P3HT onto the [(4-bromophenyl)methyl]dioctylphosphine oxide (DOPO-Br)-functionalised CdSe nanoparticle surface.[10] The bifunctionalised ligand DOPO-Br contains a phosphine oxide group at one end, to anchor to the nanoparticle surface, and an arylbromide at the other end to allow for grafting process.[10] A similar

method was used by Ren *et* al. whereby CdS quantum dots were grafted onto P3HT nanowires, which resulted in a power conversion efficiency of 4.1%,[11] possibly the highest performing P3HTCdS device in the literature.

In addition to increasing the electronic coupling, a key factor in maximising the photovoltaic performance, as has been displayed in this thesis, is control over the morphology of hybrid organic/inorganic blends. One of the methods that can be employed is modification of the polymer in order to direct the morphology of the resulting spin cast film. As well as improving the electronic coupling between the polymer and nanoparticle, the amino end-functionalised P3HT discussed before has been shown to increase the photovoltaic performance of P3HT/CdSe blends by a factor of three, due to the improved morphology generated by increasing the dispersion of the nanoparticles throughout the film.[9] Also an ester-functionalised side chained P3HT has been utilised to enhance the photovoltaic performance of thin P3HT/ZnO blends by increasing the mixing between organic and inorganic phases.[12] In thicker films however, a reduction in performance was observed, put down to a lack of percolation due to too fine a morphology, similar to what was observed in Chapter 4 of the thesis, with the P3HT/CdS blends.

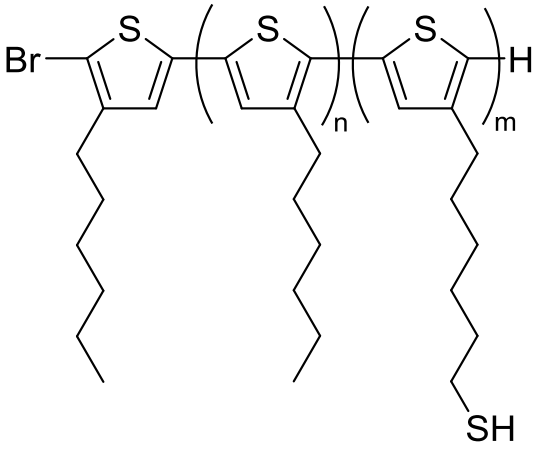



*Figure 6.1 - Chemical structure of thiol-functionalised block copolymer P3HT-SH.*

In an attempt to maximise both the electronic coupling between both the polymer and $Bi_2S_3$ and optimise the morphology of said blends, the synthesis of a thiol-functionalised block copolymer was developed based on P3HT (Figure 6.1). The structural properties and interaction with $Bi_2S_3$ were studied at ICFO using grazing angle X-ray diffraction and photoluminescence spectroscopy. The efficacy of these blends as active layers in photovoltaic devices was also studied. The section of the study that was carried out as part of this thesis was the characterisation and analysis of these heterojunctions using TAS. In doing so, a better understanding of the efficiency and mechanism of charge generation in these systems was obtained. The hypothesis that the thiol-functionalisation resulted in an increase in the charge generation yield, through the increase in electronic coupling, was also studied.

Secondly, nanostructured $Bi_2S_3$ rods grown from a flat $TiO_2$ substrate and then infiltrated by a hole conductor were studied. Throughout this thesis the concept of tailoring the morphology in order to optimise the device efficiency by finding a balance between charge generation and charge transport has been studied. The idea of the ideal bulk heterojunction is often described as a 3D comb-like structure, where one component extends into another. The logic behind this ideal structure is that an extremely fine a mixing is generated, with domain sizes such that the charge generation yield is maximised, whilst retaining perfectly percolating pathways to each electrode. One device structure that conforms to this ideal morphology is structured inorganic scaffolds filled with a semiconducting organic material.

The idea of filling structured inorganic semiconductors with polymers has been attempted for a range of materials. The method by which the structures are fabricated take two main forms, either, nanoparticles are templated to give the desired idealistic comb shape, or, pillars are grown from a flat substrate and the gaps between the pillars are filled in. Using the former concept, Wang *et* al. created a $TiO_2$ interconnected network structure using a polystyrene-block-polyethylene oxide diblock copolymer as a templating agent and titanium isopropoxide as a $TiO_2$ source.[13] The diblock copolymer and the $TiO_2$ precursor were spin coated together, yielding the designed bicontinuous network, followed by an annealing step of 400°C in order to generate and sinter the $TiO_2$ as well as removing the templating polymer through burning. MEH-PPV was then infiltrated into the gaps where the diblock copolymer used to be to act as a light absorber and hole transport material. A photovoltaic device efficiency of 0.71% was achieved.[13] Goh *et* al. used a different approach to nanostructuring $TiO_2$ by first a fabricating mold into which the sol-gel $TiO_2$ could be inserted and therefore templated.[14] They began with an anodic alumina template (AAO) with pore diameters of approximately 50 nm into which polymethylmethacrylate (PMMA) was infiltrated, followed by covering with a poly(dimethylsiloxane) (PDMS) coating and wet etching the AAO template. By embossing the PMMA mold into a sol-gel based of titanium ethoxide, a $TiO_2$ replica of the AAO was obtained. Using this technique and infiltrating the pores with P3HT Williams *et* al. achieved photovoltaic device efficiencies of 0.6%.[15]

As mentioned, as well as templating nanoparticles, another way to achieve the desired comb structure is to grow oriented nanorods. Kang *et* al. demonstrated a power conversion efficiency of 1.06% using vertically aligned CdTe nanorods combined with poly(3-octylthiophene) (P3OT).[16] The CdTe pillars were grown using, again, an AAO template and electrodeposition from an aqueous solution. A similar method was also employed to fabricate CdS pillars filled with MEH-PPV resulting in an overall efficiency of 0.60%.[17] Vertically aligned ZnO nanorods have been demonstrated by several groups and there are several different routes to their synthesis. The rods produced are most often seen as a replacement for $TiO_2$ in dye-sensitised solar cells (DSSCs)[18] or in quantum dot sensitised solar cells (QD-SSCs),[19] although they are also used in structures similar to what has already been discussed, by infiltration with a

semiconducting polymer. Yin *et* al. electrochemically deposited monocrystalline ZnO nanorods onto reduced graphene oxide films, which were then filled with P3HT. The resulting power conversion efficiency achieved was 0.31%.[20] This efficiency was slightly improved on by Olson *et* al. who, using long-temperature solution growth based techniques to fabricate the aligned rods, managed a power conversion efficiency of 0.53% also using P3HT in the pores.[21]

In this work Yiming Mao fabricated vertically aligned $Bi_2S_3$ rods grown on a flat $TiO_2$ surface, which was then infiltrated with SPIRO. The devices showed the best efficiency when coated with $Ag_2S$ to form a core-shell type material. At the time of this work, the best device had a photovoltaic efficiency of 1.68%, however, this is now up to 2.22%. In this work the charge transfer efficiency in these systems was studied using TAS and the role of the $Ag_2S$ was investigated. The main observation was that the presence of $Ag_2S$ appeared to "switch on" the functionality of the device, even after only small amount was added. However, TAS measurements showed that it was not the charge generation that was being "switched on", upon addition of $Ag_2S$, as without it, the charge generation efficiency was similar.

# Experimental

## Polymer/$Bi_2S_3$ Nanoparticle Blends

This method is adapted from the experimental section of the paper that resulted from this work.[4]

Glass/ITO-coated glass substrates (ITO for devices) were first washed in acetone for 10 minutes followed by a 10 minute bath in ethanol, both under strong sonication. The substrates were then rinsed with abundant DI water and dried with nitrogen. A ZnO electron transport layer was then grown using a sol–gel method. Briefly, zinc acetate dihydrate (0.5 g) was dissolved in a mixture of methoxyethanol (5 ml) and ethanolamine (0.142 ml). The solution was spin-cast onto the ITO-coated glass substrates at 3000 rpm and annealed at 200°C for 30 minutes in air. The bismuth sulfide and polymer blend (P3HT, P3HT-SH or mixture of the two) was then spin-cast on top of ZnO layer at 3000 rpm and subjected to a ligand exchange process in a 10 minute bath in 1,2-ethanedithiol (EDT) 1 vol% in acetonitrile (ACN). The unreacted ligands were removed in an ACN bath followed by annealing on a hotplate at 110 °C for 7 minutes. The films after this stage were used in for the TAS measurements and the remaining steps were used to fabricate the completed devices. A second layer of the blend product was then spin-cast dynamically onto the substrate, followed by an additional EDT 1% in ACN bath, rinsing and annealing steps (110 °C for 7 minutes). Next, a drop of P3HT solution in 1,2-dichlorobenzene (DCB) (40 g $l^{-1}$) was deposited onto the spinning (3000 rpm) substrate as the HTL, followed by a final annealing step at 110°C for 7 minutes. Finally, the $MoO_3$ (15 nm) and Ag (150 nm) electrodes were thermally evaporated in a Kurt J. Lesker Nano36 system.

The synthesis is the P3HT-SH and the $Bi_2S_3$ nanoparticle synthesis are available elsewhere.[4,6]

## $Ag_2S$ Coated $Bi_2S_3$ Nanowires

This method is adapted from the experimental section of the paper that resulted from this work.[5]

This method first required the synthesis of bismuth sulfide nanocrystalline seeds. $Bi(OAc)_3$ (2.8 mmol) and oleic acid (34 mmol) were heated and degassed under vacuum at 100°C overnight, and the reaction temperature was raised to 170°C. When the reactions flask reached 170°C, hexamethyldisilathiane (0.9 mmol) mixed with 1-octadecene (5 ml) was quickly injected to the flask, and the heating temperature lowered to 100°C. After 2 h at 100 °C, the reaction was quenched by removing the heating mantle and by adding toluene (10 ml) and methanol (20 ml). The oleate-capped bismuth sulfide nanocrystals were isolated after centrifugation. Purification of the nanocrystals was performed by

successive dispersion and precipitation in toluene and methanol. Finally, the nanocrystals were dispersed in anhydrous toluene.

Bismuth sulfide nanocrystalline seeds were deposited on a $TiO_2$-coated FTO substrate by a dip-coating process. To graft the as-synthesized bismuth sulfide nanoparticles onto the substrate, the $TiO_2$/FTO was immersed in 1,2-ethanedithiol (EDT). The EDT-modified substrate was dipped in a solution of bismuth sulfide nanoparticle in toluene (2 mg/ml) for 40 s, rinsed with toluene, and dried.

Bismuth sulfide nanowire arrays were grown from the seeds via mild aqueous chemistry. The aqueous bath solution was prepared by mixing a solution of $Bi(NO_3)_3$ (0.2 M, 1 ml) and thiourea (0.1 M, 6 ml). The $Bi(NO_3)_3$ solution was prepared by dissolving of $Bi(NO_3)_3 \cdot 5H_2O$ (0.097 g) in concentrated nitric acid (0.2 ml) and then diluting the volume to 1.0 ml with deionised water. The as-prepared seeded substrate was immersed in the 55°C aqueous bath solution. After growth, the solution was cooled down to room temperature, and the bismuth sulfide nanowire film was rinsed with deionised water and ethanol and dried.

Fabrication of bismuth sulfide core/silver sulfide shell structures by SILAR. The core-shell structures were prepared by SILAR method. Briefly, the as-grown bismuth sulfide nanowire film was immersed in a solution of $AgNO_3$ in ethanol (0.1 M) for 20 s, rinsed with ethanol, then dried. The film was dipped in Na2S·9H2O (0.1 M) aqueous solution for 40 s, rinsed with deionized water, and dried. The above process was repeated to get desired structures and is referred to as 1 cycle.

Devices were fabricated by first annealing the core-shell films at 100°C for 5 min in $N_2$ and soaking the films in a solution of EDT in acetonitrile (0.24 M) for 20 min. The SPIRO solution was prepared by dissolving SPIRO (60 mg) in cholorobenzene (500 µl) via heating at 80°C in the glovebox for 30 min. Then a solution of lithium bistrifluoromethanesulfonimidate (LiTFSI) in acetonitrile (8.33 µl, 85 mg/ml) and 4-tertbutylpyridine (24.4 µl) were added into the SPIRO solution. The SPRIO solution was put on the bismuth sulfide nanowire or core-shell films and kept static for 30 sec before spinning at 2000 rpm for 30 sec. The SPIRO infiltrated films were annealed at 90°C for 15 min in air. Devices were finished with $MoO_3$ (10 nm) and Ag (150 nm).

# Results and Discussion

## Polymer/$Bi_2S_3$ Nanoparticle Blends

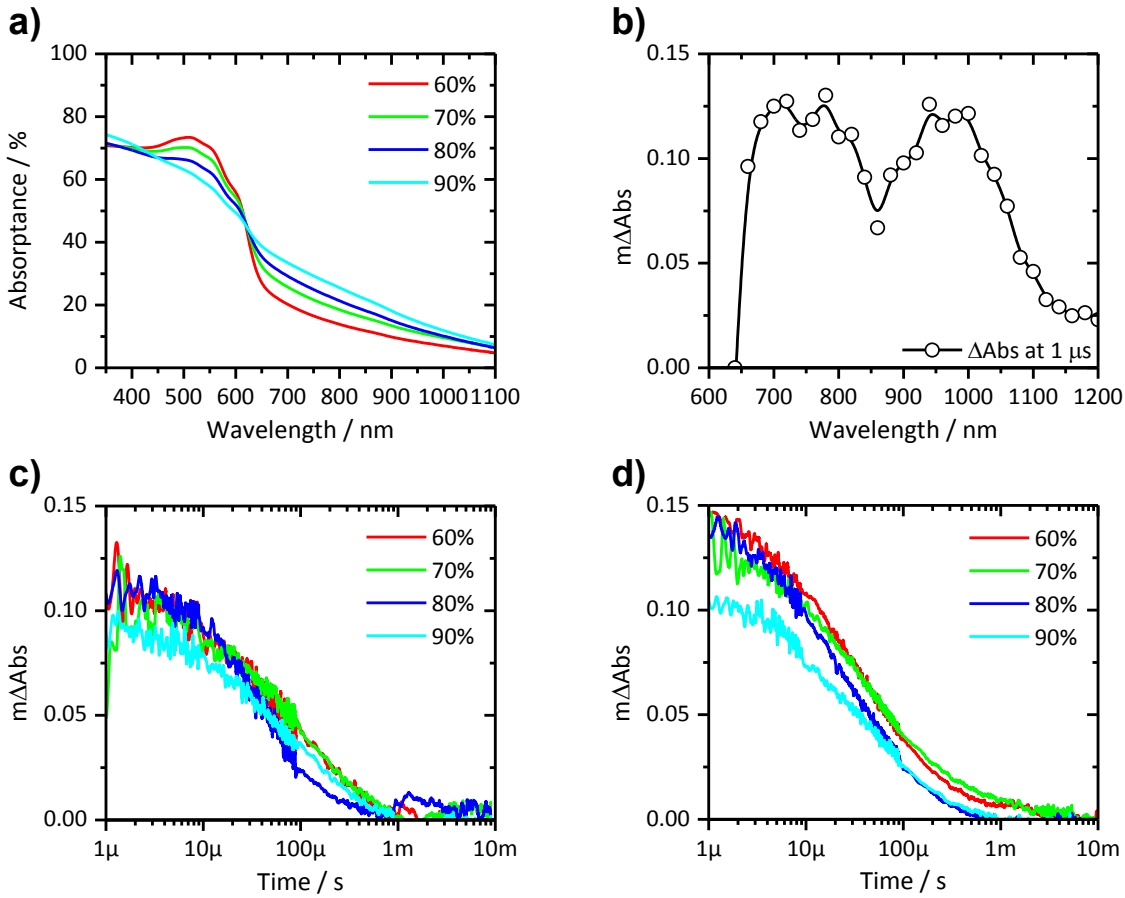



*Figure 6.2 - a) UV-Vis absorptance measurements of P3HT/$Bi_2S_3$ blend films with a range of blend ratios, labelled by the relative weight percent of $Bi_2S_3$ in the film. b) TAS spectrum of an 80% film using an excitation wavelength of 510 nm and plotting the ΔAbs at 1 µs after excitation. c) Transient absorption decays of the range of blend films excited at 700 nm and probed at 980 nm. d) The same films after excitation at 510 nm, probing at 980 nm. Both sets of decays are excited using the same approximate number of photons and are scaled for the number of photons absorbed.*

The UV-Vis absorptance of P3HT/$Bi_2S_3$ blends with a range of blend ratios was first measured (Figure 6.2a). The absorption profile of these blend films appears to be slightly different to those fabricated from the xanthate method. The slow onset in the low energy portion of the spectrum is similar, however this slow slope continues upwards across the visible region, whereas with the xanthate formed $Bi_2S_3$ there was relatively more absorption in the visible region. This is most easily visible in the film containing 90% $Bi_2S_3$ by weight where the curve has almost the shape of an exponential rise. It would be extremely hard to provide any relevant comment on the reasons for this apparent difference and therefore any differences in performance will have to be judged by a different method.

The effectiveness of these blends at photogenerating charges was then tested, using TAS. First, a transient spectrum was produced (Figure 6.2b) using the blend ratio of 80% and exciting the sample

with a wavelength of 510 nm, exciting both the $Bi_2S_3$ nanocrystals and the P3HT phases. Here, a typical P3HT polaron signal is observed, similar to what has been measured by others in P3HT/PCBM systems.[22,23] The positive signal in this case is greater in intensity than the negative signal generated by the ground-state bleach. This is converse to what was observed in Chapter 5 where a completely negative signal was observed for the blends (Figure 5.4) and in the mesostructured films only one peak of the P3HT polaron was observed with the other was masked by the bleach (Figure 5.11a). The reasons for this could be simply due to the relatively lower amount of $Bi_2S_3$ in these blend samples, which appear reasonably transparent to the naked eye, in comparison to the completely black onyx-like xanthate formed blend and mesostructured films.

The TAS decays of these blend films were then measured, exciting solely the $Bi_2S_3$ at 700 nm (Figure 6.2c) and both components at 510 nm (Figure 6.2d). The ability to excite solely the $Bi_2S_3$, and compare the results to the measurement where both components are excited, allows for knowledge to be gained about the relative amounts of electron and hole transfer in the system. When exciting solely the nanoparticles, the traces all appear relatively similar in amplitude and shape. There appears to be a slight measurement error in the 80% sample, as the step shape is highly unlikely to be anything other than an artefact. The similarity of the other traces suggests that the morphology of the films remains reasonably constant with an increase in the $Bi_2S_3$ amount. The signals do increase with the increased amount of $Bi_2S_3$, however the signals are scaled for the amount of pump light absorbed and so this is not seen. There is perhaps a very small decrease in amplitude in the 90% case, which could be due to the P3HT content becoming so low that the heterojunction surface area is reducing, due to high levels of nanoparticle aggregation, and as a result the charge transfer yield decreases. The lifetime of the signals are relatively long, similar to what was observed in the meso-structured $Bi_2S_3$ structures and in contrast to the P3HT/CdS blends. When using an excitation wavelength of 510 nm, absorbed by both the $Bi_2S_3$ and P3HT components, the situation looks very similar. All traces are of a similar amplitude, with the 90% films being slightly lower. The amplitudes are, in comparison, higher than when solely exciting the $Bi_2S_3$ suggesting that both hole and electron transfer are occurring in this system. The underperformance of the 90% sample reaffirms the hypothesis that the amount of P3HT is so low in this sample that the heterojunction surface area is becoming reduced, and, as a result, a relatively smaller increase in the amount of charges generated is observed when exciting both components compared to just exciting the $Bi_2S_3$ in this film.

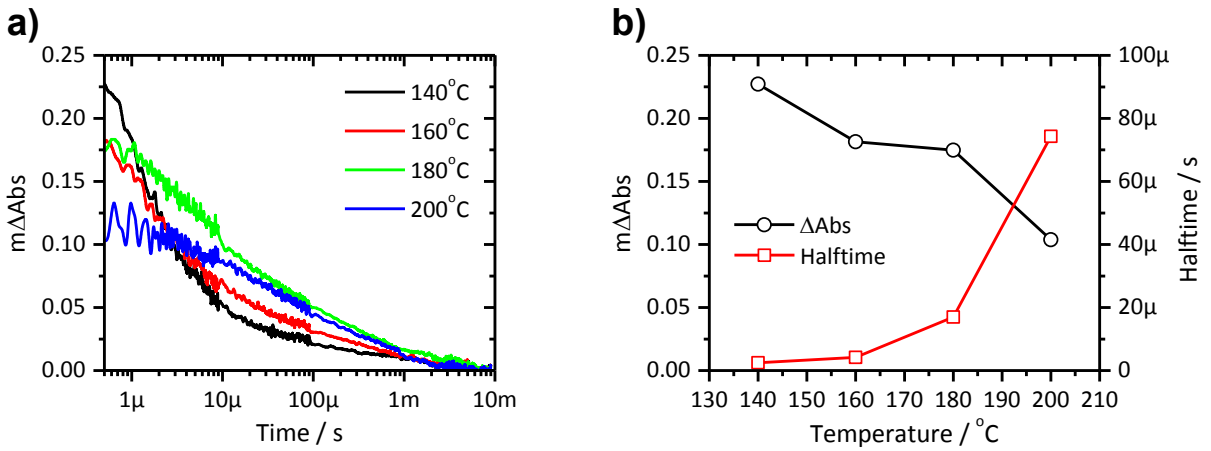



*Figure 6.3 - a) TAS decays of films of P3HT/$Bi_2S_3$ blends containing an 80% weight ratio of $Bi_2S_3$ annealed at a range of temperatures under atmospheric conditions. Samples were excited with at 510 nm, probed at 980 nm and are scaled for the amount of pump light absorbed. b) The initial amplitudes (500 ns) and halftimes of these same films.*

The effect of annealing these heterojunctions was then investigated, using 80% weight ratio films. The films were annealed under atmospheric conditions, as it was under these conditions that devices were made. The results of this study are shown in Figure 6.3. The first observation is that at all annealing temperatures the signals are higher than when no annealing was performed, but the lifetimes are much shorter (See Figure 6.2d). This effect of annealing was similarly observed in the mesoscopic $Bi_2S_3$ films. There is also a distinct trend in both the initial amplitude and the halftime of the samples, most clearly seen in Figure 6.3b. As the annealing temperature is increased the initial amplitude, and therefore the charge generation yield, is decreased. This decrease in initial amplitude is accompanied by an increase in the halftime of the charges. Although with this information alone it is impossible to know exactly what is happening, it can be speculated that, due to the fact that the films are annealed in air, the P3HT is likely to become oxidised to a certain extent. The amount of P3HT oxidised is likely to be dictated by the temperature at which the films are annealed. This oxidation would be expected to have a negative effect on the amount of charges generated, but could possibly increase the halftime of the charges, due to an increase in the mobility of the effectively doped polymer. An increase in P3HT mobility due to mild oxidation was hypothesised previously in P3HT/$Sb_2S_3$ bilayer devices. Here light soaking in air significantly improved the PCE of the photovoltaic devices.[24]

One of the key fabrication steps that these hybrid films undergo is a ligand exchange process, whereby the long ligands of oleic acid, that were used to synthesise the $Bi_2S_3$, are replaced by shorter ones in order to increase the performance of the devices. This is achieved by linking the particles together, so there is electronic communication between adjacent particles, and then charges can hop from particle to particle. It is said that a when shorter ligand is used it also allows for an increase in charge generation, due to the closer proximity that is achieved between donor and acceptor.

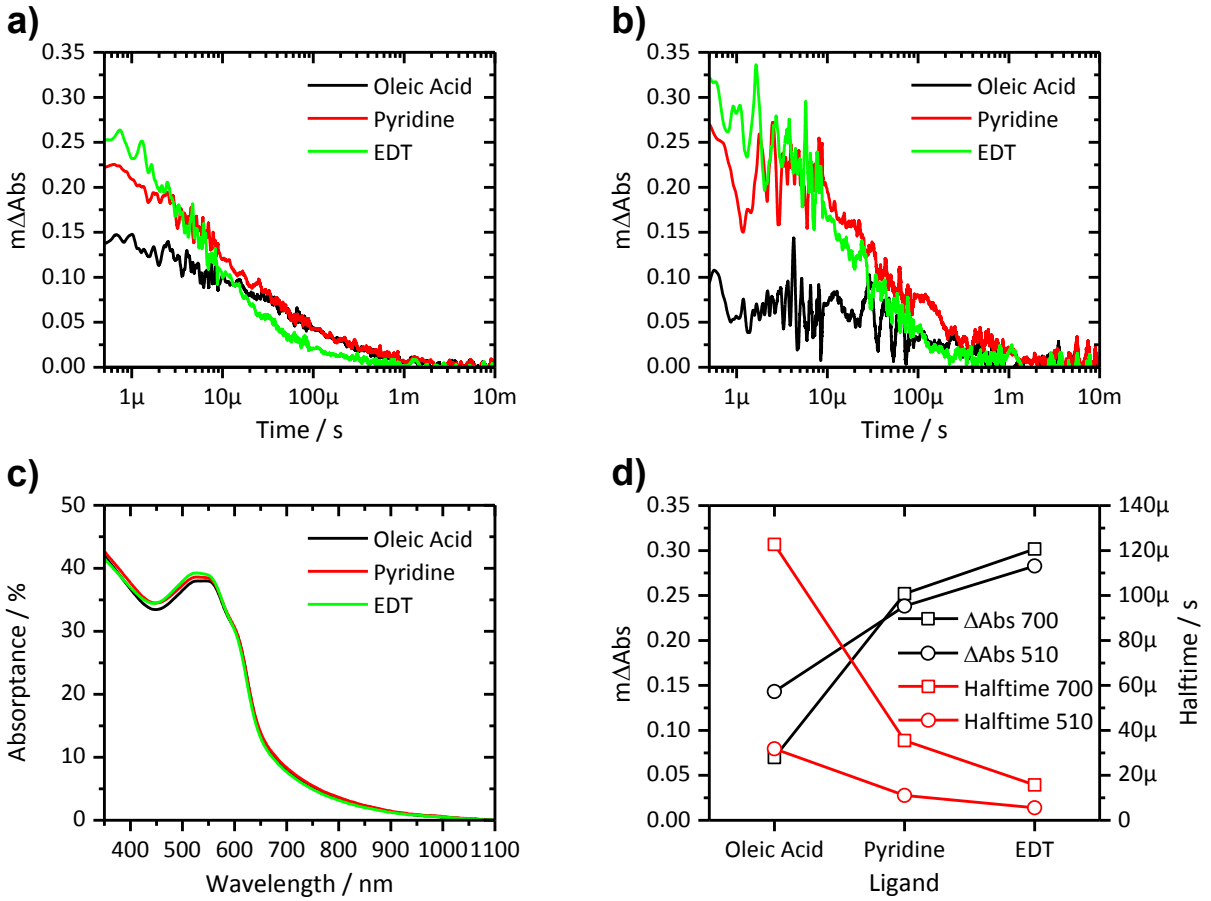



*Figure 6.4 - Transient absorption decays of P3HT/$Bi_2S_3$ films fabricated with no ligand exchange and with either an exchange with pyridine or EDT, excited at either 510 nm a) or 700 nm b) and probing at 980 nm. All traces are excited using approximately the same number of photons and are scaled for the amount of pump light absorbed. c) UV-Vis absorptance spectra of the same three films. d) Initial amplitudes (500 ns) and halftimes of the traces plotted for each of the ligands.*

TAS decays of films fabricated with either no ligand exchange (black) or an exchange with pyridine (red) or ethanedithiol (EDT) (green) are shown in Figure 6.4a and b. These ligands were chosen as the EDT gave the best performance in devices and pyridine is another typical ligand used in hybrid devices,[25] which lies in-between oleic acid and EDT sizewise, although considerably closer to EDT. The samples were excited either exciting solely the nanoparticle at 700 nm (Figure 6.4b), or both components at 510 nm (Figure 6.4a). The ΔAbs at 500 ns for each of these traces, along with the halftimes are shown in Figure 6.4d. In comparison to before, there is not an obvious increase in the amplitude of signals when exciting the P3HT compared to just the $Bi_2S_3$. The reliability of this observation is lower than previously, due to the high level of noise in the traces generated from exciting just the $Bi_2S_3$ (Figure 6.4b). This high level of noise is due to the low level of absorption at 700 nm in these samples. These particular measurements were performed on samples that were fabricated in a manner as close to the optimum for device performance. This compromised the signal to noise ratio of the measurements, but ensured the samples were as close to the full devices as possible.

One thing that is clear is the effect that the ligand exchange has on yield and halftimes of the samples. In both excitation cases as a smaller ligand is used (Oleic Acid > Pyridine > EDT) the yield of charge generation increases. The ligand exchange appears to have the same amount of influence on the hole and electron transfer, considering the fact that the trend in amplitude at 500 ns, plotted in Figure 6.4d, roughly overlays for both the 510 nm and 700 nm excitation. As well is the increase in amplitude, when a smaller ligand is used, there is also an observed decrease in halftime of the decays. This is because the size of the ligands dictate the proximity of the nanoparticles to each other and increasing this distance can help keep the separated charges away from each other and reduce the recombination rate. It is this increase in separation that also reduces the ability of the interfaces to photogenerate charges as the polymer cannot get in as close to the nanoparticles when a longer ligand is in the way. The UV-Vis absorptance of each film has been included to show that the ligand exchange has no obvious effect on the chemical composition of the films (Figure 6.4c).

After the initial study of the efficiency of these P3HT/$Bi_2S_3$ heterojunctions at generating charges an attempt was made to increase the overall performance of these devices by both increasing the charge transfer yield and also improving the nanomorphology of the active layers in order to better extract the generated charges. Both of these issues were tackled by utilising a thiol-functionalised block copolymer based on P3HT shown in Figure 6.1 and referred to as P3HT-SH.

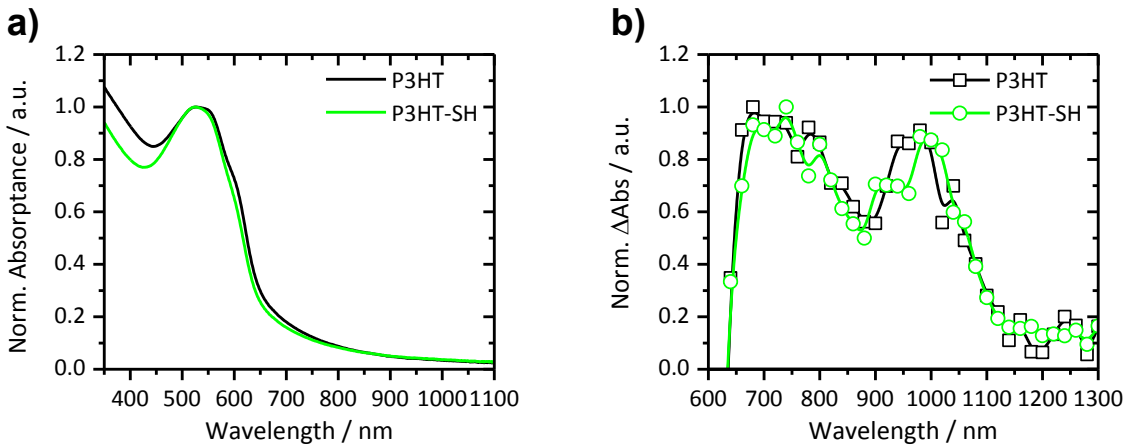



*Figure 6.5 - a) Normalised UV-Vis absorption spectra of a typical polymer/Bi2S3 fabricated with either P3HT (black) or the block copolymer P3HT-SH (green). b) TAS spectra of the same films, excited at 510 nm and normalised to the maximum ΔAbs value.*

Normalised absorptance spectra of thin films formed using both P3HT and P3HT-SH are shown in Figure 6.5a. One observable difference is that there appears to be a considerable reduction in the amount of fine structure in the polymer part of the P3HT-SH. The P3HT spectrum shows the typical 3 peaks seen with P3HT and in the P3HT-SH sample these features are much less distinguishable. Particularly, the shoulder seen in the P3HT sample at approximately 600 nm is much less pronounced in the P3HT-SH. This can be attributed to a reduction in the aggregation of the polymer, or in other words, a reduction

in the crystallinity between polymer chains.[26] This reduction in aggregation could either be due to the way which the polymer structure itself alters the stacking between polymer chains, or could be due to the fact that the polymer is more miscible with the nanoparticles and as a result a much more homogenous film is generated, without many pure polymer domains.

Figure 6.5b shows the TAS spectra of the same two films, using a pump wavelength of 510 nm, exciting both the polymer and nanoparticles. The data has been normalised to highlight the shape of the two spectra. Both spectra are extremely similar in shape, which is not surprising considering the P3HT LUMO has been modelled to be almost completely on the backbone.[27] This similarity in shape allows for convenient spectroscopic comparisons to be made, as the kinetics of all samples can be measured using the same probe wavelength of 980 nm.

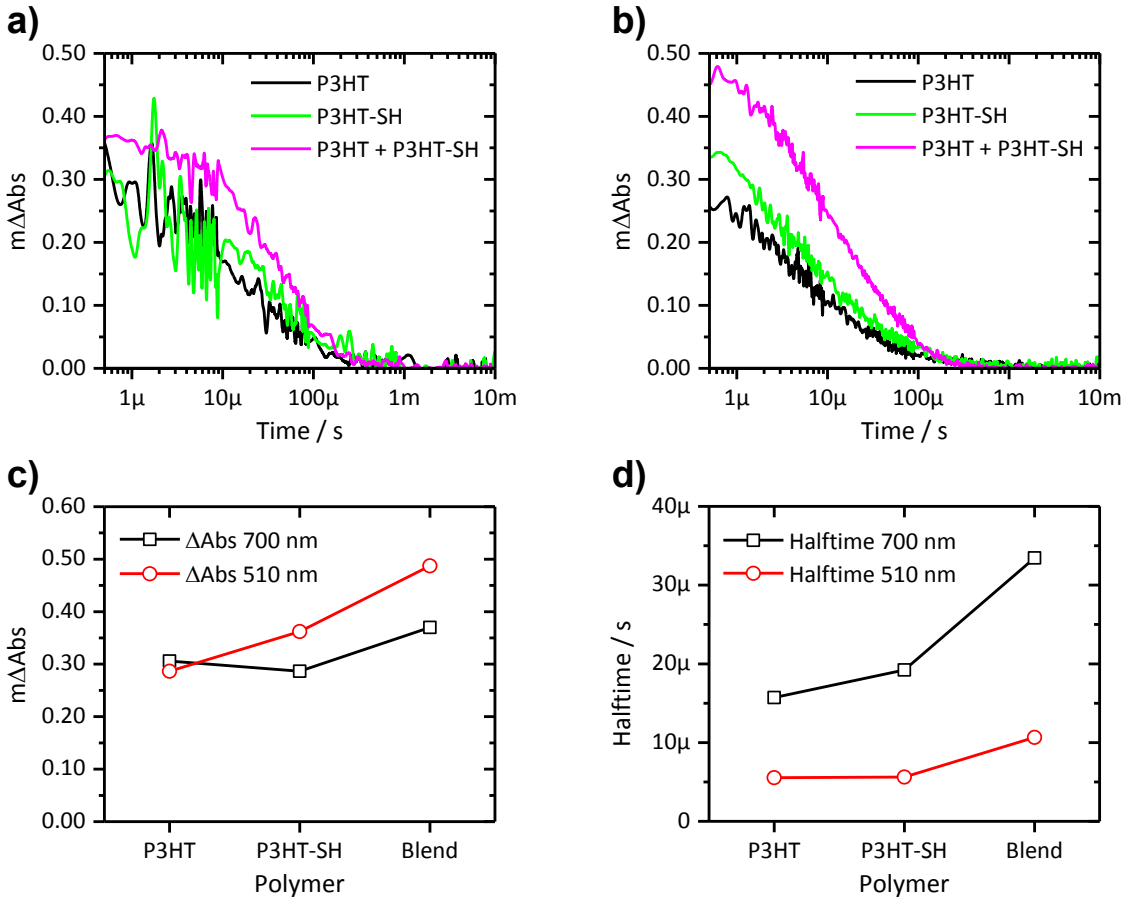



*Figure 6.6 - TAS decays of polymer/$Bi_2S_3$ blend films containing P3HT (black), P3HT-SH (green) or a mixture of both (magenta) excited at either 700 nm a) or 510 nm b). All decays are probed at 980 nm, excited with approximately the same number of photons and scaled for the amount of pump light absorbed. c) Initial ΔAbs of the decays (500 ns) as well as the halftimes d).*

In Figure 6.6 the TAS decays are presented for the same samples as in Figure 6.5 with the addition of a sample containing a 70:30 blend of P3HT and P3HT-SH with an identical $Bi_2S_3$ nanoparticle loading, exciting either solely the nanoparticles (Figure 6.6a) or a mixture of polymer and nanoparticles (Figure 6.6b). Considering first the decays where only the nanoparticles are being excited, further indicated by

the black points and lines in Figure 6.6c and d, the amplitude at 500 ns appears to be relatively unaffected by the change in polymer. There is perhaps a slightly higher signal in the blend system, but this is likely due to the fact that the signals are being observed after a small amount of recombination in the other two samples. In fact if stretched exponential fits are used and the ΔAbs is extrapolated back $t_0$ the values are even more similar. Something that does change more considerably is the lifetime of the charges. The P3HT and P3HT-SH show a small difference, within the inaccuracy associated with the fit, but the blend sample shows a considerably higher halftime. This difference is suggested to be due to an energy cascade that is measured to be present in the films, which would drive charges away from the interface. Cyclic voltammetry measurements were used to determine that the P3HT-SH HOMO sat approximately 50 meV deeper than the P3HT and a similar value was determined using photoelectron spectropscopy.[4] Figure 6.7 shows the approximate energy landscape of these ternary heterojunctions. It is reasonable to assume that the energy cascade created here will increase the lifetime of free charges relative to the binary systems containing only one of either P3HT or P3HT-SH, due to the spatial separation that a transfer through this cascade would produce. Though this energy cascade is only 50 meV, a similar effect was observed to be key in polymer/PCBM systems.[28] Here the generation of a pure PCBM phase, which had a HOMO 100 meV deeper than disordered PCBM near the polymer/PCBM interface was seen to be a key driver for high charge generation yields.

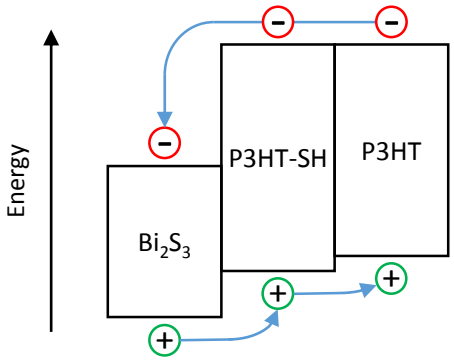



*Figure 6.7 - Diagram of the energy level alignment in the ternary P3HT:P3HT-SH/$Bi_2S_3$ blend heterojunctions. All energy levels are not to scale and are intended solely to illustrate to approximate shape of the energy landscape.*

Considering next the decays where both the nanoparticles and polymers are being excited, there is a much larger dependence of the initial amplitude with the polymer used. There is approximately a 25% increase when using the P3HT-SH instead of the P3HT and an 80% when using the blend in comparison to P3HT. There are two possible reasons for this increase in yield, either, better electronic coupling between the polymer and nanoparticles is achieved when using P3HT-SH, facilitated by the SH moiety, or a more optimum morphology for charge generation, i.e. a more well mixed system is generated when

using the P3HT-SH. It is likely that a combination of both of these explanations play a role. The concept of better coupling is supported by the observation that in equivalent solutions of P3HT/P3HT-SH and the $Bi_2S_3$ nanoparticles an increase in the amount of photoluminescence quenching was seen in the P3HT-SH solution.[4] The fact that this experiment is performed in solution removes the morphological argument from the equation and supports the hypothesis that adding the SH moiety to the P3HT solubilising chains would in fact increase the charge transfer by anchoring the polymer to the nanoparticles. In the case of the blend, the increase in charge generation cannot be solely attributed to an increased coupling, as in fact there is only 30% of the P3HT-SH used and 70% P3HT. Here, it is likely that a combination of the previously explained improvement in electronic coupling is improving charge generation in addition to a more optimal morphology. The reason that as large an increase was not seen in the case of the 700 nm excitation case, is consistent with what was observed before, in that hole transfer yields from CdS to P3HT were less affected by the morphology (Figure 4.10d) and also in another study, the hole transfer efficiency was not changed by the loading of CdS in P3HT.[29] In both these cases the reason for this is that a free hole generated in a CdS domain is not limited by mobility in the same way an exciton generated in P3HT is limited by a diffusion length of approximately 10 nm.

Interestingly, the lifetime of charges generated from the 510 nm excitation are much shorter-lived than in the 700 nm excitation case. The halftime for blends in the 510 nm excitation case is a third of that from the nanoparticle excitation case. The reason for this is most likely due to the charge density in the device. Although in the blend there appears to be only a small increase in the ΔAbs in the 510 nm excitation case in comparison to the 700 nm, this data has been scaled for the amount of pump light absorbed in order to allow the charge generation efficiency to be compared. The actual number of charges in the device vary by a factor of 5 and this increased number of charges after 510 nm excitation could be the reason that a shorter lifetime is observed as the increase in number of charges also increases the likelihood that a free charge will meet another charge and recombine. Such a high dependence on charge density suggests that the system is in fact very well mixed.

*Table 6.1 - Tabulated characteristic parameters of solar cells fabricated using each of the different polymer/$Bi_2S_3$ combinations.*

| Polymer | $V_{oc}$ / V | $J_{sc}$ / mA cm$^{-2}$ | FF / % | PCE / % |
|---|---|---|---|---|
| P3HT | 0.31 ± 0.01 | 7.71 ± 0.25 | 35.6 ± 0.8 | 0.85 ± 0.02 |
| P3HT-SH | 0.29 ± 0.01 | 1.64 ± 0.14 | 47.5 ± 5.2 | 0.22 ± 0.02 |
| P3HT:P3HT-SH | 0.34 ± 0.01 | 7.19 ± 0.30 | 41.0 ± 1.3 | 1.01 ± 0.04 |

Table 6.1 shows the characteristic device parameters for the optimised solar cells fabricated using the different polymer/nanoparticle combinations. Devices were fabricated with the structure ITO/ZnO/BHJ/P3HT/$MoO_3$/Ag, where BHJ is a mixture of $Bi_2S_3$ nanocrystals and the polymers, of the

same ratios as used for the previous measurements. The devices fabricated using P3HT-SH as the polymer showed a relatively poor photovoltaic performance compared to P3HT (PCE = 0.22 vs 0.85%), a result primarily caused by a low short circuit current ($J_{sc}$ = 1.64 vs 7.71 mA $cm^{-2}$). This is attributed to an excessive covering of the nanocrystal surface by the thiol-functionalised block copolymer, which could hinder charge transport between $Bi_2S_3$ nanocrystals. The same effect could also be the reason why other studies attempted using functionalised polymers with nanocrystals have not achieved higher power conversion efficiencies.[12] The devices fabricated using a blend of P3HT-SH and P3HT show slightly improved photovoltaic performance (PCE = 1.01 vs 0.85%), due to predominantly an increase in open circuit voltage ($V_{oc}$ = 0.34 vs 0.31 V) and fill factor (FF = 41.0 vs 35.6%). This observation is consistent with the previous measurement of the halftime of photogenerated charges in TAS (Figure 6.6d). This showed that, in the blend case, the biggest difference compared to the neat P3HT and P3HT-SH was an increase in the lifetime, or in other words, a reduction in the recombination rate with the blends. As with the P3HT/CdS and P3HT/fullerene blends a reduction in recombination rate often translates to an observed increase in the fill factor and open circuit voltage.[30,31]

Although the increase in photovoltaic device performance is relatively modest here, this study shows, as a proof of concept, that the incorporation of functionalisation into polymer backbones can be used as a useful tool to increase PCEs in polymer/nanoparticle BHJs.

## $Ag_2S$ Coated $Bi_2S_3$ Nanowires

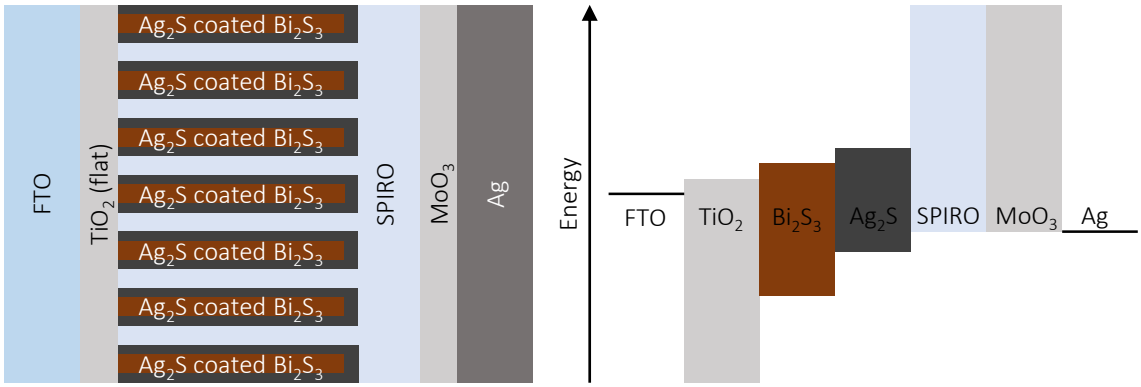



*Figure 6.8 - (left) Diagram of the device architecture used in this section along with the a cartoon of the approximate energy levels of each of the different layers (right). The energy levels are not to scale and are ended solely as guide to illustrate the energy landscape.*

The complete structure of these hybrid devices based on grown $Bi_2S_3$ rods is shown in Figure 6.8. They are constructed of a flat $TiO_2$ layer that is deposited onto an FTO substrate. $Bi_2S_3$ rods are then grown from this $TiO_2$ surface and are coated with a layer of $Ag_2S$ in various amounts. Increasing amounts of $Ag_2S$ are achieved by performing several cycles of successive ionic layer adsorption and reaction (SILAR). The gaps between the coated rods are then filled in with SPIRO and finally a hole selective layer of $MoO_3$ and a back electrode of Ag are evaporated on top to complete the device. The approximate energy levels (not to scale) are also shown, illustrating the rough energy landscape within the device. The $Bi_2S_3$ rods absorb the majority of the visible light, due to its band gap of approximately 950 nm and the $Ag_2S$ absorbs any remaining visible light and also extends the absorption into the infra-red to over 1200 nm. The energy level alignment of all the components is such that a perfect energy cascade is set up, with electrons in the $Ag_2S$ conduction band being able to transfer into the $Bi_2S_3$ conduction band or directly into the $TiO_2$ and electrons in the $Bi_2S_3$ conduction band can also inject into the $TiO_2$. Equally, holes in both absorbing materials can cascade to SPIRO, which can conduct the charges to the counter electrode.

*Table 6.2 - Tabulated characteristic device parameters for the optimum device achieved using varied amounts of $Ag_2S$ to coat the $Bi_2S_3$ rods.*

| Device | $V_{oc}$ / V | $J_{sc}$ / mA $cm^{-2}$ | FF / % | PCE / % |
|---|---|---|---|---|
| No $Ag_2S$ | 0.13 | 0.46 | 39 | 0.02 |
| 4 Cycles | 0.28 | 9.62 | 31 | 0.83 |
| 16 Cycles | 0.31 | 13.1 | 41 | 1.66 |
| 32 Cycles | 0.3 | 16.02 | 35 | 1.68 |

The main interest these devices present for study, is to understand the role of $Ag_2S$, which is theoretically not required for them to work. In Table 6.2 the characteristic parameters for the optimum devices achieved with different amounts of $Ag_2S$ are shown. With no $Ag_2S$ the devices have an extremely low photovoltaic performance (PCE = 0.02%), which is mainly due to a relatively low short circuit current ($J_{sc}$ = 0.46 $mAcm^{-2}$) but also a reduced open circuit voltage ($V_{oc}$ = 0.13 V). When a small amount of $Ag_2S$ is added to the surface of the rods the open circuit voltage was returned to the typical values expected from an organic/$Bi_2S_3$ heterojunction.[4,7] The biggest difference, however, was a 35-fold increase in the short circuit current when 32 cycles of SILAR were performed. The overall result was a near 100-fold increase in the photovoltaic performance and a reasonable efficiency of 1.68% was achieved. It was proposed that the $Bi_2S_3$/SPIRO interface is not optimum for charge generation and therefore $Ag_2S$ was needed to "switch on" charge generation and allow the devices to function. It was also expected that further efficiency gains were made with the addition of more $Ag_2S$, which also introduced a significant amount of current generated from IR absorption, obtained due to the lower band gap of $Ag_2S$.

To test this hypothesis TAS was first performed on as close to optimum devices as possible. Only the $MoO_3$ and Ag back contact was removed to allow light to pass through the sample. Also only 16 Cycles of SILAR was performed to save time in the fabrication process and as the PCE compared to 32 Cycles was not significant. A pump light of 510 nm was used that excited both the $Bi_2S_3$ and $Ag_2S$, as shown in Figure 6.9a. TAS spectra at different time intervals are shown in Figure 6.9b. The shape of the spectra obtained are not what is typically expected of this type of system. There appears to be three features, with peaks at 1600, 1200 and 600 nm. If everything is functioning as is expected any photogenerated electrons will be in the $TiO_2$, or perhaps remaining in either the conduction band of $Bi_2S_3$ or $Ag_2S$. However, the extinction coefficient of electrons is relatively small compared to holes and, as a result, electrons are not often identified in TAS. There are three possible sites where a hole could be located, and there are examples of what the shape of similar species' TAS spectra look like.[32] The hole in metal chalcogenides is thought to lie on the sulfur, which explains why the TAS spectra of CdS and $Sb_2S_3$ on $TiO_2$ look very similar, with a peak at around 600-700 nm and long tail out 1600 nm. It is possible that this is what is being observed here. The TAS spectrum of SPIRO is also well studied and has been shown to have two peaks at 1600 and 600 nm.[32,33] This is also likely to be contributing to the overall signal observed here.

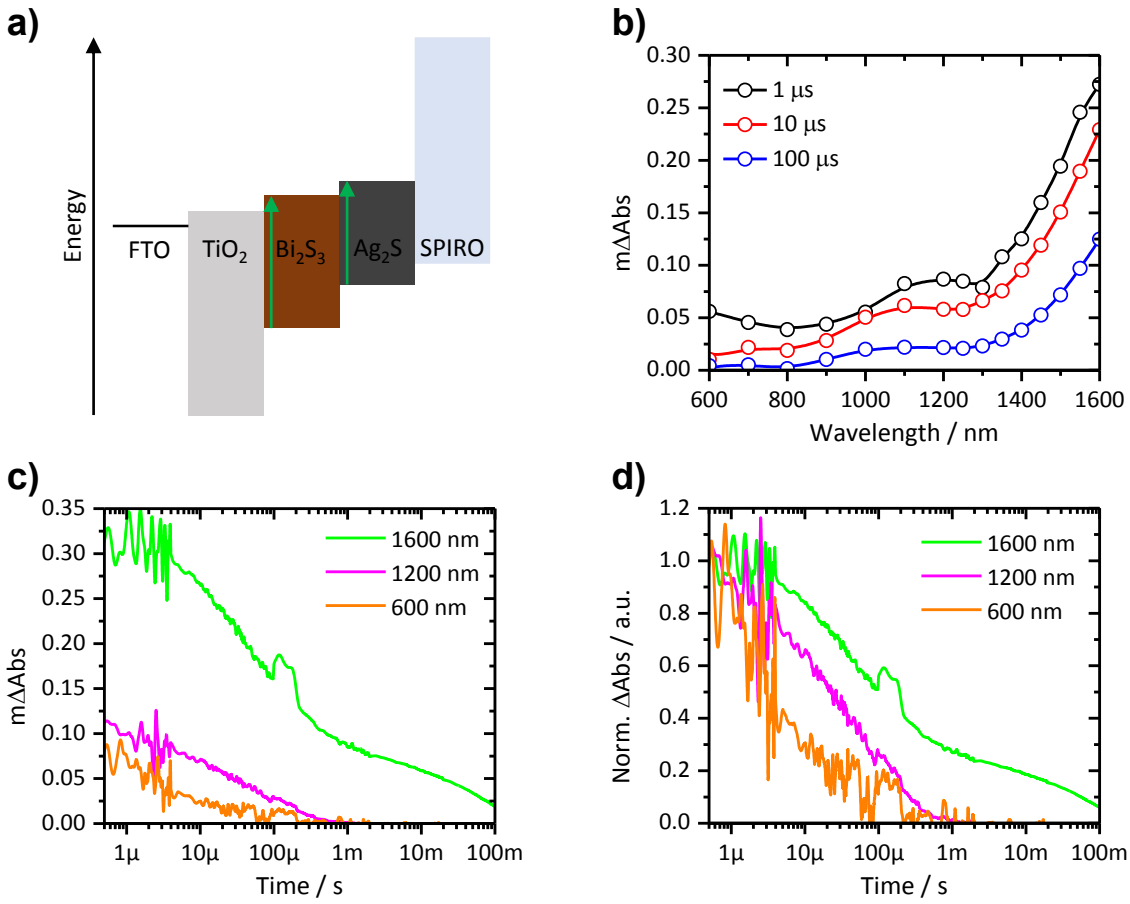



*Figure 6.9 - a) Cartoon energy level diagram of the heterojunction used in this measurement. The green arrows represent the absorption of the 510 nm pump light from the laser. b) TAS spectra of the system at a range of times after excitation. c) TAS decays at the wavelengths of interest from the spectra. d) The same decays normalised to the same initial amplitude. All signals are scaled for the amount of pump light absorbed.*

To help identify the species being observed, the TAS decays are plotted at the wavelengths corresponding to the peaks in the spectra. These decays are presented in Figure 6.9c along with the three traces normalised to the same initial amplitude in Figure 6.9d. The most obvious observation is that decays are all very different in shape, indicating that they correspond to different species or processes. It is also apparent from the green trace, taken at 1600 nm, that at this wavelength there are two separate processes. There is an initial phase which has finished by approximately 1 ms and beyond this time a slower decay remains. The fact that the other two decays also end at 1 ms suggests that the early parts of all three decays are due to the same species or process and at 1600 nm there is also a second species that is much longer lived. In order to identify the species more easily, the system was simplified to narrow down the options for the origin of the signals.

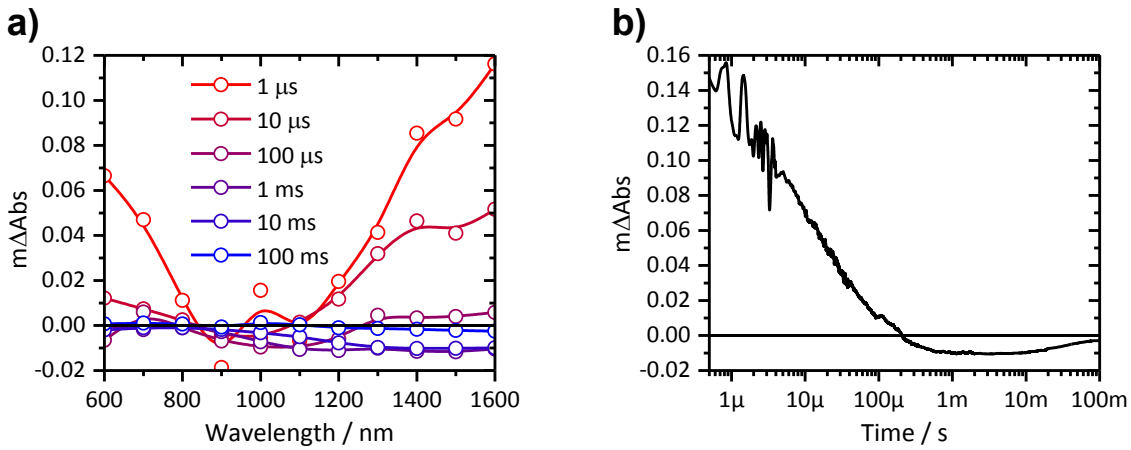



*Figure 6.10 - a) TAS spectra, at various times, of a heterojunction with a structure identical to that in Figure 6.9, only with the FTO replaced with plain glass. b) TAS decay at 1600 nm. Both sets of data are pumped at 510 nm and is scaled for the amount of pump light absorbed.*

The first component that was removed to simplify the system was FTO, which was replaced with plain glass. The previous systems that have been studied have all been obtained on glass and this layer was replaced to remove any possible electron injection from $TiO_2$ in FTO. The experiment was repeated exactly as before and the results can be seen in Figure 6.10. The first observation is that at early times (1 µs) the shape of the spectrum looks very similar to the typical spectra observed for SPIRO.[32,33] The long lived positive signal that was observed at 1600 nm has now been replaced by an equally long-lived negative signal. The long-lived positive signal previously seen is therefore likely due to an electron in the FTO, injected from the $TiO_2$. This is something that has been observed in another system of FTO/$TiO_2$/Perovskite/SPIRO.[24] Here, the long-lived signal was also no longer visible after the replacement of FTO with plain glass. Finally, the shoulder at 1000-1200 nm has also now disappeared at early times. This indicates that either this signal was also due to electrons in the FTO, or, and perhaps more likely, was due to holes in the $Bi_2S_3$ near the thin $TiO_2$ layer that were facilitated by having such a large electron sink in close proximity due to the FTO. The assignment of holes in the $Bi_2S_3$ rather than electrons in FTO is due to the fact that the signal here has decayed to zero many orders of magnitude before the long-lived signal at 1600 nm on FTO. In summary, after the replacement of FTO with plain glass, at early times, the signal appears to be solely due to hole polarons in SPIRO. This signal decays to leave a long-lived negative signal, the identity of which is yet to be assigned.

A negative signal in TAS is caused by the disappearance of an absorption after the pump pulse that was there before the excitation. This is normally observed at wavelengths where there is a large ground-state absorption that, after excitation, has been reduced as free charges have been generated and as a result less of the material is in its ground-state. A good example of this was previously seen with the P3HT/$Bi_2S_3$ blends (Figure 5.4). In this case the reason for the long-lived bleach is quite hard to identify as there is not any obvious ground-state absorption from any component that stretches as far into the

infra-red as 1600 nm. To help answer the question, various components were removed from the structure systematically, to see when the bleach signal was and wasn't present. The results of this analysis are presented in Figure 6.11.

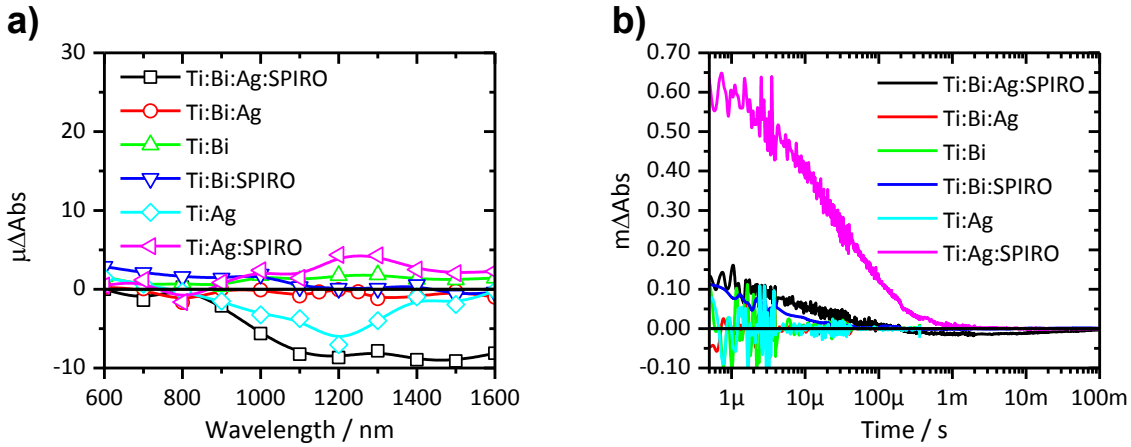



*Figure 6.11 - a) TAS spectra at 300 μs for different structures containing $Bi_2S_3$ (Bi), $Ag_2S$ (Ag) and SPIRO on $TiO_2$ (Ti) b) TAS decays of the same structures at 1600 nm. All samples are excited with a pump wavelength of 510 nm with the same power and decays are scaled for the amount of pump light absorbed.*

Before discussing the results it is pertinent to note that, as the SILAR process requires a scaffold from which to grow, a nanoporous $TiO_2$ was used in the case of Ti:Ag and Ti:Ag:SPIRO. This allowed the $Ag_2S$ to grow and resulted in potentially a similarly porous structure into which the SPIRO could be filled. Considering first the multiple spectra in Figure 6.11a, the only ones that have any signal left by 300 μs are the systems containing some $Ag_2S$. The complete system as measured before (black) shows the broad bleach starting at 800 nm and stretching all the way to 1600 nm, the system of $Ag_2S$ grown on nanoporous TiO2 displays a bleach at the ground-state onset peaking at around 1200 nm and the nanoporous system with SPIRO perhaps also shows a very small positive signal. It is worth highlighting the fact that the axis here is μΔAbs instead of the usual mΔAbs and these signals are very low in magnitude. The decays at 1600 nm allow for a better interpretation (Figure 6.11b). The only systems that show any signal of note are the ones containing SPIRO. The system of $Ag_2S$ on nanoporous $TiO_2$ with SPIRO shows the highest signal. This is not surprising considering the typical surface area of nanoporous $TiO_2$ in comparison to the morphology of the $Ag_2S$ coated $Bi_2S_3$, which will be discussed further into this chapter. This decay however does not show any negative character. The Ti:Bi:Ag:SPIRO decay (now again with flat $TiO_2$) has been seen already previously and this system without the $Ag_2S$ shows a similar signal but also doesn't appear to have a negative component to the decay. The effect of the addition of $Ag_2S$ to the $Bi_2S_3$ will be discussed in more detail in the next section. It appears that the only system that shows this negative bleach at 1600 nm is the complete system. This is somewhat unfortunate as it makes the origins of the signal hard to systematically work out, with many components involved when it is seen. However, there are two possible reasons that can be postulated. The first, and

probably the more unlikely of the two explanations, is due to charge-transfer state excitation directly from SPIRO to $Bi_2S_3$. This is illustrated in Figure 6.12 by the red arrow. This is a ground-state transition that is possible and would be suppressed by a reduction in ground-state SPIRO due to its oxidation after hole transfer from $Ag_2S$. It is however hard to conceive of a reason why this transition doesn't occur without the $Ag_2S$, when the SPIRO is directly in contact with the $Bi_2S_3$. The possibility of a similar transition occurring into the $Ag_2S$ conduction band is ruled out due to the fact that no negative signal is observed in the $TiO_2$:$Ag_2S$:SPIRO case. The second possibility is represented by the blue arrows in Figure 6.12. It is likely that there a many trap or surface states in the metal sulfides, as it is fair to assume that perfect crystals have not been produced and as a result many defects will be present. There is likely a small amount of ground-state absorption into these trap states and it is possible that what is being observed is a ground-state trap bleach. That is, the absorption into these trap states is supressed when charges are transferred into the SPIRO after photoexcitation. This is the more likely of the two possible explanations but it is hard to say with any degree of certainty.

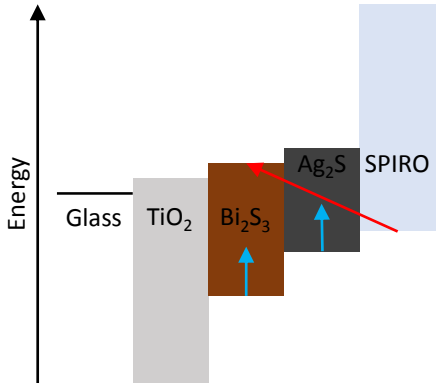



*Figure 6.12 - Diagram illustrating the possible ground-state transitions that could result in a negative TAS signal at sub-band gap energies (1600 nm) due to their suppression after excitation. The red arrow represents direct excitation of an electron from the HOMO of SPIRO into the conduction band of $Bi_2S_3$ and the blue arrows represent the excitation into sub-band gap trap/surface states in the metal sulfides.*

After a reasonable handle has been grasped on what the TAS signals observed mean, the hypothesis previously mentioned, that the $Ag_2S$ "switched on" charge generation, was tested. This was done with the same architecture as used previously but the amount of $Ag_2S$ was varied by changing the number of SILAR cycles that was performed, before infiltrating the pores with SPIRO. The samples made used cycle amounts to match the devices fabricated, whose characteristic parameters were given in Table 6.2. The resulting data is presented in Figure 6.13.

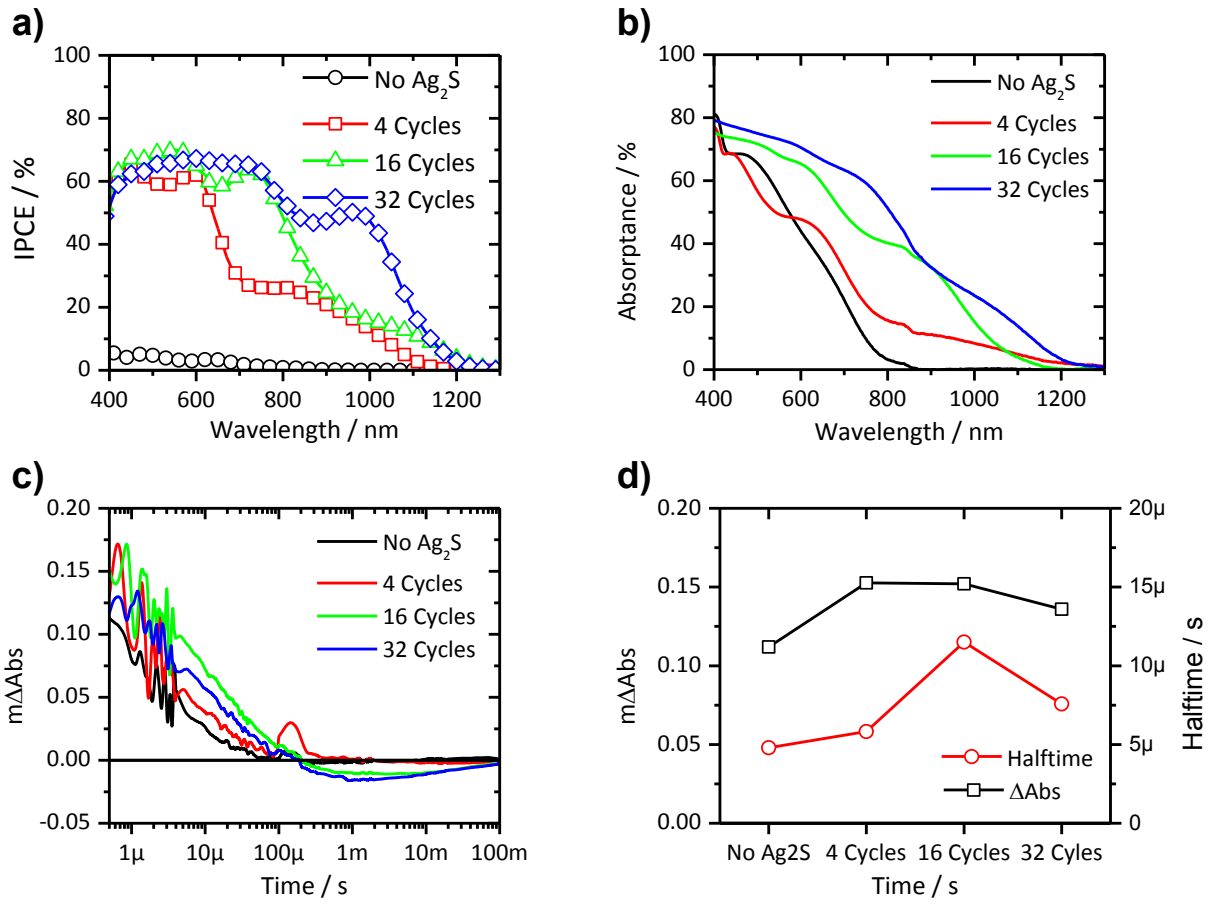



*Figure 6.13 - a) Incident photon conversion efficiencies (IPCEs) of the 4 devices presented in Table 6.2 with different amounts of $Ag_2S$. b) Steady-state absorptance measurements of the analogous heterojunctions used for the spectroscopy. c) TAS decays measured after a 510 nm excitation and probed at 1600 nm for the heterojunctions along with the amplitudes at 1 µs and the halftimes d). Al samples were excited using the same approximate number of photons and were scaled for the amount of pump light absorbed.*

Looking first at the IPCE data in Figure 6.13a, it is clear to see where the hypothesis comes from. The device with no $Ag_2S$ shows almost no current generation across the spectrum. However, when a small amount of $Ag_2S$ (4 Cycles) is added the device shows reasonable current generation in the visible region and some current generated from photons absorbed all the way out to 1200 nm. When more $Ag_2S$ is added the visible portion of the IPCE doesn't change much, but the infra-red region is increased to almost match the visible section. It is not unreasonable to question whether the $Bi_2S_3$ is doing anything other than acting as a scaffold for the $Ag_2S$. However, considering the steady-state absorptance measurements in Figure 6.13b, particularly the 4 Cycles sample, the absorption in the visible region is not changed much after adding $Ag_2S$. This is because the absorption at 500 nm is mainly due to the $Bi_2S_3$. The shape of the 4 Cycles absorptance matches the IPCE shape and suggest that current generated from $Bi_2S_3$ absorption is "switched on" by the addition of $Ag_2S$ and also a small amount of IR generation is present as well. As more $Ag_2S$ is added the absorption in the IR region increases significantly and this in turn is utilised to generate more current. It is worth noting that the IPCE values in the IR region actually exceed the percentage amount of light absorbed in the equivalent region. This is could possibly be due

to slight difference in the sample thickness when produced on FTO compared to plain glass or could be due a calibration error in the IR region of the IPCE equipment.

Considering now the TAS data it is apparent that the hypothesis is not exactly correct. Although the sample with no $Ag_2S$ generates a very low amount of current and there is over an order of magnitude difference in IPCE at 510 nm, the amplitude of the TAS decays show a very different trend. The amount of charge generated after excitation at 510 nm is relatively similar. The sample with no $Ag_2S$ does show the lowest yield, however this is only ~25% less than that of the highest signal observed in TAS and can't account for the difference in the IPCE. The effect is also not due to a dramatic change in lifetime of the charges. The halftime measurements shows that there is only perhaps a small increase in how long charges live when the amount of $Ag_2S$ is increased. The reason for the "switching on" of the current is therefore unknown, but it can be said that this observation cannot be explained by a "switching on" of charge generation or due to a large change in the charge carrier lifetime. It could be speculated that the addition of the $Ag_2S$ passivates surface traps in the $Bi_2S_3$ that, in absence of any $Ag_2S$, fails to transport electrons to the $TiO_2$ and eventually FTO. Without the $Ag_2S$ it is possible that, although these trap states limit the current generated by the device, they have little effect the recombination dynamics with the SPIRO.

After addition of the $Ag_2S$ the charge generation efficiency does increase slightly. As the signal is scaled for the amount of pump photons absorbed, this increase is not due to the fact that more light is being absorbed at 510 nm upon the addition of the $Ag_2S$. The reason for the increase in the efficiency is either due to the $Ag_2S$ more efficiently transferring holes to SPIRO than the $Bi_2S_3$, or that the addition of the $Ag_2S$ increases the efficiency of hole transfer from $Bi_2S_3$ to SPIRO, perhaps through the creation of the energy cascade. The high signals seen for the hole transfer of $Ag_2S$ to SPIRO on nanoporous $TiO_2$ suggest that perhaps the former explanation is the more likely of the two. As more $Ag_2S$ is added the amplitude starts to decrease slightly. The reason for this becomes apparent when looking at the morphology of these films as viewed by scanning electron microscopy (SEM) (See Figure 6.14).

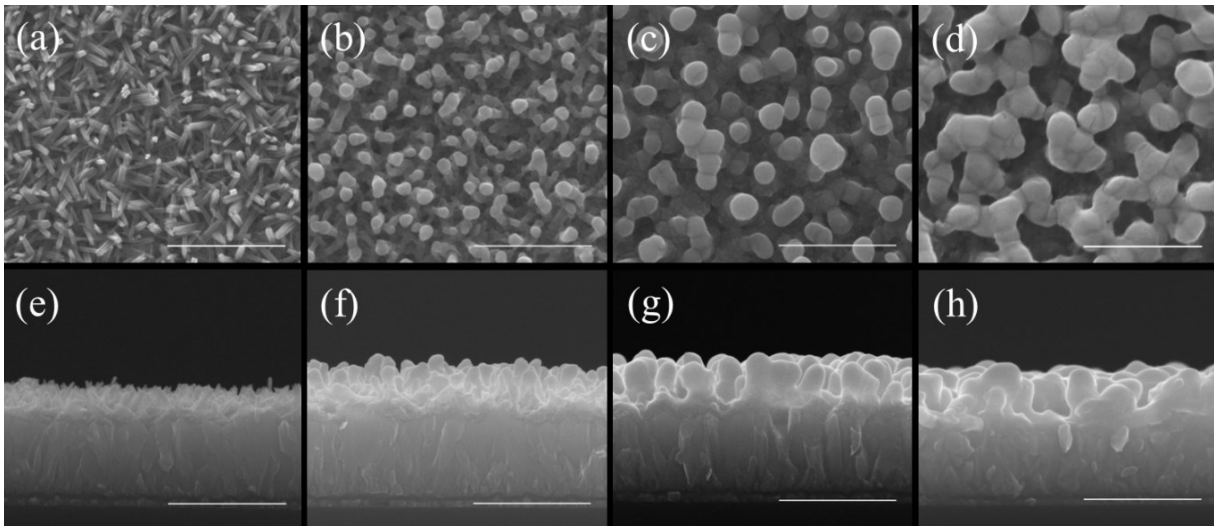



*Figure 6.14 - (a,b,c,d) Top-down SEM images of nanostructures fabricated with no $Ag_2S$, 4 Cycles, 16 Cycles and 32 Cycles respectively. (e,f,g,h) Side-on SEM images of the same sample as is located above. Scale bars are 500 nm. Figure kindly provided by Yiming Cao.*

In Figure 6.14a, where only the $Bi_2S_3$ rods are present and no $Ag_2S$, very fine rods can be observed, with a large amount of empty space in between them. As the $Ag_2S$ is added, it does more than just coat the outside of the rods, it also causes the coated rods to aggregate together into what look like smooth blobs. The observation of this unusual morphology fits with the observation of the "switching on" of the current with the addition of $Ag_2S$ and also the trend in amplitude of the TAS decays. It appears that after 4 Cycles of SILAR (Figure 6.14b) the outside of the $Bi_2S_3$ rods is completely coated. Whatever the mechanism by which this coating "switches on" on the current can still only be speculated upon, however it is clear that it is only a coating that is required. The extra $Ag_2S$ that is added and as a result enhances the IPCE in the IR is due to the extra absorption of $Ag_2S$. As more of this is added however, even though the IPCE is enhanced, the charge generation efficiency is decreased, most likely due to the reduction in surface area of the SPIRO/$Ag_2S$ interface. The reduction in surface area also has a small effect on the lifetime of charges and a small increase in halftime is observed. It is reasonable to assume that if even more SILAR cycles were performed then the amplitude would continue to decrease and the lifetime would also increase. At a certain point this would begin to affect the photovoltaic performance of the device, as the decrease in charge generation efficiency overweighed the increase in IR light absorption.

## Conclusions

In conclusion, transient absorption spectroscopy (TAS) has been shown to be a useful tool in the study of two separate organic semiconductor/$Bi_2S_3$ heterojunctions. First of which was a P3HT/$Bi_2S_3$ nanoparticle blend solar cell. The charge generation yield in this system was investigated and a trade-off between generation yield and charge lifetime was highlighted, with higher annealing temperatures causing a reduction in yield but an increase in lifetime. These blends were then compared to a novel thiol-functionalised P3HT based block copolymer (P3HT-SH) that, when blended with P3HT and $Bi_2S_3$ nanoparticles, demonstrated superior photovoltaic performance in comparison to a blend of P3HT/$Bi_2S_3$. TAS showed that the electron transfer yield from the P3HT/P3HT-SH to the $Bi_2S_3$ was increased in comparison to P3HT, thought to be due to a combination of a finer morphology and enhanced electronic coupling between the polymer and nanoparticles, as demonstrated by an increase in exciton quenching in solution-based photoluminescence spectroscopy. The lifetime of photogenerated charges was observed to increase in the case of the blend, thought to be due to an energy cascade that could exist within the films, due to a HOMO energy offset that was measured between the P3HT-SH and P3HT.

Secondly, TAS was used to obtain a better understanding of the charge transfer at several interfaces in a vertically structured $Bi_2S_3$ nanorod array, the pores of which were filled with SPIRO. These devices showed almost no photovoltaic performance without performing SILAR on the $Bi_2S_3$ rods to coat them with a layer of $Ag_2S$. The addition of the $Ag_2S$ appeared to “switch on” the functionality of the device as well as extending the light absorption into the IR. However, TAS showed that the charge generation yield and lifetime without the $Ag_2S$ was approximately the same and that the lack of performance was therefore due to another factor, such as electron transport in the $Bi_2S_3$. The increasingly coarse morphology of these layers generated by a high number of SILAR cycles was linked to an eventual decrease in the charge generation of these devices, due to a reduction in the pore size and as a result the interfacial area between the inorganic and organic hole transporting phase. The charge lifetime was however seen to increase with this decrease in yield.

TAS has once again demonstrated that it can act as a very simple tool that can be used to obtain a more detailed understanding of the charge generation and charge dynamics within hybrid heterojunctions. This collaboration also highlights the fact that $Bi_2S_3$, when fabricated with a high degree of control, can be manufactured into a working solar cell. This work also provides valuable information about the parameters that can influence device performance, such as, electronic coupling, morphology, energy cascades and nanoparticle surface modification, which could all be combined in order to push up the efficiency of non-toxic hybrid solar cells.

# References


(1) *2001: A Space Odyssey.* [Film] Directed by: Stanley Kubrick. USA: Metro-Goldwyn-Mayer; 1968.

(2) Riley, D. J.; Waggett, J. P.; Wijayantha, K. G. U. *J. Mater. Chem.* 2004, *14*, 704.

(3) Zhao, L.-D.; Zhang, B.-P.; Liu, W.-S.; Zhang, H.-L.; Li, J.-F. *J. Solid State Chem.* 2008, *181*, 3278.

(4) Martinez, L.; Higuchi, S.; MacLachlan, A. J.; Stavrinadis, A.; Miller, N. C.; Diedenhofen, S. L.; Bernechea, M.; Sweetnam, S.; Nelson, J.; Haque, S. A.; Tajima, K.; Konstantatos, G. *Nanoscale* 2014, *6*, 10018.

(5) Cao, Y.; Bernechea, M.; Maclachlan, A.; Zardetto, V.; Creatore, M.; Haque, S. A.; Konstantatos, G. *Chem. Mater.* 2015, *27*, 3700.

(6) Martinez, L.; Bernechea, M.; de Arquer, F. P. G.; Konstantatos, G. *Adv. Energy Mater.* 2011, *1*, 1029.

(7) Martinez, L.; Stavrinadis, A.; Higuchi, S.; Diedenhofen, S. L.; Bernechea, M.; Tajima, K.; Konstantatos, G. *PCCP* 2013, *15*, 5482.

(8) Querner, C.; Benedetto, A.; Demadrille, R.; Rannou, P.; Reiss, P. *Chem. Mater.* 2006, *18*, 4817.

(9) Liu, J.; Tanaka, T.; Sivula, K.; Alivisatos, A. P.; Fréchet, J. M. J. *J. Am. Chem. Soc.* 2004, *126*, 6550.

(10) Xu, J.; Wang, J.; Mitchell, M.; Mukherjee, P.; Jeffries-El, M.; Petrich, J. W.; Lin, Z. Q. *J. Am. Chem. Soc.* 2007, *129*, 12828.

(11) Ren, S.; Chang, L. Y.; Lim, S. K.; Zhao, J.; Smith, M.; Zhao, N.; Bulovic, V.; Bawendi, M.; Gradecak, S. *Nano Lett.* 2011, *11*, 3998.

(12) Oosterhout, S. D.; Koster, L. J. A.; van Bavel, S. S.; Loos, J.; Stenzel, O.; Thiedmann, R.; Schmidt, V.; Campo, B.; Cleij, T. J.; Lutzen, L.; Vanderzande, D.; Wienk, M. M.; Janssen, R. A. J. *Adv. Energy Mater.* 2011, *1*, 90.

(13) Wang, H.; Oey, C. C.; Djurišić, A. B.; Xie, M. H.; Leung, Y. H.; Man, K. K. Y.; Chan, W. K.; Pandey, A.; Nunzi, J.-M.; Chui, P. C. *Appl. Phys. Lett.* 2005, *87*.

(14) Goh, C.; Coakley, K. M.; McGehee, M. D. *Nano Lett.* 2005, *5*, 1545.

(15) Williams, S. S.; Hampton, M. J.; Gowrishankar, V.; Ding, I. K.; Templeton, J. L.; Samulski, E. T.; DeSimone, J. M.; McGehee, M. D. *Chem. Mater.* 2008, *20*, 5229.

(16) Kang, Y. M.; Park, N. G.; Kim, D. *Appl. Phys. Lett.* 2005, *86*.

(17) Kang, Y.; Kim, D. *Sol. Energy Mater. Sol. Cells* 2006, *90*, 166.

(18) Saito, M.; Fujihara, S. *Energy Environ. Sci.* 2008, *1*, 280.

(19) Lee, W.; Min, S. K.; Dhas, V.; Ogale, S. B.; Han, S.-H. *Electrochem. Commun.* 2009, *11*, 103.

(20) Yin, Z.; Wu, S.; Zhou, X.; Huang, X.; Zhang, Q.; Boey, F.; Zhang, H. *Small* 2010, *6*, 307.

(21) Olson, D. C.; Piris, J.; Collins, R. T.; Shaheen, S. E.; Ginley, D. S. *Thin Solid Films* 2006, *496*, 26.

(22) Clarke, T. M.; Ballantyne, A. M.; Nelson, J.; Bradley, D. D. C.; Durrant, J. R. *Adv. Funct. Mater.* 2008, *18*, 4029.

(23) Hwang, I.-W.; Moses, D.; Heeger, A. J. *J. Phys. Chem. C* 2008, *112*, 4350.

(24) O'Mahony, F. T. (2014) *Solution-Processed Inorganic Semiconductors in Hybrid Photovoltaics: Mechanisms of Charge Separation and Effects of Interface Structure.* PhD Thesis. Imperial College London.

(25) Lokteva, I.; Radychev, N.; Witt, F.; Borchert, H.; Parisi, J. r.; Kolny-Olesiak, J. *J. Phys. Chem. C* 2010, *114*, 12784.

(26) Korovyanko, O. J.; Österbacka, R.; Jiang, X. M.; Vardeny, Z. V.; Janssen, R. A. J. *Phys. Rev. B* 2001, *64*, 235122.

(27) Noori, K.; Giustino, F. *Adv. Funct. Mater.* 2012, *22*, 5089.

(28) Jamieson, F. C.; Domingo, E. B.; McCarthy-Ward, T.; Heeney, M.; Stingelin, N.; Durrant, J. R. *Chemical Science* 2012, *3*, 485.

(29) Dowland, S. A.; Reynolds, L. X.; MacLachlan, A.; Cappel, U. B.; Haque, S. A. *J. Mater. Chem. A* 2013, *1*, 13896.

(30) Andersson, L. M.; Müller, C.; Badada, B. H.; Zhang, F.; Würfel, U.; Inganäs, O. *J. Appl. Phys.* 2011, *110*.

(31) Credgington, D.; Hamilton, R.; Atienzar, P.; Nelson, J.; Durrant, J. R. *Adv. Funct. Mater.* 2011, *21*, 2744.

(32) Lutz, T.; MacLachlan, A.; Sudlow, A.; Nelson, J.; Hill, M. S.; Molloy, K. C.; Haque, S. A. *PCCP* 2012, *14*, 16192.

(33) O'Mahony, F. T. F.; Lutz, T.; Guijarro, N.; Gomez, R.; Haque, S. A. *Energy Environ. Sci.* 2012, *5*, 9760.

# Chapter 7

## Conclusions and Future Work

*Marty McFly: Doc, about the future…*

*Dr. Emmett Brown: No! Marty! We've already agreed that having information about the future can be extremely dangerous. Even if your intentions are good, it can backfire drastically!*

*Back to the Future (1985)*[1]

# Conclusions

This work has intended to gain further insight into the potential of *in-situ* fabricated polyer/metal sulfide photovoltaics. The ability to tune the morphology of *in-situ* blends was first investigated for P3HT/CdS and then P3HT/$Sb_2S_3$ blends. A fully non-toxic hybrid system was then tested in P3HT/$Bi_2S_3$, something that proved more difficult than expected. The charge photogeneration in *ex-situ* polymer/$Bi_2S_3$ systems was then studied to shed some light on the efficiency of this key process in at these hybrid $Bi_2S_3$ interfaces.

In Chapter 4, this study shows how the nanomorphology of *in-situ* prepared hybrid solar cells can be tuned efficiently by the design of the molecular nanocrystal precursors. Small changes in the structure of the used metal xanthates induce significant changes in the obtained absorber layer nanomorphologies. In the case of the cadmium xanthates studied, the longer alkyl chains of the xanthate moieties lead to a better mixing of the polymer and nanoparticle phase, to smaller domain sizes and a lower crystallinity of the polymer phase in the P3HT/CdS absorber layers. In the case of the antimony xanthates studied, the ligand moiety of metal xanthate precursors has been shown, again, to have an influence on the morphology of *in-situ* fabricated polymer/nanoparticle blends. In contrast to the cadmium xanthates, when the pentyl ligand was used, larger domain sizes were observed, in comparison to equivalent films fabricated from the ethyl precursor.

The different nanomorphologies strongly influence the optoelectronic properties of the absorber layers and in turn also the performance of the hybrid solar cells and a complex interplay between these parameters is disclosed by the performed characterisations. The highest level of quenching of the photoluminescence of the polymer phase by the CdS nanocrystals was found for the heptyl sample, indicating that the heptyl sample was the most intimately mixed. This was also supported by fs-TAS showing the shortest P3HT exciton lifetime in this system. However, optimum charge generation, probed by µs-TAS, was observed in the pentyl sample. Overall, the best power conversion efficiencies were obtained with hybrid solar cells prepared using propyl xanthates. This originates from the fact that besides efficient charge generation also charge transport and recombination play a crucial role in the devices, which were found out to become more and more an issue when going to finer mixed morphologies.

In Chapter 5, this study presents the proof of concept that bismuth xanthate complexes can be used as precursors to $Bi_2S_3$ for use in hybrid solar cells. Their use has been shown to grow needle-like structures in a solid state polymer matrix and also porous mesostructures have been created that can be infiltrated with a hole conductor. The nature of the material created in both cases has been shown to be highly crystalline, even when processed at low temperatures, and shows no sign of containing impurities. Both

the blends and mesostructures exhibit remarkably high absorption across the entire visible region of the spectrum.

The efficacy of these materials has been difficult to measure spectroscopically due to the large ground-state absorption, but in the mesostructured case long-lived charge separation is observed, initiated primarily by hole transfer from the mesostructure to the organic polymer. The charge transfer in the mesostructured system was seen to be highly dependent on a surface treatment of the structure with pyridine, perhaps passivating surface states on the $Bi_2S_3$ and effectively turning on the charge generation.

Devices fabricated from these two systems were inefficient to say the least, with the control neat polymer devices showing the highest power conversion efficiency in all cases. Despite this, the mesostructured devices did show a contribution to the photocurrent from the $Bi_2S_3$ as measured by the IPCE. This measurement shows that it is possible to fabricate devices using this method, and with more time and investigation into the processing, use of additives and trialling of a range of different polymers, perhaps a device with a PCE of a higher significance could be obtained.

In Chapter 6 TAS was shown to be a useful tool in the study of two separate organic semiconductor/$Bi_2S_3$ heterojunctions. First of which was a P3HT/$Bi_2S_3$ nanoparticle blend solar cell. The charge generation yield in this system was investigated and a trade-off between generation yield and charge lifetime was highlighted, with higher annealing temperatures causing a reduction in yield but an increase in lifetime. These blends were then compared to a novel thiol-functionalised P3HT based block copolymer (P3HT-SH) that, when blended with P3HT and $Bi_2S_3$ nanoparticles, demonstrated superior photovoltaic performance in comparison to a blend of P3HT/$Bi_2S_3$. TAS showed that the electron transfer yield from the P3HT/P3HT-SH to the $Bi_2S_3$ was increased in comparison to P3HT, thought to be due to a combination of a finer morphology and enhanced electronic coupling between the polymer and nanoparticles, as demonstrated by an increase in exciton quenching in solution-based photoluminescence spectroscopy. The lifetime of photogenerated charges was observed to increase in the case of the blend, thought to be due to an energy cascade that could exist within the films, due to a HOMO energy offset that was measured between the P3HT-SH and P3HT.

Secondly, TAS was used to obtain a better understanding of the charge transfer at several interfaces in a vertically structured $Bi_2S_3$ nanorod array, the pores of which were filled with SPIRO. These devices showed almost no photovoltaic performance without performing SILAR on the $Bi_2S_3$ rods to coat them with a layer of $Ag_2S$. The addition of the $Ag_2S$ appeared to “switch on” the functionality of the device as well as extending the light absorption into the IR. TAS, however, showed that the charge generation yield and lifetime without the $Ag_2S$ was approximately the same and that the lack of performance was

therefore due to another factor, such as electron transport in the $Bi_2S_3$. The increasingly coarse morphology of these layers generated by a high number of SILAR cycles was linked to an eventual decrease in the charge generation of these devices, due to a reduction in the pore size and as a result the interfacial area between the inorganic and organic hole transporting phase. The lifetime time was however seen to increase with this decrease in yield.

Overall, this work provides two key observations, which will be of use to the wider community of hybrid photovoltaics.

1. The structure ligand moiety of metal xanthate complexes plays an important role in the *in-situ* fabrication of hybrid polymer/nanoparticle devices. Modification of precursor materials will be a useful tool in the fabrication of a range of inorganic compounds for use in such hybrid devices.
2. TAS measurements of CdS, $Sb_2S_3$ and $Bi_2S_3$ have shown that hole transfer is a relatively more efficient process in hybrid systems than electron transfer and that this hole transfer is less affected by the morphology of the heterojunction. This reaffirms the belief that the focus of hybrid research should be towards finding an inorganic low band gap material that is combined with a polymer that acts as mainly a hole transport material.

## Suggestions for Further Work

It would be easy to list several areas of new research that I believe would be interesting and could achieve high impact results. Perhaps a relevant question is: What would I research if I had 6 more months of PhD remaining?

### Antimony Sulfide Blends

- Investigate a further range of ligand moieties, including and beyond those studied for CdS. If the domain size is reduced to the 10s of nanometres scale then I believe efficiencies of above 5% can be achieved.
- Optimise the device structure of these $Sb_2S_3$ devices and test with a range of high mobility state-of-the-art hole conductors.

### Untested Multi-Component Sulfide Blends

- The xanthate methodology has been shown to work for ternary systems and there are many more non-toxic low band gap semiconductors yet to be attempted.

# References

(1) *Back to the Future.* [Film] Directed by: Robert Zemeckis. USA: Universal Pictures; 1985.